X-ray analysis of a complete sample of galaxy clusters

Dissertation
zur
Erlangung des Doktorgrades (Dr. rer. nat.)
der
Mathematisch-Naturwissenschaftlichen Fakultät
der
Rheinischen Friedrich-Wilhelms-Universität Bonn

vorgelegt von
Gerrit Schellenberger
aus
Kronach

Bonn, 2015

Angefertigt mit Genehmigung der Mathematisch-Naturwissenschaftlichen Fakultät der Rheinischen Friedrich-Wilhelms-Universität Bonn

1. Gutachter:	Prof. Dr. Thomas H. Reiprich
2. Gutachter:	PD Dr. Jürgen Kerp
Tag der Promotion:	9.3.2016
Erscheinungsjahr:	2016

Abstract

Modern cosmology tries to trace the history and predict the future of our Universe. Great achievements have been made by the discovery of the accelerated expansion, the claim for Dark Matter and Dark Energy, the detection and interpretation of the cosmic microwave background (CMB), or the study of the visible large scale structure of our Universe.
Galaxy clusters can be described as the most massive and gravitationally bound systems that evolved out of collapsed overdensities in the early Universe, and therefore witness its history. Observationally one can study galaxy clusters at almost any wavelength, but the X-ray regime takes a key role due to the visibility of the hot plasma between the galaxies, which is the most massive visible component. The aim of this work is to analyze a complete sample of galaxy clusters in detail and constrain cosmological parameters, like the matter density, Ω_m, or the amplitude of initial density fluctuations, σ_8. The purely flux limited sample (HIFLUGCS) consists of the 64 X-ray brightest galaxy clusters, which are excellent targets to study the systematic effects, which can bias results and lead to wrong conclusions.
With current X-ray observatories like Chandra and XMM-Newton, galaxy clusters can be analyzed in detail, e.g., by measuring the plasma temperature and the surface brightness to constrain the total gravitating mass. This quantity is of extraordinary importance for cosmological studies. Unfortunately, the calibration of X-ray instruments is challenging, because of the absence of absolute calibration targets. In a cross calibration study of the instruments onboard Chandra and XMM-Newton using the HIFLUGCS galaxy clusters sample, I find that systematic differences exist, which cause temperature measurements to deviate significantly and systematically: Chandra ACIS gives higher temperatures than any XMM-Newton EPIC detector (MOS1, MOS2, PN), and the difference increases with increasing temperature (23% between ACIS and EPIC-PN in the full energy band at 10 keV plasma temperature). Even the three EPIC detectors do not agree with each other. In the hard energy band the differences are not significant. Systematics like the different angular resolutions or possible multitemperature structure of the gas do not explain the observed differences. Tests such as a comparison of the soft band absorption by the Milky Way ISM (free-N_H), or the consistency between soft and hard band temperatures of the same instrument seem to theoretically be able to select the best calibrated instrument, but due to large uncertainties (abundance distribution of heavy elements, multitemperature structure) no clear conclusion can be made.
In a second part I derive the total (hydrostatic) and gas masses of all HIFLUGCS clusters individually from the X-ray data. The cosmological analysis of the HIFLUGCS masses using Chandra data (HICOSMO) involves a likelihood estimation of a halo mass function with a Markov Chain Monte Carlo algorithm. The result is $\Omega_\mathrm{m} = 0.168^{+0.021}_{-0.019}$ and $\sigma_8 = 0.898^{+0.051}_{-0.048}$, assuming a flat ΛCDM Universe. Since the sample consists of local clusters, no tight constraints can be made for the Dark Energy. The gas mass fraction of each galaxy cluster is also compared with simulations, which constrain $\Omega_\mathrm{m} = 0.246^{+0.007}_{-0.007}$. Since the halo mass function results deviate from current CMB anisotropy results, several tests to understand the systematics involved are performed. Subsamples containing only the high redshift clusters ($z > 0.05$) or relaxed objects seem to show more agreement with WMAP9 results, especially when adding a hydrostatic bias of 10-30%, which increases all hydrostatic masses due to nonthermal pressure in the gas. Also galaxy groups, which are not represented in the high redshift sample, seem to influence results, as shown by the decrease of the predicted number of groups in the halo mass function, which also shifts results toward the CMB constraints. The more dominant influence of baryonic physics in galaxy groups cannot be proven to solve the discrepancy, since a mass function including feedback, gas heating and radiative cooling has almost no influence on the results. Since also the f_gas test suggests an insufficient modeling of low mass systems by the simulations, this aspect needs to be studied in more detail in future hydrodynamic simulations.
The final chapter looks in more detail at one galaxy cluster (Z8338) experiencing an interesting interaction of the cluster ICM with the gas of an infalling galaxy, which leads to one of the longest X-ray tails ever observed. In this case, the tail, caused by stripping of galactic gas, is offset from the galaxy, which has never been observed so clearly before, but predicted by simulations. This scenario can show how the cluster environment is enriched with heavy elements and helps to understand the evolution of galaxy clusters.
Future prospects include the study of the larger flux limited sample (eHIFLUGCS) to further quantify the effect of galaxy groups and reduce the uncertainties by the $\sim 50\%$ increase in statistical power. Instrumental uncertainties can be solved, e.g., by incorporating the emission line ratio temperatures in the analysis and increase the number of objects for the free-N_H test.

Contents

CHAPTER 1

Introduction

Galaxy clusters are the largest gravitationally relaxed objects in the Universe. In cosmology they can be used to trace the large scale structure of the Universe and witness the structure formation history to solve some of the fundamental questions in science: What is the Universe made of? How does it evolve in the future? As we currently believe, the two most important components in terms of energy today are Dark Matter and Dark Energy, which we both understand very poorly. As I will explain in this work, galaxy clusters play a key role in understanding the Universe. Any cosmological theory needs to be able to explain the distribution and composition of galaxy clusters.

Most of the galaxy clusters even in our local Universe have not even been found yet. Roughly around 10 000 confirmed galaxy clusters are know, but this number will increase dramatically in the near future. So we are facing a golden age of cosmology and especially X-ray astronomy, since many new missions will be started soon and almost always galaxy clusters are one of the leading science topics, because they can be observed in many wavelengths under various aspects.

In this work I focus my analysis on a complete and flux limited sample of 64 nearby but very bright galaxy clusters, in order to understand physical processes and systematics involved in cosmological constrains based on X-ray galaxy cluster data. Some aspects presented here have never been shown in a cosmological context before.

I start by introducing galaxy clusters and their observational characteristics (Section 1.1), followed by a brief description of the sample of interest here (Section 1.1.3). Two wavelength regimes and their relation to galaxy clusters are introduced, X-rays (Section 1.1.4, which is of special interest here and remark on important missions is added (Section 1.2), and the sub-millimeter band with the Sunyaev-Zeldovich effect (Section 1.3).

Chapter 2 deals with the cosmological background for this work and introduce the important elements. Of special importance here is the theory of structure formation (Section 2.2) and the halo mass function (Section 2.3).

Chapter 3 was published in Schellenberger et al. (2015)[1] and shows the instrumental calibration uncertainties among five instruments on the major X-ray observatories, Chandra and XMM-Newton.

Chapter 4 is shows the detailed analysis of the HIFLUGCS clusters from Chandra X-ray data, by determining the hydrostatic masses individually and discussing the cosmological constraints. Staring from a detailed overview on the sample (Section 4.2), I describe the crucial steps of the data reduction (Section 4.3). Of particular interest here is the substructure classification (Section 4.3.3), finding the optimal energy band (Section 4.3.4), the temperature deprojection (Section 4.3.5) and the mass extrapolation techniques (Section 4.3.6). The cosmological analysis is presented in Section 4.4, followed by a detailed discussion (Section 4.5) on the systematic effects, e.g., extrapolation differences (Section 4.5.2), galaxy cluster physics (Section 4.5.3), and assumptions in the theoretical model (Section 4.5.5).

Chapter 5 was published in Schellenberger and Reiprich (2015)[2] and describes the newly found X-ray tail in the cluster Z8338 and illustrates its possible origin.

[1] Schellenberger, G., Reiprich, T. H., Lovisari, L., Nevalainen, J., and David, L.: 2015, A&A 575, A30
[2] Schellenberger, G. and Reiprich, T. H.: 2015, A&A 583, L2

In Chapter 6 I summarize the important aspects and give conclusions. Furthermore, I give for two specific examples, the line ratio temperature determination and the $L_x - T$ relation for eHIFLUGCS clusters, an outlook for future projects.

1.1 Clusters of galaxies

One can look at galaxy clusters not only as grown and collapsed overdensities of an initial matter density distribution, as some theoretical considerations do (Chapter 2), but also as unique astrophysical laboratories. Many fascinating subjects of galaxy clusters can be studied:

- The constituents of galaxy clusters, e.g., the mass fraction of baryonic matter, can also be related to the whole Universe.
- The enrichment and distribution of heavy elements in the Universe is traced very well in galaxy clusters, since, unlike galaxies, they retain all the gas. Elements can be traced in galaxy clusters and their distribution allows to draw conclusions on the origin and how they are removed from stellar systems and galaxies.
- Some emission lines of elements can only be detected under these extreme conditions, like in the hot intracluster gas. This gives new insights to atomic physics.
- The most energetic collisions of matter happen when galaxy clusters collide. This is a unique test for Dark Matter models to study the gravitational, and maybe even non-gravitational interactions. Furthermore, the frequency of these events challenges the cosmological model.

1.1.1 Discovery of galaxy clusters

When Ernest Öpik (Öpik, 1922) calculated the distance to the Andromeda nebula by comparing the velocity dispersion to the luminosity, a surprisingly high value (450 kpc) clearly identified this object to be outside the Milky Way and opened the epoch of extragalactic astronomy. Even before a nebulae concentration in the Perseus constellation was found (Wolf, 1906) and referred to as "cluster". As technology improved, more and more of these galaxy overdensities were found. The famous Abell catalog (Abell, 1958) containing 2712 nearby galaxy clusters with many member galaxies (plus 1361 from the southern hemisphere added later) is still important today and clusters in there are referred to as the "Abell" clusters.
A breakthrough for galaxy cluster astrophysics was the conquest of the X-ray regime for astronomy. An Aerobee rocket launched in 1965 detected X-ray emission in the Virgo Cluster (Byram et al., 1966) which proved the existence of a hot ionized intra cluster medium (ICM), a gas that fills the voids between galaxies in a cluster. In order to further explore the X-ray sky, satellites were needed, so years later *Uhuru*, the first X-ray satellite was launched and detected many sources outside the galactic plane (Giacconi et al., 1972). These newly detected X-ray sources were related to known galaxy clusters.

At this time the field of cosmology had already made several discoveries with enormous impact on how we see the Universe, like the cosmological redshift (Hubble, 1936) implying an expanding Universe, or the claim for an unknown type of matter (Dark Matter), which was introduced by Fritz Zwicky when he noticed the high velocity dispersions of galaxies in galaxy clusters (Zwicky, 1933). Fritz Zwicky did not know about the X-ray bright gas in galaxy clusters, which is one order of magnitude more massive then all the member galaxies, when introducing the new type of matter. His claim was confirmed later by detailed X-ray observations measuring the ICM mass from the X-ray surface brightness, because it turned out that neither the galaxies nor the ICM are the dominant matter component in galaxy clusters, but an invisible, most likely non baryonic type of matter, whose mystery is still not solved.

1.1.2 Observational characterization of galaxy clusters

Galaxy clusters are very interesting objects and the studied properties and considered context varies among wavelengths. In the radio band, radio lobes, halos, relics and active galactic nuclei (AGNs) reveal interesting insights about the astrophysical processes within galaxy clusters, e.g., how heavy elements are mixed in the medium or how the cooling of the gas is controlled. Sub-millimeter observations measuring

the Sunyaev-Zeldovich (SZ) effect have become extremely popular, especially with the current powerful instruments like Planck, SPT or ACT. SZ surveys provide catalogs of clusters of galaxies with different selection properties then optically or X-ray selected samples: Due to a signal-to-noise cut, SZ samples often show at lower redshifts a pure mass cut. Of course with optical instruments one is able to identify galaxy overdensities and even determine the mass of this clusters via weak lensing studies, while in γ-rays one can only study possible non-thermal emission or try to detect Dark Matter annihilation signals. So in order to define galaxy clusters, one can consider them as a local gravitationally bound overdensity of galaxies which are pervaded by a hot optically thin gas visible in X-rays. An overview on how these objects have been formed is given in Chapter 2. Four main components are necessary to build a galaxy cluster (see e.g. Sarazin, 1988; Reiprich, 2001):

- **Galaxies**: Clusters of galaxies consist of roughly 100 – 1000 gravitationally bound galaxies (without dwarf galaxies). Agglomerations of fewer galaxies are usually called galaxy groups (Hickson, 1982). Galaxy clusters can be characterized by their *richness*, i.e. how many galaxies are associated with the cluster. For this purpose, all galaxies should be counted within a characteristic radius and a magnitude limit (Abell, 1958).

- **Intra cluster Medium (ICM)**: The ICM is the gas between the galaxies in the cluster. It is $\sim 5-10$ times more massive than all the stars in all the cluster member galaxies and has a temperature of several 10^7 K, usually expressed in keV ($\frac{1\,\mathrm{keV}}{k_\mathrm{B}} \approx 1.16 \times 10^7$ K, k_B is the Boltzmann constant). More parameters of this medium are explained in Section 1.1.4.

- **Dark Matter**: The sum of the mass of all galaxies in a cluster and the mass of the ICM is not sufficient to explain velocity dispersions of galaxies in the cluster. To solve this problem, an unknown matter component (Dark Matter) is added. This new matter component can also explain anisotropies in the Cosmic Microwave Background radiation (CMB), and should not interact electromagnetically, i.e. no radiation (apart from possible annihilation signals) is emitted. Recent studies showed that an emission line visible in the X-rays at 3.5 keV found in stacked galaxy cluster spectra (Bulbul et al., 2014), Andromeda (Boyarsky et al., 2014) and the Milky Way center (Riemer-Sorensen, 2014) can be attributed to sterile neutrinos with a mass of 7.1 keV. Theoretical models would not exclude such a particle, but other studies raised doubts (e.g., Jeltema and Profumo, 2015), whether the detected emission line could really be attributed to a new particle, or not better be explained e.g., by some overabundance of potassium. When comparing a Dark Matter distribution of a merging galaxy cluster (inferred from weak lensing) with the distribution of individual galaxies, one could detect a small offset between the two, which was explained by a self interaction of Dark Matter causing the collisionless galaxies to move along faster (Massey et al., 2015). Up to now Dark Matter was expected to only interact gravitationally, so also a self-interaction was not expected. Neutrinos are referred to as Hot Dark Matter and have a free-streaming length, in contrast to the Cold Dark Matter. Most of the particle candidates for Cold Dark Matter haven't been observed yet.

- **Relativistic particles**: Velocities close to the speed of light enable these particles to emit diffuse synchrotron radiation (Willson, 1970). Their contribution to the total mass is negligible, but they are of importance to understand mixing processes in individual clusters.

Despite the many possibilities to characterize galaxy clusters, especially in X-rays, such as luminosity or temperature, the most fundamental quantity is the gravitating mass, since it is not restricted to any wavelength or constituent, but can be directly compared to theoretical predictions.

Cool-core and AGN

A very important quantity to look at when analyzing the ICM emsission of galaxy clusters is the timescale on which the cluster is able to cool down. This cooling time (t_cool) is defined as the ratio of the internal energy of the gas and its emissivity and can be simplified to:

$$t_\mathrm{cool} = \frac{3(n_\mathrm{e} + n_\mathrm{i})k_\mathrm{B}T}{2\epsilon} \ , \tag{1.1}$$

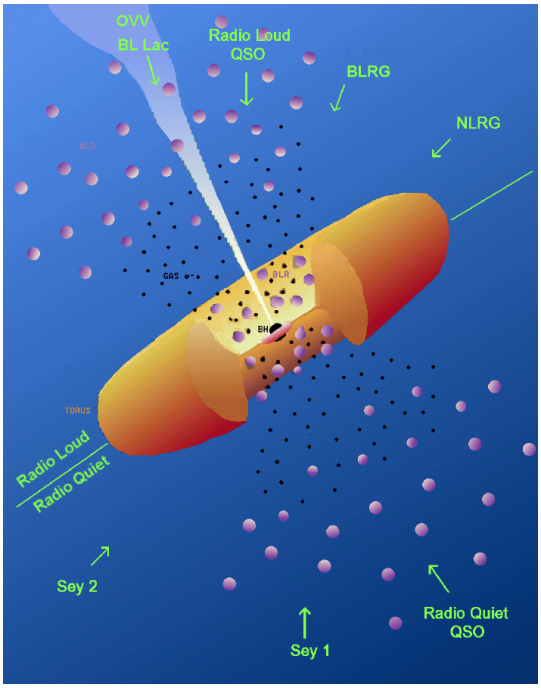

Figure 1.1: Unified AGN model showing the different classifications based on the inclination angle (green arrows). Seyfert type 1 and type 2 galaxies (Sey 1/2) are the equivalent to BLRG and NLRG galaxies but without radio emission. Diagram by M. Polletta, ITESRE/CNR, Bologna, Italy; based on Urry and Padovani (1995).

where T is the electron temperature of the gas and n_e and n_i are the electron and ion number densitities, respectively. The emissivity ϵ is the luminosity per volume (see Equation 1.5). In low density regions of hot clusters this timescale is larger than the age of the Universe, but it drops dramatically in the central, high density regions leading to the "cooling flow" model (Fabian, 1994). Since this cooling flow has not been observed, there must exist a heating source in the cluster center. Active galactic nuclei (AGNs) are one of the best candidates for this heating mechanisms. For this analysis, the outer regions of galaxy clusters are more important, and therefore the effects of AGN feedback are not discussed in more detail. For completeness, I briefly summarize the import aspects of these objects:

First evidence of AGNs were seen in strong emission lines in the center of spiral galaxies (Fath, 1909; Seyfert, 1943). Objects could be subdivided into those with narrow (Seyfert type 2 galaxies), and those with broad emission lines (Seyfert type 1 galaxies). In the radio regime strong sources were found independently, and also characterized as radio galaxies (broad and narrow line radio galaxies; BLRG, NLRG). Later, also X-ray instruments detected counterparts of these objects. One can unify these different observations to the same type of a highly luminous object: In the center of a galaxy is a supermassive black hole ($M \sim 10^7\,\mathrm{M}_\odot$), which is surrounded by an accretion disk and a dust torus. The source of energy for the emission is the mass accretion process, which accumulates infalling gas in the rotating disk and turns about half of the potential energy into heat. Perpendicular to the layer of the disk (and torus) is a jet of relativistic particles. Dependent on the inclination angle, one can either see the broad emission lines (from a region between the torus and the black hole), narrow emission lines (from gas outside the torus), or blazars, when the line of sight falls into the jet (see also Fig. 1.1). In general AGNs are highly luminous objects across wavelengths, with emission originating from a very small region. A special type of AGNs are the quasi-stellar radio sources (Quasars), which are a strong radio source with an optical counterpart. Often the term Quasar (or also QSO, for sources without radio emission) are used generically for AGNs.

X-ray selected samples of galaxy clusters

Apart from X-rays, galaxy clusters can be selected in the optical and SZ regime (see Section 1.3), which leads to different selection functions implying certain properties of the selected clusters. The first samples

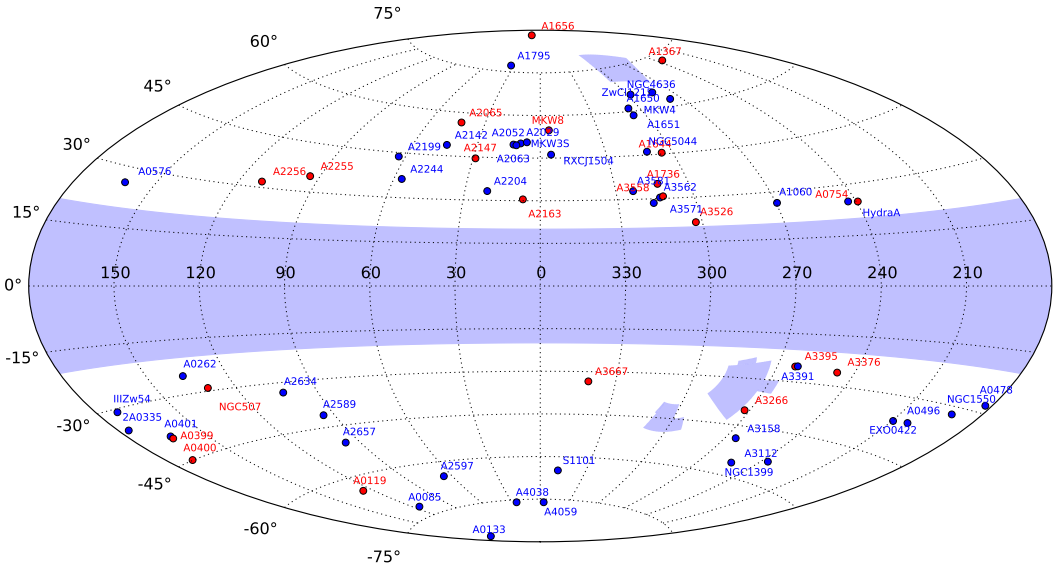

Figure 1.2: Map in galactic coordinates (in Aitoff projection) showing the position of the 64 HIFLUGCS clusters. The red circles indicate disturbed clusters as characterized in Vikhlinin et al. (2009a). The shaded area represents the excluded regions by HIFLUGCS.

were constructed from an optical selection leading to projection effects and a large uncertainty in the mass determination. The SZ effect is in principle redshift independent as long as the angular size of the cluster is not much smaller than the PSF of the instrument. But until today the most effective way to determine galaxy clusters is in X-rays (Giles et al., 2015): The high X-ray luminosity of galaxy clusters and the number of different probes to trace the true mass of the cluster, like X-ray luminosity, gas temperature, gas mass, $Y_X = M_{\rm gas} \cdot k_{\rm B}T$ (proportional to the thermal pressure of the gas) or even the hydrostatic mass, which can be directly inferred from X-ray imaging spectroscopy, makes this wavelength regime ideal to detect and analyze galaxy clusters even out to high redshifts. New studies also try to detect galaxy clusters only with the weak lensing signal, which makes the selection function independent of baryonic physics (e.g., a bright cool core).

X-ray selected samples can be derived either using an all-sky survey like the ROSAT All-Sky Survey (RASS), or systematically scanning over a fraction of the sky with an X-ray instrument, e.g., XMM-LSS Survey (Pacaud et al., 2006). In contrast to optically selected samples, X-ray selected clusters are dynamically collapsed and can be detected as a single and extended object (see Giacconi and Burg, 1993).

1.1.3 HIFLUGCS

In this work I analyze the HIghest X-ray FLUx Galaxy Cluster Sample (HIFLUGCS; Reiprich and Böhringer, 2002), which is X-ray selected from RASS with a minimum flux of $2 \times 10^{-11}\,\mathrm{erg\,s^{-1}\,cm^{-2}}$ in the $(0.1 - 2.4)\,\mathrm{keV}$ band and a Galactic latitude $|b| \geq 20°$. Also the region of the Small and Large Magellanic Cloud as well as the Virgo Cluster region were removed. After these criteria, HIFLUGCS clusters were selected from 8.14 sr, which means a sky coverage of about 64.78 % (Fig. 1.2). Because of its size, completeness and high X-ray flux, HIFLUGCS is one of the best currently available samples of local (median redshift 0.05) clusters. To find the clusters which fulfill these requirements, nine catalogs containing extended X-ray sources from the RASS were browsed, among them REFLEX (Böhringer et al., 2001), NORAS (Böhringer et al., 2000), NORAS II (Retzlaff, 2001) and BCS (Ebeling et al., 1998). For more details see Section 4.2 and (Reiprich, 2001, p. 23-27). After selecting candidates from these catalogs with a lower flux limit, all fluxes are redetermined with ROSAT PSPC pointing observations, where feasible, and then the previously mentioned flux limit was applied to end up with the HIFLUGCS clusters.

By lowering the flux limit it has been extended to eHIFLUGCS ($f_{\rm lim} = 9 \times 10^{-12}\,{\rm erg\,s^{-1}\,cm^{-2}}$) in the same energy band as HIFLUGCS was selected. All objects in this sample have been observed at least by one of the major X-ray instruments (Chandra, XMM-Newton, Suzaku).

One HIFLUGCS cluster (RXCJ1504) was included later, since it was initially believed to be strongly contaminated by AGN emission and the total flux was only slightly above the flux limit. With high spatial resolution data from Chandra it became clear that this cluster has to be included, so the sample comprises now 64 clusters (see Table 3.3).

Table 1.1: List of the 64 HIFLUGCS clusters. Column a) defines the name of the cluster as it is used in this work, in column b) an alternative name is given. Columns c) and d) give the emission peak coordinates in J2000 as defined in Hudson et al. (2010) and e) is the redshift taken from Zhang et al. (2011a). The angular diameter distance D_A is calculated using the redshift assuming $\Omega_\Lambda = 0.7$ and $\Omega_{\rm m} = 0.3$ (see Section 2.1 for details).

Cluster Name (a)	**Alternative Name** (b)	**RA** (c)	**DEC** (d)	z (e)	$\boldsymbol{D_A}$ [Mpc] (f)
2A 0335+096	RBS 0456	03h38m35.3s	+09d57m55s	0.0349	136
ABELL 0085		00h41m37.8s	-09d20m33s	0.0556	208
ABELL 0119		00h56m21.4s	-01d15m47s	0.044	168
ABELL 0133		01h02m39.0s	-21d57m15s	0.0569	214
ABELL 0262		01h52m50.4s	+36d08m46s	0.0161	62.3
ABELL 0399		02h57m56.4s	+13d00m59s	0.0715	269
ABELL 0400		02h57m38.6s	+06d02m00s	0.024	94.7
ABELL 0401		02h58m57.0s	+13d34m56s	0.0748	275
ABELL 0478		04h13m20.7s	+10d28m35s	0.09	326
ABELL 0496		04h33m37.1s	-13d14m46s	0.0328	129
ABELL 0576		07h21m24.2s	+55d44m20s	0.0381	154
ABELL 0754		09h08m50.1s	-09d38m12s	0.0528	213
ABELL 1060		10h36m51.3s	-27d31m35s	0.0114	55.6
ABELL 1367		11h44m29.5s	+19d50m21s	0.0216	92.3
ABELL 1644		12h57m14.8s	-17d21m13s	0.0474	188
ABELL 1650		12h58m46.2s	-01d45m11s	0.0845	316
ABELL 1651		12h59m23.0s	-04d11m10s	0.086	320
ABELL 1656	Coma Cluster	12h59m48.7s	+27d58m50s	0.0232	95.8
ABELL 1736		13h26m52.2s	-27d06m33s	0.0461	182
ABELL 1795		13h49m00.5s	+26d35m07s	0.0616	241
ABELL 2029		15h10m56.0s	+05d44m41s	0.0767	292
ABELL 2052		15h16m45.5s	+07d00m01s	0.0348	142
ABELL 2063		15h23m01.9s	+08d38m22s	0.0354	140
ABELL 2065		15h22m42.6s	+27d43m21s	0.0721	275
ABELL 2142		15h58m16.1s	+27d13m29s	0.0899	337
ABELL 2147		16h02m17.2s	+15d53m43s	0.0351	139
ABELL 2163		16h15m34.1s	-06d07m26s	0.201	665
ABELL 2199		16h28m38.5s	+39d33m06s	0.0302	120
ABELL 2204		16h32m45.7s	+05d34m43s	0.1523	526
ABELL 2244		17h02m44.0s	+34d02m48s	0.097	355
ABELL 2255		17h12m31.0s	+64d05m33s	0.08	301
ABELL 2256		17h03m43.5s	+78d43m03s	0.0601	222
ABELL 2589		23h24m00.5s	+16d49m29s	0.0416	157
ABELL 2597		23h25m18.0s	-12d06m30s	0.0852	313
ABELL 2634		23h38m18.4s	+27d01m37s	0.0312	120
ABELL 2657		23h44m51.0s	+09d08m40s	0.0404	153
ABELL 3112		03h17m52.4s	-44d14m35s	0.075	282

continued on the next page

Cluster Name	Alternative Name	RA	DEC	z	D_A [Mpc]
ABELL 3158		03h42m39.6s	-53d37m50s	0.059	228
ABELL 3266		04h31m11.9s	-61d24m23s	0.0594	226
ABELL 3376		06h00m43.6s	-40d03m00s	0.0455	179
ABELL 3391		06h26m15.4s	-53d40m52s	0.0531	200
ABELL 3395		06h27m31.1s	-54d23m58s	0.0498	197
ABELL 3526	Centaurus Cluster	12h48m51.8s	-41d18m21s	0.0103	50
ABELL 3558		13h27m54.8s	-31d29m32s	0.048	190
ABELL 3562		13h33m31.8s	-31d40m23s	0.0499	193
ABELL 3571		13h47m28.9s	-32d51m57s	0.0397	157
ABELL 3581		14h07m27.5s	-27d01m15s	0.0214	95.3
ABELL 3667		20h12m30.1s	-56d49m00s	0.056	213
ABELL 4038		23h47m37.0s	-28d07m42s	0.0283	115
ABELL 4059		23h56m40.7s	-34d40m18s	0.046	181
EXO 0422	RBS 0540	04h25m50.7s	-08d33m25s	0.039	157.1
HydraA	ABELL 0780	09h18m30.4s	-12d15m40s	0.0538	215
MKW 03s		15h21m51.9s	+07d42m31s	0.045	180
MKW 04		12h03m57.7s	+01d53m18s	0.02	84.9
MKW8	WBL 518	14h40m43.1s	+03d27m11s	0.027	110
NGC 0507		01h23m40.0s	+33d15m20s	0.0165	62.6
NGC 1399	Fornax	03h38m29.1s	-35d27m03s	0.0046	18.2
NGC 1550		04h19m37.9s	+02d24m36s	0.0123	49
NGC 4636		12h42m49.8s	+02d41m16s	0.0037	17.4
NGC 5044		13h15m24.0s	-16d23m08s	0.009	41.9
RXJ1504.1-0248	WHL J150407.5-024816	15h04m07.5s	-02d48m16s	0.2153	709
S1101	ABELL S1101	23h13m58.5s	-42d43m39s	0.058	220
Zw III 054		03h41m17.6s	+15d23m44s	0.0311	126
ZwCl 1215.1+0400		12h17m41.4s	+03d39m32s	0.075	289

1.1.4 X-ray Observations of galaxy clusters

Galaxy clusters can be characterized in X-rays by a diffuse, thermal emission of the hot intra cluster medium (ICM). Often these objects appear almost spherical or elliptical. Central gas number densities of the hot gas can reach values around $n_{\rm gas} \approx 0.1\,{\rm cm}^{-3}$. The densities decrease toward the outskirts. The ASCA X-ray observatory showed in the late 1990s that the temperature structure is not isothermal and first temperature profiles could be measured (Markevitch et al., 1998). But before looking at the emission properties in more detail, several quantities need to be defined.

Important quantities

In the following a quick overview of the most important physical quantities is given. For more complete reviews see, e.g., Rybicki and Lightman (1979) or Reiprich et al. (2013). General assumptions are an isotropic radiating source and conservation of energy.

The *luminosity* L_X is the power of the emitted photon energy, E,

$$L_X = \frac{{\rm d}E}{{\rm d}t}\ . \tag{1.2}$$

The restriction to an X-ray energy band of $(0.5-2)\,{\rm keV}$ yields typical values of galaxy clusters of $10^{44}\,{\rm erg\,s^{-1}}$.

The *flux* in X-rays, f_X, is the energy of photons E passing through a surface A during a time interval t.

$$f_X = \frac{{\rm d}E}{{\rm d}A\,{\rm d}t} \tag{1.3}$$

Typical values for galaxy clusters in HIFLUGCS are several $10^{-11}\,{\rm erg\,s^{-1}\,cm^{-2}}$ in the $(0.1-2.4)\,{\rm keV}$ band.

By measuring the solid angle Ω of a source, one can also define the *surface brightness*:

$$S_X = \frac{\mathrm{d}E}{\mathrm{d}t\,\mathrm{d}A\,\mathrm{d}\Omega} \tag{1.4}$$

For practical usage it is also useful not to use energy for the surface brightness but the number of photons in a given energy range. So in the following S_X^{phot} will denote the photon surface brightness and S_X^{en} the energy surface brightness as in Eq. 1.4. The emissivity ϵ is the luminosity divided by the volume V of the source,

$$\epsilon = \frac{\mathrm{d}L_X}{\mathrm{d}V}. \tag{1.5}$$

All these quantities can be given for a specific frequency, indicated by the index ν (e.g., f_ν).

Free-free emission

In the hot ICM plasma electrons are accelerated and photon emission is induced. The acceleration of the nuclei can be neglected ($m_\mathrm{e} << m_\mathrm{p}$). A quantum mechanical treatment, which differs from a classical approach by the gaunt factor $g_\mathrm{ff}(\omega, \nu)$ (a function of electron and photon energy), is given in e.g., Karzas and Latter (1961). The emissivity of free-free emission is given by

$$\epsilon_\nu^\mathrm{ff} = \underbrace{\frac{2^5\pi e^6}{3m_e c^3}\left(\frac{2\pi}{3m_e k_\mathrm{B}}\right)^{0.5}}_{=A} Z^2 n_e n_i T^{-\frac{1}{2}} \exp\left(-\frac{h\nu}{k_\mathrm{B}T_e}\right) g_\mathrm{ff}\ , \tag{1.6}$$

with

$$A = 6.8\times10^{-38}\,\mathrm{erg\,K^{\frac{1}{2}}\,cm^3\,s^{-1}\,Hz^{-1}}, \tag{1.7}$$

where Z is the ion charge, m_e the electron mass, e the absolute value of the electron charge, n_e and n_i the electron and ion number densities and T_e the electron temperature.

The most important parameter for free-free emission is T_e. The transition from the power-law regime at lower energy and the exponential drop at high energies is called the *cut-off*. It is located where the photon energy is roughly equal to the energy of the electrons $k_\mathrm{B}T_\mathrm{e}$ (Fig. 1.3). So a very good way to determine T_e when the redshift is known, is to look for the exponential cut-off.

Line emission

When a bound electron changes to a lower energy level in an atom, a photon is emitted with the energy corresponding to the difference between the two atomic states. This process is called bound-bound radiation or line emission, because the energy distribution is almost a sharp line, only broadened according to Heisenberg's energy-time uncertainty relation. The spectral shape of the natural line broadening can be described by a Breit-Wigner distribution. A further line broadening is introduced by the temperature of the gas. The movement of the atoms, following a Maxwell-Boltzmann distribution, causes a Doppler shift of the line, resulting in a Gaussian broadening of the spectral line. The convolution of a Breit-Vigner and a Gaussian profile is called Voigt profile. In the context of CCD imaging spectroscopy, the spectral resolution is the limiting factor for the observed line width.

For Hydrogen the important emission lines are in the UV and optical (Lyman or Balmer series), or at even lower energies. For ionized heavy elements the transitions shift toward the X-ray regime (see Figure 1.3). Due to their high relative abundance Iron and Oxygen are the most important ones, but also other elements can be studied, especially with high resolution X-ray gratings, or micro-calorimeters in the near future.

For example Iron has some important ion configurations: The Fe-L complex (electron transitions to main quantum state 2) is located around 1 keV and the Fe-K complex (electron transition to main quantum state 1) at roughly 6.8 kev. Note that emission lines can also be used to constrain plasma temperatures, independently of the free-free emission. More details are given in Chapter 6.

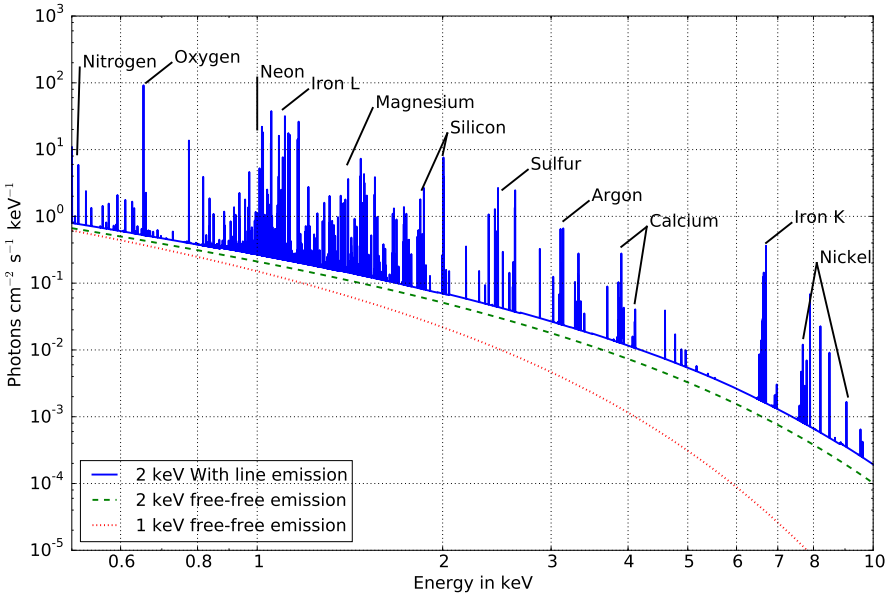

Figure 1.3: Flux density as a function of energy for three different models in the X-ray regime. Red and green (dotted and dashed) show pure free-free radiation for 1 and 2 keV, respectively. The solid blue line shows a thermal, optically thin model at 2 keV which includes free-free, line emission and recombination. The most important emission lines are indicated.

Other emission processes

Some other processes contribute little to the complete continuum radiation of a hot thermal plasma in X-rays: The radiative and dielectronic recombination and the two photon decay. Especially the two photon decay is negligible, but a detection is a good test for the theory.

- Radiative recombination is also called free-bound transition. An electron gets captured by an ion and produces a photon with the energy equal the kinetic energy of the electron plus the binding energy of the ion.

- Dielectronic recombination (DR) is less important than radiative recombination (RR). In the case of DR the captured electron does not release a photon, but turns the atom into an excited state. This new double-excited state of the atom is turned into a singly-excited state by emitting a photon. Since the energy of the original electron must match the excitation energy it is a resonant process.

- Two photon transitions: Some transitions are highly forbidden and therefore the transition can only occur with the emission of two photons. Important examples are for Hydrogen-like atoms $2s\,^2S_{1/2} \rightarrow 1s\,^2S_{1/2}$ and for Helium-like atoms $1s2s\,^1S_0 \rightarrow 1s^2\,^1S_0$. For X-ray astronomy, these processes are even less important than recombination.

- The inverse Compton process (IC) is a non-thermal emission process. Only the scattering of the CMB photons, either with the hot ICM (called Sunyaev-Zeldovich effect), or with relativistic electrons (leading X-ray emission), can produce IC emission in galaxy clusters. The IC emission associated with relativistic electrons has not clearly been observed, yet. For low energy photons (like CMB radiation) the energy increase due to IC is roughly the squared Lorentz factor, $\gamma^2 = \left(1 - \frac{v^2}{c^2}\right)^{-1}$, where v is the velocity of the electrons. The total spectral shape of the IC emission depends on the velocity distribution of the electrons. If the latter is a powerlaw, the IC spectrum is also a powerlaw.

Figure 1.4 shows the two recombination methods described above compared with free-free emission. Above a plasma temperature of 500 eV free-free emission is dominant.

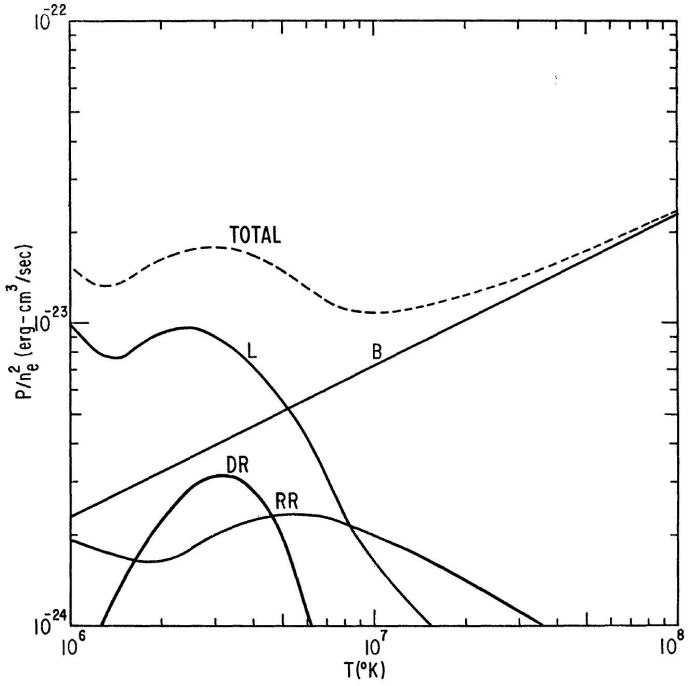

Figure 1.4: Cooling rates for different plasma temperatures. `B` is free-free emission, `L` is collisional induced line emission, `RR` and `DR` are radiative and dielectronic recombination, respectively. Image from Tucker and Gould (1966).

Absorption

Heavy elements have a significant cross section in the soft X-ray regime. Therefore radiation from extragalactic sources will be partially absorbed by the heavy elements in the inter stellar medium (ISM) of the Milky Way. To correct for this absorption one has to know the column density of the heavy elements and the cross sections $\sigma(E)$ of the elements as a function of photon energy. For simplicity the heavy elements are usually traced by the Hydrogen column density, which can be quantified for each line of sight via radio HI observations like the LAB survey (Kalberla et al., 2005). Since the radio data used here has a lower angular resolution, this value from the survey is only an estimate and the actual hydrogen column density N_{H} can locally be different. Also the scaling from Hydrogen to the individual heavy elements is based on an abundance table (such as Anders and Grevesse, 1989) which adds further uncertainties. Relative abundance tables are created using data from meteorites and observations of the solar photosphere. Differences between the sun and meteorites are important especially for iron. The absorption can be estimated by

$$I_{\mathrm{abs}}(E) = I_0(E) \cdot \exp^{-N_{\mathrm{H}}\sigma(E)} \ , \tag{1.8}$$

where the photo-electric cross section $\sigma(E)$ is needed to correct for the absorption. These cross sections are also given in publications like Morrison and McCammon (1983), which are used for the *xspec* `wabs` model. Unfortunately, this model automatically uses an older abundance table (Anders and Ebihara, 1982). Figure 1.5 shows the contribution of the different elements to the total cross section. The `phabs` model allows to change the relative abundance table and there exist even newer models (`tbabs` and `tbnew`) to precisely account for grain phase ISM and molecules. For CCD spectral resolution the `phabs` model is appropriate to account for any ISM absorption.

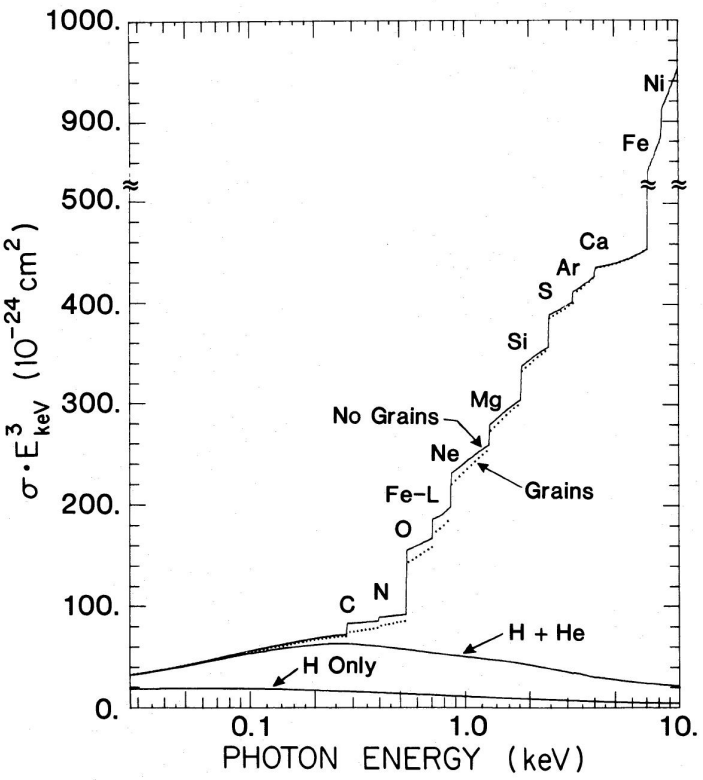

Figure 1.5: Photoelectric absorption cross section as a function of energy normalized to one Hydrogen atom. The scaling $\sigma \cdot E^3$ is only for presentation reasons. Taken from Morrison and McCammon (1983)

1.2 Important missions

Despite this work is focused on the Chandra X-ray observatory and the XMM-Newton satellite, there are other important X-ray missions to be mentioned here to also understand the context and prospects of future missions. The brightest X-ray source on the sky is the sun, due to its vicinity. If one ignores some bright transients or strongly variable sources (like gamma ray bursts), the brightest source outside the solar system is Scorpius X-1, which was discovered by the Aerobee rocket experiments (1962). After the balloon and rocket based X-ray detectors, the first real X-ray satellite was Uhuru, which scanned 95% of the sky with a much higher sensitivity than previous rocket experiments and detected 339 sources. Then, after HEAO-I and HEAO-B (also known as Einstein Observatory, the first imaging X-ray telescope with $3''$ angular resolution) and EXOSAT, which could record long-duration light curves, ROSAT was launched on the 1st of June 1990 with twice the effective area of Einstein. On board was an X-ray telescope with position-sensitive proportional counters (PSPC) sensitive especially to low energies $< 2\,\mathrm{keV}$ and a field of view diameter of 2°. Within half a year ROSAT produced the first imaging all-sky survey, which is still commonly used, especially to analyze astrophysical background components and for extended source catalogs. After that, some other missions were launched like ASCA (first CCD X-ray detector), RXTE (very high time resolution) and BeppoSAX (low instrumental background).

A breakthrough was the launch of Chandra and XMM-Newton, both in 1999. XMM-Newton and Chandra provide until today the best instruments to observe galaxy clusters in X-rays. Chandra (Weisskopf et al., 2000) has an angular resolution of $0.492''$ and a large effective area. It was placed in a high Earth orbit with a high eccentricity, most of the time being out of the Earth's magnetosphere. The instruments on board are the Advanced CCD Imaging Spectrometer (ACIS) consisting of 10 CCD chips and the High Resolution Camera (HRC), a microchannel plate with a larger field of view than ACIS. Finally two diffraction gratings, the Low Energy Transmission Grating (LETG) for energies of $(0.07 - 0.2)\,\mathrm{keV}$ used with the HRC and the High Energy Transmission Grating (HETG) for energies of $(0.4 - 10)\,\mathrm{keV}$ used with

the ACIS, can produce high resolution spectra.
XMM-Newton (Jansen et al., 2001) has three telescopes with each 58 mirror shells, which gives an effective area more than three times that of Chandra. XMM is also in an elliptic orbit and has three imaging cameras (EPIC), where each of them has its own telesope. One of them (PN) uses a new type of CCD which has a higher quantum efficiency, especially at higher energies, for details see Strüder et al. (2001).
Suzaku (Mitsuda et al., 2007) was a Japanese/U.S. mission launched in 2005 with imaging CCD detectors and a calorimeter which was damaged shortly after the launch and was unusable. Suzaku was in a low-Earth orbit and therefore had a low instrumental background. It was turned off in 2015 due to battery and solar panel degradation. Important missions are summarized in Table 1.2.

Mission	**Year**	**Main Instrument**	**Energy range** keV	**Maximum eff. area** cm^2	**Angular resolution** arcsec	**Comment**
Uhuru	70-73	PC1	2-18	840	120	First X-ray satellite
HEAO1	77-79	A1	1-20	3300	-	Flux-limited survey & X-ray Background study
Einstein	79-81	IPC	0.2-4.5	150	3	first imaging satellite
EXOSAT	83-86	CMA	0.04-2	11	5	AGN variability studied
ROSAT	90-99	PSPC	0.2-2	250	30	All-sky survey
ASCA	93-01	SIS	0.4-10	200	180	First CCD satellite & good spectral resolution
BeppoSAX	96-02	MECS	1.3-10	150	72	Low Background
Chandra	99-	ACIS	0.2-10	600	0.5	Best spatial resolution
XMM	99-	EPIC	0.2-15	2150	6	High eff. area over large energy band
Suzaku	05-15	XIS	0.3-10	1360	120	Low instrumental background
NuSTAR	12-	FPMA/B	3-79	500	40	Hard X-ray detector
Astro-H	16-	SXS	0.3-12	210	78	Microcalorimeter with 7 eV spectral resolution
		SXI	0.4-12	360	78	Low instrumental background & wide FOV
eROSITA	17-	7pn CCDs	0.2-10	1365	15	All-sky survey to detect 10^5 galaxy clusters
Athena	28-	WFI	0.1-12	20000	5	Wide Field Imager with 0.35 deg^2 FOV
		X-IFU	0.3 -10	20000	5	Microcalorimeter with few eV spectral resolution

Table 1.2: Important missions and the properties of selected detectors on board. Adopted from Aschenbach (1985), Boella et al. (1997), Seward and Charles (2010), Merloni et al. (2012), Takahashi et al. (2014), `http://www.cosmos.esa.int/web/athena/about-athena`.

1.3 Sunyaev-Zeldovich effect

The thermal Sunyaev-Zeldovich effect (SZ, Sunyaev and Zeldovich, 1972, 1980) is a distortion of the blackbody spectrum of the cosmic microwave background (CMB) photons due to the inverse Compton scattering with the high energy electrons of the ICM of galaxy clusters. The cosmic microwave background is the radiation originating from the epoch of recombination in the early Universe (e.g., Kaiser and Silk, 1986): Due to the expansion the temperature in the Universe dropped and made it possible that electrons could recombine for the first time to produce neutral atoms, allowing the decoupling of matter and radiation. The CMB radiation follows a blackbody spectrum (the most accurate measured to date),

$$I_\nu = \frac{2h\nu^3}{c^2}\left(e^{\frac{h\nu}{\mathrm{k}T_\mathrm{e}}} - 1\right) \ , \tag{1.9}$$

where ν is the frequency, h is the Planck constant, c is the speed of light, k is the Boltzmann constant and T_e the electron temperature. The further expansion from redshift ~ 1100 to today reduced the temperature to a value of 2.725 48 K (Fixsen, 2009). Detailed all-sky studies with COBE (Boggess et al., 1992), WMAP (Dunkley et al., 2009) or Planck (see Fig. 1.6, Planck Collaboration et al., 2011) have shown that, after correcting for effects like the dipole anisotropy (due to the Earth's movement), there exist tiny temperature fluctuations on the order of $\frac{\Delta T}{T} \approx 5 \times 10^{-6}$ (Gorski et al., 1996). The SZ effect predicts a temperature

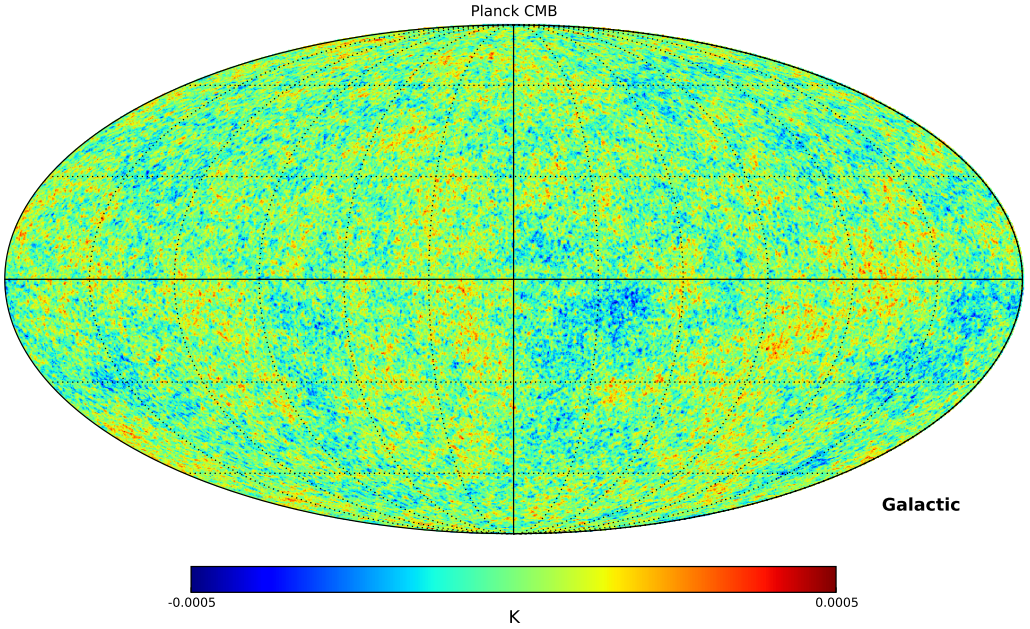

Figure 1.6: Cosmic microwave background temperature fluctuations as measured by the Planck satellite. Galactic coordinates in Mollweide projection centered on the Galactic center and with Galactic longitude increasing toward the right.

decrement in the low energy (Rayleigh-) part of the spectrum (see Fig. 1.7). This is in general much easier to detect than the high energy increment, due to the exponential drop. Temperature anisotropies can be related to the SZ effect by

$$\frac{\Delta T_\mathrm{CMB}}{T_\mathrm{CMB}} = f(x) \cdot y = f(x)\sigma_\mathrm{T} \int n_\mathrm{e}(l) \frac{\mathrm{k}T_\mathrm{e}}{m_\mathrm{e}c^2} \,\mathrm{d}l \ , \tag{1.10}$$

where m_e is the electron mass, n_e is the electron density as a function of the distance, σ_T is the Thomson cross-section and $f(x)$ is a function depending on frequency and temperature, which has a value -2 in the non-relativistic, low-energy (Rayleigh-Jeans) case (for more details see Birkinshaw, 1999). y is called the

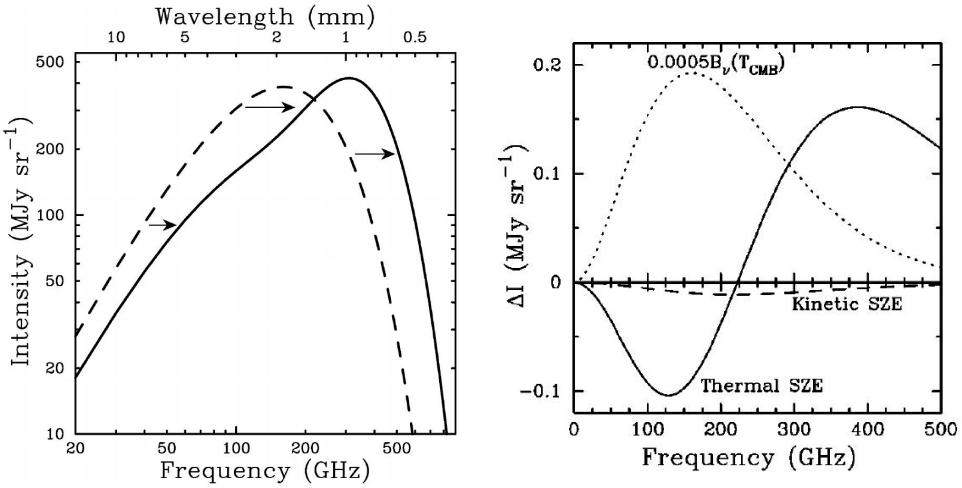

Figure 1.7: Impact of the SZ effect on the spectrum of the CMB. *Left:* The solid line shows the spectrum after invers compton scattering, the dashed one the original CMB blackbody spectrum. *Right:* The difference spectrum before and after the thermal/kinetic SZ effect. Taken from Carlstrom et al. (2002).

Compton parameter. One can also rewrite 1.10 in terms of the electron pressure p_e,

$$\Delta T_\mathrm{CMB} = -2\frac{\sigma_\mathrm{T}}{m_\mathrm{e}c^2}\int p_\mathrm{e}\,\mathrm{d}l\ , \tag{1.11}$$

which means $y \propto \int p_\mathrm{e}\,\mathrm{d}l$. Note that there is no redshift dependence in y. Integrating, under the assumption of spherical symmetry, the y parameter over the solid angle of a cluster, $\mathrm{d}\Omega = \mathrm{d}A\,D_\mathrm{A}^{-2}$, returns the volume integrated pressure:

$$Y_\mathrm{SZ} = \int y\,\mathrm{d}\Omega = \int \frac{y}{D_\mathrm{A}^2}\,\mathrm{d}A = \frac{2\pi}{D_\mathrm{A}^2}\int y\cdot r\,\mathrm{d}r \propto \frac{1}{D_\mathrm{A}^2}\int P\,\mathrm{d}V\ . \tag{1.12}$$

Since $P \propto n_\mathrm{e}T_\mathrm{e}$, Y_SZ is proportional to the total number of electrons weighted by the temperature,

$$Y_\mathrm{SZ} \propto \frac{1}{D_\mathrm{A}^2}\underbrace{N_\mathrm{e}}_{\propto M_\mathrm{gas}}\cdot\langle T_\mathrm{e}\rangle\ , \tag{1.13}$$

which is related to the total mass (Arnaud et al., 2010). So the Y_SZ parameter is a tracer of the gas or, assuming a constant gas mass fraction, the total mass of the galaxy cluster, which is independent of the redshift.

The SZ effect described up to now is called the thermal SZ effect, because there also exists a kinetic (kinematic) SZ effect: The bulk velocity of the galaxy cluster can distort the spectrum due to the Doppler effect. As indicated in Fig. 1.7 this effect is much smaller than the thermal SZ (on the order of 8.5%, see Eq. 88 in Birkinshaw, 1999).

Several surveys exist to detect the galaxy clusters using the SZ effect. Some important facilities are the *Atacama Cosmology Telescope* (Hasselfield et al., 2013), the *South Pole Telescope* (Reichardt et al., 2013; Liu et al., 2015) and the *Planck Satellite* (Planck Collaboration et al., 2015d,b).

CHAPTER 2

Theoretical framework

Fundamental questions about the Universe as a whole, like, *how old is it?*, *what are the constituents?* or *what will happen to it in the future?* are probably as old as mankind. Also answers have changed many times, since it was found that they were based on wrong assumptions. Within the last 100 years for the first time scientifically motivated and systematic approaches have been made to solve many of these mysteries of the Universe. Based on Einstein's field equations it is possible to characterize the interior design of the Universe. One way is to look at the large scale structure.

A theoretical formulation is important to understand the impact of the results achieved, e.g., by the galaxy cluster analysis. In Section 2.1 the main ideas of the standard model of cosmology are summarized. Section 2.2 and 2.3 introduce the main ideas of structure formation and show how to deal with the cluster mass function. Useful reviews are Peacock (1999); Rich (2001); Carroll (2001); Peebles and Ratra (2003).

2.1 Basics

On large scales two important principles are applied to all cosmological analyses: Isotropy and homogeneity. Isotropy states that, although on small scales there might be variations, the Universe around an observer looks the same in every direction. Homogeneity means that the density (on large scales) is constant in the Universe. In a expanding Universe, isotropy is no longer implied by homogeneity. The only case that both principles hold in an expanding Universe is if the expansion is radial. In the following the parameter H will characterize the expansion and all spatial dependencies are reduced to a radial dependence. So the expansion rate $\dot{r}$ is given by

$$\dot{r} = Hr \ . \tag{2.1}$$

But to measure distances in an expanding Universe with non-zero space curvature K (see below) one has to apply Einstein's field equations (see Walker, 1935; Robertson, 1935; Carroll, 2001). The resulting metric,

$$\mathrm{d}s^2 = c^2\mathrm{d}t^2 - a^2(t)\left(\mathrm{d}\omega^2 + f_K^2(\omega)(\mathrm{d}\theta^2 + \sin^2\theta\mathrm{d}\psi^2)\right) \tag{2.2}$$

is called Robertson-Walker metric, where t is the cosmic time, $a(t) = \frac{r(t)}{r(t_0)}$ is the scale factor normalized today's value and ω is the comoving radial coordinate. f_K is a function depending on the space curvature K:

$$f_K(\omega) = \begin{cases} \frac{1}{\sqrt{K}}\sin\left(\sqrt{K}\omega\right) & K > 0 \\ \omega & K = 0 \\ \frac{1}{\sqrt{-K}}\sinh\left(\sqrt{-K}\omega\right) & K < 0 \ , \end{cases} \tag{2.3}$$

where $|K|^{-1/2}$ is the curvature radius and the dimensions of K are length^{-2}. $K > 0$ describes a closed Universe with finite size but without boundaries and the angular sum of a triangle is larger than 180°; $K < 0$ is the open case with angular sum smaller than 180°; and $K = 0$ is a flat Universe with infinite size. $K = 0$ is the only case where the sum of angles in the triangular is 180°. The redshift z can be defined

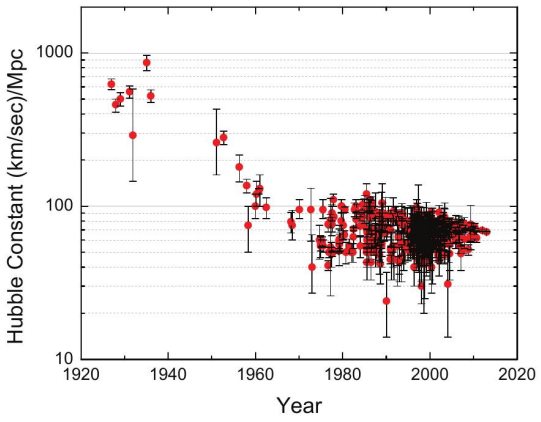

Figure 2.1: Historical evolution of the H_0 measurements, taken from Pritychenko (2015).

observationally as the relative change between observed and emitted wavelength of a photon,

$$z = \frac{\lambda_{\rm obs} - \lambda_{\rm em}}{\lambda_{\rm em}} \ , \tag{2.4}$$

and if one considers only the expansion of the Universe as the source for redshifted photons, one can relate the redshift to the scale factor

$$z = \frac{1}{a(t_{\rm em})} - 1 \ . \tag{2.5}$$

Equation 2.5 holds for any cosmological model.

Starting from Einstein's field equation, the evolution of the scale factor $a(t)$ can be described by the Friedmann equations,

$$H(t)^2 = \frac{\dot{a}(t)^2}{a(t)^2} = \frac{8\pi G}{3}\rho(t) - \frac{Kc^2}{a(t)^2} \tag{2.6}$$

$$\frac{\ddot{a}(t)}{a(t)} = -\frac{4\pi G}{3c^2}(\rho(t)c^2 + 3p(t)) \ , \tag{2.7}$$

where energy conservation was used. ρ denotes the energy density and p the pressure of all components. There exists a certain density that defines the borderline between a collapsing and forever expanding Universe. In a Universe with only matter and radiation, this is called the critical density $\rho_{\rm crit}$. Equation 2.6 can be used to derive this quantity:

$$\rho_{\rm crit}(z) = \frac{3H(z)^2}{8\pi G} = E(z)^2\rho_{\rm crit,0} \ , \tag{2.8}$$

where $E(z)$ is the evolution of the Hubble parameter $H(z) = H_0E(z)$. In the past the value of H_0 was very uncertain in the range of $(50 - 100)\,{\rm km\,s^{-1}\,Mpc^{-1}}$. Current measurements seem favor a value around $70\,{\rm km\,s^{-1}\,Mpc^{-1}}$, depending on the method (e.g., CMB results from WMAP9, Hinshaw et al., 2013 give $70.0 \pm 2.2\,{\rm km\,s^{-1}\,Mpc^{-1}}$) one finds some scatter among the measurements (see Fig. 2.1) and it is common to factor out the H_0 dependence in terms of h, using $H_0 = h \cdot 100\,{\rm km\,s^{-1}\,Mpc^{-1}}$.

The density ρ is a combination of all contributors (pressure-less mass: m, radiation: r, vacuum energy: vac) and so one can assume that it can be split up. The vacuum energy is motivated by quantum mechanics and described the lowest energy quantum state.

$$\Omega(z) = \frac{\rho(z)}{\rho_{\rm crit}(z)} = \frac{\rho_{\rm m}(z) + \rho_{\rm r}(z) + \rho_{\rm vac}(z)}{\rho_{\rm crit}(z)} = \frac{\rho_{\rm m}(z) + \rho_{\rm r}(z) + \rho_{\rm vac}(z)}{E(z)^2\rho_{\rm crit,0}} = \Omega_{\rm m}(z) + \Omega_{\rm r}(z) + \Omega_{\rm vac}(z) \ . \tag{2.9}$$

For practical usage, it is convenient to normalize the densities to the critical density of the Universe. All

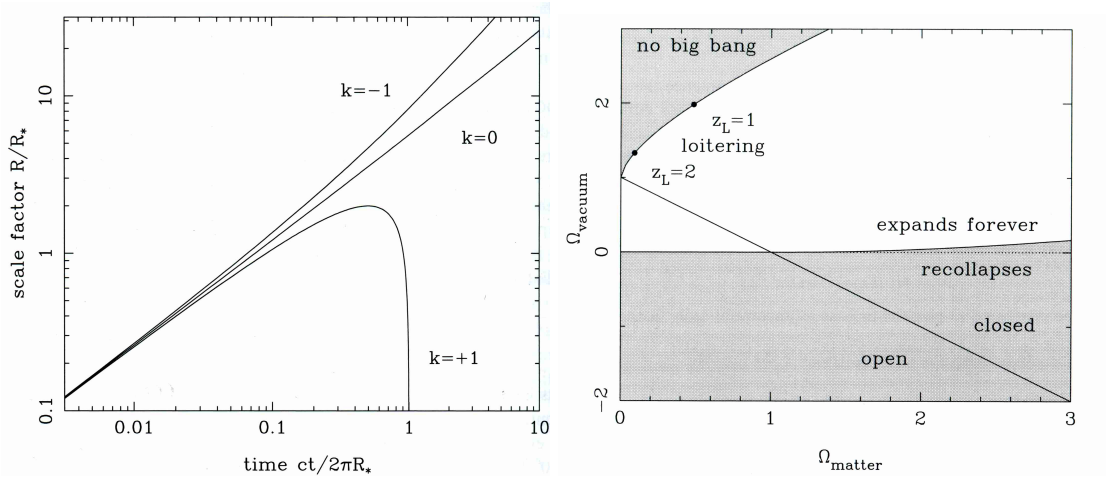

Figure 2.2: Illustration of properties for different models of Universes. *Left:* Evolution of the scale factor a with time for an open, closed and flat matter dominated Universe ($R_\star$ is a characteristic radius). *Right:* Certain combinations of $\Omega_{\rm m0}$ and $\Omega_{\rm vac0}$ build up different Universes. Both taken from Peacock (1999).

the quantities in (2.9) depend on redshift, but the evolution can be easily resolved for the different species. Since matter (including Dark Matter) is considered as pressureless, one finds that the matter density just scales with the volume expansion of the Universe:

$$\rho_{\rm m} = \rho_{\rm m,0} \cdot a^{-3} \rightarrow \Omega_{\rm m}(z) = \Omega_{\rm m0} \cdot \frac{a^{-3}}{E(z)^2} \ , \tag{2.10}$$

The radiation pressure depends linearly on the photon energy density and relativistic neutrinos (see Section 4.5.5), so $\rho_{\rm r}$ is diluted by the volume expansion and redshift:

$$\rho_{\rm r} = \rho_{\rm r,0} \cdot a^{-4} \rightarrow \Omega_{\rm r}(z) = \Omega_{\rm r0} \cdot \frac{a^{-4}}{E(z)^2} \ , \tag{2.11}$$

The vacuum energy density is considered as constant with time, so the pressure is negative:

$$\rho_{\rm vac} = \rho_{\rm vac,0} \rightarrow \Omega_{\rm vac}(z) = \Omega_{\rm vac0} \cdot \frac{1}{E(z)^2} \ . \tag{2.12}$$

The index '0' denotes today's value. Using (2.6),(2.8) and (2.9) one finds

$$\Omega(z=0) - 1 = \Omega_0 - 1 = \frac{Kc^2}{H_o^2} \ , \tag{2.13}$$

which can then all plugged into (2.6) to end up with the most common form of the first Friedmann equation, showing the evolution of all the energy density parameters:

$$\begin{aligned} H^2(a) &= H_0^2 \left[\left(\Omega_{\rm vac} + \Omega_{\rm m} a^{-3} + \Omega_{\rm r} a^{-4} \right) E(z)^2 - (\Omega_0 - 1) a^{-2} \right] \\ &= H_0^2 \left(\Omega_{\rm vac0} + \Omega_{\rm m0} a^{-3} + \Omega_{\rm r0} a^{-4} - (\Omega_0 - 1) a^{-2} \right) \ . \end{aligned} \tag{2.14}$$

With this equation, models can be calculated and a few of them are shown in Figure 2.2. It becomes clear that independent of a Universe being spatially open, flat or closed, it is possible to expand forever depending on the $\Omega_{\rm vac0}$ value. If $\Omega_{\rm vac0}$ is negligible small compared to $\Omega_{\rm m0}$ but still $\neq 0$, it is also possible that the Universe recollapses. Only in a matter dominated Universe the open, flat or closed status determines the evolution of the Universe.
Cosmological distances can be defined in various ways. The luminosity distances is given by a flux f and

relating it to the luminosity L of the object,

$$D_{\rm L} = \sqrt{\frac{L}{4\pi f}} \ , \tag{2.15}$$

while the apparent (angular) Θ and real extent A of an object perpendicular to the line of sight (angular diameter distance) is

$$D_{\rm A} = \frac{A}{\Theta} \ . \tag{2.16}$$

These two distance measurements do not necessarily need to a agree.

Note that the definition of the luminosity (1.2) in a given energy band is different in the source rest frame (SRF) and the observer rest frame (ORF). The ratio of SRF and ORF luminosities (or fluxes) is the so called K factor

$$K = \frac{L_{\rm band,srf}}{L_{\rm band,orf}} \ . \tag{2.17}$$

The K factor for thermal, optically thin hot plasma (galaxy cluster ICM) is a non-analytic function that depends on the redshift, plasma temperature and metallicity.

The comoving distance is the distance between two objects without the effect of the expansion of the Universe and is found by setting $\mathrm{d}s = 0$ in Eq. 2.2. For a flat Universe this simplifies to

$$D_{\rm C} = \int_t^{t_0} \frac{c}{a(t')}\,\mathrm{d}t' = \int_{z_1}^{z_2} \frac{c}{H(z)}\mathrm{d}z \ , \tag{2.18}$$

where z_1 and z_2 are the redshifts of the objects, whose distance is to be measured. The different distance measurements are related in a flat Universe as follows:

$$D_{\rm A} = \frac{D_{\rm C}}{1+z} \ , \tag{2.19}$$

$$D_{\rm L} = D_{\rm C} \cdot (1+z) \ , \tag{2.20}$$

$$D_{\rm A} = \frac{D_{\rm L}}{(1+z)^2} \ . \tag{2.21}$$

Figure 2.3 shows a comparison of the different distance measurements as a function of redshift for two different cosmologies. Note that for high redshifts D_A becomes smaller again, since the space was also much smaller at earlier times. Also for higher matter densities, when the expansion is slowed down, distances are also smaller. From now on for simplicity and consistency with literature the normalized density parameters $\Omega_{\rm x}$ refer to the values today $\Omega_{\rm x0}$ (e.g., from now on $\Omega_{\rm m}$ means $\Omega_{\rm m0}$) and redshift dependent density parameters are explicitly marked like $\Omega_{\rm x}(z)$.

Up to now I included the vacuum energy into the energy density ρ. But Einstein modified the field equation and added the cosmological constant Λ, which would also show up explicitly in the Friedmann equations. Practically, it makes no difference to use the vacuum energy density $\Omega_{\rm vac}$, or a cosmological constant,

$$\Omega_\Lambda = \frac{\Lambda c^2}{3H_0^2} \ . \tag{2.22}$$

So the terms vacuum energy or cosmological constant can be used interchangeable in this context. Unfortunately, measurements of the vacuum energy is about 120 orders of magnitude lower than required for a cosmological constant.

2.1.1 Components of the Universe

In cosmology, any component of the Universe can be considered as a perfect fluid at first, i.e. it follows the fluid equation,

$$\dot{\rho} = -3\frac{\dot{a}}{a}\left(\frac{p}{c^2} + \rho\right) \ , \tag{2.23}$$

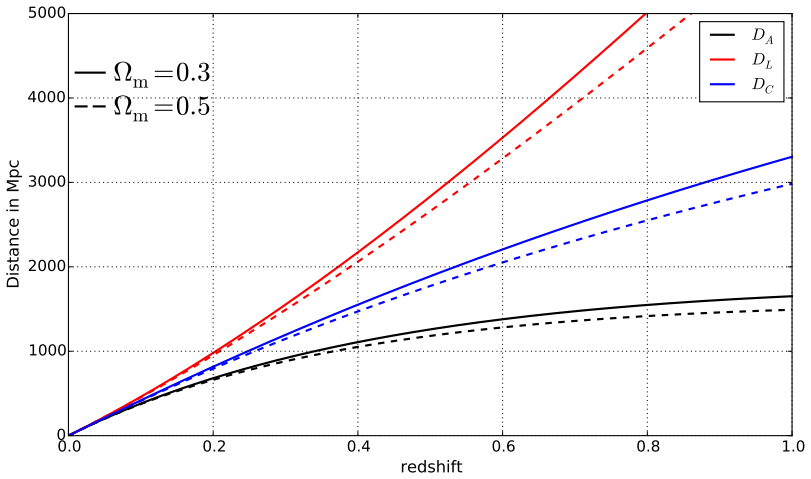

Figure 2.3: Comparison of different distance measurements as a function of redshift. Solid lines correspond to $\Omega_m = 0.3$ and $\Omega_\Lambda = 0.7$, dashed lines represent $\Omega_m = 0.5$ and $\Omega_\Lambda = 0.5$. Black lines (lowermost pair) are angular diameter distances, blue comoving (middle pair) distances and red (uppermost pair) luminosity distances.

which can be derived by subtracting (2.7) from the time derivative of (2.6). The relation for each component between the pressure p and density ρ can be described by the equation of state (EOS),

$$w = \frac{p}{c^2 \rho} \ , \tag{2.24}$$

where w is a dimensionless parameter. For radiation and relativistic particles $w = \frac{1}{3}$, for pressureless matter $w = 0$. For the dimensionless curvature term $k = K \cdot R_0^2$, where R_0 is the present not normalized scale factor, $w = -\frac{1}{3}$. It is important to note that the normalized density parameter for the curvature is defined as

$$\Omega_k = \frac{-kc^2}{H_0^2 r_0^2} = \Omega_0 - 1 \tag{2.25}$$

Plugging (2.24) into (2.23) one obtains the differential equation

$$\frac{\dot{\rho}}{\rho} = -3\frac{\dot{a}}{a}(1+w) \ , \tag{2.26}$$

which can be solved for constant w:

$$\rho = \rho_0 a^{-3(1+w)} \tag{2.27}$$

Equation (2.27) explains now the dependencies of (2.10) - (2.12).

Dark Matter

Any matter component without pressure is considered within ρ_m. This includes Baryons and Dark Matter. So one can write

$$\Omega_m = \Omega_b + \Omega_{DM} \ . \tag{2.28}$$

When it was discovered that Dark Matter is needed, first invisible baryonic matter (MACHOS - massive compact halo objects Alcock et al., 1993, e.g., brown dwarfs or black holes), was thought to solve the problem. From the CMB power spectrum one knows that Dark Matter cannot consist of Baryons. But again, non-baryonic Dark Matter can be subdivided into hot Dark Matter (HDM), which means particles with relativistic velocities (e.g., neutrinos) and cold Dark Matter (CDM), see Blumenthal et al. (1984), with currently only hypothetical particles. CDM seems to be a much better candidate, since it is defined

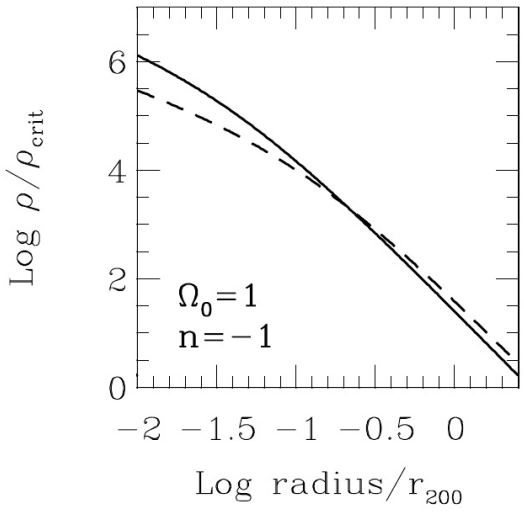

Figure 2.4: Fitted Dark Matter density profiles for a flat ΛCDM cosmology. Dashed line represents the high-mass halo, the solid line the low-mass one. Image adopted from Navarro et al. (1997).

non-relativistic and able to collapse, while HDM smoothes out structures on small scales. Also neutrinos are much too rare to explain the mass needed for the Dark Matter halos (see Freese, 1986).

Simulations have shown a universal density profile for cold Dark Matter might exist. One of the most used profiles is the NFW profile by Navarro et al. (1996),

$$\frac{\rho(r)}{\rho_{\rm crit}} = \frac{\delta_{\rm c}}{(r/r_{\rm s})(1+r/r_{\rm s})^2} \ , \tag{2.29}$$

where $r_{\rm s} = r_{200}/c$ is a characteristic radius and $\rho_{\rm crit}$ the critical density of the Universe and

$$\delta_{\rm c} = \frac{200}{3}\frac{c^3}{\ln(1+c) - \frac{c}{1+c}} \ , \tag{2.30}$$

where c is the concentration parameter (see also Section 4.3.6). This profile shows a lower density for massive Dark Matter halos in the center then for low-mass ones (see Fig. 2.4).
A very famous example for observational "detection" of Dark Matter is the bullet cluster (1E0657-558) at redshift $z \approx 0.3$, which shows a merging event of two clusters. As one can see in Fig. 2.5, the baryonic matter (black) lacks behind the Dark Matter because of interactions, which is also indicated by the clearly visible cold front. Dark Matter is collisionless, shows no shocks and the Dark Matter halos of the two cluster pass through each other.

Dark Energy

The vacuum energy (used up to now) or the cosmological constant Λ introduced by Einstein in the field equation, have an equivalent effect on the Universe and can be used interchangeable. A constant density for the Λ-term results in $w = -1$. Dark Energy is a more general classification for any component with negative pressure, so it is possible that $w \neq -1$. Equation 2.7 states that for an accelerated expansion $\ddot{a} > 0$ and therefore $w < -\frac{1}{3}$. Since many aspects of Dark Energy are still unknown it is also possible to have a time variable EOS, $w = w(a)$, which results in:

$$\rho_{\rm DE} = \rho_{\rm DE0} \cdot \exp\left(3\int_0^z 1 + w(z')\mathrm{d}\ln(1+z')\right) \ . \tag{2.31}$$

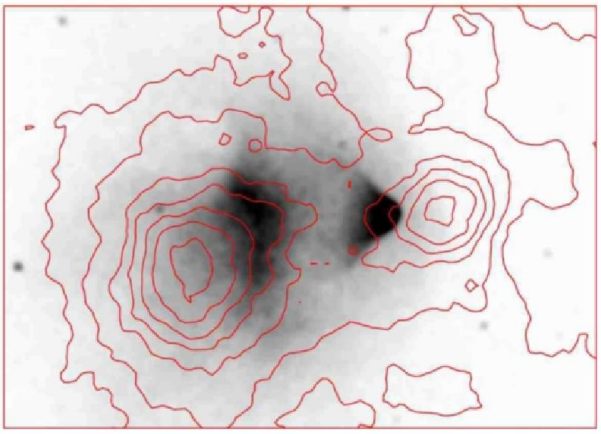

Figure 2.5: Bullet cluster. Red contours are from weak lensing and traces the total matter. The black image is a Chandra observation and traces the visible matter. Image taken from Clowe et al. (2007).

The consensus concordance cosmological model ΛCDM is commonly used and assumes $w = -1$. But testing w with many different probes is one goal of modern cosmology to solve the mystery of Dark Energy.

2.2 Structure formation

An essential part of this work is the cosmological interpretation of observed galaxy clusters, since they can be considered as the largest gravitationally bound objects. For this interpretation a theory of structure formation is needed, i.e. the evolution of bound structures in a homogeneous and isotropic Universe, especially how many galaxy clusters can evolve with a certain mass. Details are given for example in Padmanabhan (1993); Peebles (1993); Peacock (1999); Rich (2001).

As shown in Sec. 2.1 the components of the Universe (matter, radiation, curvature, Dark Energy) evolve differently with time. So one can define certain epochs in which one component is clearly dominant among the others in terms of energy density. Radiation scales as a^{-4} so it is important at very early times, until the matter dominated era began. The transition at which the two species had the same energy density is called time of matter radiation equality:

$$\Omega_{\rm m} a^{-3} = \Omega_{\rm r} a^{-4} \rightarrow a_{\rm eq} = \frac{\Omega_{\rm r}}{\Omega_{\rm m}} \approx \frac{1 \times 10^{-4}}{0.3} \approx 3 \times 10^{-4} \ , \tag{2.32}$$

which corresponds to a redshift of $z_{\rm eq} \approx 3000$. Following the same procedure one can also define the transition between the matter dominated phase and the Dark Energy epoch at around $z_{\rm m=\Lambda} \approx 0.33$ using $\Omega_\Lambda = 0.7$ and $\Omega_{\rm m} = 0.3$.

To describe the growth of structure, I consider an initial density field that contains overdensities. Using the continuity equation for mass conservation, the Euler equation for conservation of momentum and the Poisson equation for gravitational potentials, one can derive (in linear theory, i.e. for small density contrast, $\delta = \frac{\Delta\rho}{\rho} << 1$) a differential equation that describes the evolution of overdensities,

$$\frac{\partial^2 \delta}{\partial t^2} + \frac{2\dot{a}}{a}\frac{\partial \delta}{\partial t} - \frac{3H(a)^2\Omega_{\rm m}}{2a^3}\delta = 0 \ . \tag{2.33}$$

After a separation of the spatial and time dependencies one finds

$$\delta(\vec{x}, t) = D_+(t)\Delta_+(\vec{x}) + D_-(t)\Delta_-(\vec{x}) \ , \tag{2.34}$$

where $+$ denotes the growing solution (which is of interest here) and $-$ the decaying solution.

An overdensity evolves now differently in each of the phases, which is dominated by a certain species.

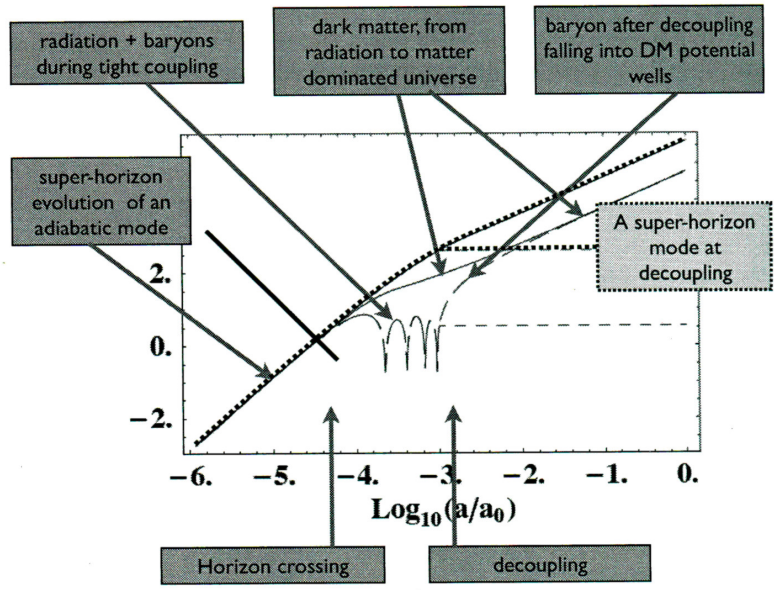

Figure 2.6: The density contrast versus the scale factor a for different species: Photons (dashed lines), baryons (long dashed lines) and Dark Matter (solid lines). The thin line shows a perturbation that crosses horizon before matter radiation equality, while the perturbation represented by the thick line crosses after equality. Taken from Bernardeau (2009).

On scales larger than the horizon,

$$r_{\mathrm{H}} = \int_0^{\hat{t}} \frac{c\,dt}{a(t)} \ , \tag{2.35}$$

which defines the maximum distance at a certain time where interaction could have happened, all perturbations grow as

$$\delta \ \propto \ a^2 \ \text{ in radiation dominated phase,} \tag{2.36}$$

$$\delta \ \propto \ a \ \text{ in matter dominated phase.} \tag{2.37}$$

$$\tag{2.38}$$

When cold Dark Matter enters the horizon before matter radiation equality (i.e. the horizon enters in the radiation phase), the growth is strongly suppressed (almost 0). But for larger perturbations that enter the horizon in the matter dominated phase, no suppression is occurring (see also Fig. 2.6). So the growth is for both, sub- and superhorizon perturbations now proportional to a. This is explained in more detail in Figure 2.6, including the growth of baryons (long dashed line) and radiation (dashed line) and Dark Matter (solid line). So considering only Dark Matter, the growth of small scale perturbations is strongly suppressed. This behavior is usually expressed by the Transfer Function $T(k)$, where k is the wavenumber ($k = \frac{2\pi}{\lambda}$) of the perturbation,

$$\frac{\delta_0}{\delta_0(k_s)} = T(k)\frac{\delta_i(k)}{\delta_i(k_s)} \ , \tag{2.39}$$

where the indices 0 and i denote the values today and initial, respectively. k_s are very small wavenumbers, i.e. much larger scales than the horizon. Since the superhorizon perturbations grow $\propto a^2$ during the radiation phase, the growth of two different scales of perturbations is proportional to k^2, because small scale perturbations are frozen in that phase. This can be seen in the left panel of Fig. 2.7, where the dashed line represents the CDM case. For larger scales (smaller k) the perturbations increase by a factor of k^2.

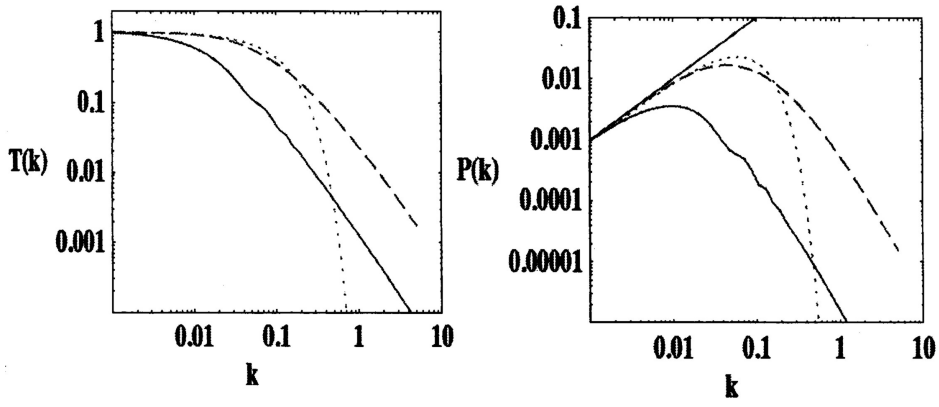

Figure 2.7: The shape of the transfer function $T(k)$ and matter power spectrum $P(k)$ for three different cosmologies: ΛCDM Universe with baryons (solid), EdS without baryons (dashed) and a hot Dark Matter cosmology (dotted). Taken from Bernardeau (2009), slightly adopted.

Often this is presented in form of the (present day) matter power spectrum $P(k)$ (right panel of Fig. 2.7):

$$P(k) = A\, k^{n_s}\, T(k)^2 \ . \tag{2.40}$$

A is a normalization constant and $n_s \approx 1$ is the slope of the primordial power spectrum, because for early times in the Universe $T(k)$ becomes 1. So apart from the normalization, the shape of the power spectrum is fully predicted in a CDM Universe: At large scales it is $\propto k$, while at small scales $\propto k^{-3}$. Often the normalization is not given explicitly by the A parameter, but through some observationally motivated quantity σ, which denotes the (square root of the) variance of matter density fluctuations,

$$\sigma^2 = \frac{\langle (M - \langle M \rangle)^2 \rangle}{\langle M \rangle^2} = \frac{1}{2\pi^2} \int \mathrm{d}k\, P(k)\, W^2(kR)\, k^2 \ . \tag{2.41}$$

W is the Fourier Transform of the tophat window function and $\langle M \rangle = \frac{4}{3}\pi R^3 \rho_\mathrm{m}$, where ρ_m is the mean density of the Universe at redshift z,

$$\rho_\mathrm{m} = \rho_\mathrm{crit}(z) \cdot \Omega_\mathrm{m}(z) \ . \tag{2.42}$$

The size of spheres over which the dispersion of the matter density contrast is averaged is defined as $R = 8h^{-1}\mathrm{Mpc}$. This leads to the definition of

$$\sigma_8^2 = \sigma(8h^{-1}\mathrm{Mpc})^2 = \frac{A}{2\pi^2} \int k^{2+n_s}\ T(k)^2\ W(k\, h^{-1}\,\mathrm{Mpc})^2\, \mathrm{d}k \ , \tag{2.43}$$

which describes the amplitude of the power spectrum at galaxy cluster scales.

In order to form structures, the spherical overdensities have to collapse. An overdense region has a slower expansion (due to gravity) than the average Universe. This effects the overdensity to become larger and eventually collapse after reaching a critical point of maximum expansion of the overdense region. In an EdS Universe (Einstein-de-Sitter, a flat Universe with $\Omega_\mathrm{m} = 1$) this can be calculated analytically, resulting in a linearly extrapolated critical overdensity of $\delta_c \approx 1.69$. In nonlinear theory (but still matter dominated Universe) the density of an overdensity at the point of maximum expansion exceeds the mean density by a factor of 5.55. Using the virial theorem and energy conservation one knows that the density of the collapsed structure is 8 times higher than at the turnover point (maximum expansion), while at the same time the mean density of the Universe was decreased by a factor of 4 due to expansion. So the density of the collapsed structure is around 178 times higher than the mean density (in an EdS Universe), i.e. that structures are gravitationally bound if they reach an overdensity of 178. Despite the fact that for a ΛCDM Universe this value will be significantly lower, 200 is still used to characterize the virial mass of

galaxy clusters, e.g. $M_{\rm vir} \approx M_{178} \approx M_{200}$, which means that within a certain radius (R_{200}), the average density of the galaxy cluster is 200 times the critical density of the Universe at cluster redshift z,

$$M_{200} = 200 \cdot \rho_{\rm crit}(z)\, \frac{4\pi R_{200}^3}{3} \ . \tag{2.44}$$

The time evolution term in (2.34) D_+ now characterizes the evolution of a collapsed overdensity

$$\delta(z) = \delta_0 \frac{D(z)}{D(0)} \ . \tag{2.45}$$

$\frac{D(z)}{D(0)}$ is called the growth factor and can be expressed analytically for Universe with a cosmological constant ($w = -1$), while for any other case the differential equation 2.34 needs to be solved numerically.

2.3 Halo Mass Function

One of the most interesting cosmological probes is the number density of collapsed structures, or Dark Matter halos (galaxy clusters), as a function of halo mass and redshift, which is called the halo mass function (HMF),

$$\frac{{\rm d}n}{{\rm d}M}(M, z) \ .$$

As shown by Press and Schechter (1974); Jenkins et al. (2001) the functional form of the HMF is universal for a given cosmology,

$$\frac{{\rm d}n}{{\rm d}M}(M, z) = f(\sigma, z) \frac{\rho_{\rm m}(z=0)}{M} \frac{{\rm d}\ln(\sigma^{-1}(M, z))}{{\rm d}M} \ . \tag{2.46}$$

In the Press-Schechter theory (Press and Schechter, 1974) the halo mass function is based on simple assumptions: The initial density fluctuations are described by a Gaussian random field and only regions with $\delta > \delta_c$ collapse and form structures. The probability P for a collapsed structure of mass M at redshift z is given by the integral over the random field, starting from the minimum density contrast,

$$P = \frac{1}{\sqrt{2\pi}\sigma(M, z)} \int_{\delta_c}^{\infty} \exp\left(-\frac{\delta^2}{2\sigma^2(M, z)}\right) {\rm d}\delta = \frac{1}{2}{\rm erfc}\left(\frac{\delta_c}{\sqrt{2}\sigma(M, z)}\right) \ , \tag{2.47}$$

where erfc is the complementary error function, which has the derivative given by

$$\frac{{\rm d}\,{\rm erfc}(x)}{{\rm d}x} = -\frac{2}{\sqrt{\pi}} \exp\left(-x^2\right) \ , \tag{2.48}$$

where x can be identified by $x = \frac{\delta_c}{\sqrt{2}\sigma(M,z)}$. This probability can also be seen as a number density of objects. The corresponding volume of an object of mass M is

$$V = \frac{M}{\rho_{\rm m}} \ . \tag{2.49}$$

Putting the pieces together gives

$$\frac{{\rm d}n}{{\rm d}M} = \frac{1}{V}\frac{{\rm d}P}{{\rm d}M} = \frac{1}{V}\frac{{\rm d}P}{{\rm d}x}\frac{{\rm d}x}{{\rm d}M} = \frac{\rho_{\rm m}}{M}\frac{\delta_c}{\sqrt{2\pi}\sigma(M, z)} \left|\frac{{\rm d}\ln\sigma^{-1}(M, z)}{{\rm d}M}\right| \exp\left(-\frac{\delta_c^2}{2\sigma^2(M, z)}\right) \ . \tag{2.50}$$

Integrating the number density over the whole mass range one gets 0.5, so the probability is not normalized correctly. This means that all objects with a smaller density contrast than δ_c are not accounted, even if they end up in larger halos. Usually this is solved by multiplying everything by 2, which gives the final

Press-Schechter mass function,

$$\frac{\mathrm{d}n}{\mathrm{d}M} = \frac{\rho_\mathrm{m}\delta_c\sqrt{2}}{M\sqrt{\pi}\sigma(M,z)}\left|\frac{\mathrm{d}\ln\sigma^{-1}(M,z)}{\mathrm{d}M}\right|\exp\left(-\frac{\delta_c^2}{2\sigma^2(M,z)}\right) \ . \tag{2.51}$$

From Eq. 2.51 it is clear that the number density drops exponentially at the high mass end, which means the halo mass function is very sensitive to massive galaxy clusters.

More recent mass functions are calculated from N-body simulations. In Pillepich et al. (2010) the authors summarize and compare the most important parametrizations of $f(\sigma)$ over the recent years. With several parametrizations of $f(\sigma)$ authors have shown with simulations (Sheth and Tormen, 1999; Jenkins et al., 2001; Warren et al., 2006) the validity of the $f(\sigma)$ term, i.e. the universality is given independent of cosmological parameters. Tinker et al. (2008) restrict the universality to a redshift dependent parametrization yielding 5% accuracy compared with simulations. More recently efforts were spent to also derive a mass function beyond the 5-10% limit and include e.g., the effects of Dark Energy (wCDM) model (Bhattacharya et al., 2011), of baryons in the mass function (Bocquet et al., 2015) or an extension to higher redshifts (Watson et al., 2013). Two ways to characterize halos within the simulations commonly exist, the friends-of-friends algorithm (FOF) and the spherical overdensity (SO) definition. A FOF algorithm detects structures based on their physical proximity compared to a threshold value (linking length). In general the FOF method lowers the scatter in the $f(\sigma,z)$ fitting, but cannot be easily applied to observations. SO algorithms detect isolated, local overdensities in the simulation and show good agreement with the mass measurements of galaxy clusters. This is the requirement for any cosmological interpretation of number densities of galaxy clusters.

In this work I mainly focus on the Tinker et al. (2008) halo mass function, since it is widely used and can be easily compared to observables. Using

$$f(\sigma,z) = A\left[\left(\frac{\sigma}{b}\right)^{-a}+1\right]\exp\left(-\frac{c}{\sigma^2}\right) \ , \tag{2.52}$$

with the values (and second derivatives) of A,a,b,c (which all except c depend on the redshift) given for 9 different overdensities in Tinker et al. (2008). Unfortunately, uncertainties or a covariance matrix for these parameters is not provided, so I assume that these values are precise. The halo mass function is shown in Fig. 2.8 including the effect of three important quantities, the redshift, the matter density Ω_m, and the amplitude of initial density fluctuations σ_8. More matter in the Universe (higher Ω_m) will also increase the the halo mass function, at all masses. Since structure in the Universe formed hierarchically, in the past (higher redshift) the Universe had less massive clusters. Finally, the high mass end of the halo mass function is very sensitive to σ_8, which means the most massive clusters in the Universe basically determine this parameter.

One weakness of this approach is that galaxy clusters are not perfectly symmetric objects, but often have an elliptical apparent shape (e.g., Kolokotronis et al., 2001). Theory has predicted an ellipsoidal shape of Dark Matter halos due to various reasons (Warren et al., 1992; Dubinski, 1994; Jing et al., 1995; Thomas et al., 1998; Tormen, 1997). For example structures are assumed to build hierarchically by major mergers and the attraction of smaller objects (Press and Schechter, 1974; Blumenthal et al., 1984), and these substructures cause linear theory to fail (Diaferio, 1999). This aspect needs to be studied in more detail in future simulations.

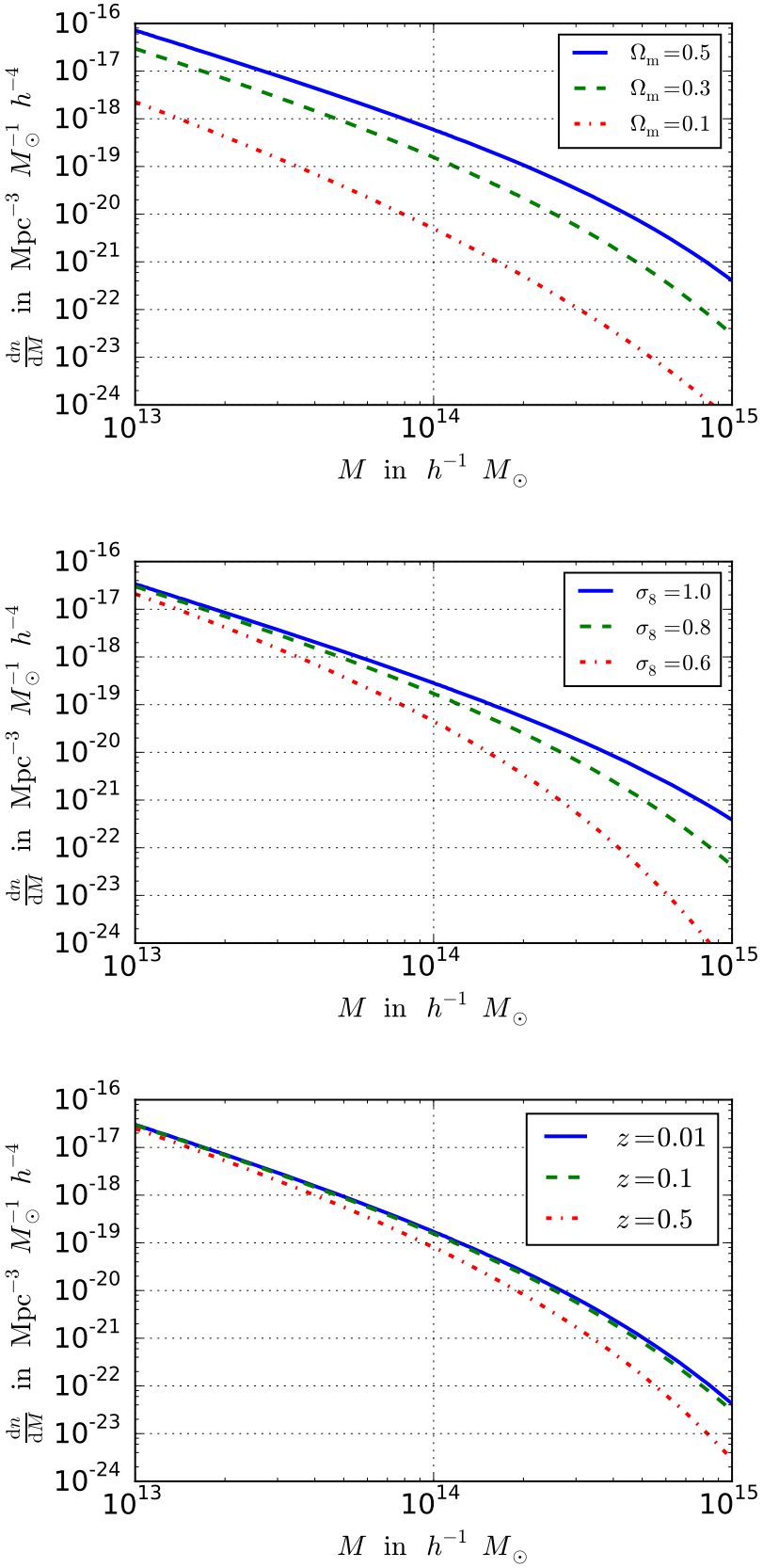

Figure 2.8: Tinker et al. (2008) halo mass function. The default setup is a flat ΛCDM Universe with $\Omega_m = 0.3$, $\sigma_8 = 0.8$, $z = 0.01$. The three plots show the effect of these three parameters.

CHAPTER 3

Chandra – XMM-Newton Cross Calibration

X-ray observations of galaxy clusters provide the unique potential of measuring the mass of the hot intra cluster medium and the total gravitating mass assuming hydrostatic equilibrium. This information can be used to infer cosmology and give an independent measurement of parameters like $\Omega_{\rm M}$ and σ_8. But any interpretation of X-ray data depends crucially on the accuracy of the instrumental calibration. If those uncertainties are not explicitly incorporated, unknown biases will be introduced. For X-ray telescopes with CCD detectors, several aspects have to be studied to achieve reliable results:

- Energy and spatial dependence of the effective area, which contains the mirror geometric area, reflectivity, vignetting and quantum efficiency of the detector. Also the absorption due to contamination layers on the CCD filters is often factored in the effective area.
- The response of the detector, i.e. the energy and spatial dependence of the probability function to convert from photon energies to detector channels.
- The energy and spatial dependence of the point spread function (PSF).
- The time dependence of the three aspects mentioned above, i.e. the calibration has to be revised on a regular base.

Despite the expensive ground calibrations before launch and regular observation of calibration targets, there are still significant differences between the current major X-ray instruments as shown in Nevalainen et al. (2010) and Kettula et al. (2013). These studies have only shown the pure effective area calibration uncertainties and the impact and temperature and flux measurements with small samples ($N = 11$). In the following I will show in detail the calibration uncertainties between the five X-ray instruments, EPIC-MOS1/MOS2/PN onboard XMM-Newton and ACIS-I/S onboard Chandra and quantify the influence on temperature measurements and the cosmological parameters.

This chapter has been published in Schellenberger et al., 2015 (Schellenberger, G., Reiprich, T. H., Lovisari, L., Nevalainen, J., and David, L.: 2015, A&A 575, A30).

Abstract

Robust X-ray temperature measurements of the intracluster medium of galaxy clusters require an accurate energy-dependent effective area calibration. Since the hot gas X-ray emission of galaxy clusters does not vary on relevant timescales, they are excellent cross-calibration targets. Moreover, cosmological constraints from clusters rely on accurate gravitational mass estimates, which in X-rays strongly depend on cluster gas temperature measurements. Therefore, systematic calibration differences may result in biased, instrument-dependent cosmological constraints. This is of special interest in light of the tension between the Planck results of the primary temperature anisotropies of the CMB and Sunyaev-Zel'dovich-plus-X-ray cluster-count analyses. We quantify in detail the systematics and uncertainties of the cross-calibration of the effective area between five X-ray instruments, EPIC-MOS1/MOS2/PN onboard XMM-Newton and ACIS-I/S onboard Chandra, and the influence on temperature measurements. Furthermore, we assess the

impact of the cross-calibration uncertainties on cosmology. Using the HIFLUGCS sample, consisting of the 64 X-ray brightest galaxy clusters, we constrain the ICM temperatures through spectral fitting in the same, mostly isothermal regions and compare the different instruments. We use the stacked residual ratio method to evaluate the cross-calibration uncertainties between the instruments as a function of energy. Our work is an extension to a previous one using X-ray clusters by the International Astronomical Consortium for High Energy Calibration (IACHEC) and is carried out in the context of IACHEC. Performing spectral fitting in the full energy band, $(0.7-7)$ keV, as is typical of the analysis of cluster spectra, we find that best-fit temperatures determined with XMM-Newton/EPIC are significantly lower than Chandra/ACIS temperatures. This confirms the previous IACHEC results obtained with older calibrations with high precision. The difference increases with temperature, and we quantify this dependence with a fitting formula. For instance, at a cluster temperature of 10 keV, EPIC temperatures are on average 23% lower than ACIS temperatures. We also find systematic differences between the three XMM-Newton EPIC instruments, with the PN detector typically estimating the lowest temperatures. Testing the cross-calibration of the energy-dependence of the effective areas in the soft and hard energy bands, $(0.7-2)$ keV and $(2-7)$ keV, respectively, we confirm the previously indicated relatively good agreement between all instruments in the hard and the systematic differences in the soft band. We provide scaling relations to convert between the different instruments based on the effective area, gas temperature, and hydrostatic mass. We demonstrate that effects like multitemperature structure and different relative sensitivities of the instruments at certain energy bands cannot explain the observed differences. We conclude that using XMM-Newton/EPIC instead of Chandra/ACIS to derive full energy band temperature profiles for cluster mass determination results in an 8% shift toward lower $\Omega_{\rm M}$ values and $< 1\%$ change of σ_8 values in a cosmological analysis of a complete sample of galaxy clusters. Such a shift alone is insufficient to significantly alleviate the tension between Planck cosmic microwave background primary anisotropies and Sunyaev-Zel'dovich-plus-XMM-Newton cosmological constraints.

3.1 Introduction

Galaxy clusters are excellent tools for studying cosmology, in particular the phenomena of dark matter and dark energy, because they are the most massive gravitationally relaxed systems in the Universe. Especially the cluster mass function, which is the number density of clusters with a certain mass, is a sensitive probe of cosmological parameters. By determining the temperature using X-ray emission from the hot intracluster medium (ICM), one traces the most massive visible component of clusters and can derive both the total gravitating mass and the mass of the emitting medium.

Robust cosmological constraints require accurate estimates of the cluster masses without any systematic bias. There are at least two important sources of possible biases in the hydrostatic method: a) the previously reported results of the International Astronomical Consortium for High Energy Calibration IACHEC[1] on the cross-calibration uncertainties of the effective area between XMM-Newton/EPIC and Chandra/ACIS (Nevalainen et al., 2010, N10), the two major current X-ray missions and b) the hydrostatic bias (e.g., Nagai et al., 2007) whereby a fraction of the total pressure in the ICM has a non-thermal origin, e.g., due to bulk motions. In the latter case, the assumption of the gas pressure balancing the gravity underestimates of the total mass.

Both biases may be affecting the recent Planck results (Planck Collaboration et al., 2013a,b), whereby the cosmological constraints driven by the primary temperature anisotropies of the cosmic microwave background radiation (CMB) and Sunyaev-Zel'dovich (SZ) analyses do not agree with each other. For the SZ analysis a relation between the Compton Y parameter and the mass for galaxy clusters derived using XMM-Newton data was used and even allowing for a possible hydrostatic mass bias factor in the range $0.7-1.0$, no full agreement between the two probes is achieved. As mentioned before, reasons for the discrepancy can be the breakdown of the hydrostatic assumption, the underestimation of calibration uncertainties in the X-ray, but also in the microwave regime, or an incomplete cosmological model (e.g., the lack of massive neutrinos).

As pointed out in von der Linden et al. (2014), the XMM-Newton-based cluster masses in the Planck sample are significantly lower than the values obtained from a weak lensing analysis. This difference is mass dependent and might be explained by (i) a temperature-dependent calibration uncertainty and/or (ii)

[1] `http://web.mit.edu/iachec/`

a failing hydrostatic assumption. We address the question of whether a Chandra-derived scaling relation could solve this tension, i.e., whether systematic cross-calibration uncertainties between Chandra and XMM-Newton can explain the inconsistent Planck results. The results in Israel et al. (2014a), where Chandra X-ray masses agree with cluster masses of a weak-lensing analysis indicate that the hydrostatic assumption does not cause a major bias with respect to weak-lensing masses. While we clearly isolate here the systematic uncertainty resulting directly and only from X-ray calibration uncertainties, a comparison of mass estimates and/or cosmological constraints from different sources is much more complicated (Rozo et al., 2014).

We show in this work how reliable the current (December 2012) calibrations are by using nearby galaxy clusters as reference objects and comparing the measured XMM-Newton temperatures with the results from Chandra. Galaxy clusters are Megaparsec-scale objects, and their X-ray emission from the hot ICM does not vary on human timescales.

The XMM-Newton/Chandra effective-area cross-calibration uncertainties as reported in N10 yielded that Chandra/ACIS measures $\sim 10-15\%$ higher temperatures in the $(0.5-7)$ keV energy band compared to XMM-Newton/EPIC. Since the N10 sample was relatively small (11 galaxy clusters), it is important to evaluate the XMM-Newton/Chandra effective area cross-calibration uncertainties with a large cluster sample to gain more statistical precision for comparing XMM-Newton and Chandra temperatures. Furthermore, the cosmological implications of cross-calibration uncertainties have not been studied by N10. In more recent works (e.g., Mahdavi et al., 2013; Martino et al., 2014; Donahue et al., 2014) the authors still find significant differences in temperatures between Chandra and XMM-Newton by comparing the data of typically of about of 20 galaxy clusters.

Here we use the HIFLUGCS cluster sample (Reiprich and Böhringer, 2002), which provides the 64 galaxy clusters with the highest X-ray flux. High quality Chandra/ACIS and XMM-Newton/EPIC data are available for all of them except one (Hudson et al., 2010; Zhang et al., 2011a). This work is an extension of N10 in the sense that it updates the calibration information (as in Dec 2012) with about five times more objects and that the cosmological impact is quantified. The current data can be used to evaluate both the energy dependence and the normalization of the cross-calibration uncertainties. We are interested in the cross-calibration effect on the cluster mass function, which depends on the temperature and only on the gradient of the gas density. Therefore, the normalization of the effective areas is not relevant for the current work and will be addressed in detail in an upcoming paper.

In this paper we first describe the properties of the galaxy clusters we use in Section 3.2. We give an overview of our data reduction for the two satellites in Section 3.3 and describe the background subtraction in Section 3.4 in more detail. Section 3.5 deals with the analysis method, and finally we present the results in Section 3.6 and discuss the various effects that might have an influence on the results in Section 3.7. In this section we also describe the cosmological impact on the normalized matter density parameter, $\Omega_{\rm m}$, and the amplitude of the linear matter power spectrum on $8h^{-1}$Mpc scale, σ_8.

Throughout this paper we use a flat ΛCDM cosmology with the following parameters:
$\Omega_{\rm m} = 0.3$, $\Omega_\Lambda = 0.7$, $H_0 = h \cdot 100\,{\rm km\,s^{-1}\,Mpc^{-1}}$ with $h = 0.71$.

3.2 Cluster properties

The whole HIFLUGCS cluster sample consists of 64 clusters with a redshift up to $z = 0.215$ for RXCJ1504. The average redshift of this sample is $z = 0.053$ with a dispersion of 0.039. All clusters are listed in Table 3.3. Chandra ACIS data are available for all 64 clusters, XMM-Newton EPIC data for all except A2244, which will be observed in AO13.

In Hudson et al. (2010) a galaxy cluster is defined as a cool-core cluster if the central cooling time is less than 7.7 Gyr. The authors also show that NCC clusters of the HIFLUGCS sample exhibit a temperature drop toward the center of less than 20%, while CC clusters show a decrease in the temperature by a factor of 2 to 5. More details on this phenomenon including the categorization of the HIFLUGCS clusters in CC and NCC clusters can be found in Hudson et al. (2010). To minimize possible biases introduced by multitemperature ICM (Section 3.7.1) we exclude the cool core regions of clusters as provided by Hudson et al. (2010)[Table 2].

The greatest limitation for the choice of the extraction region size is imposed by ACIS-S. In order not to lose a fraction of the cluster annulus owing to a relatively limited ACIS-S field of view (FOV), we set the

outer extraction radius to $3.5'$ around the emission peak, as defined in Hudson et al. (2010).

Finally we always added $15''$ on all cool core radii and point-source radii (as determined from Chandra data using a wavelet algorithm) to minimize the scattering of emission into the annulus because of the XMM-Newton PSF. We marked bad columns and chip gaps in the observations of the three EPIC instruments and excluded them from all spectral analyses.

Furthermore, this assures that regions are fully covered by Chandra's FOV for almost all clusters. All this leads to the following procedure:

- For cool-core clusters, the cool core region (plus $15''$) was excluded, and the temperature was measured within an annulus between the cool core and the $3.5'$.
- Non-cool-core clusters are assumed to have no big temperature variations, so the region used here is the full $3.5'$-circle. We assume that the azimuthal temperature variations can be neglected for our purpose.
- For five clusters, the $3.5'$ enclose regions outside the ACIS-S chips. Since this could bias our results, we changed the outer border for these clusters (for both XMM-Newton and Chandra) from the usual $3.5'$ to a smaller radius that lies completely on the chips. The new outer borders are:
  - $2'$ for Abell 754
  - $2'$ for Abell 1367
  - $2.1'$ for Abell 2256
  - $2.4'$ for Hydra A
  - $2.3'$ for NGC 1550
- For seven clusters[2], the cool core is larger than $3.5'$. These clusters were excluded from our analysis. To see whether these clusters would bias our result, we analyzed them within the full $3.5'$ circle as well (see Fig. 3.9). The check revealed that these clusters do not show any special behavior in any direction as compared to the other clusters. Apart from the previously mentioned figure and the stacked residual ratio analysis (Section 3.5.2), these seven clusters are always excluded.

Within these regions the source-to-background count-rate ratio in the sample is between 9 and 135 in the $(0.7 - 2.0)\,\mathrm{keV}$ band.

3.3 Data processing

3.3.1 Chandra

Chandra data reduction was performed using the *CIAO* software (CIAO 4.5, CALDB 4.5.5.1) and the *HEASOFT* tools (6.12), including the *Xspec* fitting package (12.7.1d and AtomDB 2.0.2)[3]. We first created the level-2 event files using the contributed script `chandra_repro`, for example, to correct for afterglows from cosmic rays. In the next step the chips comprising the selected regions (I-chips were combined for I-observations) were cleaned from solar flares by creating a lightcurve with the suggested values from Markevitch's Cookbook[4] and the `lc_clean` algorithm. Point sources detected by the `wavdetect` algorithm were excluded, but each observation was visually inspected for false and insignificant detections, and if necessary, the list of point sources was edited manually. The `acis_bkgrnd_lookup` script helped us to find the blank-sky background file from the CALDB matching to the observation. Finally background files were reprojected to match the orientation of the cluster observation, before continuing. For VFAINT observations only the events with status bits = 0 were used because all background files were taken from VFAINT observations.

Unfortunately, the quiescent particle background varies with time, so we had to compensate for this behavior by rescaling the background count rate with a normalization factor. This factor is the ratio of

[2] A2142, A2256, A3526, HydraA, NGC1399, NGC4636, NGC5044
[3] `http://www.atomdb.org`
[4] `http://cxc.harvard.edu/contrib/maxim/acisbg/COOKBOOK`

the count rates in the $(9.5 - 12)$ keV energy range of the blank sky files and the observations, because the effective area of Chandra is almost zero in this energy interval and almost all events are related to the particle background. This factor is then multiplied by the BACKSCALE value of the background spectral file. To create the spectra and response files, we used the `specextract` task and created the weighted RMFs and ARFs. The spectra were grouped to have at least 30 counts per bin.

3.3.2 XMM-Newton

The XMM-Newton data reduction is different in some parts from the Chandra treatment. The software we used was the SAS package version 12.0.1 with CCF calibration files from 14.12.2012. With `emchain` and `epchain`, we created the initial event lists excluding flagged events (`FLAG==0`) and setting `PATTERN<=12` for MOS and `PATTERN==0` for PN. The decision that only single events be selected for EPIC-PN is because there are still significant gain problems for the double events (see XMM-Newton release note XMM-CCF-REL-309). Blank-sky background files are also available for XMM-Newton and can be downloaded from the website[5]. One has to make sure to use the correct file for each observation in terms of used filter, pointing and recording mode. Solar flares are a tremendous issue for XMM, so we cleaned the lightcurve in two steps to remove them. To obtain the good time intervals we fitted a Poisson distribution function to a 100 s binned histogram of the high energy lightcurve, i.e. $(10 - 12)$ keV for MOS and $(12 - 14)$ keV for PN. Events belonging to a count rate higher than $2\sqrt{\mu}$ above the mean count-rate, μ, were rejected.

In a second step, the lightcurve was filtered in the full energy band from $(0.3 - 10)$ keV by the same method as described. The same thresholds were applied to the background files. We visually inspected all final full-energy band lightcurves and, if necessary, removed strong flares that were not detected by the previously mentioned method. Since Chandra has much better spatial resolution, we used the detected point sources from the Chandra analysis and removed the same regions here. We excluded chip gaps and bad columns of the EPIC instruments from all observations. This exclusion criterion changes the best-fit temperature on the order of 0.5%. The normalization of the background files due to the changing particle background level is done in the same way as for Chandra except that the high energy interval, $(9.5 - 12)$ keV for Chandra, $(10 - 12)$ keV for EPIC-MOS and $(12 - 14)$ keV for EPIC-PN, is different because of Chandra's lower effective area in the high energy. For the EPIC spectra we used the same spectral grouping parameters as for Chandra of 30 counts per bin.

3.4 Background treatment

X-ray observations are always contaminated with events not related to the source, which we call background in the following. It usually consists of:

- the particle background: Energetic particles produce charges on the detector while penetrating it, or induce fluorescent emission lines in the surrounding material;
- the so-called soft protons: These particle events should be removed by the flare reduction process to a significant amount;
- the cosmic X-ray background (CXB): It can be subdivided into the local hot bubble emission, the thermal emission of the galactic halo, and the contribution of unresolved point sources (most likely AGNs, see, e.g., Hickox and Markevitch, 2006);
- solar wind charge exchange emission (SWCX): Highly ionized particles interacting with neutral atoms. For more details, see Wargelin et al. (2004); Snowden et al. (2004).

Generally it is very important to properly account for all background components because they affect the cluster temperature resulting from the spectral fit. The HIFLUGCS clusters are nearby objects, so they cover almost the whole field of view of the two instruments, and the background cannot be estimated from the observation itself. We decided to use the blank-sky observations for both Chandra and XMM-Newton, because our selection criteria ensure that the background is much lower than the source count rate (see Table 3.4). These archival observations of regions without astronomical sources are not always the best

[5] `http://xmm2.esac.esa.int/external/xmm_sw_cal/background/blank_sky.shtml`

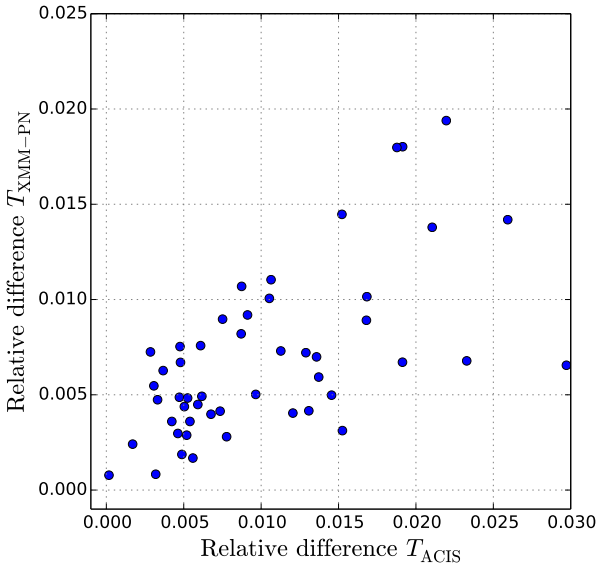

Figure 3.1: Relative temperature difference resulting from raising the background level by 10 % for energies below 2 keV.

description for every observation, but when extracting spectra out to only 3.5′ for these very bright objects, the error is negligible, because the background level is at least one order of magnitude lower than the cluster emission. To verify this assumption, we increased the background normalization by 10% up to an energy of 2 keV (see Fig. 4.11). Beyond that energy the spectrum remains unchanged. This should simulate a different foreground/CXB emission level but leaves the particle background unchanged, which is dominant beyond 2 keV. For ACIS, 91% of the clusters exhibit a difference in the best-fit temperature of less than 2%, while EPIC-PN temperature changes are less than 2% for all clusters. RXCJ1504 has a temperature difference for ACIS of almost 3% after changing the background. Still this is not significant, since this cluster is one of the hottest in the sample, and it has a temperature difference between ACIS and EPIC-PN of more than 35% in the full energy band (see Table 3.4).

Apart from a systematic under- or overestimation of the background level, an energy dependence of the background spectrum mismatch can be introduced by the photo-electric absorption of the blank sky background: The observations from which the blank sky background is extracted were taken at different sky positions and undergo different absorptions. The mean hydrogen column density along the line of sight, N_{H}, of all these regions will not agree with most of the cluster observation. For all the clusters we checked the effect of changing the background spectra by absorbing it according to the cluster N_{H} minus the exposure-weighted average hydrogen column density of the background file. This method produces a background spectrum as it would have been observed through the cluster line-of-sight absorption. For all clusters the temperature difference is below 3%, and it is below 1% for almost 90% of the clusters. This is also expected since the source to background count rate ratio in the relevant energy band is very high.

In summary, our results are robust against systematic uncertainties in the background estimation.

3.5 Analysis

3.5.1 Spectral fitting method

To obtain the emission model and temperature for each region, we fit an *apec*-model (Smith et al., 2001) and a photoelectric absorption model (*phabs*) using the cross sections from Balucinska-Church and McCammon (1992). The column density of neutral hydrogen N_{H} and the redshift z are frozen to the values from Zhang et al. (2011a), where most of the hydrogen column densities are consistent with the values from the LAB HI survey (Kalberla et al., 2005). For two clusters, Abell 478 and Abell 2163, our spectral fits resulted in a very poor χ^2, so we used N_{H} values from spectral fits with the hydrogen column density left free to

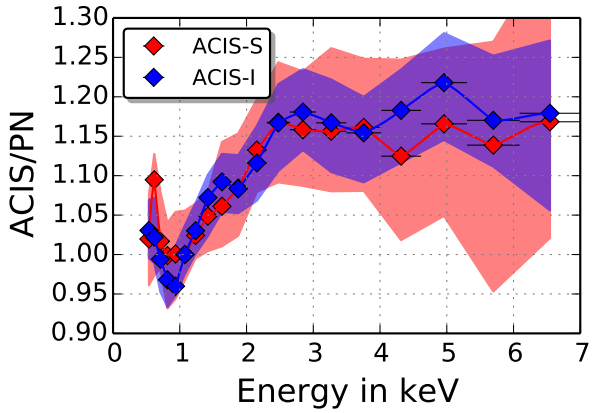

Figure 3.2: Stacked residuals ratio, rescaled to unity at 1.1 keV. The shaded region represents the 68% confidence level from 10 000 bootstrap simulations. For a detailed description see text.

vary. For Abell 478 we used $3 \times 10^{21}\,\mathrm{cm}^{-2}$ and for Abell 2163 $2 \times 10^{21}\,\mathrm{cm}^{-2}$. Both values are around 100% higher than the LAB values, and they produced a $\chi^2_{\mathrm{red}} < 1.6$ for the spectral fit. The new values also agree roughly with the $N_{\mathrm{H,tot}}$ values, as discussed in Section 3.7.2.

For Abell 478 and Abell 3571, we did not consider the redshifts from Zhang et al. (2011a), because all X-ray instruments agree with the new redshift values from the spectral fit (0.0848 instead of 0.0900 for Abell 478 and 0.0374 instead of 0.0397 for Abell 3571).

By default the abundance table presented in Anders and Grevesse (1989) (AnGr) was used for the absorption and emission model. Additionally, all values were recomputed using the relative abundance of elements from Asplund et al. (2009) (Aspl).

We performed the spectral fits in the full $(0.7-7)\,\mathrm{keV}$, hard $(2-7)\,\mathrm{keV}$, and soft $(0.7-2)\,\mathrm{keV}$ energy bands. This is different from the definition in N10, where the low energy threshold of the full and soft bands was at 0.5 keV. We also excluded the events below 0.7 keV to avoid the emission lines around 0.6 keV due to the cosmic X-ray background or SWCX. We also excluded all events above 7 keV because of the prominent EPIC-PN fluorescent lines (Ni at 7.5 keV, Cu at 8 keV, and Zn at 8.6 keV) and the small Chandra effective area. It should be mentioned that the soft band spectral fits for high temperature clusters provides poor constraints on the parameters because the change in the slope of different temperature models is very small, and there are almost no emission lines in this energy band. For the full- and hard-band fits all χ^2_{red} are below 1.6, while for the soft band fits the maximum χ^2_{red} is 2.3 (although for more than 88% the χ_{red} are below 1.3). The possibility and influence of a temperature-abundance degeneracy will be discussed in Section 3.7.1

3.5.2 Stacked residuals ratio

The effective area cross-calibration uncertainties between a pair of instruments as a function of energy can be obtained using the stacked residual ratio method (see Kettula et al., 2013 and Longinotti et al., 2008). Using the definition from Kettula et al. (2013) for the stacked residual ratio,

$$R_{ij} = \frac{\mathrm{data}_i}{\mathrm{model}_j \otimes \mathrm{response}_i} \times \frac{\mathrm{model}_j \otimes \mathrm{response}_j}{\mathrm{data}_j}\,, \tag{3.1}$$

we can test instrument i and use instrument j as reference. We briefly summarize the steps:

- The results on the relative cross-calibration uncertainties do not depend on the choice of the reference detector.
- The data of the reference detector are fitted with an absorbed `apec`-model in the $(0.5-7.0)\,\mathrm{keV}$ energy range. We also experimented by using an absorbed `mekal`-model to be more consistent with previous works (Kettula et al., 2013, N10) using the stacked residual ratio method, but we did

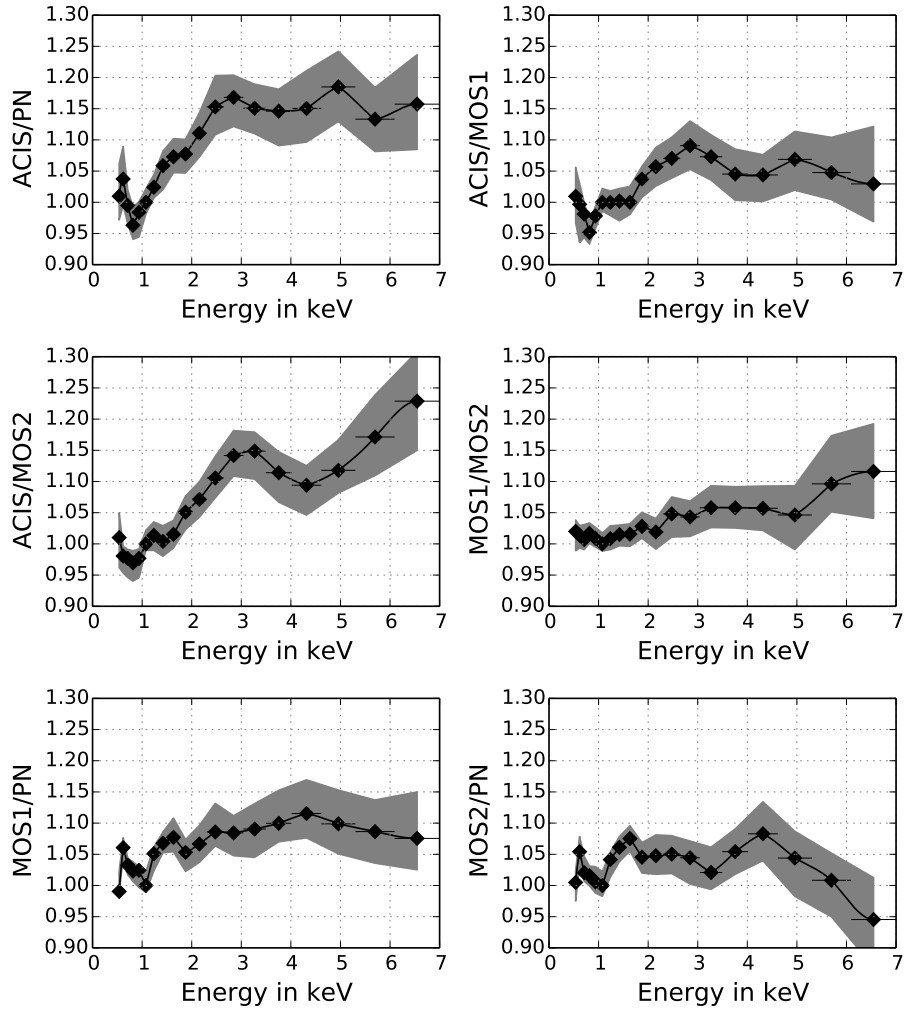

Figure 3.3: Stacked residuals ratios are rescaled to unity at 1.1 keV. The shaded region represents the 68% confidence level from 10 000 bootstrap simulations. For a detailed description, see text. Apart from choosing EPIC-PN as the reference instrument, we also show the ACIS/MOS1, ACIS/MOS2, and MOS1/MOS2 stacked residuals.

not find any significant differences. This fitting procedure defines our reference model and is not changed any more in the following. We included the $(0.5-0.7)$ keV energy band for the stacked residual ratio test in order to stay close to previous analyses.

- Each spectral data point of all the instruments (ACIS-S, ACIS-I, MOS1, MOS2, and PN) is divided by the reference model folded with the response (RMF and ARF) of the current instrument. This gives us the residuals.
- In the next step we calculated the residual ratio (Eq. 3.1) for each cluster and instrument pair by dividing the residuals of ACIS-S, ACIS-I, MOS1, and MOS2 by the residuals of the reference instrument (PN). The second term in Eq. 3.1 corrects for possible deviations between the data and model prediction of the reference instrument; i.e., after this correction the reference model agrees with the reference data. Thus, the details of the reference model (e.g., single temperature or multitemperature) are not important. Since the detectors use a different energy binning, we perform a linear interpolation to be able to calculate the residuals ratio at exactly the same energies for different instruments before dividing the residuals.
- In the full $(0.5-7.0)$ keV energy range, we define 19 energy bins (with equal separation in log-space), within which we calculate the median value of the residuals ratio of all the clusters to be analyzed. This yields the stack residuals ratio. We estimated the uncertainty by performing 10 000 bootstrap simulations and taking the 68% confidence interval around the median of the 10 000 sample medians.
- We normalized the stacked residual ratios to unity at 1.1 keV because we are not studying the cross-calibration of the normalization of the effective area in this work, since it does not affect the temperature measurement.

Applying the stacked residual ratio method we end up with 53 clusters. Some observations[6] had to be discarded because the source region is not completely within one chip for ACIS-S observations.

3.6 Results

3.6.1 Stacked residuals ratio

The analysis yielded that ACIS-S and ACIS-I stack residuals, using EPIC-PN as the reference, are consistent at all energies (see Fig. 3.2). This indicates that there are no energy-dependent effective area calibration biases between the two ACIS instruments at the 5-10% level of the statistical uncertainties. Thus, in the following we combine ACIS-S and ACIS-I to a single group called ACIS. The uncertainties coming from the bootstrap simulation are on average 60% higher for ACIS-S/PN than for ACIS-I/PN, because only 13 observations were done with ACIS-S.

Furthermore, the flat ACIS and MOS1 vs. PN stacked residuals imply that at energies above 3 keV there are no significant energy-dependent effective area cross-calibration uncertainties between these instruments. However, the MOS2/PN stacked residuals deviate significantly from a flat ratio (see Fig. 3.3). Given that MOS2 is the only instrument that indicates energy-dependent features above 3 keV, it is likely that MOS2 has the larger calibration uncertainties, in the sense that with increasing energy in the 3–7 keV band, the MOS2 effective area is increasingly overestimated. The bias reaches $\sim$10% at 7 keV for MOS2/PN. Consequently, the MOS2 temperatures in the hard band are lower than values obtained with MOS1 or ACIS (see below). A similar effect was suggested by N10, who did not study the effect in more detail owing lack of statistical precision.

The situation is more problematic at lower energies. In general, the EPIC-PN vs. ACIS soft band differences are consistent with those reported in N10, but the better statistics and the systematic usage of stacked residual method in the present paper yield a more detailed view of the situation. ACIS and MOS1 vs. PN stacked residuals exhibit a systematic decrease when moving from 3 keV to 1 keV. The amplitudes are different: $\sim$20% for ACIS/PN and $\sim$10% for MOS1/PN. The MOS2/PN and MOS1/MOS2 ratios have smaller ($\sim$5%) and insignificant changes when moving from 3 keV to 1 keV. Especially in the $(0.5-2)$ keV band, the MOS1/PN and MOS2/PN residuals show very similar behavior. If the shape of the effective

[6] A262, A1367, A2029, A2052, A2589, A2634, A3571, A3581, A4059, NGC1550

area of PN is very accurately calibrated, the above results indicate that the ACIS (MOS1) effective area is overestimated by a factor of ∼20% (∼10%) at 1 keV.

The sudden increase in the stacked residual ratio at energies $(1 - 0.5)$ keV by ∼5% in all instruments compared to PN indicates problems with PN effective area calibration at these energies. The simplest explanation of the data is that the PN effective area is underestimated by 5% at 0.5 keV. We also detect this increase between ∼ 1 keV and 0.5 keV in the ACIS/MOS1 and ACIS/MOS2 ratios but at a lower level (< 5%).

While preparing this work, a paper by Read et al. (2014) appeared on arXiv, that employs stacked residuals of on-axis point sources. While their results are mostly consistent with ours, there is an indication of a slightly different behavior in their default analysis method (*stack+fit*) of the MOS2/PN case at high energies. They only see a drop in the stacked residuals for MOS2/PN, if they use the *fit+stack* method, as we do here. In Read et al. (2014), the authors mention "negative spectral bins that can sometimes occur in the individual source spectra" as the reason for the MOS2/PN drop in the *fit+stack* method. We tested this by excluding all spectra from the stacked residuals analysis, which have at least one negative bin. Since no different behavior can be detected, we conclude that negative bins do not matter in our analysis.

3.6.2 Temperatures

The results of the stacked residuals imply a multitude of temperature agreements and disagreements between different instruments in different energy bands (reported in Figs. 3.4 - 3.7 and Table 3.4). In the following we compare these temperatures and evaluate the significance of temperature differences for one cluster of the sample, as well as for the whole sample.

Temperature comparison of individual clusters

We evaluate the temperature differences and their significances ξ by defining

$$\xi = \frac{T_{I_X} - T_{I_Y}}{\sqrt{\Delta T_{I_X}^2 + \Delta T_{I_Y}^2}} \ , \tag{3.2}$$

where T_{I_X} and T_{I_Y} denote the temperatures measured with two instruments to be compared and ΔT_{I_X} and ΔT_{I_Y} denote the statistical uncertainties of the temperature for the two instruments. Here, ξ is calculated for each cluster and instrument combination individually. The ξ distributions for the detector combinations are not symmetric, but we are able to calculate the median ξ for each combination and the percentage of clusters with ξ above 3 (see Table 3.1). For a non-systematic temperature difference (e.g., scatter) the median should not be significantly different from zero.

As indicated by the consistent ACIS-I/PN and ACIS-S/PN stacked residuals, the ACIS-I and ACIS-S temperatures are consistent in all bands (see Figs. 3.4 and 3.19, right). In the hard band, as indicated by the flat stack residuals, the temperatures are more consistent (most of the clusters with a $\xi < 3$, see Table 3.1). The feature of the MOS2/PN declining stacked residuals above 4.5 keV is not seen in the temperature comparison. This might be explained by the low statistical weight that this band gets in the spectral fit because of the low number of counts. In the soft band, as expected due to the systematic effect in the stacked residuals, the PN temperatures are systematically lower than those of MOS1, MOS2, and ACIS, and MOS1 and MOS2 are showing very good agreement (no cluster with ξ above 3). In the full energy band, the complex stacked residuals behavior as a function of energy results in MOS1 delivering higher temperatures than PN (due to soft band problems) and MOS2 delivering lower temperatures than MOS1 and ACIS and yielding approximate agreement with PN (see Figs. 3.5).

To enable a comparison with the literature, we also combined the three XMM-Newton instruments by performing a simultaneous fit (which we call "combined XMM-Newton" from now on) in the different energy bands and linking temperatures and metallicities while the normalizations are free to vary. In the combined EPIC fit, the systematic soft-band stacked residuals feature for ACIS-PN and MOS1-PN (see Fig. 3.3) results in lower full band EPIC temperatures (see Figs. 3.5, 3.6, 3.7). The ACIS-EPIC temperature differences increase with temperature in all bands. We think this is due to the spectra of the lowest temperature clusters not having enough statistics to weight the $(1 - 3)$ keV band cross-calibration feature significantly.

Table 3.1: Median of the significance of temperature differences, ξ, and probability of HIFLUGCS clusters to deviate more than 3 ξ from zero for the three energy bands.

Energy band	Detector X–Y	Median	$P(\xi > 3)$
Full	ACIS–PN	7.1	84%
$(0.7 - 7.0)$ keV	ACIS–MOS1	4.0	61%
	ACIS–MOS2	5.4	80%
	MOS1–MOS2	1.5	12%
	MOS1–PN	2.3	34%
	MOS2–PN	1.3	14%
Soft	ACIS–PN	3.3	54%
$(0.7 - 2.0)$ keV	ACIS–MOS1	1.5	16%
	ACIS–MOS2	1.3	27%
	MOS1–MOS2	0.2	0%
	MOS1–PN	1.6	20%
	MOS2–PN	1.4	20%
Hard	ACIS–PN	0.9	4%
$(2.0 - 7.0)$ keV	ACIS–MOS1	0.9	2%
	ACIS–MOS2	1.1	4%
	MOS1–MOS2	0.6	0%
	MOS1–PN	0.5	2%
	MOS2–PN	-0.1	2%

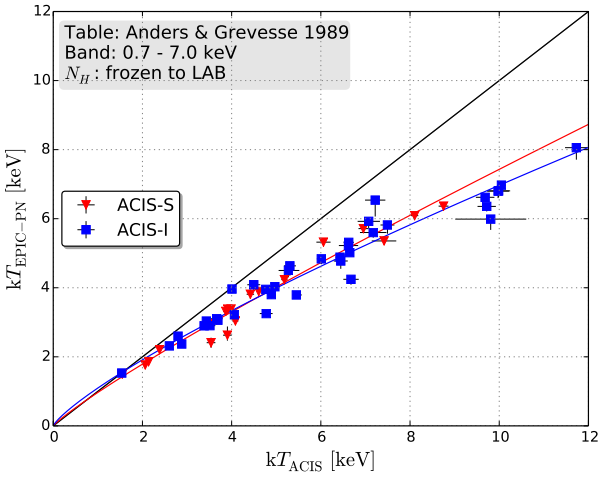

Figure 3.4: Comparison of EPIC-PN full energy band temperatures with those obtained with ACIS-I (blue squares) and ACIS-S (red triangles). The $N_{\rm H}$ is frozen to the radio value of the LAB survey. For a comparison of the resulting best-fit parameters see also Fig. 3.19 and Table 3.2. The red and blue lines show the powerlaw best-fit function (Eq. 3.3) to the ACIS-S and ACIS-I subsamples, respectively.

Scaling relations of temperatures between different instruments

The distribution of temperature differences for any detector combination shows a Gaussian behavior in logarithmic space. We quantified this by modeling the temperatures obtained with one instrument as a powerlaw function of the values obtained with another instrument, in a given energy band, as

$$\log_{10} \frac{kT_{\mathrm{I_Y,band}}}{1\,\mathrm{keV}} = a \times \log_{10} \frac{kT_{\mathrm{I_X,band}}}{1\,\mathrm{keV}} + b \ . \tag{3.3}$$

We included intrinsic scatter ζ in the fitting process (see Table 3.2), which is determined by requiring $\chi^2_{\mathrm{red}} = 1$ (as done, e.g., by Maughan, 2007). The intrinsic scatter is added in quadrature to the statistical uncertainty of the data to calculate the χ^2 of the model. The degeneracy between the two parameters, a and b, is shown in Appendix 3.9.2, Figure 3.18) and in Figure 3.8 for the ACIS–XMM-Newton combined case. Neglecting the intrinsic scatter would result in tighter constraints of the fit parameters, hence in higher significances of temperature differences. From Figure 3.18 we conclude that for our sample the temperatures deviate for all detector combinations at least by 5σ in the full energy band, while in the soft energy band only MOS1 and MOS2 show good agreement. In the hard band no instrument combination shows deviations larger than 4.4σ. For individual clusters the average significance of differences between temperatures is smaller, as shown in Section 3.6.2.

We see more than a 4σ deviation between ACIS and PN even in the hard band. Looking at the stacked residual ratio for ACIS/PN (Fig. 3.3, top left) we see an increase in the $(2-3)\,\mathrm{keV}$ band, which might be responsible for the temperature difference in the hard band. However, this 4σ deviation is still small compared to the other bands. N10 conclude that the hard-band temperatures of ACIS and PN agree (0.88σ according to our analysis method), which was probably driven by the lower number of objects in the N10 sample. Even though N10 find consistent ACIS and PN temperatures in the hard band and we detect a more than 4σ deviation, the ellipses in the a-b-plane overlap (Fig. 3.19, right panel). Since we use more than five times more objects and compare two high precision instruments here, our significance increases.

In the full band, EPIC-PN temperatures are on average 29% lower than ACIS temperatures at a cluster temperature of 10 keV (see Table 3.2). All detector combinations are plotted individually in Figure 3.15 for the full energy band, 3.16 for the soft and 3.17 for the hard energy band. Within the uncertainties, the best-fit N10 relation agrees with our full band relation (see Fig. 3.19), implying persistent calibration uncertainties since 2009. Although this work deals with the Chandra CALDB 4.5.5.1, we cross-checked our results of ACIS using the new ACIS QE contamination model vN0008 included in CALDB 4.6.1 . Comparing the Chandra CALDB 4.5.5.1 (default in this work) and 4.6.1, we get 1.9 % lower temperatures (2.9 % scatter) using CALDB 4.6.1 for low and medium temperature clusters. For cluster temperatures above 8 kev we find 5.4 % (4.8 % scatter) lower temperatures with CALDB 4.6.1. In a future work, we will study the effect of the new contamination model in more detail.

We want to mention here that we also tested the self consistency of the instruments by comparing the soft and hard band temperatures of the same instrument. However, the conclusions of these results depend strongly on the multitemperature structure of the ICM. Details are provided in Appendix 3.9.3.

The combined EPIC and ACIS temperatures indicate that the clusters that are excluded because of the overly large cool core radius (see Section 3.2) do not show any systematic behavior compared to the other clusters (see Fig. 3.9).

We modeled the energy dependence of the cross-calibration uncertainties by cubic spline interpolation (e.g., Press et al., 1992, Chapter 3.3). This was applied in Figs. 3.2, 3.3 and Table 3.5 to the stacked residual ratios (see Section 3.6.1). These splines can be used to estimate the effect of the effective area cross-calibration uncertainties on the spectral analysis performed with a given EPIC or ACIS instrument. The effective area of a given instrument must be multiplied by the corresponding spline to obtain best-fit temperatures when assuming that the reference instrument is precisely calibrated. To convert, for example, from ACIS to EPIC-PN, one should multiply the effective area of ACIS with the energy-dependent spline values of ACIS/PN from Table 3.5. The underlying assumption is, that the reason for the temperature differences between the detectors is the uncertainty in the effective area calibration. As an example, we pick the most extreme case, ACIS versus EPIC-PN: We find that indeed temperatures between ACIS and EPIC-PN (Fig. 3.10) are now consistent. The significance of temperature differences between ACIS and PN is now $2.7\,\sigma$ in the full band, while before we had a more than $8\,\sigma$ deviation. To enable the use of our results for calibration work, we present the spline parameters for each instrument pair in Table 3.5 and we

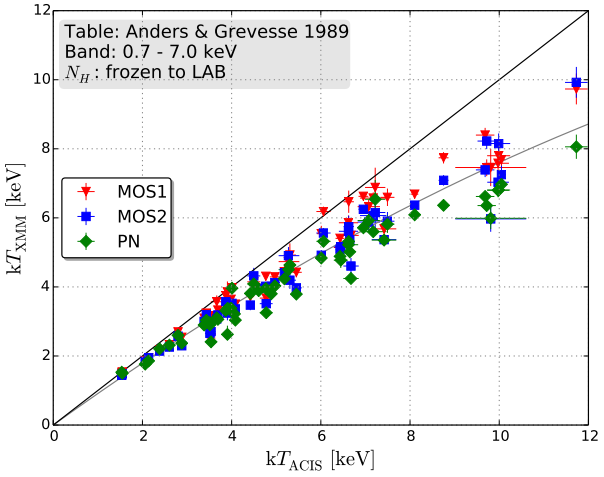

Figure 3.5: Comparison of the full energy band temperatures obtained with the three individual XMM-Newton detectors (every detector combination has 56 objects) with those obtained with ACIS. The $N_{\rm H}$ is frozen to the radio value of the LAB survey. The gray line shows the powerlaw best-fit function (Eq. 3.3) to the simultaneously fitted XMM-Newton temperatures, see also Fig.3.8.

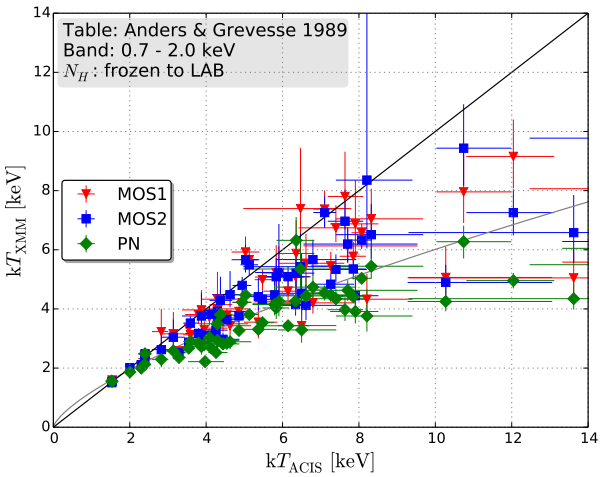

Figure 3.6: Same as Fig. 3.5, except in the soft energy band $(0.7 - 2)$ keV.

provide a tool to modify the effective area based on the splines of the stacked residual ratios[7].

3.7 Discussion

In the previous section we have shown that systematic temperature differences exist between ACIS and the EPIC detectors. We investigate the consequences arising when our assumption of a single-temperature plasma breaks down and we have to deal with a multitemperature structure. Finally, we compare measured and independently derived hydrogen column density values and estimate the cosmological impacts of our results.

[7] `https://wikis.mit.edu/confluence/display/iachec/Data3`

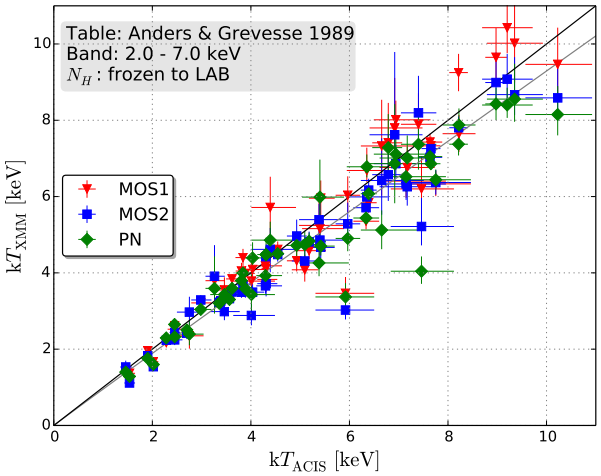

Figure 3.7: Same as Fig. 3.5, except in the hard energy band $(2-7)$ keV.

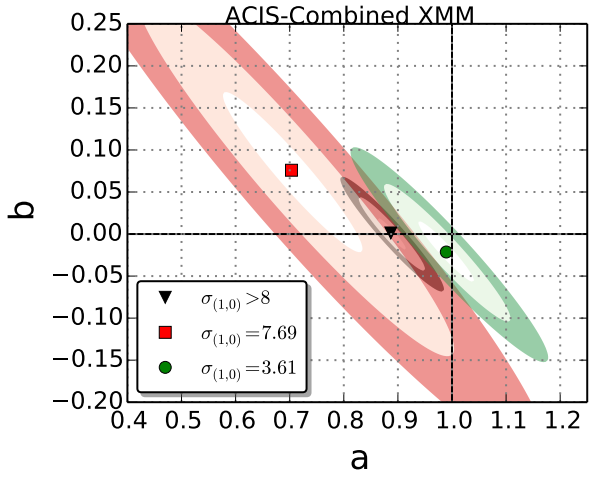

Figure 3.8: Degeneracy of the fit parameters (see Eq. 3.3) for the ACIS – Combined XMM-Newton fit. The shaded regions correspond to the 1σ, 3σ, and 5σ confidence levels. The red square represents the soft energy band, the green circle the hard, and the gray triangle the full band. Equality of temperatures is given for $a = 1$ and $b = 0$. The deviation in σ from equality is given in the legend.

3.7.1 Systematics

Multiphase ICM

While we know the relative calibration uncertainties from the stacked residual ratios (see Section 3.6.1), we discuss here the possibility that the observed temperature differences between the instruments and detectors are not caused by calibration uncertainties but by the different effective areas and the multitemperature structure of the ICM. The role of the multiphase ICM has been discussed in detail in Mazzotta et al. (2004), Vikhlinin (2006), and Reiprich et al. (2013), among others. As shown in Reiprich et al. (2013), one can conclude from the effective areas of the instruments that Chandra is more sensitive to the harder spectra and higher temperatures than XMM-Newton, which may explain the higher temperatures if a multitemperature structure plays an important role. In the following we quantify whether this effect is significant and if a multitemperature structure is important by performing simulations. We show later that the restrictions on the two-temperature plasma cannot be fulfilled. We also show examples, where we expect a strong multiphase structure of the ICM, such as the cool core regions of CC clusters or the full $(3.5')$ region of clusters with a cool core larger than this size. Finally we compare the results from

Table 3.2: Parameters a and b for the powerlaw fits of instrument X versus Y temperatures using the parameterization of Eq. 3.3. We also give the parameters for the temperatures from N10 in a slightly different full- and soft-energy band. Δ is the resulting relative temperature difference between the two instruments at the temperature of instrument X.

Instruments X–Y	Energy band	a	b	Intr. scatter $\zeta_{\log_Y}$	$\Delta_{2\,\mathrm{keV}}$	$\Delta_{5\,\mathrm{keV}}$	$\Delta_{10\,\mathrm{keV}}$
ACIS–MOS1	Full	$0.920^{+0.005}_{-0.005}$	$-0.001^{+0.004}_{-0.004}$	0.024	6%	12%	17%
ACIS-MOS1	Soft	$0.802^{+0.013}_{-0.013}$	$0.060^{+0.009}_{-0.009}$	0.052	0%	17%	27%
ACIS-MOS1	Hard	$1.019^{+0.009}_{-0.004}$	$-0.021^{+0.005}_{-0.005}$	0.024	4%	2%	0%
ACIS–MOS2	Full	$0.909^{+0.005}_{-0.005}$	$-0.017^{+0.003}_{-0.004}$	0.024	10%	17%	22%
ACIS-MOS2	Soft	$0.789^{+0.009}_{-0.009}$	$0.058^{+0.007}_{-0.007}$	0.043	1%	19%	30%
ACIS-MOS2	Hard	$1.028^{+0.009}_{-0.009}$	$-0.048^{+0.007}_{-0.007}$	0.043	9%	6%	5%
ACIS–PN	Full	$0.836^{+0.005}_{-0.005}$	$0.016^{+0.004}_{-0.004}$	0.029	7%	20%	29%
ACIS–PN[N10]	Full	$0.837^{+0.007}_{-0.010}$	$0.053^{+0.007}_{-0.007}$	0.023	-1%	13%	22%
ACIS[S]-PN	Full	$0.885^{+0.010}_{-0.010}$	$-0.014^{+0.005}_{-0.007}$	0.030	11%	20%	26%
ACIS[I]-PN	Full	$0.803^{+0.007}_{-0.007}$	$0.040^{+0.005}_{-0.004}$	0.028	4%	20%	30%
ACIS-PN	Soft	$0.652^{+0.009}_{-0.009}$	$0.074^{+0.007}_{-0.007}$	0.041	7%	32%	47%
ACIS-PN[N10]	Soft	$0.769^{+0.017}_{-0.020}$	$0.075^{+0.014}_{-0.014}$	0.038	-1%	18%	30%
ACIS-PN	Hard	$0.947^{+0.009}_{-0.009}$	$0.006^{+0.007}_{-0.005}$	0.034	2%	7%	10%
ACIS-PN[N10]	Hard	$0.926^{+0.010}_{-0.014}$	$0.058^{+0.009}_{-0.009}$	0.020	-9%	-2%	4%
ACIS–Combined XMM	Full	$0.889^{+0.005}_{-0.003}$	$0.000^{+0.004}_{-0.004}$	0.025	7%	16%	23%
ACIS-Combined XMM	Soft	$0.703^{+0.021}_{-0.021}$	$0.076^{+0.018}_{-0.016}$	0.129	3%	26%	40%
ACIS-Combined XMM	Hard	$0.989^{+0.009}_{-0.009}$	$-0.021^{+0.005}_{-0.007}$	0.042	5%	6%	7%
MOS1–MOS2	Full	$0.983^{+0.003}_{-0.003}$	$-0.012^{+0.002}_{-0.003}$	0.014	4%	5%	6%
MOS1–MOS2	Soft	$0.976^{+0.009}_{-0.010}$	$0.006^{+0.005}_{-0.005}$	0.008	0%	3%	4%
MOS1–MOS2	Hard	$1.001^{+0.010}_{-0.009}$	$-0.021^{+0.006}_{-0.006}$	0.030	5%	4%	4%
MOS1–PN	Full	$0.908^{+0.003}_{-0.003}$	$0.019^{+0.003}_{-0.002}$	0.013	2%	10%	16%
MOS1–PN	Soft	$0.785^{+0.010}_{-0.010}$	$0.040^{+0.006}_{-0.005}$	0.027	6%	22%	33%
MOS1–PN	Hard	$0.947^{+0.007}_{-0.007}$	$0.016^{+0.005}_{-0.005}$	0.014	0%	5%	8%
MOS2–PN	Full	$0.921^{+0.005}_{-0.003}$	$0.031^{+0.003}_{-0.003}$	0.017	-2%	5%	10%
MOS2–PN	Soft	$0.802^{+0.009}_{-0.009}$	$0.038^{+0.005}_{-0.005}$	0.018	5%	21%	31%
MOS2–PN	Hard	$0.940^{+0.007}_{-0.007}$	$0.038^{+0.005}_{-0.005}$	0.018	-5%	1%	5%

Chandra event files that were smoothed to the XMM-Newton resolution.

In summary, we demonstrate that none of the studied possible effects can explain the observed temperature differences.

Simulations To test the effect on the measurements of a multitemperature plasma, we simulated a set of spectra for the different XMM-Newton detectors and for ACIS-I following the same approach presented in Reiprich et al. (2013, Sect. 4.6). To isolate the influence of multitemperature structure on best-fit temperatures, we assumed here that the instruments are perfectly calibrated. We used as test cases for the cold component three different temperatures, 0.5, 1, and 2 keV, and three different metal abundances (0.3, 0.5, and 1 times solar). The temperature of the hot component was varied from 3 to 10 keV, while the metallicity was kept fixed to 0.3 solar, a value typical of the clusters in our sample. The relative contribution of the second plasma component has been estimated by varying the emission measure ratios (from 10% to equal emission measure). We then fitted the resultant spectra with a single-temperature model and also left the metallicity free to vary. The best-fit values and the 68% errors have been taken from the distribution of 100 realizations.

We found that when the cold component is ~ 2 keV, the fit is always good ($\chi^2 < 1.1$) independent of the amount of "cold gas" present in the cluster and of the metallicity of this gas. For cooler temperatures

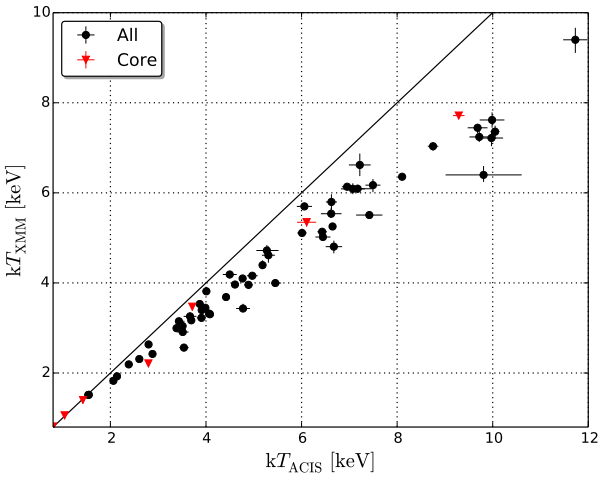

Figure 3.9: Combined XMM-Newton versus Chandra temperature. The excluded objects (too large core radius) are marked here by red triangles.

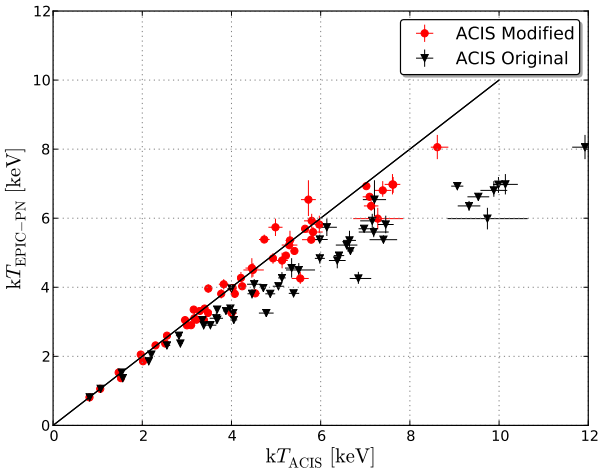

Figure 3.10: Temperatures before and after modifying the ARF files of ACIS spectra according to the energy-dependent calibration uncertainties shown in Fig. 3.3. This plot shows the 53 clusters from the stacked residual ratio sample (Section 3.5.2).

the amount of cold gas and its metallicity play an important role. Clearly, if the cold gas were very enriched the fit would yield a bad χ^2 (> 2) in almost all the cases (i.e., also with only 10% of cold gas with respect to the hot component), while for lower abundance it also depends on the amount of gas. Since in the observations we do not see such bad $\chi^2_{\rm red}$, we excluded all the combinations with a $\chi^2_{\rm red} > 2$. Each dataset of the simulated spectra contains 10 000 counts. This is a conservative approach, since we typically have more counts in our spectra from the observed data. Owing to the higher statistics of the observed spectra with respect to the simulated ones, we would expect to find an inappropriate model (e.g., due to multitemperature structure) first in the observed data. We checked the difference in temperature between Chandra and XMM-Newton of the simulated spectra and found that the fitted temperature of the two instruments starts to be significantly different only when the second component is very cold (i.e., 0.5 keV). In Fig. 3.11 we only show this case. We note that to explain the observed difference between Chandra and EPIC-MOS2, an emission measure ratio (EMR) of almost 0.2 is required. We show in the next paragraphs that this is not the case. Furthermore, an EMR = 0.2 is not able to explain the observed difference between Chandra and MOS1/PN. Thus, we conclude that although a multi temperature ICM cannot be excluded, it cannot explain the observed difference in temperature between the different instruments. We also note

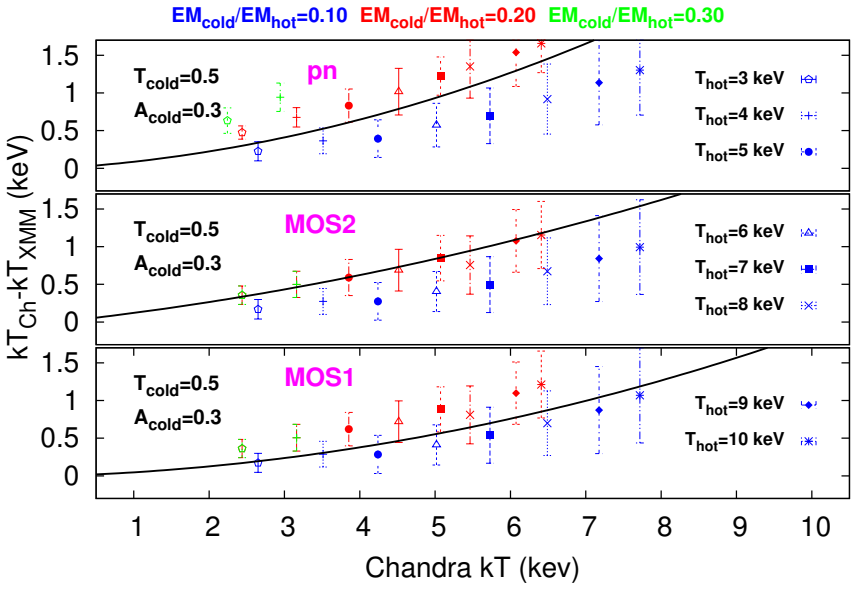

Figure 3.11: Difference between Chandra and XMM-Newton single-temperature fits to two-temperature component mock spectra vs. the Chandra best-fit temperature. The three colors correspond to different emission measure ratios (EMR) of the cold and hot components, the symbols represent 8 different temperatures of the hot component, while its metallicity is frozen to 0.3 of the solar value and the redshift to 0.05, which corresponds to the mean HIFLUGCS redshift. The temperature and metallicity of the cold component are always fixed to 0.5 and 0.3, respectively. The black curve shows the measured temperature difference between Chandra and XMM-Newton as presented in Table 3.2.

here that a higher EMR always gives a bad χ^2 that we do not observe in the real observations.

Two-temperature fits To test the results from the simulations we selected the clusters with the highest number of counts in both XMM-Newton and Chandra: Abell 2029 has 210 000 counts in Chandra and roughly 62 000 counts in PN and a Chandra temperature of 8.7 keV. For both instruments, we fit a two-temperature model, fixing the temperature of the second component to 0.5 keV and the metallicity to 0.3. The temperature of the first component increased for both instruments by 3% to 4% compared to the single-temperature model. The normalization of the second component is for both instruments 1% to 5% of the first component. This is far too low to explain any temperature differences obtained by the two instruments. Also fixing the normalization of the second component to 20% of the first component increases the reduced χ^2 to almost 4 for PN and > 15 for ACIS.

Another good example is the cool-core cluster Abell 2142 with more than 180 000 counts in both instruments and a Chandra temperature above 9 keV. This cluster has a cool core radius larger than $3.5'$, so in an observation within this threshold, more than one temperature component should be present. For Chandra the normalization of a 0.5 keV component is consistent with zero. This is also true if the temperature of the cold component is frozen to 2 keV. For PN the normalization of the 0.5 keV component is below 1.5%, and for a fitted temperature of 2.7 keV of the cold component, the normalization is about 17% of the first component. From the simulations we conclude that every cold component above 2 keV cannot explain the observed difference, so we cannot find any hint of a multiphase ICM being the reason for the inconsistency of the instruments.

Multitemperature plasmas Since galaxy clusters, in general, and especially cool-core clusters do not show only one dominant temperature, but a temperature profile, we select now regions, where a clear multiphase ICM structure is present, the cool cores of CC clusters and the whole circular region until $3.5'$. Assuming that a multitemperature structure contributes significantly to the observed temperature

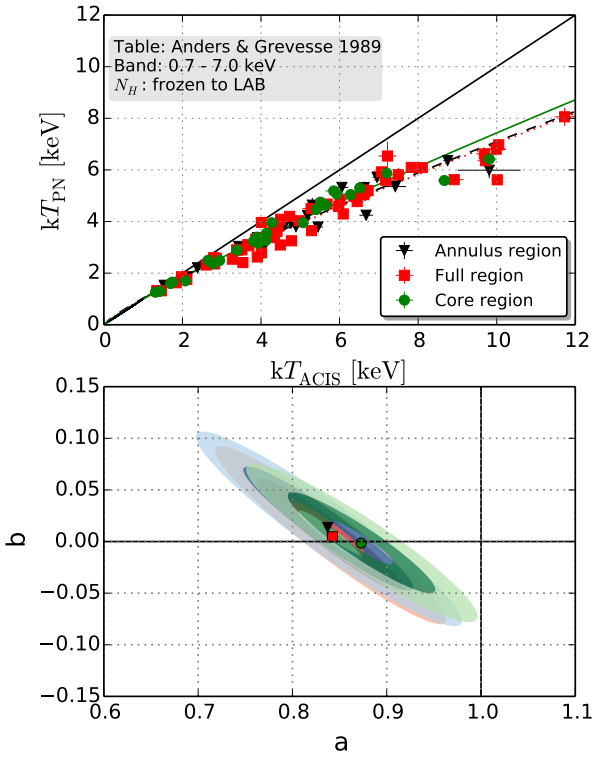

Figure 3.12: *Top:* XMM-Newton EPIC-PN versus Chandra ACIS temperatures in the full energy band. The different colors correspond to the 3 different regions where the spectra could be extracted: The full 3.5′ circle (red squares), the cool core region (green circles), and the annulus between the two (black triangles). In the cool core region, the strongest influence of multitemperature plasma is expected. *Bottom:* Degeneracy between the parameters a and b for the three cases shown above. The shaded regions correspond to 1σ, 3σ, and 5σ confidence levels.

differences, we would then expect to find significantly larger temperature differences. We do not observe this, though. We have already demonstrated in Figure 3.9 that the restriction to isothermal regions does not introduce any bias, but we verify this again especially for the cool core regions. We ended up with 28 cool core region clusters and 56 clusters where we used the full circular region and compared this to the 28 clusters using the annulus region. To choose the extreme case, we only used the PN detector for XMM-Newton. As can be seen in Fig. 3.12, the best-fit curves do agree, and we can be sure that the multitemperature structure of clusters has no significant effect on our measurements of the instrumental differences.

Summary of the multiphase ICM tests In this section we show that assuming the observed temperature differences are only caused by multitemperature structure of the ICM (i.e., the calibrations are perfect), we can set up restrictions on the cold plasma component (EMR $\approx 20\%$ and kT $= 0.5\,$keV). These restrictions were derived by fitting two simulated plasma components with a single component and requiring the observed temperature difference between detectors to be reproduced with the simulations, as well as $\chi^2_{\rm red} < 2$. Applying this to real high quality observations by fitting two plasma components we cannot recover the required emission measure of the cold component. Also we cannot see any hint of a different behavior of the temperature difference for regions with a clear multi phase structure (e.g., the cool core region), which would be expected, if the multitemperature structure is responsible for the measured temperature differences.

Temperature - abundance degeneracy

The two parameters, temperature and abundance of heavy elements, are not completely independent of each other (e.g., Gastaldello et al., 2010; Buote, 2000b). Since for many of our clusters, the constrained abundance also does not agree within the different instruments, it is possible that a degeneracy of the two parameters is producing inconsistent values for both of them. To make certain that this degeneracy is not the reason for the detected temperature difference, we refit the XMM-Newton data of all clusters by freezing the metallicity to the one obtained by Chandra. On average the EPIC-PN temperature increased by 0.8% compared to the best-fit temperature where the relative abundance is free to vary. For only 8 of the 56 clusters the EPIC-PN temperature increased by more than 2% (at maximum by 8.7%), but for none of these cases does the new (with frozen relative abundance to Chandra ACIS) EPIC-PN temperature agree with Chandra ACIS. Therefore, any inconsistency in the temperatures cannot be explained by wrongly constrained abundance, and because the temperature change described in this section is not systematic in one direction.

Effects of the point spread function (PSF)

The last case to discuss here is the possible scatter of the cool core emission into the annular region due to the broader XMM-Newton PSF. We used the Chandra cleaned events files and redistributed the position of all photons using a Gaussian smoothing kernel with a σ between $1''$ and $70''$. This scenario is different than what we simulated in Section 3.7.1 since we assumed there that the detectors "see" the same photon distribution, but are sensitive to different parts of the spectrum, which is more complicated than our one-component model. Then the instrument has to deal with the different photon distributions caused by the different PSFs. We tested this for four clusters, where we detect a temperature difference between XMM-Newton and Chandra and which have a strong cool core: Abell 85, Abell 133, Abell 2204, and Abell 3112. In all four cases, the temperature is very constant up to a threshold of the smoothing kernel σ. A significant drop in the temperature is detected beyond $30''$, then the temperature drops constantly with increasing σ. Even if the Gaussian shape of the PSF (constant with photon energy) is not the best approximation of the real PSF behavior, we can conclude from this test that the PSF of XMM-Newton (half power diameter of $15''$ on axis) is not sufficient to scatter enough emission from cooler regions.

3.7.2 Influence of N_{H} and the abundance table

In this section we show the influence of the heavy elements abundance table and the hydrogen column density in the absorption model. We demonstrate that the N_{H} constrained in a spectral fit can be compared to independently determined reference values. This comparison could help to evaluate the calibration status of a detector through the level of agreement with reverence values, but the conclusions depend on the abundance table.

The relative abundance table gives the number densities of atoms of a certain element relative to hydrogen. Most of the abundance tables are established using measurements of the solar photosphere and corona and from meteorites. It is still very common to use the (`xspec` default) table presented in Anders and Grevesse (1989), but we also want to test for a dependence of our results on the choice of the table by using the Asplund et al. (2009) relative abundances, which represent more recent measurements. In our analysis we are able to see a systematic effect by using this abundance table. Temperatures derived using Aspl are on average 5% higher. These higher temperatures are produced independently of the detector (ACIS and EPIC). Since this effect is much bigger than expected, we tested whether the absorption or the emission component is responsible for this change. When using the `wabs` instead of the `phabs`-model for the absorption fixes, the abundance table for the absorption model to the hard-wired abundance table from Anders and Ebihara (1982), while `phabs` self-consistently uses the same abundance table for absorption and emission. With the `wabs` model, the temperature change is then very tiny, and the results are always consistent within the errorbars. The reason for this large change in temperature by using the Aspl abundance table is given in the absorption.

The step during the spectral fitting process of accounting for the absorption of heavy elements along the line of sight is important. The absolute abundance of these metals can be traced by measuring the neutral hydrogen column density (e.g., with HI 21cm radio measurements) and assuming relative abundances as in

the solar system. A widely used HI survey is the Leiden/Argentine/Bonn (LAB) survey (Kalberla et al., 2005). The cross-calibration uncertainties of the effective area are larger at the lowest energies (Section 3.6.2), where the Galactic absorption is significant. If a) one detector had its effective area very accurately calibrated in the full energy band, and b) the emission modeling was accurate (i.e. correctly treating the possible multitemperature structure), the best-fit hydrogen column densities obtained with this instrument should be consistent with the Galactic values. Thus the free $N_{\rm H}$ test could yield some information on the calibration accuracy.

We refit the full energy band EPIC-PN and ACIS spectra, allowing the temperature, metal abundance, emission measure, and the hydrogen column density to be free parameters. Using the PN detector as representative of XMM-Newton, we can conclude that Chandra systematically finds higher $N_{\rm H}$ values than XMM-Newton (on average around 40%). Also compared to the LAB values, a Chandra-detected $N_{\rm H}$ is systematically higher (on average 20% using AnGr), while PN detects 33% lower column densities using AnGr. Comparing the detected $N_{\rm H}$ values using the Aspl abundance table with the detected column densities using AnGr reveals a strong trend toward detecting 20% to 30% higher column densities with the more recent abundance table.

The dominant element responsible for this temperature increase is oxygen, since its relative abundance value is reduced by almost 50% in the Aspl table compared to the default AnGr. This decreased relative oxygen abundance causes the detected $N_{\rm H}$ values to increase, since the absolute number of oxygen atoms along the line of sight should stay constant. Conversely if the $N_{\rm H}$ value is frozen, the absolute number of oxygen atoms along the line of sight is reduced by switching to the Aspl table, so the effect of absorption is lower and the temperature needs to increase to compensate for this effect.

The radio surveys measure the hydrogen column density from the HI-21 cm line. This only provides the neutral hydrogen along the line of sight, so the molecular and ionized hydrogen is not accounted for. Even if the neutral hydrogen usually contributes most to the total hydrogen, an easy method exists to account for the molecular hydrogen (for more details see Willingale et al., 2013). One can use the dust extinction $E(B-V)$ measured in the B and V band as a tracer for the molecular hydrogen.

We therefore define the total hydrogen column density as

$$N_{\rm H,tot} = N_{\rm HI} + 2N_{\rm H_2} = N_{\rm HI} + 2N_{\rm H_2,max} \times \left(1 - e^{-\frac{N_{\rm HI}E(B-V)}{N_c}}\right)^{\alpha}, \tag{3.4}$$

with $N_{\rm H_2,max} = 7.2 \times 10^{20}\,{\rm cm}^{-2}$, $N_c = 3 \times 10^{20}\,{\rm cm}^{-2}$, and $\alpha = 1.1$ as given by Willingale et al. (2013). The relation has been calibrated using X-ray afterglows of gamma ray bursts. A webtool[8] is available to calculate $N_{\rm H,tot}$ for a given position using the infrared data from IRAS and COBE/DIRBE (Schlegel et al., 1998).

We compared the obtained hydrogen column density values with those derived including the molecular hydrogen Willingale et al. (2013) (see Fig. 3.13). The median difference and the 68% scatter between the X-ray derived $N_{\rm H}$ to that of Willingale et al. (2013) for ACIS and EPIC-PN are $-0.1^{+1.9}_{-1.5}10^{20}\,{\rm cm}^{-2}$ and $-2.6^{+2.3}_{-1.4}10^{20}\,{\rm cm}^{-2}$, respectively, when using abundance table of AnGr. That Chandra constrained $N_{\rm H}$ values are in better agreement with the total hydrogen column density than XMM-Newton PN could give a hint that the Chandra calibration is more reliable; however, using the Aspl abundances instead, the corresponding values are $2.0^{+2.8}_{-2.1}10^{20}\,{\rm cm}^{-2}$ for ACIS and $-1.4^{+2.8}_{-1.7}10^{20}\,{\rm cm}^{-2}$ for EPIC-PN. Thus, the choice of the abundance table (i.e., the relative abundances of the elements responsible for absorption) and the scatter of the measurements make it difficult to interpret the results: The AnGr abundance table favors the ACIS derived column densities, while no conclusion can be drawn when using Aspl.

We have demonstrated that even though the most reliable calibrated instrument can be identified theoretically by comparing the constrained hydrogen column densities with references, the systematics of the abundance table that is being used, have to be taken into account.

3.7.3 Cosmological impact

Galaxy clusters are excellent tools for cosmology, because they trace the dark matter and large scale structure in the Universe. In X-rays one can see the emission of the most massive visible component of galaxy clusters and measure this mass from the surface brightness profile (see, e.g., Nulsen et al., 2010).

[8] `http://www.swift.ac.uk/analysis/nhtot/index.php`

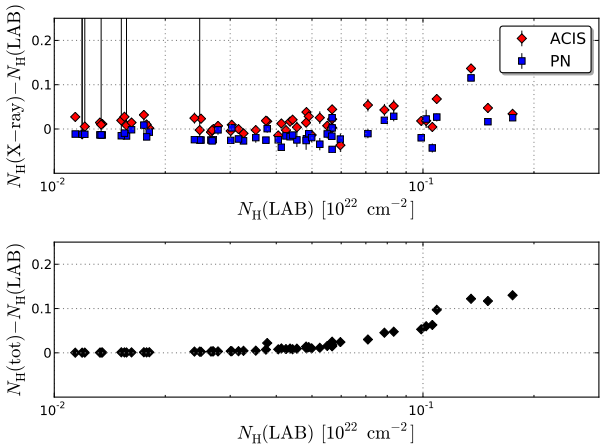

Figure 3.13: *Top:* Determined $N_{\rm H}$ values for Chandra (red diamonds) and EPIC-PN (blue squares). *Bottom:* Comparison of the $N_{\rm H,tot}$ and the LAB hydrogen column density values for the HIFLUGCS clusters. The y-axis is in units of $10^{22}\,{\rm cm}^{-2}$, and the abundance table used is AnGr.

By assuming hydrostatic equilibrium the total mass can be calculated. The temperature profile of the galaxy cluster enters into this calculation as absolute value at a given radius and its logarithmic derivative (the former usually dominates, as shown in Reiprich et al., 2013, Fig. 3). To get a good handle on the cluster masses, one therefore needs accurate temperature measurements. As shown above, there is a bias depending on the X-ray instrument used. We want to quantify what effect the temperature difference between Chandra and XMM-Newton has on the cosmological parameters. Therefore we calculated the total hydrostatic masses of all HIFLUGCS clusters by establishing a temperature and density profile for each using Chandra data. The same was done to get "XMM-Newton masses" by rescaling the Chandra temperatures to "combined XMM-Newton" temperatures (see Table 3.2) and with that, obtaining "XMM-Newton masses". Although it is not being used for the cosmological analysis, we present here our scaling relation for the hydrostatic masses of the different instruments for comparison reasons:

$$M_{500}^{\rm XMM} = 0.859^{+0.017}_{-0.016} \cdot \left(M_{500}^{\rm Chandra}\right)^{1.00\,\pm\,0.02} \tag{3.5}$$

(see Appendix 3.9.4 for more details). Since only the gradient of the density profile enters the hydrostatic equation, it is not necessary to have an accurate flux calibration for this comparison. Establishing a cluster mass function with both Chandra and XMM-Newton masses, and comparing it to the Tinker et al. (2008) halo mass function gives us constraints on the cosmological parameters $\Omega_{\rm M}$ and σ_8. The details about this full analysis is part of a further paper on the HIFLUGCS cluster sample and is beyond the scope of the present paper, so we use a self-consistent analysis of the Chandra data, whose purpose is only to quantify the relative effect of the calibration uncertainties on the cosmological parameters.

The resulting shift of cosmological parameters is mainly a shift toward lower $\Omega_{\rm M}$ when using the XMM-Newton masses. We find an 8% lower $\Omega_{\rm M}$ and a $< 1\%$ higher σ_8 for the XMM-Newton masses (see Fig. 3.14). Still, the 68% confidence levels in the $\Omega_{\rm M} - \sigma_8$ plane show some overlap. For precision cosmology it is necessary to quantify all systematic biases, but it seems clear that calibration differences alone cannot account for the Planck CMB primary anisotropies and Sunyaev-Zel'dovich differences (Planck Collaboration et al., 2013a,b) as also shown in Figure 3.14 where the relative difference between Planck SZ and Planck CMB are indicated by the unfilled ellipses. We do note that the precise shift of best-fit cosmological parameter values is expected to depend on the cluster sample under consideration. We point out that Chandra and Planck CMB overlap in this figure simply because both are arbitrarily normalized to zero for comparison reasons. This does not imply cosmological constraints from Planck CMB and Chandra galaxy clusters agree perfectly. We want to stress that the relative difference between Planck CMB and SZ best-fit values is significantly larger than the difference between Chandra and XMM-Newton derived results in the $\Omega_{\rm M}$–σ_8–plane.

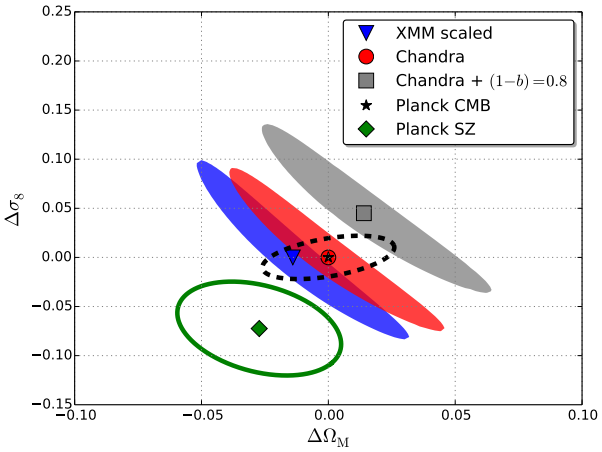

Figure 3.14: Shift of the two cosmological parameters, $\Omega_{\rm M}$ and σ_8, relative to the Chandra best-fit values for the X-ray analysis and relative to the Planck CMB results for the Planck analysis. The Chandra error ellipses are derived from hydrostatic masses of the HIFLUGCS clusters using Chandra temperature profiles and the Tinker halo mass function, the gray ellipse giving the results assuming a 20% hydrostatic bias. The XMM-Newton error ellipses are derived using the Chandra temperature profiles and by rescaling these profiles using Eq. 3.3 and Table 3.2. The Planck error ellipses are approximated from Planck Collaboration et al. (2013b).

In our analysis we also tested a hydrostatic bias,

$$(1-b) = \left\langle \frac{M_{\rm X-ray}}{M_{\rm true}} \right\rangle = 0.8 \ , \tag{3.6}$$

by upscaling the Chandra masses by 25% to simulate the strongest bias still allowed by the weak lensing (WL) masses determined by Israel et al. (2014a). We found a 7% higher $\Omega_{\rm M}$ and 6% higher σ_8 for the WL masses compared to the Chandra analysis. This would correspond to a 14% difference in $\Omega_{\rm M}$ and 6% difference in σ_8 for XMM-Newton masses compared to WL. In Figure 3.14 we indicate the contours of upscaled Chandra masses in the $\Omega_{\rm M}$ - σ_8 plane assuming $(1-b) = 0.8$ by a gray square.

In the Planck SZ contours, the assumption of a uniformly varying bias in the range $[0.7, 1.0]$ enters, while the results from Israel et al. (2014a) indicate the absence of any bias and allow a maximum bias of about 20% based on the uncertainty of the intercept method. Without a marginalization of $(1-b)$ over the range $[0.7, 1.0]$, the difference between the cosmological parameters $\Omega_{\rm M}$ and σ_8 of the Planck primary CMB anisotropies and the SZ analyses would be even more significant, which makes it even more unlikely that the X-ray calibration uncertainties between Chandra and XMM-Newton can be responsible for this difference alone.

3.8 Summary and conclusions

We tested the calibration of Chandra and XMM-Newton using a large sample of very bright galaxy clusters. Analyzing the same regions, we found significant systematic differences. First, in a direct way using the stacked residual ratio method, we quantified the relative effective area uncertainties in the most extreme case (ACIS vs. EPIC-PN) by an increase of ∼20% when moving in energy from 1 keV to 3 keV. Then more indirectly, but also more physically relevant, we quantified the gas temperature differences, where again the most extreme case is Chandra ACIS and XMM-Newton EPIC-PN at high cluster temperatures (i.e., EPIC-PN, yielding 29% lower temperatures at 10 keV in the full energy band.)

We showed that physical effects like multitemperature structure cannot cause the observed temperature differences. From

- using different energy bands for spectral fitting,
- an energy-dependent difference of the stacked residual ratio, and

- hydrogen column density studies,

we concluded that systematic effective area calibration uncertainties in the soft energy band $(0.7 - 2)\,\mathrm{keV}$ cause the observed differences. We provided fitting formulae to convert between Chandra and XMM-Newton using either effective area calibration files, temperatures, or masses (App. 3.9.4).

To illustrate the cosmological relevance, we showed that using XMM-Newton instead of Chandra for the cluster mass function determination would result in an 8% lower Ω_M and $< 1\%$ different σ_8. While this implies that for future high precision cluster experiments, e.g. with eROSITA (Pillepich et al., 2012; Merloni et al., 2012), this calibration needs to be improved, it also means that this systematic uncertainty alone cannot account for the Planck CMB/SZ difference.

3.9 Appendix

3.9.1 Tables

Table 3.3: List of the 63 HIFLUGCS clusters (without Abell 2244). Column (a) defines the name of the cluster as used in this work. Columns (b) and (c) give the coordinates in J2000 as defined in Hudson et al. (2010). (d) is the redshift and (e) the hydrogen column density (both from Zhang et al., 2011a, except for Abell 478, Abell 2163, and Abell 3571, see Section 3.2). Column (f) gives the radius of the cool core region for only CC clusters (for details see Section 3.2). Columns (g) and (h) give the observation IDs used and (i) and (j) are the cleaned exposure times for Chandra ACIS and XMM-Newton EPIC-PN, respectively. The * marks Chandra ACIS-S observations.

Cluster name	RA	DEC	z	$N_{\rm H}$	$r_{\rm core}$	Chandra	XMM	$t_{\rm ACIS}$	$t_{\rm PN}$
				[10^{21} cm^{-2}]	[kpc]	OBSID	OBSID	[ks]	[ks]
(a)	(b)	(c)	(d)	(e)	(f)	(g)	(h)	(i)	(j)
2A0335	54.6714	9.9672	0.0349	1.76	89.86	7939*	0147800201	49.5	79.9
A0085	10.4600	-9.3031	0.0556	0.28	132.07	904	0065140101	38.2	7.4
A0119	14.0668	-1.2557	0.0440	0.33	0.00	7918	0505211001	44.8	6.6
A0133	15.6741	-21.8822	0.0569	0.16	77.87	9897	0144310101	68.8	14.2
A0262	28.1926	36.1541	0.0161	0.64	27.17	7921*	0109980101	110.5	12.1
A0399	44.4727	13.0313	0.0715	1.05	0.00	3230	0112260101	48.6	5.1
A0400	44.4233	6.0271	0.0240	0.83	0.00	4181	0404010101	21.5	14.2
A0401	44.7361	13.5777	0.0748	0.99	0.00	14024	0112260301	134.5	6.5
A0478	63.3548	10.4649	0.0848	3.00	122.51	1669*	0109880101	42.2	40.4
A0496	68.4081	-13.2611	0.0328	0.40	92.02	4976*	0135120201	58.8	9.4
A0576	110.3761	55.7641	0.0381	0.55	0.00	3289*	0205070301	29.0	6.8
A0754	137.3194	-9.6891	0.0528	0.48	0.00	10743	0556200501	93.7	41.0
A1060	159.1781	-27.5283	0.0114	0.50	0.00	2220	0206230101	30.6	24.2
A1367	176.2512	19.6751	0.0216	0.19	0.00	514*	0061740101	40.5	15.0
A1644	194.2991	-17.4090	0.0474	0.40	109.87	7922	0010420201	51.3	8.6
A1650	194.6728	-1.7619	0.0845	0.13	46.12	5823	0093200101	39.6	25.9
A1651	194.8423	-4.1970	0.0860	0.15	0.00	4185	0203020101	9.6	3.3
A1656	194.8989	27.9597	0.0232	0.09	0.00	9714	0124711401	29.6	11.7
A1736	201.7161	-27.1741	0.0461	0.45	0.00	4186	0505210201	14.7	4.0
A1795	207.2191	26.5925	0.0616	0.10	147.96	493*	0097820101	19.6	22.3
A2029	227.7336	5.7448	0.0767	0.33	92.48	4977*	0551780401	77.5	14.4
A2052	229.1813	7.0222	0.0348	0.27	40.59	10478*	0109920101	118.3	17.4
A2063	230.7713	8.6075	0.0354	0.27	0.00	6263*	0550360101	16.8	11.1
A2065	230.6222	27.7062	0.0721	0.31	103.06	3182	0112240201	27.7	7.7
A2142	239.5860	27.2303	0.0899	0.38	604.90	5005	0674560201	44.6	34.0
A2147	240.5699	15.9738	0.0351	0.28	0.00	3211	0505210601	17.9	5.9
A2163	243.9445	-6.1501	0.2010	2.00	0.00	1653	0112230601	71.0	3.8
A2199	247.1597	39.5503	0.0302	0.09	32.72	10748	0008030201	40.4	10.5
A2204	248.1956	5.5754	0.1523	0.61	140.25	7940	0112230301	76.4	10.9
A2255	258.1423	64.0699	0.0800	0.23	0.00	894	0112260801	38.9	2.7
A2256	255.8094	78.6500	0.0601	0.43	345.45	2419*	0401610101	11.2	9.7
A2589	350.9892	16.7772	0.0416	0.29	32.59	7190*	0204180101	53.2	17.7
A2597	351.3330	-12.1243	0.0852	0.25	101.51	7329*	0147330101	58.8	27.1
A2634	354.6219	27.0317	0.0312	0.51	0.00	4816*	0002960101	49.3	3.9
A2657	356.2395	9.1919	0.0404	0.60	0.00	4941	0402190301	16.0	4.6
A3112	49.4902	-44.2384	0.0750	0.39	98.35	13135	0105660101	42.2	14.0
A3158	55.7178	-53.6321	0.0590	0.12	0.00	3712	0300211301	31.0	3.6
A3266	67.8047	-61.4531	0.0594	0.18	0.00	899	0105260901	29.8	11.9
A3376	90.5360	-39.9468	0.0455	0.44	0.00	3202	0151900101	44.3	16.0
A3391	96.5854	-53.6936	0.0531	0.56	0.00	4943	0505210401	16.5	13.4
A3395	96.7073	-54.5427	0.0498	0.74	0.00	4944	0400010301	20.3	17.9
A3526	192.2035	-41.3122	0.0103	0.85	54.41	4954*	0406200101	87.9	66.4
A3558	201.9870	-31.4953	0.0480	0.40	112.22	1646*	0107260101	13.8	28.0
A3562	203.4054	-31.6714	0.0499	0.39	0.00	4167	0105261301	19.2	21.2
A3571	206.8680	-32.8660	0.0374	0.42	0.00	4203*	0086950201	33.6	18.1
A3581	211.8758	-27.0196	0.0214	0.43	36.62	12884*	0205990101	84.3	24.8
A3667	303.1778	-56.8468	0.0560	0.46	26.38	5751	0206850101	126.8	39.7
A4038	356.9299	-28.1420	0.0283	0.15	0.00	4992	0204460101	33.5	20.0
A4059	359.2539	-34.7593	0.0460	0.12	42.87	5785*	0109950201	91.7	12.5
EXO0422	66.4635	-8.5605	0.0390	0.81	47.63	4183	0300210401	10.0	24.2
HydraA	139.5254	-12.0958	0.0538	0.43	209.98	4969*	0109980301	84.9	10.3
IIIZw54	55.3235	15.3936	0.0311	1.47	0.00	4182	0505230401	23.5	20.4
MKW3S	230.4656	7.7080	0.0450	0.29	106.48	900	0109930101	57.3	21.5
MKW4	181.1128	1.8961	0.0200	0.17	22.19	3234*	0093060101	29.9	6.7
MKW8	220.1795	3.4660	0.0270	0.23	0.00	4942	0300210701	23.1	13.0
NGC1399	54.6213	-35.4502	0.0046	0.14	20.13	319*	0400620101	56.0	51.6
NGC1550	64.9082	2.4101	0.0123	0.98	20.13	5800*	0152150101	44.3	15.9
NGC4636	190.7080	2.6868	0.0037	0.18	16.50	3926	0111190701	74.2	42.2
NGC5044	198.8495	-16.3852	0.0090	0.51	51.87	9399*	0037950101	82.7	10.3
NGC507	20.9159	33.2560	0.0165	0.56	35.48	2882	0080540101	43.3	22.2
RXCJ1504	226.0313	-2.8047	0.2153	0.60	324.84	5793	0401040101	39.0	22.2
S1101	348.4933	-42.7253	0.0580	0.11	89.22	11758	0123900101	97.1	15.7
ZwCl1215	184.4238	3.6551	0.0750	0.18	0.00	4184	0300211401	12.1	13.2

Table 3.4: Best-fit temperatures and 68% confidence levels for the 4 different detectors (plus EPIC combined) in the $(0.7-7)$ keV band. The annulus region was used for cool-core clusters. For details on the excluded spectra, see Section 3.2. The last column gives the ratio of source and background count rates in the $(0.7-2.0)$ keV band.

Cluster name	kT_{ACIS} [keV]	kT_{MOS1} [keV]	kT_{MOS2} [keV]	kT_{PN} [keV]	$kT_{\mathrm{EPIC,\,Combined}}$ [keV]	SC/BKG
2A0335	$3.99^{+0.05}_{-0.05}$	$3.64^{+0.06}_{-0.06}$	$3.38^{+0.04}_{-0.04}$	$3.38^{+0.02}_{-0.02}$	$3.45^{+0.02}_{-0.03}$	25.69
A0085	$6.63^{+0.12}_{-0.12}$	$6.47^{+0.32}_{-0.32}$	$5.75^{+0.32}_{-0.31}$	$5.32^{+0.23}_{-0.19}$	$5.80^{+0.17}_{-0.17}$	71.51
A0119	$6.45^{+0.16}_{-0.16}$	$5.14^{+0.25}_{-0.25}$	$5.16^{+0.28}_{-0.27}$	$4.78^{+0.23}_{-0.23}$	$5.02^{+0.15}_{-0.07}$	21.97
A0133	$4.89^{+0.09}_{-0.09}$	$3.88^{+0.14}_{-0.14}$	$4.02^{+0.13}_{-0.13}$	$3.80^{+0.11}_{-0.11}$	$3.96^{+0.05}_{-0.09}$	22.71
A0262	$2.38^{+0.02}_{-0.02}$	$2.17^{+0.05}_{-0.02}$	$2.14^{+0.04}_{-0.03}$	$2.21^{+0.05}_{-0.05}$	$2.19^{+0.03}_{-0.03}$	24.69
A0399	$7.49^{+0.16}_{-0.16}$	$6.59^{+0.25}_{-0.25}$	$5.90^{+0.27}_{-0.26}$	$5.82^{+0.26}_{-0.25}$	$6.17^{+0.14}_{-0.16}$	48.96
A0400	$2.60^{+0.06}_{-0.06}$	$2.33^{+0.07}_{-0.07}$	$2.26^{+0.07}_{-0.07}$	$2.32^{+0.06}_{-0.06}$	$2.31^{+0.04}_{-0.04}$	22.36
A0401	$10.05^{+0.10}_{-0.10}$	$7.69^{+0.25}_{-0.25}$	$7.25^{+0.26}_{-0.26}$	$6.97^{+0.22}_{-0.24}$	$7.36^{+0.13}_{-0.16}$	77.50
A0478	$6.95^{+0.11}_{-0.11}$	$6.62^{+0.08}_{-0.08}$	$6.25^{+0.07}_{-0.07}$	$5.71^{+0.07}_{-0.07}$	$6.14^{+0.06}_{-0.03}$	49.05
A0496	$5.18^{+0.07}_{-0.07}$	$4.44^{+0.18}_{-0.15}$	$4.41^{+0.17}_{-0.15}$	$4.23^{+0.13}_{-0.11}$	$4.39^{+0.11}_{-0.08}$	41.73
A0576	$4.42^{+0.08}_{-0.08}$	$3.72^{+0.16}_{-0.16}$	$3.47^{+0.15}_{-0.15}$	$3.81^{+0.13}_{-0.14}$	$3.69^{+0.09}_{-0.07}$	29.60
A0754	$9.72^{+0.21}_{-0.21}$	$7.45^{+0.24}_{-0.24}$	$8.22^{+0.23}_{-0.23}$	$6.36^{+0.14}_{-0.14}$	$7.24^{+0.13}_{-0.11}$	75.28
A1060	$3.69^{+0.05}_{-0.05}$	$3.33^{+0.04}_{-0.04}$	$3.19^{+0.03}_{-0.03}$	$3.06^{+0.03}_{-0.03}$	$3.17^{+0.03}_{-0.01}$	92.29
A1367	$3.54^{+0.10}_{-0.10}$	$2.52^{+0.15}_{-0.15}$	$2.71^{+0.15}_{-0.14}$	$2.41^{+0.14}_{-0.15}$	$2.56^{+0.08}_{-0.08}$	13.92
A1644	$5.31^{+0.14}_{-0.13}$	$4.92^{+0.34}_{-0.34}$	$4.20^{+0.28}_{-0.25}$	$4.63^{+0.28}_{-0.29}$	$4.61^{+0.19}_{-0.17}$	22.80
A1650	$6.43^{+0.10}_{-0.10}$	$5.41^{+0.13}_{-0.10}$	$5.09^{+0.10}_{-0.10}$	$4.88^{+0.08}_{-0.08}$	$5.14^{+0.05}_{-0.05}$	55.96
A1651	$7.07^{+0.25}_{-0.25}$	$6.32^{+0.20}_{-0.20}$	$5.88^{+0.24}_{-0.24}$	$5.92^{+0.20}_{-0.21}$	$6.09^{+0.12}_{-0.12}$	97.23
A1656	$9.68^{+0.21}_{-0.21}$	$8.40^{+0.21}_{-0.21}$	$7.39^{+0.21}_{-0.21}$	$6.62^{+0.11}_{-0.11}$	$7.44^{+0.09}_{-0.13}$	88.21
A1736	$3.67^{+0.13}_{-0.13}$	$3.57^{+0.18}_{-0.18}$	$3.07^{+0.15}_{-0.15}$	$3.10^{+0.17}_{-0.17}$	$3.26^{+0.08}_{-0.09}$	28.06
A1795	$6.06^{+0.16}_{-0.16}$	$6.18^{+0.14}_{-0.14}$	$5.56^{+0.14}_{-0.14}$	$5.32^{+0.09}_{-0.09}$	$5.70^{+0.08}_{-0.08}$	55.67
A2029	$8.75^{+0.11}_{-0.11}$	$7.74^{+0.16}_{-0.16}$	$7.09^{+0.15}_{-0.15}$	$6.36^{+0.11}_{-0.11}$	$7.03^{+0.07}_{-0.10}$	71.64
A2052	$3.51^{+0.03}_{-0.03}$	$3.16^{+0.05}_{-0.05}$	$3.00^{+0.05}_{-0.05}$	$2.96^{+0.04}_{-0.04}$	$3.04^{+0.03}_{-0.03}$	31.28
A2063	$3.87^{+0.06}_{-0.06}$	$3.75^{+0.07}_{-0.07}$	$3.58^{+0.06}_{-0.06}$	$3.31^{+0.05}_{-0.05}$	$3.53^{+0.04}_{-0.03}$	44.95
A2065	$6.68^{+0.17}_{-0.17}$	$5.49^{+0.31}_{-0.24}$	$4.61^{+0.23}_{-0.23}$	$4.24^{+0.18}_{-0.16}$	$4.81^{+0.13}_{-0.15}$	36.67
A2142	-	-	-	-	-	-
A2147	$4.50^{+0.15}_{-0.15}$	$4.15^{+0.16}_{-0.16}$	$4.32^{+0.23}_{-0.17}$	$4.09^{+0.15}_{-0.15}$	$4.19^{+0.07}_{-0.09}$	39.33
A2163	$11.73^{+0.25}_{-0.25}$	$9.73^{+0.45}_{-0.45}$	$9.92^{+0.45}_{-0.45}$	$8.06^{+0.35}_{-0.35}$	$9.40^{+0.27}_{-0.29}$	65.74
A2199	$4.77^{+0.04}_{-0.04}$	$4.31^{+0.08}_{-0.06}$	$4.02^{+0.07}_{-0.07}$	$3.95^{+0.05}_{-0.05}$	$4.10^{+0.03}_{-0.04}$	103.19
A2204	$9.97^{+0.24}_{-0.24}$	$7.58^{+0.34}_{-0.33}$	$7.03^{+0.32}_{-0.32}$	$6.80^{+0.35}_{-0.20}$	$7.22^{+0.17}_{-0.18}$	28.37
A2255	$7.22^{+0.23}_{-0.23}$	$6.88^{+0.57}_{-0.40}$	$6.15^{+0.49}_{-0.48}$	$6.54^{+0.56}_{-0.48}$	$6.62^{+0.25}_{-0.25}$	25.73
A2256	-	-	-	-	-	-
A2589	$3.91^{+0.04}_{-0.04}$	$3.51^{+0.08}_{-0.08}$	$3.34^{+0.05}_{-0.06}$	$3.38^{+0.05}_{-0.05}$	$3.40^{+0.03}_{-0.02}$	25.80
A2597	$4.08^{+0.07}_{-0.07}$	$3.50^{+0.08}_{-0.08}$	$3.36^{+0.06}_{-0.06}$	$3.04^{+0.06}_{-0.06}$	$3.30^{+0.04}_{-0.03}$	14.65
A2634	$3.91^{+0.10}_{-0.10}$	$3.85^{+0.30}_{-0.30}$	$3.24^{+0.22}_{-0.21}$	$2.63^{+0.25}_{-0.16}$	$3.22^{+0.13}_{-0.08}$	10.60
A2657	$4.01^{+0.08}_{-0.08}$	$3.97^{+0.10}_{-0.10}$	$3.52^{+0.10}_{-0.09}$	$3.96^{+0.12}_{-0.12}$	$3.81^{+0.06}_{-0.06}$	45.92
A3112	$5.45^{+0.12}_{-0.09}$	$4.42^{+0.14}_{-0.15}$	$3.97^{+0.09}_{-0.10}$	$3.79^{+0.08}_{-0.08}$	$4.00^{+0.06}_{-0.04}$	33.10
A3158	$6.01^{+0.10}_{-0.10}$	$5.54^{+0.23}_{-0.18}$	$4.92^{+0.15}_{-0.15}$	$4.84^{+0.15}_{-0.15}$	$5.11^{+0.10}_{-0.08}$	83.88
A3266	$9.99^{+0.26}_{-0.26}$	$7.80^{+0.29}_{-0.29}$	$8.15^{+0.29}_{-0.29}$	$6.81^{+0.27}_{-0.18}$	$7.62^{+0.17}_{-0.17}$	93.71
A3376	$4.78^{+0.14}_{-0.14}$	$3.68^{+0.18}_{-0.18}$	$3.52^{+0.19}_{-0.16}$	$3.25^{+0.11}_{-0.11}$	$3.43^{+0.11}_{-0.07}$	17.92
A3391	$6.62^{+0.22}_{-0.22}$	$5.86^{+0.21}_{-0.21}$	$5.61^{+0.20}_{-0.19}$	$5.22^{+0.13}_{-0.13}$	$5.54^{+0.13}_{-0.09}$	34.57
A3395	$5.27^{+0.24}_{-0.22}$	$4.73^{+0.25}_{-0.25}$	$4.91^{+0.25}_{-0.25}$	$4.50^{+0.20}_{-0.20}$	$4.72^{+0.12}_{-0.14}$	15.67
A3526	-	-	-	-	-	-
A3558	$7.42^{+0.27}_{-0.28}$	$5.68^{+0.15}_{-0.15}$	$5.37^{+0.13}_{-0.11}$	$5.36^{+0.10}_{-0.09}$	$5.51^{+0.08}_{-0.08}$	55.17
A3562	$4.97^{+0.11}_{-0.11}$	$4.29^{+0.08}_{-0.07}$	$4.13^{+0.08}_{-0.08}$	$4.03^{+0.07}_{-0.07}$	$4.16^{+0.04}_{-0.04}$	50.44
A3571	$8.10^{+0.08}_{-0.08}$	$6.69^{+0.08}_{-0.08}$	$6.37^{+0.08}_{-0.08}$	$6.09^{+0.06}_{-0.06}$	$6.36^{+0.06}_{-0.03}$	135.09
A3581	$2.06^{+0.01}_{-0.01}$	$1.86^{+0.03}_{-0.03}$	$1.84^{+0.03}_{-0.03}$	$1.76^{+0.03}_{-0.03}$	$1.83^{+0.01}_{-0.02}$	17.71
A3667	$6.65^{+0.05}_{-0.05}$	$5.48^{+0.13}_{-0.11}$	$5.37^{+0.12}_{-0.10}$	$5.02^{+0.07}_{-0.07}$	$5.25^{+0.05}_{-0.05}$	58.63
A4038	$3.38^{+0.03}_{-0.03}$	$3.09^{+0.04}_{-0.04}$	$3.00^{+0.03}_{-0.03}$	$2.90^{+0.03}_{-0.03}$	$2.99^{+0.02}_{-0.02}$	109.43
A4059	$4.61^{+0.04}_{-0.04}$	$3.93^{+0.08}_{-0.08}$	$3.96^{+0.08}_{-0.08}$	$3.89^{+0.07}_{-0.07}$	$3.96^{+0.04}_{-0.04}$	40.47
EXO0422	$3.43^{+0.12}_{-0.09}$	$3.24^{+0.05}_{-0.05}$	$3.19^{+0.05}_{-0.05}$	$3.03^{+0.04}_{-0.04}$	$3.15^{+0.03}_{-0.02}$	48.04
HydraA	-	-	-	-	-	-
IIIZw54	$2.80^{+0.06}_{-0.06}$	$2.70^{+0.05}_{-0.05}$	$2.57^{+0.05}_{-0.05}$	$2.60^{+0.04}_{-0.04}$	$2.63^{+0.02}_{-0.03}$	34.60
MKW3S	$4.06^{+0.06}_{-0.06}$	$3.48^{+0.10}_{-0.10}$	$3.31^{+0.07}_{-0.07}$	$3.22^{+0.06}_{-0.06}$	$3.32^{+0.05}_{-0.03}$	57.74
MKW4	$2.14^{+0.02}_{-0.02}$	$1.94^{+0.06}_{-0.06}$	$1.95^{+0.05}_{-0.06}$	$1.86^{+0.06}_{-0.06}$	$1.93^{+0.03}_{-0.02}$	17.30
MKW8	$3.51^{+0.12}_{-0.11}$	$3.16^{+0.11}_{-0.11}$	$2.66^{+0.09}_{-0.08}$	$2.90^{+0.09}_{-0.09}$	$2.91^{+0.06}_{-0.04}$	18.74

Table 3.4: continued.

Cluster name	kT_{ACIS} [keV]	kT_{MOS1} [keV]	kT_{MOS2} [keV]	kT_{PN} [keV]	$kT_{\mathrm{EPIC,\ Combined}}$ [keV]	SC/BKG
NGC1399	-	-	-	-	-	-
NGC1550	$1.55^{+0.02}_{-0.02}$	$1.54^{+0.04}_{-0.04}$	$1.48^{+0.04}_{-0.05}$	$1.50^{+0.03}_{-0.03}$	$1.52^{+0.02}_{-0.02}$	28.38
NGC4636	-	-	-	-	-	-
NGC5044	-	-	-	-	-	-
NGC507	$1.54^{+0.02}_{-0.02}$	$1.51^{+0.03}_{-0.03}$	$1.44^{+0.04}_{-0.04}$	$1.53^{+0.02}_{-0.02}$	$1.51^{+0.01}_{-0.02}$	21.37
RXCJ1504	$9.81^{+0.80}_{-0.79}$	$7.46^{+0.54}_{-0.54}$	$5.97^{+0.38}_{-0.37}$	$5.99^{+0.31}_{-0.31}$	$6.40^{+0.20}_{-0.16}$	8.87
S1101	$2.88^{+0.04}_{-0.04}$	$2.54^{+0.06}_{-0.06}$	$2.30^{+0.07}_{-0.07}$	$2.37^{+0.06}_{-0.06}$	$2.42^{+0.04}_{-0.03}$	20.09
ZwCl1215	$7.17^{+0.30}_{-0.30}$	$6.57^{+0.16}_{-0.16}$	$6.07^{+0.17}_{-0.17}$	$5.60^{+0.15}_{-0.15}$	$6.09^{+0.09}_{-0.09}$	59.56

Table 3.5: Spline parameters (e.g., Press et al., 1992, Chapter 3.3) for the stacked residual ratios. y denotes the stacked residual ratio value at a given energy and y'' the second derivative. All splines are normalized to unity at 1.1 keV.

Energy	ACIS/PN		MOS1/PN		MOS2/PN	
[keV]	y	y''	y	y''	y	y''
0.54	1.01	-14.69	0.99	-9.32	1.00	-11.37
0.62	1.04	-0.81	1.06	-1.23	1.05	-1.08
0.71	0.99	0.02	1.03	0.16	1.02	0.32
0.81	0.96	0.49	1.02	0.20	1.02	-0.02
0.94	0.98	-0.06	1.02	-0.34	1.01	-0.06
1.08	1.00	0.02	1.00	0.56	1.00	0.35
1.24	1.02	0.07	1.05	-0.23	1.04	-0.16
1.42	1.06	-0.10	1.07	0.01	1.06	0.02
1.63	1.07	-0.08	1.08	-0.18	1.08	-0.23
1.88	1.08	0.09	1.05	0.14	1.05	0.13
2.15	1.11	0.03	1.07	0.03	1.05	-0.00
2.48	1.15	-0.06	1.09	-0.07	1.05	-0.00
2.84	1.17	-0.09	1.08	0.02	1.04	-0.07
3.27	1.15	0.03	1.09	-0.00	1.02	0.12
3.76	1.15	-0.01	1.10	0.03	1.05	0.02
4.32	1.15	0.09	1.12	-0.06	1.08	-0.12
4.96	1.18	-0.17	1.10	0.01	1.04	0.05
5.70	1.13	0.15	1.09	-0.01	1.01	-0.12
6.55	1.16	-0.17	1.08	0.05	0.95	0.32

3.9.2 Temperature comparison

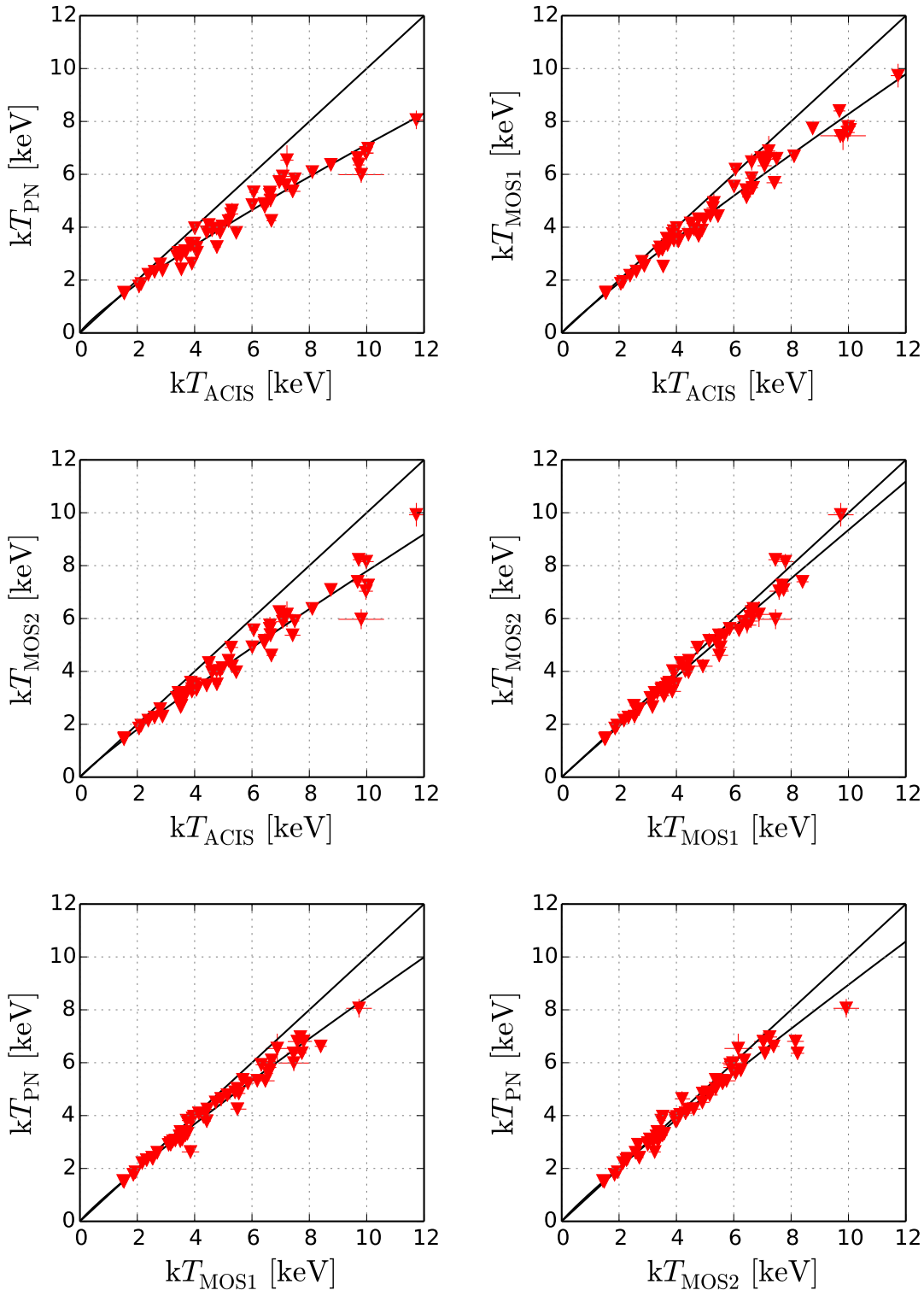

Figure 3.15: Best-fit temperatures of the HIFLUGCS clusters in an isothermal region for all detector combinations in the $(0.7 - 7.0)$ keV energy band and with N_{H} frozen to the radio value of the LAB survey. The parameters of the best-fit powerlaw (black line) are also shown in Fig. 3.18.

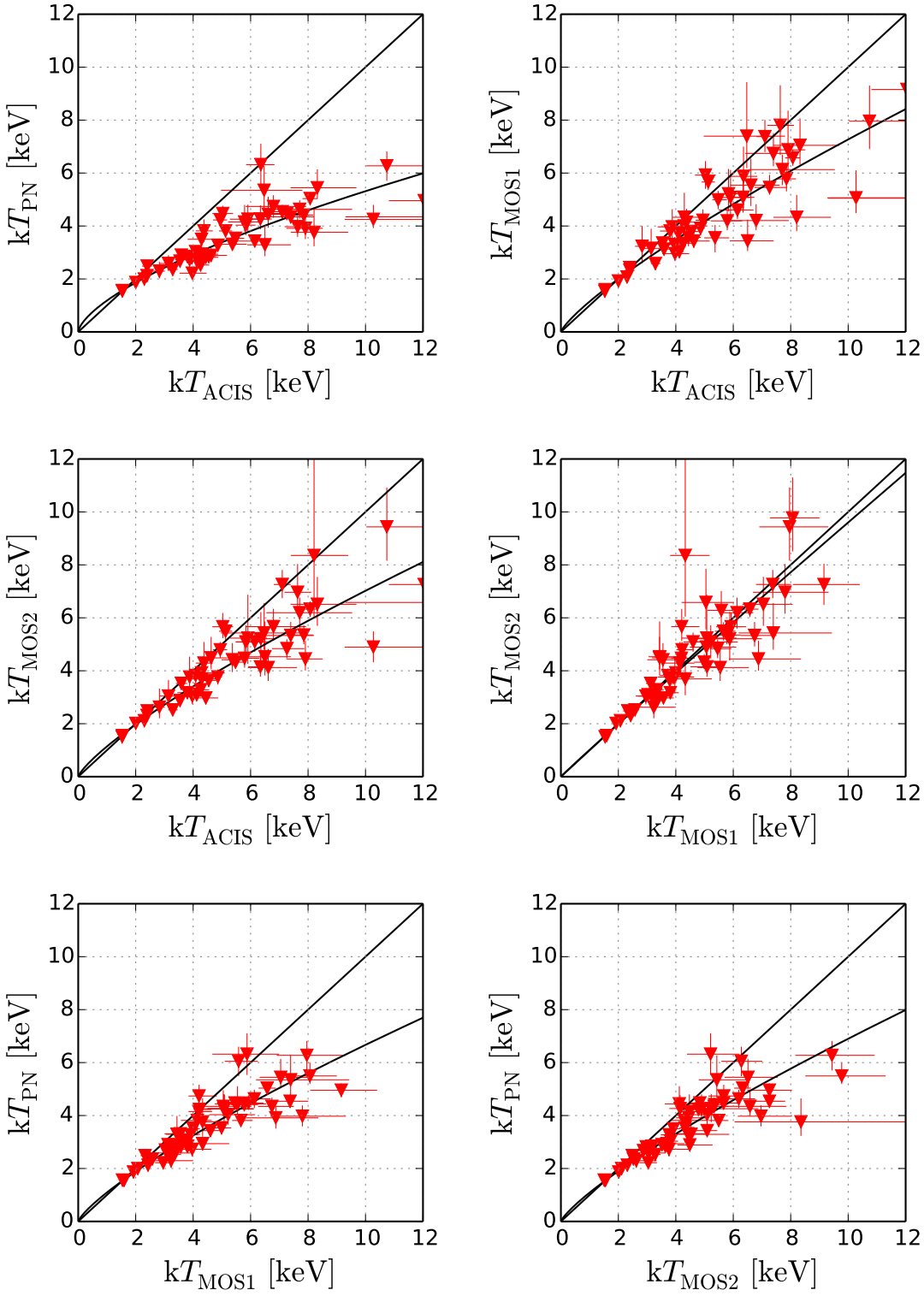

Figure 3.16: Same as Figure 3.15 but for the $(0.7 - 2.0)$ keV band.

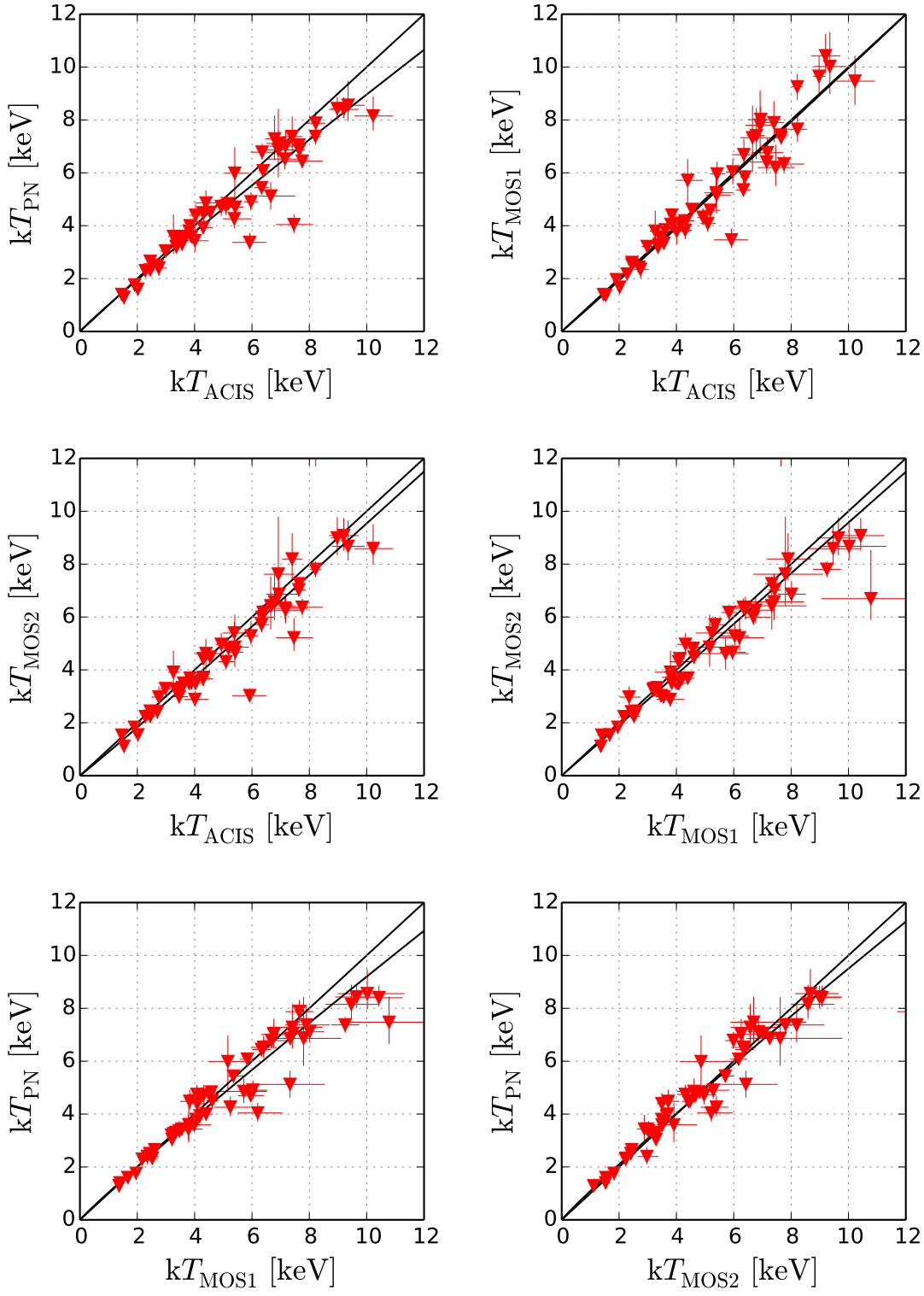

Figure 3.17: Same as Figure 3.15 but for the $(2.0 - 7.0)$ keV band.

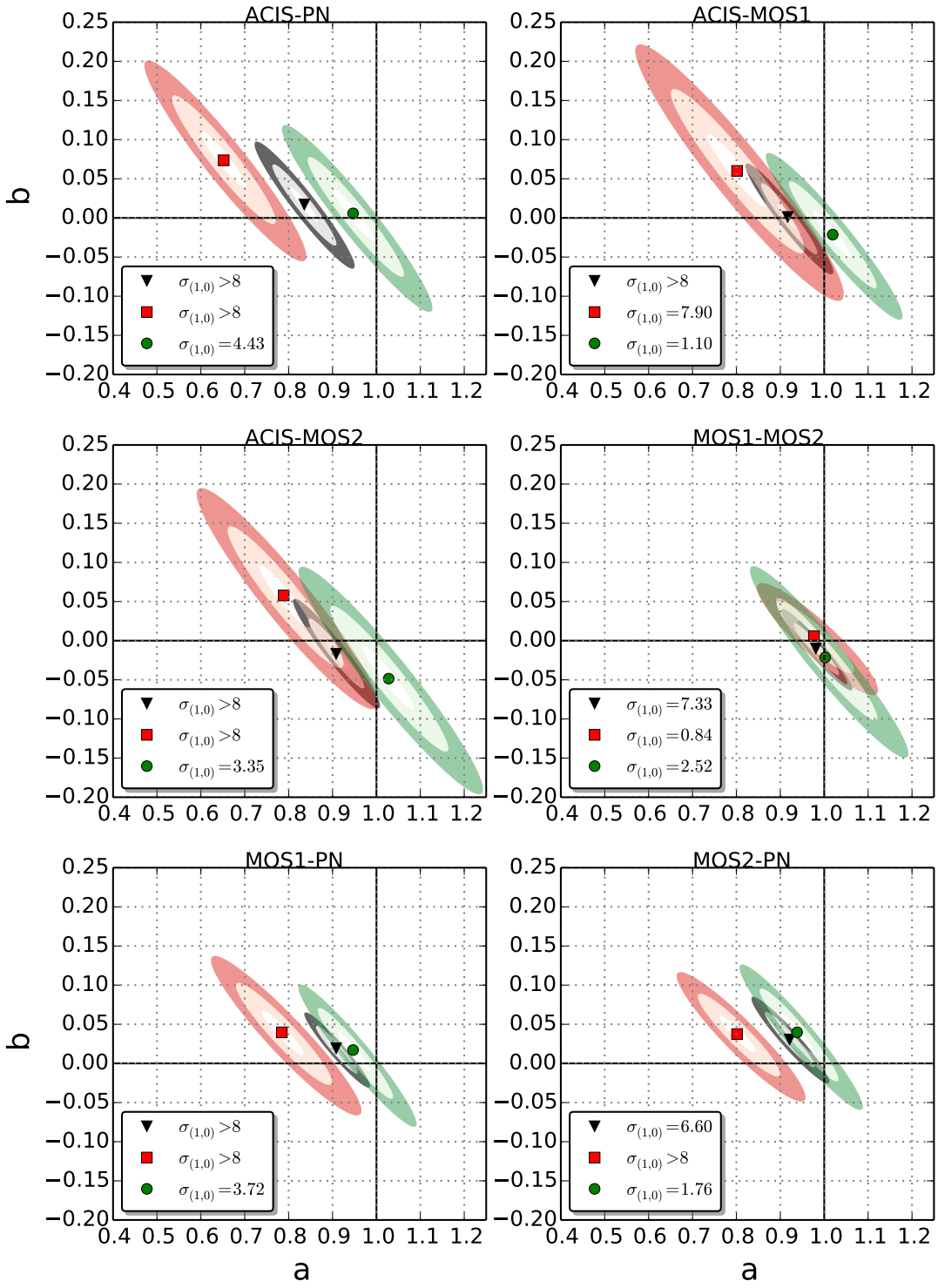

Figure 3.18: Fit parameter (see Eq. 3.3) degeneracy for the 1-, 3-, and 5-σ levels of the different detector combinations for the full (gray triangle), soft (red square), and hard (green circle) energy bands. Equality of temperatures for two instruments is given for $a = 1$ and $b = 0$. The deviation in σ from equality is given in the legend.

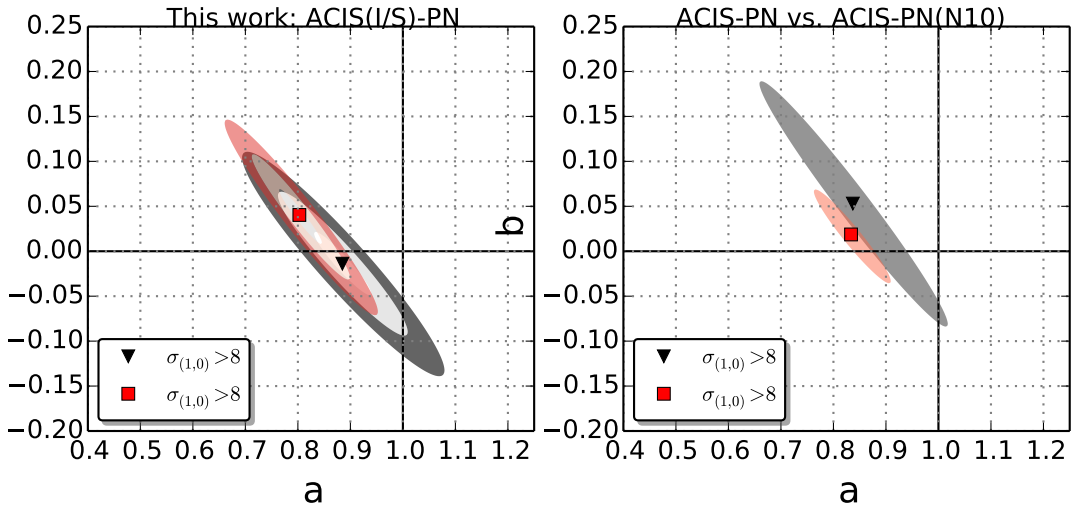

Figure 3.19: *Left:* Fit parameter degeneracy for the 1-, 3-, and 5-σ levels of ACIS - PN for the $(0.7-7)$ keV energy band. ACIS-I (red square) and ACIS-S (black triangle) HIFLUGCS subsamples are shown versus the PN data (for all ACIS data combined, see Fig. 3.18, top left panel, gray ellipse). Equality of temperatures for two instruments is given for $a = 1$ and $b = 0$. The deviation in σ from equality is given in the legend. *Right:* As in the left panel but only 3-σ levels (gray and red ellipses) of ACIS - PN with temperatures taken from N10 ($0.5-7$ keV energy band, black triangle) and complete ACIS - PN of this work ($0.7-7$ keV energy band, red square).

3.9.3 Self consistency test

In Section 3.6.2 we compared the best-fit temperatures of different instruments in the same energy band. In the case of purely isothermal emission and a very accurately calibrated effective area, the temperatures obtained in different energy bands of the same instrument should also be equal. By comparing temperatures of one instrument in different bands it is thus possible to quantify the absolute calibration uncertainties, if the assumption of isothermal emission is fulfilled.

In Figure 3.20 we demonstrate how self consistent the instruments are in terms of soft and hard band temperatures. We also quantify the expected deviation from equality of soft and hard band temperatures for a given two-temperature plasma.

Only for ACIS the temperature deviation (quoted σ value in the legend of Fig. 3.20) is less than 3σ in comparing the soft and hard energy bands. By performing simulations similar to those shown in 3.7.1, we can quantify the expected difference between soft and hard band temperatures of the same instrument in the presence of a multitemperature structure. This is shown in Fig. 3.20, where we indicate this result from simulations including a cold component with 1 keV and an EMR of 0.01, 2 keV and an EMR of 0.05, and 1 keV and an EMR of 0.05; i.e., the new symbols represent the new expected "zero points" given the multiple temperature components.

We conclude that the multitemperature structure has a strong influence on the results of this test and prevents firm conclusions on the absolute calibration. For a cold component with a temperature of ~ 1 keV and EMR higher than 0.01, the EPIC-PN instrument seems to agree with the simulations.

We want to emphasize that the non-detection of an effect of multitemperature ICM on comparing different instruments (as suggested in Section 3.7) is unrelated to multitemperature effects on the soft and hard band temperatures of the same instrument presented here, since the multitemperature influence may be much stronger.

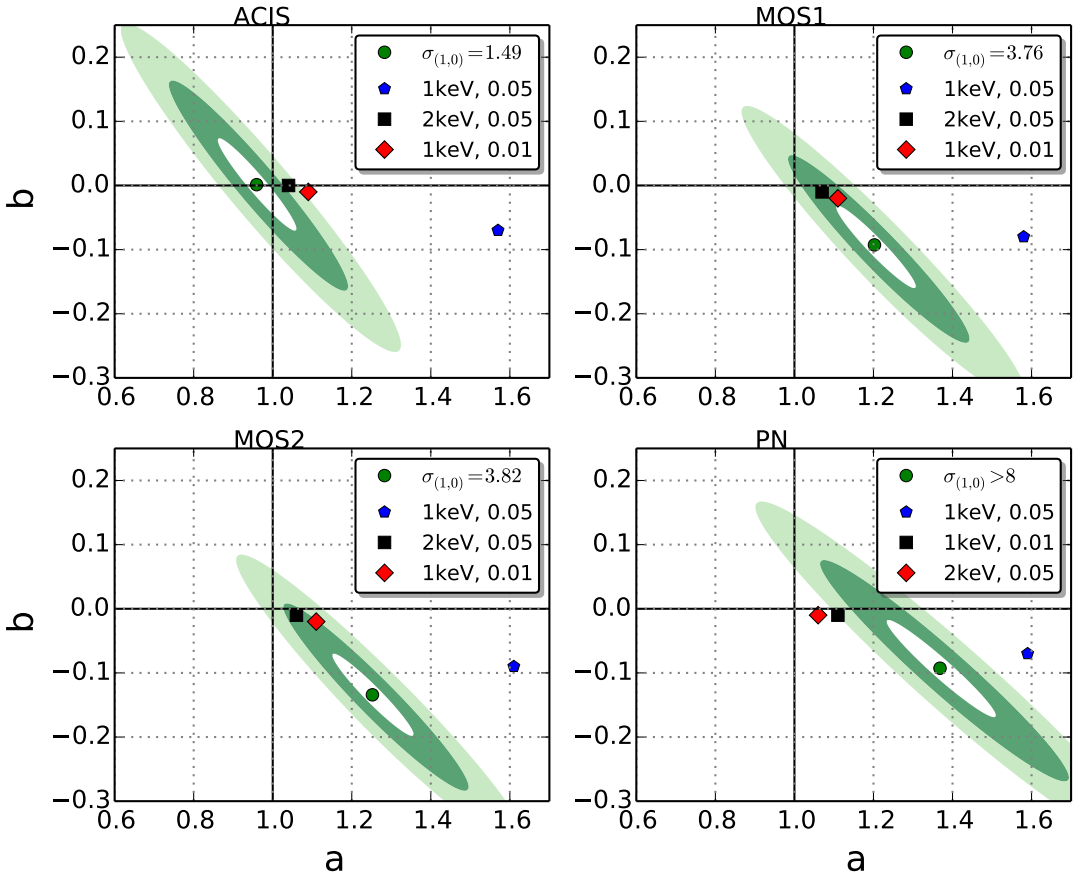

Figure 3.20: Fit parameter degeneracy for the 1-,3-, and 5-σ levels of each instrument in different energy bands. The green contours (circles) refer to the soft vs hard band. Equality of temperatures for two bands is given for $a = 1$ and $b = 0$. The deviation in σ from equality is given in the legend, as well as the expectations (blue pentagon, black square, and red diamond) for a multitemperature ICM with the parameters (temperature, emission measure ratio) of the cold component given.

3.9.4 XMM-Newton and Chandra cross-calibration formulae

There are several methods of performing a cross-calibration between two instruments such as Chandra/ACIS and XMM-Newton/EPIC using galaxy clusters. In this work we show:

- A correction formula for the effective area obtained using the stacked residual ratio method (Section 3.6.1 and Table 3.5). For example to rescale the effective area of ACIS to give EPIC-PN consistent temperatures, one has to multiply the ACIS effective area by the spline interpolation of the ACIS/PN column of Table 3.5.
- A correction formula for the best-fit ICM temperature (Eq. 3.3 and Table 3.2); for example, for an ACIS-PN conversion in the full energy band, one has to use $a = 0.836$ and $b = 0.016$ for the parameters in Eq. 3.3 (with ACIS as X and PN as Y).
- A linear relation for the hydrostatic masses (see below). The Chandra masses were calculated using the temperature and surface brightness profiles of the HIFLUGCS clusters, while the XMM-Newton masses were adopted from the rescaled Chandra temperature profiles (using Eq. 3.3 and Table 3.2).

The hydrostatic masses are shown in Figure 3.21. We found the following relation:

$$M_{500}^{\mathrm{XMM}} = 0.859^{+0.017}_{-0.016} \cdot \left(M_{500}^{\mathrm{Chandra}}\right)^{1.00 \pm 0.02} . \tag{3.7}$$

This result agrees with the derived relations in Mahdavi et al. (2013) and is also in rough agreement with Israel et al. (2014b). In Israel et al. (2014b), the authors obtained Chandra masses by using Chandra cluster temperatures assuming temperature profiles (from a scaling relation from Reiprich et al., 2013), while the XMM-Newton masses are calculated from the rescaled temperature profiles following the temperature scaling relation presented in this work. In Mahdavi et al. (2013), the authors find similar results concerning the temperature differences and also give a conversion for the hydrostatic masses between XMM-Newton and Chandra (see Fig. 3.21).

The three methods presented in this work for converting between XMM-Newton and Chandra are obviously not exactly equivalent in the context of cosmological results.

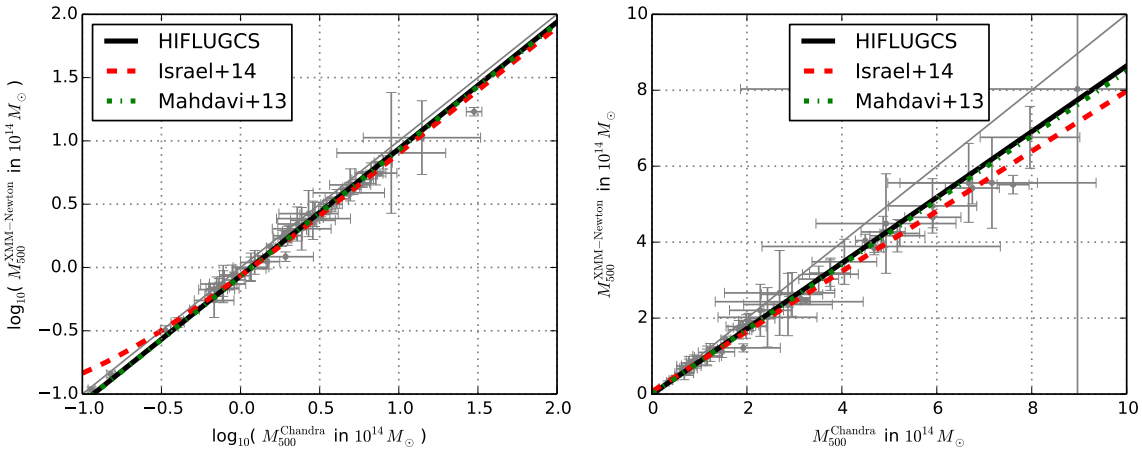

Figure 3.21: Comparison between Chandra and XMM-Newton in terms of hydrostatic masses in logspace (left) and realspace (right). Gray circles: Hydrostatic masses for Chandra (derived from data) and XMM-Newton (from rescaled Chandra temperature profiles). A best-fit relation (derived in logspace) is shown in black (Eq. 3.5), along with the results from Israel et al., 2014b (red dashed line) and Mahdavi et al., 2013 (green dotted dashed line).

CHAPTER 4

HICOSMO – The HIFLUGCS Cosmology Project

4.1 Motivation

This project aims at "measuring" the cosmological parameters of the Universe. As described before galaxy clusters are excellent tracers of the matter content of the Universe, which can be parameterized by the normalized matter density, $\Omega_{\rm M}$, and the amplitude of initial density fluctuations, σ_8. Even with local galaxy clusters these quantities can be constrained. In the past tremendous efforts were spend on breaking the degeneracy between these parameters and lowering the uncertainties by using better instruments, bigger samples and more advanced analysis methods. But instead of galaxy clusters, one can also use completely different and independent probes like the primary anisotropies of the cosmic microwave background radiation (CMB). With these completely different observables of cosmological parameters, on the one hand structure formation inferred from galaxy clusters and on the other hand the radiation from a very early epoch of the Universe, one has very complementary tools: The $\Omega_{\rm M}$ - σ_8 degeneracies are almost perpendicular to each other, which means including different probes in the analysis will shrink the uncertainties quite significantly. Although the combined analysis has advantages, it is crucial to also interpret the cosmological results of one method alone to see if systematic biases are minimized.

Unfortunately, X-ray observations of galaxy clusters as a cosmological probe require assumptions on how the total gravitating mass can be obtained. Either one can assume that the ICM is in hydrostatic equilibrium or use tracers like the luminosity or temperature for the total mass. Calibrating these scaling relations of observables and the total mass using weak lensing observations might provide a way to reliably estimate masses for big samples of galaxy clusters. Unfortunately other (maybe unknown) biases are connected with weak lensing studies, such as noise bias (e.g., Massey et al., 2013), mass sheet degeneracy (e.g., Schneider and Seitz, 1995; Bradač et al., 2004), asymmetry of the point spread function (e.g., Hirata and Seljak, 2003), false photometric redshifts and miscentering (Köhlinger et al., 2015). Also selection effects, that enter in the generation of a galaxy cluster sample (e.g., selecting only massive or intrinsically brighter objects) can bias cosmological results, if they are not accounted properly. Moreover, all measurements depend on the calibration accuracy of the instrument. Any systematic uncertainties arising from the instrument itself have to be known before the interpretation of the data can be done. As shown in Chapter 4.5.2, the situation is still relatively uncertain in the X-ray regime, because although the relative differences between two instrument, e.g., Chandra and XMM-Newton, are known, still one cannot say which instrument is correct, if any. What will be done within this study is to incorporate the known uncertainties between the two X-ray instruments mentioned before as a range of instrumental systematics. Of course, the true cluster temperatures could be even lower than XMM-Newton or higher than Chandra results, but as it has been shown with small samples that Chandra-ACIS and XMM-Newton PN mark roughly the extreme cases among 10 X-ray detectors (Grant et al., 2013; Burrows et al., 2014). Also as shown in Chapter 4.5.2, the impact of the cross calibration uncertainties between XMM-Newton and Chandra on cosmology is not larger than the statistical uncertainties for samples like HIFLUGCS, because most clusters have not very high temperatures and to calculate M_{500} the temperature is measured at R_{500}.

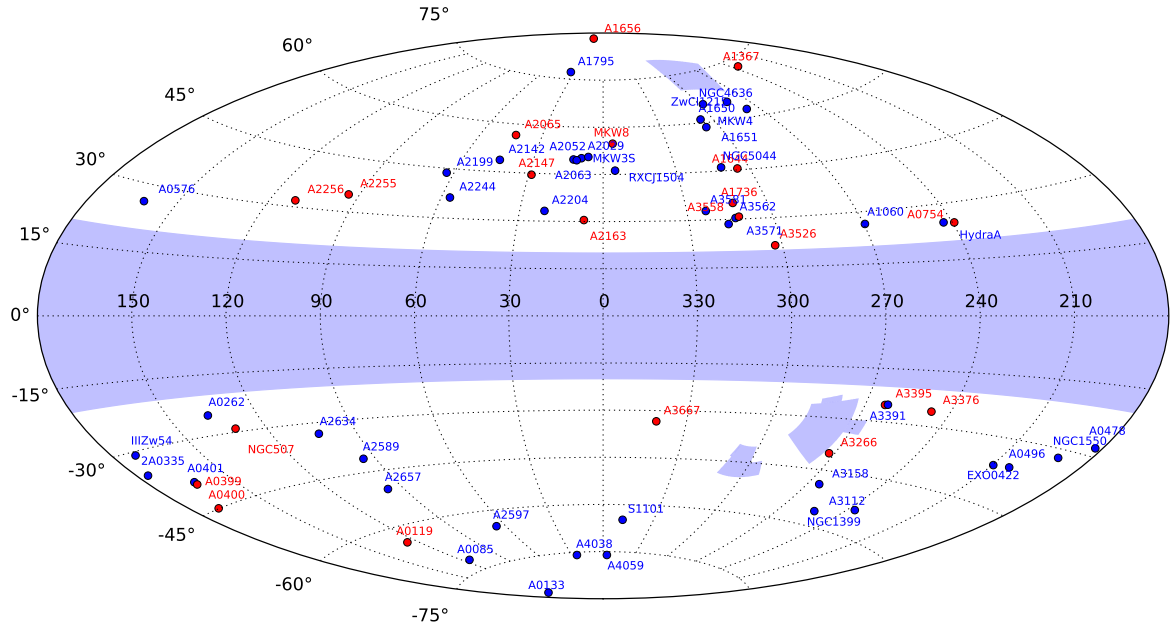

Figure 4.1: The 64 HIFLUGCS galaxy clusters (red are clusters marked as merging in Vikhlinin et al., 2009a) in galactic coordinates. The blue shaded regions denote the excluded regions (Milky way plane, Magellanic clouds and Virgo cluster).

At these outer radii for most clusters and groups the temperature has dropped significantly compared to the peak temperature at inner radii (e.g., De Grandi and Molendi, 2002; Vikhlinin et al., 2005; Rasmussen and Ponman, 2007; Leccardi and Molendi, 2008; Sun et al., 2009).

For cosmological application an X-ray flux limited sample like HIFLUGCS is of special interest: It provides high quality data of nearby galaxy clusters, which can be studied in detail including a treatment of possible substructure and contaminating point sources to get precise temperature and surface brightness profiles. It has been shown in Reiprich and Böhringer (2002) that with such a sample, Ω_m and σ_8 can be quantified, so one has an independent probe for cosmological parameters in hand. Another benefit is that the degeneracy ellipse in the Ω_m-σ_8 plane is almost perpendicular to the one from CMB primary anisotropies (e.g., Allen et al., 2003; Reiprich, 2006).

So this analysis will enable one to put constraints on at least two cosmological parameters and also to gain knowledge about the physical processes in the X-ray brightest galaxy cluster sample.

4.2 Sample

The **HI**ghest X-ray **FLU**x **G**alaxy **C**luster **S**ample (HIFLUGCS, Reiprich and Böhringer, 2002) was selected from the ROSAT All-Sky Survey (RASS, Truemper, 1982; Voges, 1992). It consists of 64 galaxy cluster above a flux limit of $2 \times 10^{-11}\,\mathrm{erg\,s^{-1}\,cm^{-2}}$ in the $(0.1 - 2.4)\,\mathrm{keV}$ band (from now on referred as ROSAT band) and within a region outside the Milky Way disk ($|b| \geq 20°$), the Magellanic Clouds and the Virgo cluster, which sums up to 64.78 % of the sky (see Fig. 4.1). This results in a sample of very bright and local galaxy clusters. Looking at it in more detail highlights the effort spent on creating a homogeneous sample.

First candidates were selected from 4 different ROSAT catalogs:

- REFLEX, Böhringer et al. (2001): This catalog covers the southern part of the sky and optical follow-up observations have been made within the ESO program. It comprises 452 galaxy clusters above a flux limit of $3 \times 10^{-12}\,\mathrm{erg\,s^{-1}\,cm^{-2}}$ in the ROSAT band. At the flux limit it is supposed to be complete at the 90% level. At redshifts above 0.2 the fraction of non-extended REFLEX sources rises above 30%, which makes it also crucial to select a local sample. Otherwise the number of AGNs

falsely identified as clusters becomes significant. REFLEX was constructed with special attention on cosmological application.

- NORAS, Böhringer et al. (2000): The northern sky of RASS is covered by NORAS, which consists of 378 clusters. The completeness is stated with 50% at the same flux level as REFLEX.
- NORAS II, Retzlaff (2001): NORAS II has a similar structure as NORAS but with a lower flux limit of $2 \times 10^{-12}\,\mathrm{erg\,s^{-1}\,cm^{-2}}$.
- BCS, Ebeling et al. (1998): BCS consists of 201 bright galaxy clusters in the northern hemisphere above a flux of $4.4 \times 10^{-12}\,\mathrm{erg\,s^{-1}\,cm^{-2}}$ and 90% completeness.

Clusters were selected from these catalogs with a slightly lower flux limit of $1.7 \times 10^{-11}\,\mathrm{erg\,s^{-1}\,cm^{-2}}$. This extended sample was then reanalyzed to obtain a homogeneous flux limited sample. It should be noted that RXCJ1504 was originally not included in HIFLUGCS, but follow-up observations later revealed that the contribution of AGN emission to the total flux is not as high as initially thought. The median redshift of the final sample is 0.05.

Detailed studies of several aspects of this sample have been carried out in the past:

- Sample details and cosmology: The sample was originally introduced by Reiprich and Böhringer (2002). More details about the sample construction, systematics and cosmological implications (for isothermal mass estimates) can be found therein.
- Mass deposition rate: Chen et al. (2007) analyzed the classical model of a cooling flow in HIFLUGCS clusters and conclude that the cool core clusters show an almost linear relation between the mass deposition rate inferred from a cooling flow model and the total cluster mass. The cooling flow model states that dense cores of galaxy clusters with a cooling time less than the Hubble time will show cool regions and condense, if there is no heating mechanism. A trend that less massive cluster more likely show a cool core is deduced. Moreover, several observables like slope and core radius of the surface brightness profile or luminosity have been tested to be a cool core tracer.
- Cool core fraction: Hudson et al. (2010) have shown that, following their definition of a cool core cluster (central cooling time $t_{\mathrm{cool}} < 7.7\,\mathrm{Gyr}$), 72% are cool core cluster, while 44% have a strong cool core with $t_{\mathrm{cool}} < 1\,\mathrm{Gyr}$.
- Radio AGNs and their influence on the ICM environment: Mittal et al. (2009) find that 75% of the HIFLUGCS clusters contain a central radio source. Of special interest are these fractions among the cool core clusters: 100% of the strong cool core clusters (according to the definition in Hudson et al., 2010) and only 45% of the non-cool core cluster have a central radio source. Since the radio luminosities of these sources seem to scale with the mass of the cluster, it points toward a self regulated cooling mechanism triggered by the AGN especially in strong cool core clusters.
- Cluster scaling relations: Zhang et al. (2011a) tested the scaling relations of galaxy clusters, especially comparing X-ray quantities like luminosity or r_{500} with the member galaxy velocity dispersion derived from optical, spectroscopic data. The results agree well with predictions from simulations or self-similarity. High scatter for low massive systems indicates the increasing influence of AGNs.
- Star formation history: In Zhang et al. (2011b) the authors interpret a (for increasing total mass) decreasing stellar mass fraction for a subsample of HIFLUGCS together with a decreasing stellar mass fraction for an increased central entropy as massive mergers and a trigger for the end of star formation in the galaxies. Furthermore, AGNs and their feedback processes can deplete and push out part of the gas in low mass systems. But these systems are observed to be more metal rich, so have a more efficient star formation.
- $L_x - T_{\mathrm{vir}}$ relation: Mittal et al. (2011) investigated how this scaling relation is influenced by the ICM. Cool core clusters are found to have the steepest slope of this relation. While the effect of AGN heating seems to affect mainly the low mass systems, the hot and massive clusters are influenced by ICM cooling. Surprisingly the clusters with the lowest cooling time don't seem to have generally the

lowest intrinsic scatter in the scaling relation. Although a dominant fraction of the scatter in the $L_x - T_{\rm vir}$ relation is due to the NCC systems, it can be significantly lowered by excising the cool core region of CC clusters.

- Biases in the sample selection: Eckert et al. (2011) study the systematic selection effects of X-ray flux limited samples. Since cool core clusters have a peaked surface brightness profile, they are more likely being included in these samples. This results in a 29% higher probability to include a cool core system, while the bias seems to increase for low massive galaxy groups. A similar effect was detected already in Hudson et al. (2010), and in more detail in Mittal et al. (2011), by characterizing cool core clusters not by a peaked surface brightness profile, but a higher X-ray luminosity.

Based on the Piffaretti et al. (2011) meta catalog, which is a homogenized compilation of 7 RASS catalogs and 5 serendipitous surveys, further X-ray flux limited samples motivated by the HIFLUGCS catalog can be established. One is *eHIFLUGCS* (Reiprich, 2012) where missing observations have been completed by Chandra in Cycle 14. It consists of 184 galaxy clusters selected from NORAS, REFLEX and BCS using the MCXC meta catalog. The lower flux limit is $9 \times 10^{-12}\,{\rm erg\,s^{-1}\,cm^{-2}}$. It is planned to also use it for cosmology. Lowering the flux limit even further will create bigger samples, but also the incompleteness of the reference catalogs is increasing, which makes cosmological interpretation more and more difficult. The enormous increase in statistical power will enable one to derive even more detailed cosmological studies of bright galaxy clusters and also be an excellent preparation and comparison for first *eROSITA* (Merloni et al., 2012) cluster catalogs.

Despite this interesting opportunities for the future, it is essential to have a reliable data analysis structure, which takes care of many sources of biases like substructure or extrapolation techniques. For this purpose, HIFLUGCS is the sample of choice to create a baseline for cluster analysis and cosmological interpretation.

4.3 Data Reduction

All galaxy clusters of the HIFLUGCS sample have been observed at least once with the Chandra X-ray observatory. For reliable hydrostatic masses one has to not only follow the standard tasks for data reduction, but also account for the following aspects:

- Point source treatment
- Substructure removal
- Instrumental and astrophysical background components
- Density profile from surface brightness in appropriate energy band
- Temperature profile parametrization
- Mass extrapolation

After giving an overview on the basic steps of the Chandra data reduction, each of the above mentioned points will be discussed in on section. Many Chandra observations are available for the 64 HIFLUGCS clusters. The basic selection criteria are:

- Only publicly available observations.
- Only ACIS detector.
- No grating observations.
- Exposure time at least 9 ks.

This selects 336 observations with a total exposure time of 12.2 Ms, all of them are listed in Tab. B.3. A subset of these observations was actually analyzed (marked green in Tab. B.3), which usually excludes short observations with a high off-axis angle (cluster outskirts), observations that were not publicly available

at the time of analysis (until beginning of cycle 13) and observations that would not add much more to an already large summed exposure time (if $\Delta t_{\rm exp} < 20\,\%$). Also cycle 0/1 observations were excluded if newer data was available, because the focal plane temperature was not stable in this very early epoch of Chandra. In total 134 observations (6331 ks) were analyzed.

4.3.1 Chandra standard data reduction tasks

In the following I briefly describe important tasks to reduce the raw Chandra data. This mainly follows the suggestions of the Chandra Data Analysis and Science Threads (`http://cxc.harvard.edu/ciao/threads/`). The analysis software that was used is

- CIAO software version 4.6,
- CALDB (calibration database) version 4.6.5 (released in December 2014 and compatible for observations until October 2014),
- Heasoft 6.16 including `Xspec` 12.8.2e.

The `chandra_repro` task applies a default treatment to the raw events files, for example badpixels and afterglows are detected and marked, and also the latest calibration is applied to update time, coordinate and pulse-height, grade and status information of the events. A lightcurve cleaning is performed in order to remove flared periods from the events file: The events file is binned in the time domain to have 1000 counts in each time bin (but at least 200 time bins). The `deflare` task using the `lc_clean` algorithm with a 3σ clipping is the default method, but for some very flared observations I switched to the iterative `lc_sigma_clip` algorithm, which is more stable, but sometimes cuts out more clean time. Many Chandra observations are not affected by flares. Any of the following region selection, either for the temperature or surface brightness profile, is centered on the emission weighted cluster center. Since Chandra does not provide a large field of view that is appropriate for this quantity, I take the emission weighted centers determined by Zhang et al. (2011a) using XMM-Newton.

4.3.2 Point source treatment

Point sources are sources which have an angular size smaller than the point spread function (PSF) of the instrument and are broadened to the PSF scale. Chandra has arcsecond spatial resolution on axis, so one can assume that all the detected point sources are AGNs. The `wavdetect` task, which uses a Mexican-Hat Wavelet transformation for the automated detection, is applied. Different scales (`1 2 4 8 16` pixel, which corresponds to roughly the same number in arcseconds due to the binned image) are used for the correlation of the image with the wavelet. Each source detection is characterized by a significance value, which I use to clip spurious detections. Figure 4.2 (left) shows the correlation between the minimum detected flux and the exposure time. Note that in Fig. 4.2 only the main observation for each cluster (see Tab. B.3) is shown. The three different colors correspond to a significance threshold of 0, 1 or 5. In any case one notices that above 50 ks the flux limit does not decrease any more. The fluxes were computed in the $(0.5-2)\,$keV band corrected for vignetting effects, dead area and detector quantum efficiency and assuming a powerlaw with 2 as spectral index. In Chandra X-ray Center Chandra Project Science (2010) a sensitivity of Chandra/ACIS of $4\times10^{-15}\,\mathrm{erg\,s^{-1}\,cm^{-2}}$ is mentioned in the $(0.4-6)\,$keV band for a 10 ks observation. This value roughly corresponds to $2.7\times10^{-15}\,\mathrm{erg\,s^{-1}\,cm^{-2}}$ in the energy band for Fig. 4.2. Applying the 5σ threshold means that some faint point sources may not be cut out (since theoretically the ACIS sensitivity limit is lower) but one gets rid of most of the spurious detections. Also the expected increasing behavior of the detected number of sources as a function of exposure time strongly favors the 5σ threshold (Fig. 4.2 right). For galaxy clusters, where more than one observation was available, the point source detection was run for all observations and the complete point source list was excluded for each observation. Only multiple detected sources (in different observations) were only removed once before taking spectra or surface brightness profiles. So all observations of one cluster use the same point source catalog.

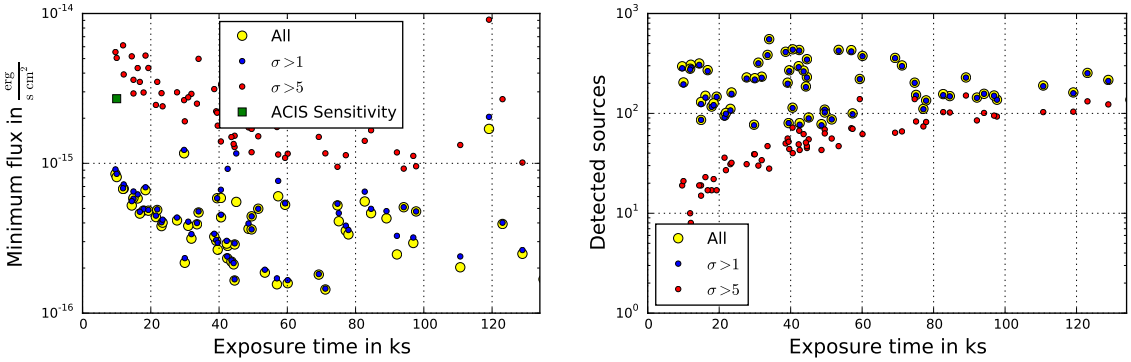

Figure 4.2: *Left:* Minimum flux of detected point sources as a function of the exposure time for different selection criteria: Blue and red points are point sources with a detection significance above 1 or 5, respectively. Yellow points mark the minimum flux among all detected sources. *Right:* Number of detected sources for each selection criterion as a function of the exposure time.

4.3.3 Substructure Selection

By assuming hydrostatic equilibrium one requires idealized objects that undergo no interaction with the surrounding neighborhood. But a complete sample of galaxy clusters also contains merging systems. In some cases, these interactions are spatially localized in one part of the cluster (e.g., if an interacting group has not passed through the cluster). By excluding the substructure area from the extraction region of the profiles it is possible to minimize the bias that would arise from strongly disturbed intracluster gas.

The dense substructure is usually visible in X-rays as excess emission to the normal ICM radiation, but often not detected by the `wavdetect` task, which is more efficient for point sources. I assume that in general the surface brightness profile of the ICM emission follows a double β-model,

$$\Sigma(r) = \Sigma_{01}\left(1+\frac{r^2}{r_{\rm c1}^2}\right)^{-3\beta_1+0.5} + \Sigma_{02}\left(1+\frac{r^2}{r_{\rm c2}^2}\right)^{-3\beta_2+0.5} , \tag{4.1}$$

where for each component $i = 1, 2$, Σ_{0i} denotes the central surface brightness value, r_{ci} the core radius and β_i characterizes the decrease of the surface brightness to the outskirts. Starting from a normal χ^2 fit to the surface brightness distribution using this model, one can detect local excess emission fairly easy. To reduce the noise I smooth both, the model and the photon flux image (corrected for vignetting, exposure time variations due to Chandra dither motion, quantum efficiency, bad pixels) of the observation with a Gaussian (16 arcsec width), before subtracting the model from the observation to get the flux difference image (see Fig. 4.3, top left).

It is now important tune the threshold of excess emission to be cut out, so that not too much emission gets excluded from very small fluctuations with respect to the model. In a histogram of the excess flux per pixel (Fig. 4.3, top right) one can recognize a peak which represents the average flux difference between model and measurement. Left of this peak are smaller differences and to the right the larger ones. One has to select flux differences above the average (Fig. 4.3, middle left) to get the strongest substructures and not Poisson noise. As default I chose the threshold to cut at a flux-difference limit, where the cumulative flux-difference is half the total flux difference summed over all pixels (note that only positive flux differences are included in this analysis):

$$\sum_i (f_{\rm OBS} - f_{\rm MODEL}) > 0.5 \sum_{\rm all\,pixel} (f_{\rm OBS} - f_{\rm MODEL}) , \tag{4.2}$$

where i are all pixels with a flux difference above a threshold (see also Fig. 4.3, middle right). The factor of 0.5 is slightly adjusted for a few observations, where still too much noise was included. This means that half of the excess flux is removed (Fig. 4.3, bottom left). A mask file (Fig. 4.3, bottom right) containing all the selected pixels (as polygons) is created and saved in a standard regions file. Since this procedure is

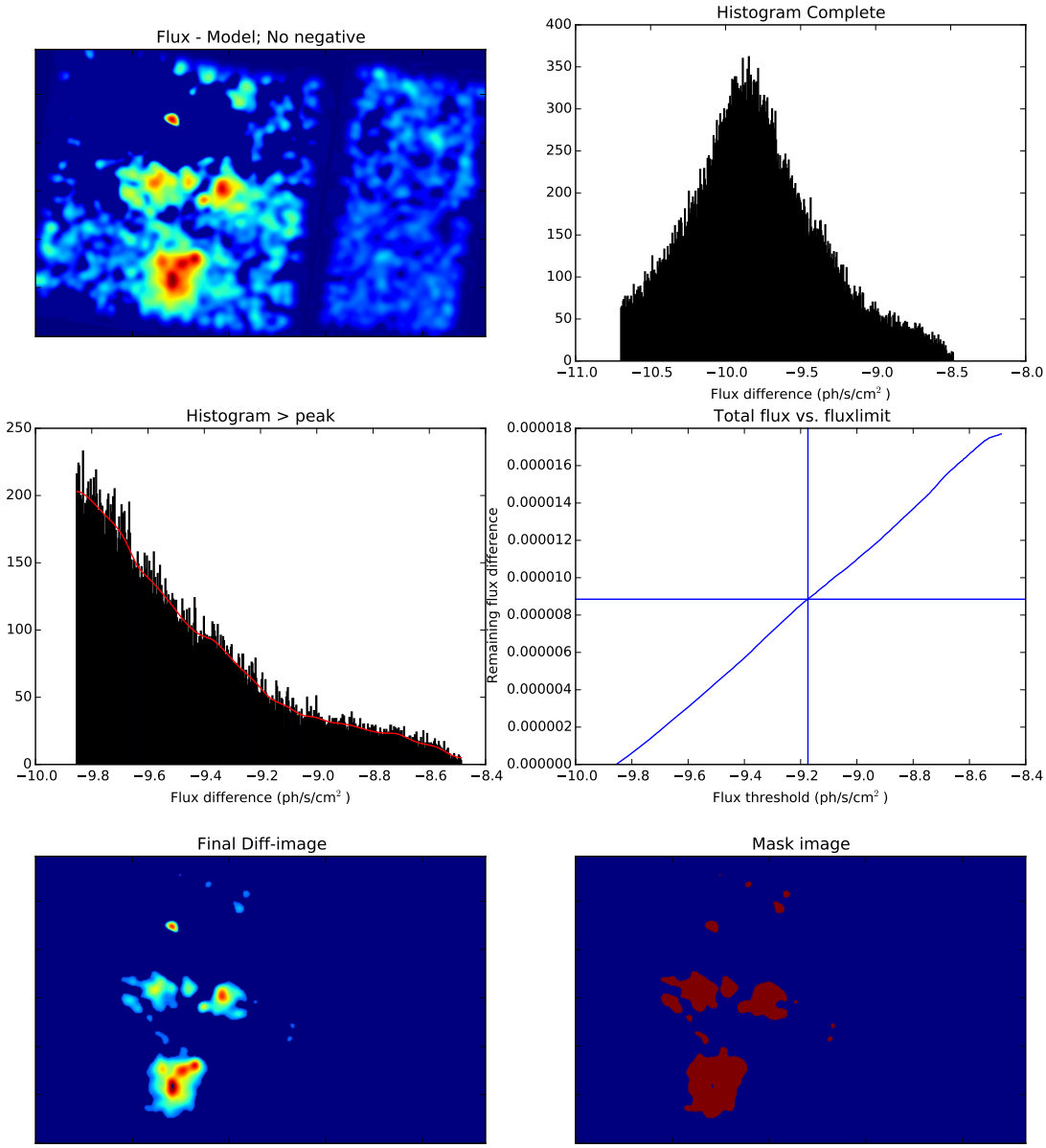

Figure 4.3: Substructure selection procedure for A85 (details see text).

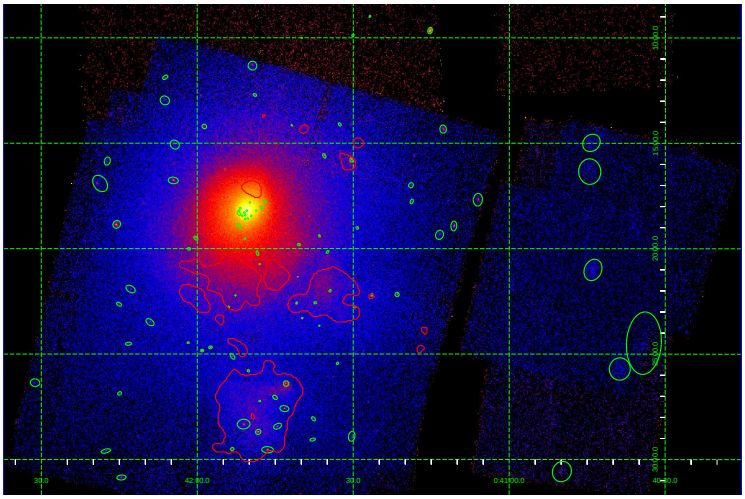

Figure 4.4: Mosaic image of all exposure corrected A85 observations that were used. Green ellipses mark the detected point sources, red polygons the substructure that has been marked.

very time consuming it is only done once per cluster for the longest exposure of a large part of the cluster (main observation ID).

Together with the combined point source region file, these are the regions that are being excluded for the spectral and surface brightness analysis in the following. One can see the final result, for Abell 85 in Fig. 4.4, which has some bright in-falling structure to the south.

4.3.4 Surface brightness and gas density profile

For an optically thin plasma the emissivity (Eq. 1.5) can be written as the product of the number densities of electrons n_e and Hydrogen atoms n_H and the cooling function Λ. The cooling function is a measure on how much energy is radiated by a plasma with a density of unity and depends on the electron temperature T_e and the abundance of heavy elements Z in the plasma. The surface brightness S_X has been defined in Eq. 1.4 and can be described as the flux of photons within a certain energy band and per solid angle. Combining these definitions one can write

$$S_X^\mathrm{phot} = \frac{L}{E_\mathrm{mean}\Omega 4\pi D_\mathrm{L}^2} = \frac{\int \epsilon \,\mathrm{d}V}{E_\mathrm{mean}\Omega 4\pi D_\mathrm{L}^2} \;, \tag{4.3}$$

where $\Omega = A/D_\mathrm{A}^2$ is the solid angle and E_mean is the emission weighted mean photon energy within an energy band,

$$E_\mathrm{mean} = h \cdot \frac{\int_{\nu_\mathrm{min}}^{\nu_\mathrm{max}} \nu\, \epsilon(\nu)\,\mathrm{d}\nu}{\int_{\nu_\mathrm{min}}^{\nu_\mathrm{max}} \epsilon(\nu)\,\mathrm{d}\nu} \;. \tag{4.4}$$

Inserting in Eq. 4.3 the definition of the emissivity gives

$$S_X^\mathrm{phot} = \frac{1}{E_\mathrm{mean}\,4\pi D_L^2\,\Omega} \int n_\mathrm{e}\, n_\mathrm{H}\, \Lambda(T_\mathrm{e}, Z)\mathrm{d}V = \frac{1}{E_\mathrm{mean}\,4\pi(1+z)^4} \int n_\mathrm{e}\, n_\mathrm{H}\, \Lambda(T_\mathrm{e}, Z)\mathrm{d}l \;. \tag{4.5}$$

Since the cooling function depends on the temperature which is variable across the cluster one cannot easily separate the Λ from the integral. Usually one chooses an energy band where the dependence of the cooling function on the temperature is very small, so one can calculate the gas mass from the surface brightness.

An analytic description derived from a King galaxy density model with isotropic velocity dispersion can

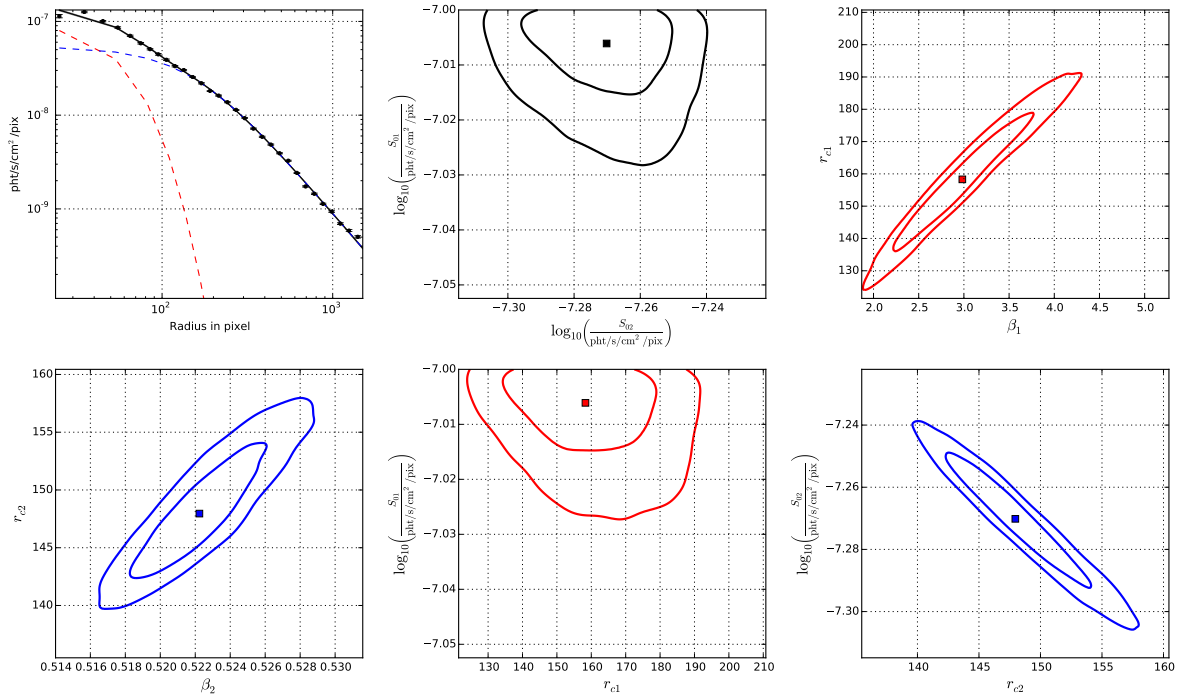

Figure 4.5: Surface brightness profile (excluding substructure) and constraints on double β model parameters for A85. Red corresponds to the inner component, blue to the outer one.

be given for the gas density distribution,

$$\rho_{\rm gas}(r) = \rho_{\rm gas}(0)\left(1+\frac{r^2}{r_c^2}\right)^{-\frac{3}{2}\beta} , \tag{4.6}$$

$$n_{\rm e}(r) = n_{\rm e}(0)\left(1+\frac{r^2}{r_c^2}\right)^{-\frac{3}{2}\beta} \tag{4.7}$$

The assumption entering here is a isothermal, ideal gas in hydrostatic equilibrium. By inserting 4.7 in 4.5 one can simplify this to

$$S_X^{\rm phot}(r) = \frac{1}{E_{\rm mean}4\pi(1+z)^4}\int \zeta n_{\rm e}^2(0)\left(1+\frac{r^2}{r_c^2}\right)^{-3\beta}\Lambda\,{\rm d}l \tag{4.8}$$

$$= S_0\left(1+\frac{r^2}{r_c^2}\right)^{-3\beta+0.5} , \tag{4.9}$$

where ζ is the ratio of Hydrogen and electron number densities.

For the double β model the procedure is more complex and has been presented in Hudson et al. (2010). While the two components of the surface brightness distribution are simply added up, for the density model the components are added in quadrature,

$$n_e(r) = \sqrt{n_{\rm e1}^2\left(1+\frac{r^2}{r_{c1}^2}\right)^{-3\beta_1} + n_{\rm e2}^2\left(1+\frac{r^2}{r_{c2}^2}\right)^{-3\beta_2}} , \tag{4.10}$$

where n_{ei} are the central electron densities of the two components.

As it can be seen in Fig. 4.5 (top left) the surface brightness profile is well fit by a double β model. Every radial bin in the surface brightness profile is usually calculated from several 1000 counts, only in very short observations of faint clusters from at least 70 counts, so a the Gaussian error distribution is a good

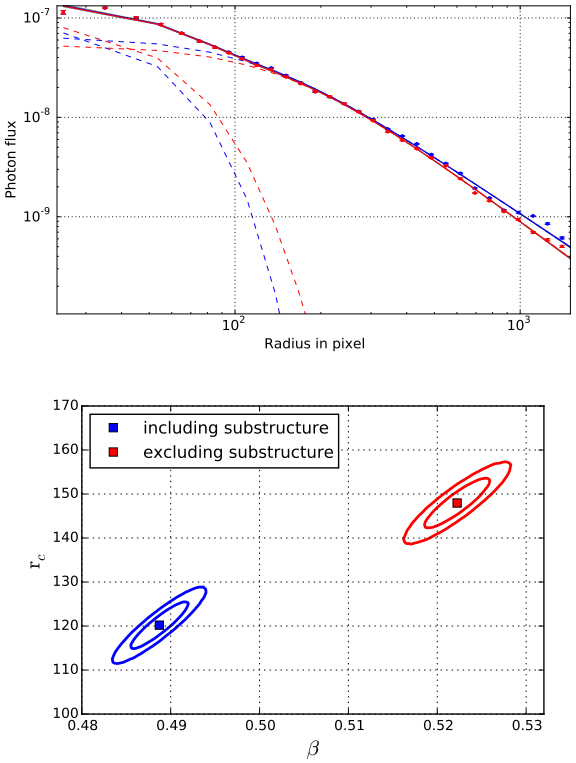

Figure 4.6: Impact on the surface brightness profile for A85 when including (blue) or excluding (red) the substructure described in Sec. 4.3.3. Point sources are excluded in both cases. 1 pixel corresponds to 0.492″. *Left:* Surface brightness profile in $\mathrm{pht\,s^{-1}\,cm^{-2}\,pix^{-1}}$, with the two components of the double β model indicated (dashed). *Right:* Constraints (68% and 95%) on β and the core radius (in pixel) for the outermost component of the double β model when including (blue) or excluding (red) the substructure in the fit.

approximation. The other graphs in Fig. 4.5 show that there exists a strong degeneracy between some double β model parameters. It is very important to take this degeneracy into account when calculating the total or gas mass from the surface brightness model, otherwise the uncertainties will be overestimated.

The impact of the substructure removal procedure is illustrated in Fig. 4.6. Especially the outer component of the model is affected by the substructure. If one would include substructure in the analysis, the total mass will be underestimated (in case the temperature would not be affected).

Cooling Function

As it has been indicated in the previous Section, one assumption to convert a surface brightness profile into a density profile (from Eq. 4.8 to Eq. 4.9) is that the cooling function does not depend on the radius, i.e. the cluster temperature or relative abundance of heavy elements is also constant with radius. The cooling function predicts the energy within a certain band which is radiated by a hot plasma and changes with composition and temperature per time. The units used here are $\mathrm{erg\,s^{-1}\,cm^3}$. Obviously the cooling function has to be calculated in the same energy in which the photon counts of the surface brightness have been measured.

An appropriate energy band is defined by the detector sensitivity and the emission characteristics of the source. Very common for X-ray instruments are the following bands:

- $(0.5 - 2.0)\,\mathrm{keV}$ – Chandra and XMM-Newton have a very high effective area in this band so it is often used for these instruments.
- $(0.1 - 2.4)\,\mathrm{keV}$ – This band was used for the ROSAT satellite, which was sensitive to softer energies. It is still used because many galaxy cluster catalogs are selected from the ROSAT All-Sky Survey.

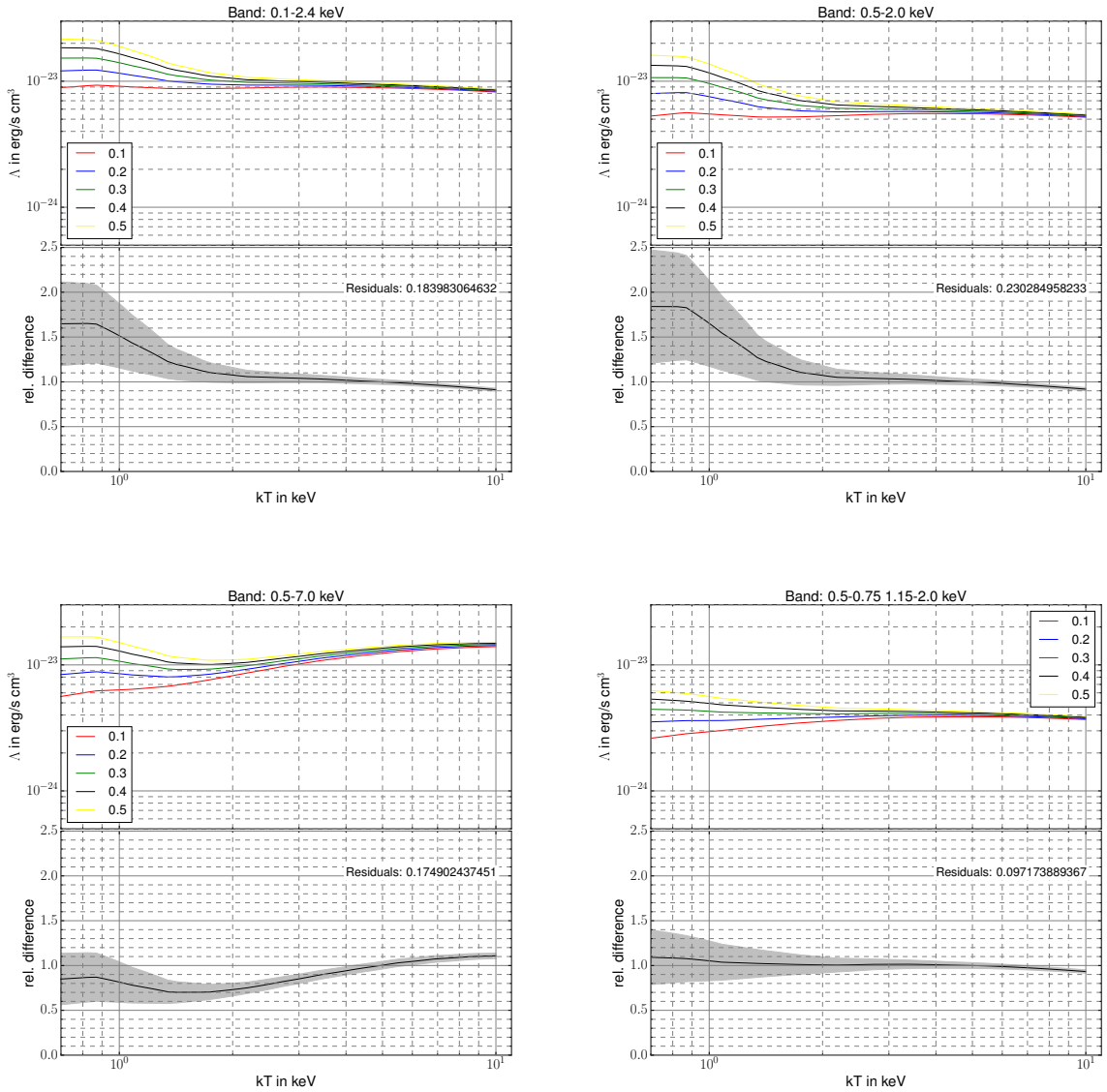

Figure 4.7: Cooling function in different energy bands for five relative abundances. Each lower panel shows the relative difference with respect to the value at 5 keV. In the lower right panel the cooling function in the optimal panel is plotted (see text for details).

It turns out that for plasma temperatures $> 2\,\mathrm{keV}$ the cooling function in the energy bands quoted above is almost constant with temperature/abundance, which can also be seen in the upper panels of Fig. 4.7.

The Fe-L line complex around 1 keV is very temperature and abundance sensitive. A combination of small bands below and above this feature turns out to be very insensitive to the plasma temperature even at temperatures below 1 keV. As it can be seen in the bottom right panel of Fig. 4.7 for a typical heavy element abundance of 0.3 the relative change in the cooling function is below 10% over the range from 0.7 keV to 6 keV. In the same temperature range the relative change of Λ in the $(0.1 - 2.4)\,\mathrm{keV}$ band is 4 times larger. The optimal energy band was determined by calculating the residuals of the cooling function to a flat distribution over $(0.7 - 10)\,\mathrm{keV}$ temperature range and the five relative abundances $0.1, 0.2, 0.3, 0.4$ and 0.5. These residuals are minimized and at the same time the average value of the cooling function maximized (to get more counts and better statistics). The resulting energy band was found to be the combination of the $(0.5 - 0.75)\,\mathrm{keV}$ band plus the $(1.15 - 2.0)\,\mathrm{keV}$ band.

Gas mass

The gas mass M_{gas} of the galaxy cluster is obtained by simply integrating the electron density profile Eq. 4.10 until r_{500} (which is iteratively calculated when deriving the total mass M_{tot} in Section 4.3.6),

$$M_{\mathrm{gas}} = 4\pi\xi \int_0^{r_{500}} n_e(r)\, r^2\, \mathrm{d}r, \tag{4.11}$$

where ξ is the ratio of the gas density ρ_{gas} and electron density n_e assuming a constant abundance of heavy elements:

$$\xi = m_{\mathrm{p}} \frac{1 + 2\left(\frac{n_{\mathrm{e}}}{n_{\mathrm{H}}} - 1\right)}{\frac{n_{\mathrm{e}}}{n_{\mathrm{H}}}} = m_{\mathrm{p}} \left(2 - \frac{n_{\mathrm{e}}}{n_{\mathrm{H}}}\right) \ , \tag{4.12}$$

where m_{p} is the proton mass and assuming a neutron to proton ratio of 1 in atoms (except Hydrogen), which is correct for most elements that are considered here (i.e. included in the abundance tables). Note that for heavier elements the number of neutrons increases. The ratio of electrons per Hydrogen atom is directly calculated from the abundance of the individual elements A_i,

$$\frac{n_{\mathrm{e}}}{n_{\mathrm{H}}} = 1 + 2 \cdot 0.083 + \sum_{i=3} A_i \cdot i \ . \tag{4.13}$$

0.083 is the Helium atom abundance. For the analysis I use the Asplund et al. (2009) solar abundance table and assume that all elements heavier than Helium have 0.3 solar abundances, which corresponds to $\xi \approx 1.144 \cdot m_{\mathrm{p}}$. The difference in ξ for 0.2 and 0.4 solar abundances is around 0.1%. Another quantity derived from the abundance of heavy elements which is of special interest, e.g., for the hydrostatic mass, is the mean molecular weight μ, which gives the average mass of a particle in m_{p} mass units,

$$\mu = \frac{\rho}{(n_{\mathrm{e}} + n_{\mathrm{ion}}) m_{\mathrm{p}}} = \frac{2\frac{n_{\mathrm{e}}}{n_{\mathrm{H}}} - 1}{\frac{n_{\mathrm{e}}}{n_{\mathrm{H}}} + \sum\limits_i A_i} \approx 0.59 \ . \tag{4.14}$$

The parameters of the surface brightness profile are calculated by a Markov Chain Monte Carlo simulation with 200 000 samples (out of which the first 50% are ignored), which also determine the uncertainty for the gas mass. The central value of the electron density is obtained from the spectrum of the innermost region outside 100 kpc in order to be clearly outside the possible emission of the BCG. This region (outside 100 kpc) was never distributed on more than one ACIS chip. For A85 the profile and the distribution of gas mass at r_{500} is shown in Fig. 4.8. Note that the uncertainty of $M_{\mathrm{gas}}(r_{500})$ is dominated by the uncertainty of r_{500}, which increases the M_{gas} uncertainty by a factor of roughly 10.

The gas mass is of particular interest for cosmology e.g., for f_{gas} test or as a calibrator for the total mass. The gas mass fraction $f_{\mathrm{gas}} = \frac{M_{\mathrm{gas}}}{M_{\mathrm{tot}}}$ can constrain the matter density of the Universe Ω_{m} assuming a Baryon density Ω_{b} (e.g., from CMB measurements or Big Bang Nucleosynthesis data). This has been shown initially by White et al. (1993b) and more recently by Mantz et al. (2014). Note that the uncertainties of

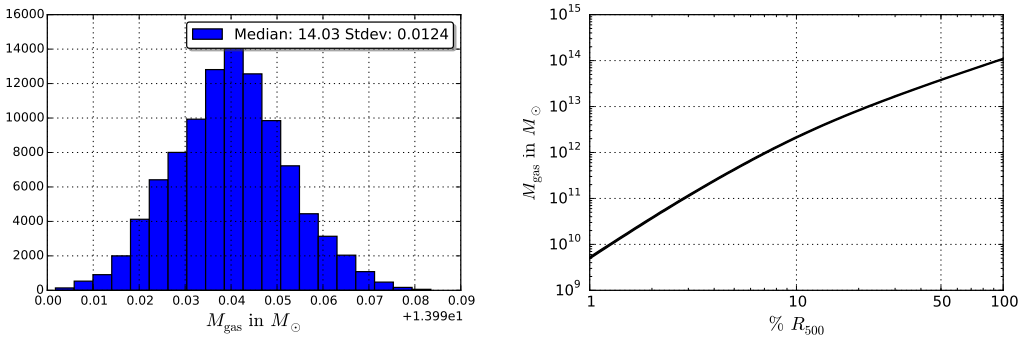

Figure 4.8: $M_{\rm gas}$ of A85. *Left:* Distribution of the gas mass at r_{500}. The values are in $\log_{10}$. *Right:* Mass profile as fraction of r_{500}.

the total and gas mass, which both enter in $f_{\rm gas}$, are both strongly dependent on the uncertainty of the radius. So the uncertainty of the gas mass fraction might be smaller. The gas mass can also be used as a tracer for the total mass which experiences low scatter (Zhang et al., 2008; Vikhlinin et al., 2009a).

4.3.5 Temperature

The temperature of galaxy clusters is crucial for the hydrostatic mass determination. Not only the value of the temperature is important but also the slope of the profile at the radius of interest enters, which makes an appropriate parametrization essential. But first I describe how to extract and model the spectra of X-ray observations.

Regions

For every observation of one cluster a counts image (OBS) and a background counts image (BKG) from the exposure corrected background file is created in the $(0.7-7)\,$keV band. Both images have point source and substructure removed. Spherical rings around the emission weighted cluster center (taken from Zhang et al., 2011a) are created based on a signal to noise threshold S/N,

$$\mathrm{S/N} = \frac{\mathrm{OBS}_i - \mathrm{BKG}_i}{\sqrt{\mathrm{OBS}_i}} \ , \tag{4.15}$$

where i denotes a certain region. Note that any OBS region contains the counts of the source and background. The minimum S/N threshold was set to 50 for all clusters, except for A3581, S1101 to 30 and for RXCJ1504, A400 and A1795 to 40, in order to get enough regions. For the bright cluster A2052 the threshold was set to 70. For a fixed aperture bright clusters would give very high S/N values, or in turn make the central regions very tiny. A high number of regions in the center would then give too much weight for the profile fit on the cluster center, which is not the primary target in this study. To avoid this I set a minimum size for a region of 25 arcsec. With this setup on average 30 regions are extracted per cluster, 17 regions on average per observation. The minimum number of regions per cluster is 8 (A1736 and EXO0422). The average maximum extraction region is 12.1 arcmin or 670 kpc, or compared to the r_{500} determined later, it is 66% on average. This means that most cluster profiles have to be extrapolated to calculate the $M_{\rm tot,500}$.

Spectral modeling

The spectral information is obtained from extraction of events within a certain region. One can describe the observed counts C as

$$C(PI) = T \int \mathrm{RMF}(PI, E) \cdot \mathrm{ARF}(E) \cdot S(E)\,\mathrm{d}E \ , \tag{4.16}$$

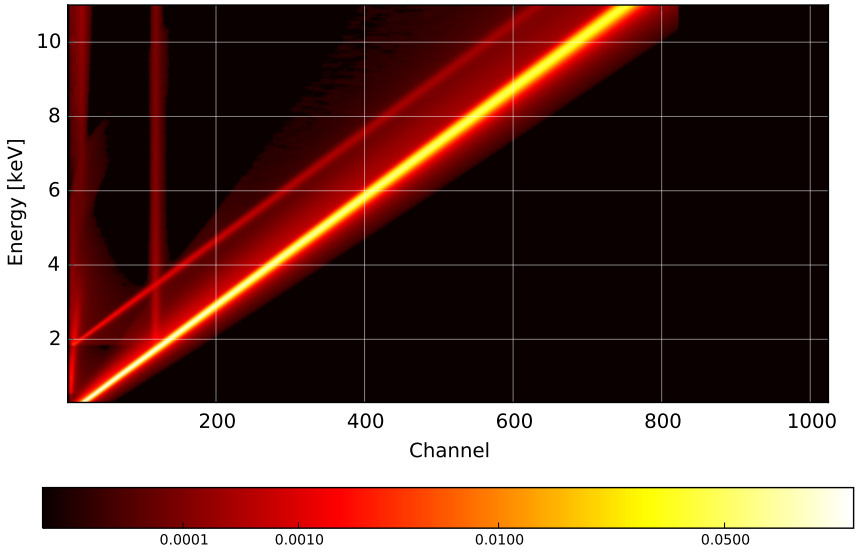

Figure 4.9: Visualization of the RMF. The colorbar values represent the detection probability density of a given photon energy in a certain detector channel.

where the response is split up into a unitless matrix (RMF) and a vector (ARF) in units of area, S is the source (energy specific) photon flux (e.g., $\mathrm{pht\,s^{-1}\,cm^{-2}\,keV^{-1}}$), T the total observing time and PI is the detector channel. The detector response (RMF), which characterizes the conversion from input photon energy to detected CCD channel, depends on the detector position, the input photon energy E and the CCD channel PI. A visualization for the Chandra ACIS-I detector is given in Fig. 4.9, in which one can see that this is not just a diagonal matrix, but other features like the electron escape peak (parallel to the main diagonal at $\sim 1.7\,\mathrm{keV}$ higher energies) or the Si fluorescent line (vertical line at a channel corresponding to Si Kα line energy). The effective area (ARF) characterizes the summarized effects of geometric area of the telescope, reflectivity, vignetting and quantum efficiency and varies with detector position and energy (example given in Fig. 4.10). The $(0.7 - 7)\,\mathrm{keV}$ energy band used in this study makes up 94% of the total effective area. For galaxy cluster analyses this energy band is an appropriate choice since at energies below $0.5\,\mathrm{keV}$ the calibration is still uncertain and between 0.5 and 0.7 keV the effects of the uncertain Galactic absorption or solar wind charge exchange (SWCX) lines might bias temperature estimates. Also at energies above $7\,\mathrm{keV}$ the particle background becomes more and more dominant so the signal to noise ratio will decrease. Furthermore, in order to convert Chandra temperatures into XMM-Newton temperatures by using the scaling relations from Schellenberger et al. (2015), one has to use the same band.

To create the spectra and response files the `specextract` task from the CIAO 4.6 software package was used. Spectra were grouped to have at least 30 counts per bin, so the uncertainties on the count rates can assumed to be Gaussian.

For the spectral fitting the astrophysical background components are determined from a simultaneous fit to data from the ROSAT All-Sky survey[1] (Snowden et al., 1997). The extraction region for the ROSAT All-Sky Survey (RASS) data is an annulus from 0.7 to 1 degree around the cluster center (for NGC4636, NGC1399 and A3526 r_{500} is larger than 0.7 degree, so the RASS data was extracted from 1.5 to 2 degree). The particle background was directly subtracted from the Chandra spectra using the stow events files from an epoch close to the observation date. The stow events files are created when the ACIS detector is in a position where it is not exposed to the sky and the HRC-I camera is in the field of view. This configuration is also called event histogram mode (EHM). As shown by comparisons to dark moon observations only

[1] `http://heasarc.gsfc.nasa.gov/cgi-bin/Tools/xraybg/xraybg.pl`

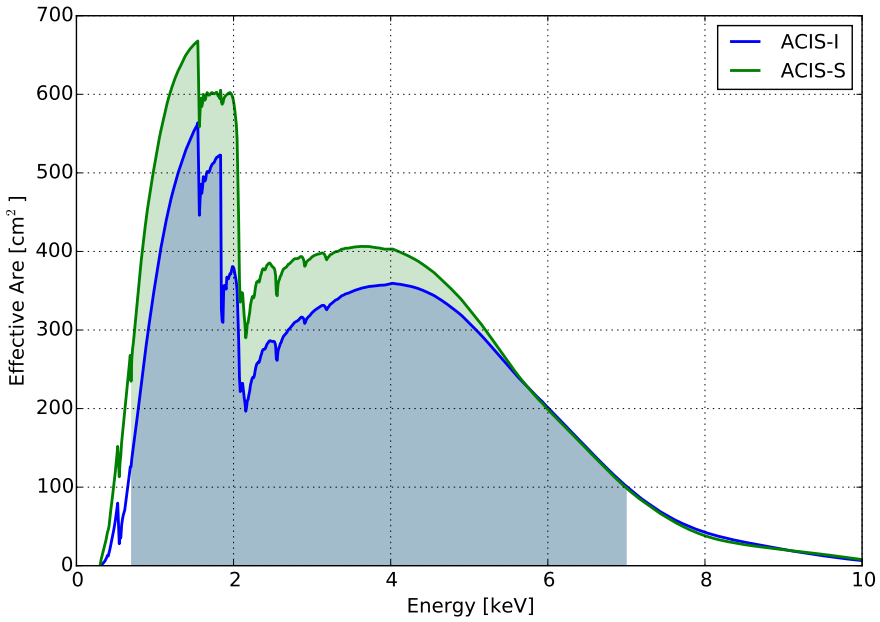

Figure 4.10: Chandra effective area as a function of energy for the two detector configurations (ACIS-I are front illuminated chips, ACIS-S back illuminated).

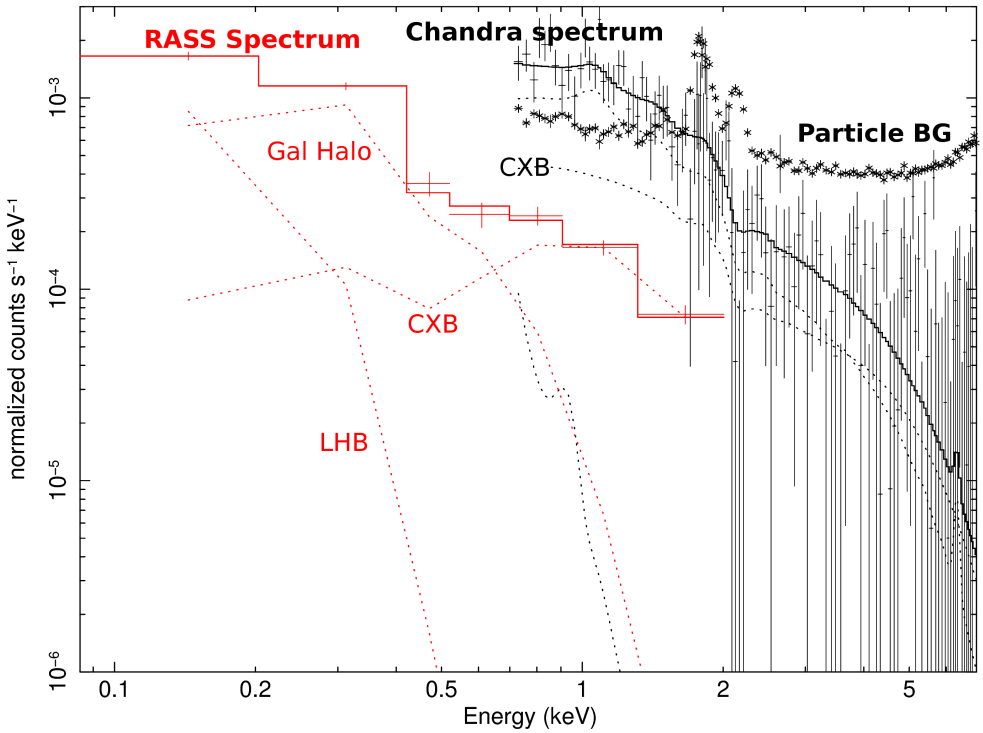

Figure 4.11: Chandra spectrum (black) of the outermost annulus of A85. The RASS spectrum (red) is used to constrain the foreground and cosmic background components. The level of the ACIS particle background is indicated by black asterisks.

particle events are recorded in the stow position (Markevitch et al., 2003; Wargelin et al., 2004). For each annulus the same detector region was used to extract the particle background spectra. These background spectra are normalized by the ratio of the $(9.5-12)$ keV band count rate of the observation and the stow events file to account for variations of the quiescent particle background component. The cluster emission is modeled by an absorbed thermal model (`phabs*apec`), where all parameters apart from the redshift and the $N_{\rm H}$ are left free to vary. The different background components are modeled as follows: The thermal emission of a hot plasma in the Galactic halo (GalHalo) has typical temperatures between $(0.15-0.3)$ keV. It is modeled by an absorbed thermal model with the temperature left free to vary and the abundance of heavy elements fixed to solar values. The local hot bubble (LHB), an hot relic in our Galactic neighborhood from the last supernovae, and SWCX (see Koutroumpa et al., 2011) is described by an unabsorbed thermal model with typical temperatures (free to vary) of around 0.1 keV and the metallicity set to unity. The cosmic X-ray background (CXB), mostly from unresolved AGNs, is the dominant astrophysical background component and can be modeled by an absorbed powerlaw with the photon index frozen to 1.41 (Kushino et al., 2002). For all background components, the normalization is left free to vary and the parameters are constrained in the simultaneous fit, but mostly by the ROSAT data.

Following Willingale et al. (2013) the hydrogen columns density used as a tracer for the X-ray absorption,

$$N_{\rm H\,tot} = N_{\rm HI} + 2\cdot N_{\rm H_2} = N_{\rm HI} + 2\cdot N_{\rm H_2 max}\cdot\left(1-\exp\left(-N_{\rm HI}\cdot\frac{E\,(B-V)}{N_{\rm c}}\right)\right)^{\alpha}\,, \tag{4.17}$$

where the parameters $N_{\rm H_2 max} = 7.2\pm0.3\times10^{20}\,{\rm cm}^{-2}$, $N_{\rm c} = 3.0\pm0.3\times10^{20}\,{\rm cm}^{-2}$ and $\alpha = 1.1\pm0.1$ were calibrated using X-ray afterglows of Gamma ray bursts. Both, the absorption $E(B-V)$ from the IRAS and COBE/DIRBE infrared dust maps (Schlegel et al., 1998) and the $N_{\rm HI}$ from Kalberla et al. (2005) are computed each cluster position. The combined effect of the uncertainties of these parameters, the scatter of this scaling relation (0.087) plus accounting for a 10% uncertainty on $N_{\rm HI}$ and $E(B-V)$ has only an 11% effect on $N_{\rm H\,tot}$, which typically affects best fit temperatures by 1%. Since this is much smaller than the typical total statistical uncertainties, any statistical uncertainty of $N_{\rm H\,tot}$ is neglected. For the relative abundance of heavy elements the Asplund et al. (2009) abundance table was used. For each observation all spectra from the different regions and chips[2] are fit simultaneously. The temperature and metallicity of spectra from the same region but different chips are linked together, while the normalizations are not because of calibration issues and variations in the surface brightness distribution. For all observations the `steppar` command was run on the temperatures. This task calculates the χ^2 for the parameter within a given range of values in order not to get best fit parameters of a local minimum of the likelihood distribution. The reduced χ^2 of all spectral fits was on average 1.03, while in 95% of the cases it was below 1.17. This gives a hint that the spectral modeling is appropriate.

Parametrization

With increasing radius of the selected region the S/N ratio decreases. The largest measured radius corresponds to the region just above the S/N threshold. For most clusters this threshold is smaller than r_{500}, so an extrapolation (e.g., using the parametrized profile) has to be performed. Furthermore, the gradient of the temperature profile enters in the hydrostatic mass equation, which makes it also necessary to parameterize the temperature by a model. Several models have shown to robustly model different types of temperature profile, e.g., where a cool core as well as the decreasing behavior to the outskirts is present. One set of models which is used in this work is given in Gastaldello et al. (2007):

The first model is the connection of two powerlaws,

$$\begin{aligned} T(r) &= \left(\frac{1}{t_1(r)^s}+\frac{1}{t_2(r)^s}\right)^{-\frac{1}{s}}\,, \\ t_i(r) &= T_{i,100}\left(\frac{r}{100\,{\rm kpc}}\right)^{p_i}\,,\ i=1,2\,. \end{aligned} \tag{4.18}$$

This model has 5 free parameters and can be used for low quality data or when the measurements are not

[2] The ACIS-I chips (0-3) are grouped together into a single spectrum.

reaching outer regions of the cluster (e.g, due to a very low redshift and the limited FOV). It was applied to three cluster profiles (A1795, NGC5044 and NGC4636).

The second model is a composition of two powerlaws smoothed by an exponential function,

$$\begin{aligned} T(r) &= T_0 + t_1(r)e^{-(r/r_p)^\gamma} + t_2(r)\left(1 - e^{-(r/r_p)^\gamma}\right) \ , \\ t_i(r) &= T_i \cdot \left(\frac{r}{r_0}\right)^{p_i} \ , i = 1, 2 \ . \end{aligned} \tag{4.19}$$

This model has 8 free parameters and can be applied to most of the clusters due to its many degrees of freedom. It was used 46 clusters, which have a median of 19 independent temperature bins per cluster.

The third model is a combination of the Allen et al. (2001) rising profile and an a falling profile.

$$\begin{aligned} T(r) &= t_1(r)e^{-(r/r_p)^\gamma} + t_2(r)\left(1 - e^{-(r/r_p)^\gamma}\right) \ , \\ t_1(r) &= a + T_1\left(\frac{(r/r_1)^{p_1}}{1 + (r/r_1)^{p_1}}\right) \ , \\ t_2(r) &= b + T_2\left(\frac{(r/r_2)^{p_2}}{1 + (r/r_2)^{p_2}}\right) \ . \end{aligned} \tag{4.20}$$

This model has 10 free parameters and is only applied to 15 clusters (with a median of 37 temperature bins per cluster). The three different models are shown on specific examples in Figure 4.12

Deprojection

The measured spectra contain information from all emitting sources along the line of sight. While the foreground and background components (e.g., particle background, galactic emission, unresolved AGNs) are either removed or modeled, the cluster emission within an annulus at an apparent radius from the cluster center is summed into the measured spectrum (see Fig. 4.13). Assuming a spherical symmetric cluster and that the outermost projected annulus is not significantly contaminated by emission from outer cluster shells, one can start to remove or account for this emission when fitting the next inner annulus. This is usually referred as the onion-peeling-technique (Fabian et al., 1981; Buote, 2000a; Gastaldello et al., 2007). I will describe several common ways to perform the deprojection with this method:

The Xspec model `projct` and the Sherpa model `deproject` use a model based approach. The spectra of all annuli are fitted simultaneously, while every annulus is fit with the same (thermal) model. Preferably one starts by freezing all other parameters apart from the last shell and fits of the outermost region. When then freezing these new parameters and fitting the next inner region, the model of the outer annulus emission is included. The area corresponding to each spectral extraction region can be set via header keywords. This procedure is continued until the cluster center is reached. Then the parameters can be thawed and the simultaneous fit is started. This procedure assures well tuned initial parameters for the final fit.

Unfortunately the method described above can lead to oscillations in the deprojected temperature profile, especially with high quality data, as it has also been reported by Fabian et al. (2006) and Russell et al. (2008). In Russell et al. (2008) the authors demonstrate a different approach by directly subtracting spectra: By taking the formula from Kriss et al. (1983) to calculate the fractional volume of an outer shell with radii R_1 and R_2 that is seen within an annulus with radii y_1 and y_2 (for example the overlap of the blue and red shaded area in Fig. 4.13),

$$V = \int_{y_1}^{y_2} \int_{\sqrt{R_1^2 - y^2}}^{\sqrt{R_2^2 - y^2}} 2\pi y \, \mathrm{d}x \, \mathrm{d}y = \frac{4}{3}\pi \left((p_1^3 - p_2^3) + (p_4^3 - p_3^3)\right) \ , \tag{4.21}$$

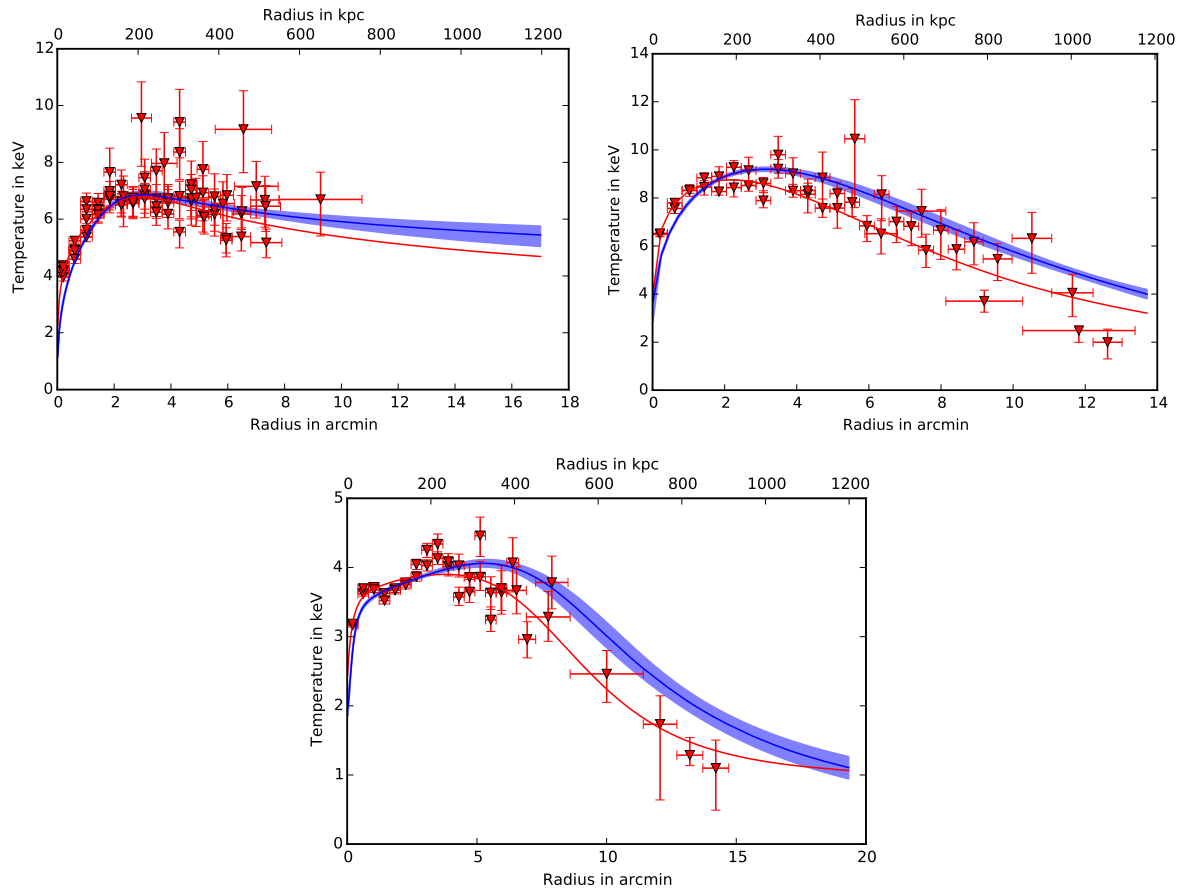

Figure 4.12: Temperature profile for A1795 (top left, model 4.18 with 5 free parameters), A2029 (top right, model 4.19 with 8 free parameters) and HydraA (bottom, model 4.20 with 10 free parameters). Red datapoints mark the observations, red lines the projected model fit and dark blue lines with the blue shaded area the deprojected profile (see Section 4.3.5) and its uncertainty.

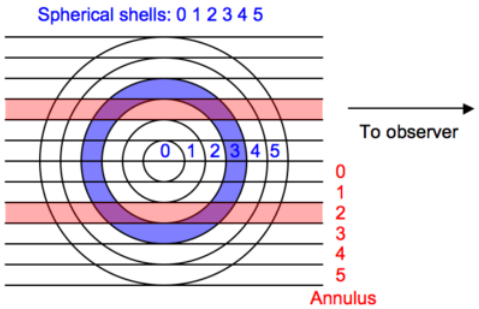

Figure 4.13: Illustrating the projection of cluster emission for different apparent radii. Taken from the sherpa website `http://cxc.harvard.edu/contrib/deproject`.

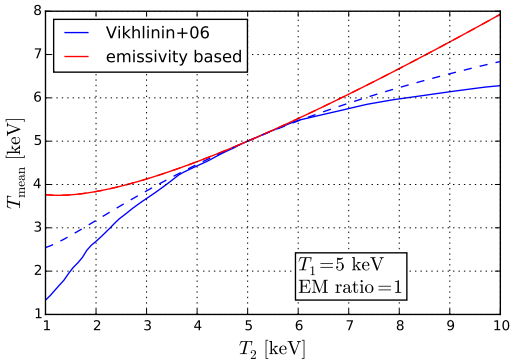

Figure 4.14: Comparison of the emissivity weighted temperature averaging (Lima Neto, 2005) and the Vikhlinin (2006) method using a two component plasma (with EMR= 1). The metallicity is 1 (solid) and 0.001 (dashed).

where p_i is given by

$$\begin{aligned} p_1 &= \sqrt{R_1^2 - y_2^2} \\ p_2 &= \sqrt{R_1^2 - y_1^2} \\ p_3 &= \sqrt{R_2^2 - y_2^2} \\ p_4 &= \sqrt{R_2^2 - y_1^2} \ , \end{aligned}$$

and if the argument of the square roots in p_i is negative, then $p_i = 0$. By dividing every spectral bin by the corresponding volume one can calculate a quantity proportional to the emissivity. In this way one can directly subtract all scaled spectra from outer annuli than the one of interest, to get rid of all projected outer shell emission. Unfortunately one needs a very high number of counts to ensure that no negative counts appear in any spectrum due to the subtraction. One could in principle regroup the spectra to achieve this, but in some cases this produced binning effects which biased the results.

A simple, analytic way to deproject the temperature profile, which requires a temperature parametrization is presented in Lima Neto (2005): Assuming the cluster emission is only free-free emission one can approximate the bolometric emissivity as

$$\epsilon \propto n_{\rm e}^2 T_{\rm e}^{\frac{1}{2}} \ . \tag{4.22}$$

Now one assumes that the measured temperature is just the temperature along the line of sight weighted by the emissivity, which is expressed by the surface brightness and 3D temperature. The integral to project the 3D temperature is inverted using the Abel integral (see also Kreye et al., 1993; Ciotti, 2000). This method is not appropriate for galaxy groups, because line emission starts to become more dominant at this plasma temperatures. Furthermore, the energy dependence of the effective area of the instrument does not justify the argument that the emission weighted temperature is equivalent to the measured projected temperature. Taking into account the response of the instrument to predict a projected (measured) temperature makes the deprojection procedure not analytically but only numerically possible to solve. Vikhlinin (2006) developed an averaging code that takes several plasma components (with each temperature, metallicity and emission measure) and calculates the corresponding single temperature that would be measured within a certain energy band for either Chandra ACIS, XMM-Newton EPIC or ASCA SIS/GIS. The emission measure, EM, in a cluster shell can be easily calculated from the density model,

$$EM = \int_V n_{\rm e} n_{\rm H} \, {\rm d}V \ , \tag{4.23}$$

where $n_{\rm e}$ and $n_{\rm H}$ are the electron and Hydrogen number densities, respectively, and V is the emitting volume. The difference to a simple emissivity weighted averaging can be seen in Fig. 4.14: For a two

component plasma with $T_1 = 5\,\mathrm{kev}$ and an EM ratio of 1 the emissivity weighting method overpredicts the "projected" temperature not only due to the missing line emission (see dashed line for $Z \approx 0$) but also because of the instrumental sensitivity, which for ACIS is highest between 1 and 2 keV (see Fig. 4.10). Other effects like absorption, redshift, the energy band and the redistribution (RMF), which are also taken into account by the Vikhlinin (2006) method, play a minor role.

I use the Vikhlinin (2006) method to deproject all cluster temperature profiles. In practice the parameters for the deprojected temperature profile are determined using a Markov Chain Monte Carlo with an adaptive Metropolis-Hastings algorithm as implemented in PyMC (Fonnesbeck et al., 2015). In each step the input temperature profile is projected along the line of sight at every radius that has a measurement. Each projected and measured temperatures (of all observations used for the cluster) are then compared assuming a Gaussian probability distribution of the measured uncertainties. After the first 50% of the samples are removed ("burn-in", samples that are needed to achieve convergence) each cluster still has 200 000 samples, which are used to characterize the deprojected temperature profile and its uncertainty.

Naively one might think that the deprojection plays a minor role since the mass estimates are performed at large radii ($\sim r_{500}$) where the projection effects are potentially weaker due to the lower number of outer shells and the flattening of the profile sometimes seen at larger radii (Pratt et al., 2007). But since the parametrization of the temperature profile at radii smaller than r_{500} is crucial for any extrapolation method the impact of the deprojection should not be neglected in a context of precision cosmology. Note that in Fig. A.1 to Fig. A.64 the deprojected and projected profiles should are not be directly related to each other, because the deprojected profiles do not use any information from the projected best fit.

4.3.6 Total Mass

Hydrostatic equilibrium

The total gravitating mass of a galaxy cluster is the most important parameter in cosmological study. Assuming that the ICM is in hydrostatic equilibrium, the total gravitational potential determines temperature and density of the gas. One can start with the simple requirement that the gravitational force (F_{grav}, toward the center of the cluster) and the force resulting from the gas pressure (F_{p}, acting against the gravity) balance each other:

$$F_{\mathrm{p}} = \mathrm{d}p\,\mathrm{d}A \stackrel{!}{=} F_{\mathrm{grav}} = -\frac{GM}{r^2}\mathrm{d}m \ , \tag{4.24}$$

where p is the pressure on an area A, G is the gravitational constant and M is the mass within a radius r. $\mathrm{d}m$ is a test mass element,

$$\mathrm{d}m = \rho\,\mathrm{d}A\,\mathrm{d}r \ , \tag{4.25}$$

where ρ is the gas density at radius r.

The two equations 4.24 and 4.25 simplify to

$$\frac{\mathrm{d}p}{\mathrm{d}r} = -\frac{GM}{r^2}\rho \ . \tag{4.26}$$

Solving 4.26 for M and using the ideal gas equation,

$$p = \frac{\rho k_{\mathrm{B}} T}{m_{\mathrm{p}}\mu} \ , \tag{4.27}$$

where k_{B} is the Boltzmann constant, m_{p} the proton mass and μ the mean molecular weight, one finally gets

$$M = -\frac{r^2}{G m_{\mathrm{p}}\,\mu\,\rho}\frac{\mathrm{d}(\rho \cdot k_{\mathrm{B}}T)}{\mathrm{d}r} \ . \tag{4.28}$$

Using the identity $x\,\mathrm{d}\ln x = \mathrm{d}x$ one can rewrite 4.28 into the well known hydrostatic equation,

$$M(<r) = -\frac{r k_{\mathrm{B}} T}{G m_{\mathrm{p}}\mu}\left(\frac{\mathrm{d}\ln\rho}{\mathrm{d}\ln r} + \frac{\mathrm{d}\ln T}{\mathrm{d}\ln r}\right) \ . \tag{4.29}$$

The assumptions that enter here are that gravity is the only external force (e.g., no magnetic fields, effect of the Dark Energy negligible), the cluster is spherical symmetric and the pressure behaves as in an ideal gas. Also μ in Eq. 4.27 must not depend on the radius r. Outside the core of galaxy clusters and excluding strong merging events these assumptions are generally fulfilled.

Since not only the gas but also the galaxies in clusters are affected by the total gravitational potential, one could use the velocity dispersion σ to estimate the cluster mass using the virial theorem,

$$2E_{\rm kin} = m\sigma^2 \stackrel{!}{=} -E_{\rm pot} = \frac{mMG}{r} \ . \tag{4.30}$$

This requires a large number of spectroscopic member galaxy measurements. Other independent methods are weak or strong gravitational lensing or measuring the Sunyaev-Zeldovich effect.

Using 4.29 the mass can be calculated in principle within any radius. In order to have a comparable quantity one usually defines M_Δ, which is the total mass within a sphere of radius R_Δ, inside which the mean density is Δ times the critical density of the Universe at cluster redshift $\rho_{\rm crit}(z)$ (see e.g., Bocquet et al., 2015). Δ is also called the overdensity and typical values are 500 or 200, sometimes also 2500. Note that with increasing values of Δ the radius and the total mass decrease. In the following the cluster masses will be compared to the prediction of the Tinker et al. (2008) halo mass function. Therein the halo mass function is given for 9 different overdensities in the range between 200 and 3200 with respect to the mean density of the Universe $\rho_{\rm mean}(z)$. The conversion between the critical and mean density is given by

$$\rho_{\rm mean}(z) = \Omega_{\rm m}(z) \cdot \rho_{\rm crit}(z) \ . \tag{4.31}$$

This means that $\rho_{\rm mean}$ has to be recalculated each time a new $\Omega_{\rm m}$ is being tested for a fixed overdensity of Δ_{500c}. For all parameters in Eq 2.52, A, a, b, c, which depend on the overdensity, second derivatives are provided that a spline interpolation (Press et al., 1992) can be performed. For typical values of $\Omega_{\rm m}$ and low redshifts the interpolation allows to calculate values up to 1000 times the critical density, which means that even with the highest overdensity given for the halo mass function most HIFLUGCS masses still need to be extrapolated. Note that with increasing overdensity deviations from the universality of the mass function increase.

HIFLUGCS masses

Following the hydrostatic equation, all one needs for the total gravitating mass of a galaxy cluster is detailed (deprojected) temperature and density information. Both quantities are parametrized, as described before, and the parameters are determined using a Markov Chain Monte Carlo approach. So it is straight forward to calculate the total mass and its uncertainty by just using the saved Markov chains. The mass at a given overdensity (for HIFLUGCS at 2500, 500 and 200 times the critical density) is determined in an iterative way. To easily compare the masses to literature I use $500\rho_{\rm crit}$ as the default overdensity (apart from other reasons described before), which will be denoted as M_{500} in the following.

In the following I describe the four different extrapolation methods used for all HIFLUGCS clusters:

- "kT extrapolate": This is the most simple extrapolation by just using the temperature and surface brightness model. For small extrapolations this might provide still robust estimates but for cases where only $0.5r_{500}$ or less can be covered by the temperature profile, the uncertainties and systematics are probably underestimated, since the model is not physically motivated and at larger radii the galaxy cluster temperature does not necessarily need to follow the inferred behavior from inner regions.

- "NFW All": This extrapolation fits an NFW profile (Navarro et al., 1996, 1997) to the cluster mass profile within a radius, where temperature measurements exist. The NFW profile is a simulation motivated well established parametrization of the Dark Matter density profile,

$$\frac{\rho(r)}{\rho_{\rm crit}} = \frac{\delta_c}{(r/r_s)(1+r/r_s)^2} \ , \tag{4.32}$$

  where r_s is a scaling radius and δ_s a scale overdensity (see also Zhao et al., 2009; Ludlow et al., 2013,

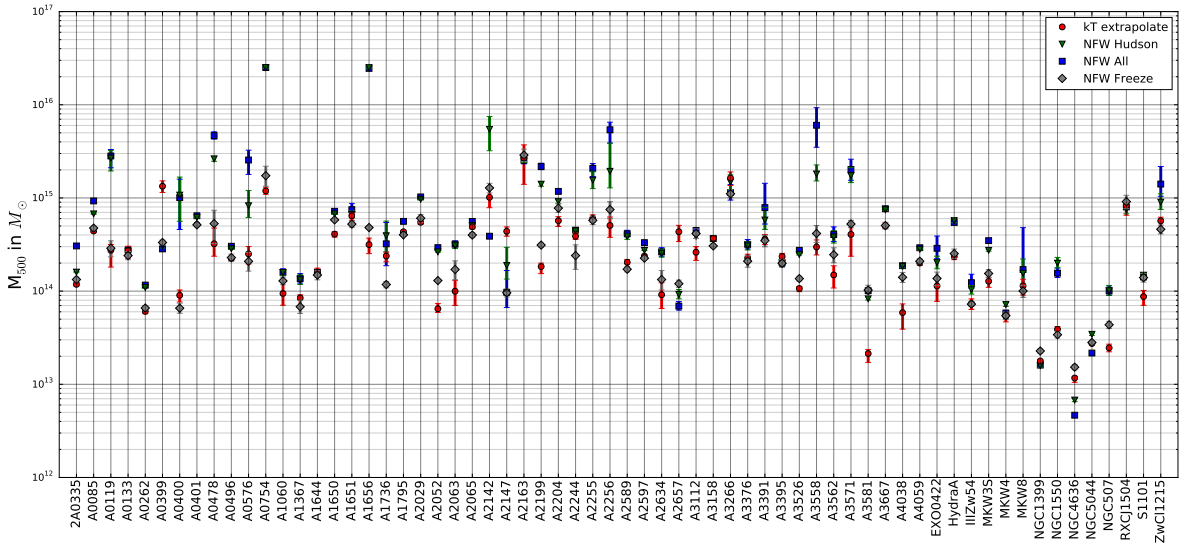

Figure 4.15: Total masses M_{500} of all HIFLUGCS galaxy clusters from the Chandra data using different extrapolation methods (see text for details).

2014). The scale parameters can be rewritten using a concentration parameter,

$$c_\Delta = \frac{r_\Delta}{r_s} \ , \tag{4.33}$$

where Δ is an overdensity with respect to $\rho_{\rm crit}$. The use of the overdensity 200 is a convention, but it is possible to use the NFW profile with respect to any overdensity, only then c should be labeled accordingly, e.g., c_{500}. It is then easy to conclude

$$\frac{c_{500}}{c_{200}} = \frac{r_{500}}{r_{200}} \ . \tag{4.34}$$

Ludlow et al. (2014) have shown that by integrating 4.32 one can write the total mass in terms of the concentration parameter,

$$M(<r) = \frac{Y\left(c_{200}\frac{r}{r_{200}}\right)}{Y\left(c_{200}\right)} \underbrace{200\rho_{\rm crit}\frac{4}{3}\pi r^3\left(\frac{r_{200}}{r}\right)^3}_{M_{200}} \ , \tag{4.35}$$

where $Y(u) = \ln(1+u) - u/(1+u)$. So the final fitting formula to extrapolate any radius to r_{500} is given by

$$M(<r) = \underbrace{M_{500}}_{\frac{4}{3}\pi r_{500}^3 \cdot 500\rho_{\rm crit}} \cdot \frac{Y\left(\frac{r}{r_{500}}c_{500}\right)}{Y(c_{500})} \ , \tag{4.36}$$

where only r_{500} and c_{500} are free parameters during the fit (again using an MCMC to account for the degeneracy between the parameters).

- "NFW Hudson": This method is almost identical to the "NFW All" case, only that the central region of the cluster mass profile is not taken into account for the NFW fit. In detail, radii smaller than the cool core radius as defined for HIFLUGCS in Hudson et al. (2010) are excluded. This is motivated by the fact that in the cool core region there might not be hydrostatic equilibrium (e.g., due to the central AGN) and the inferred mass should be taken carefully. This is not a problem for the measurements in the outer regions since no measurement from the cool core region affects

the outer mass determination (temperature and density models have enough degrees of freedom to account for a cool core).

- "NFW Freeze": In this case also an NFW model is fit to the outermost measured mass profile (i.e., the last 3-5 bins in the temperature profile), but a relation from Bhattacharya et al. (2013) between c_{200} and r_{200}, calibrated with simulations, is used to decrease the degrees of freedom:

$$c_{200} = \left(\frac{M_{200}}{2.519 \times 10^{22}\,\mathrm{M}_\odot} \right)^{-0.08} . \tag{4.37}$$

Equation 4.34 can be written as

$$\frac{c_{500}}{c_{200}} = \left(\frac{Y(c_{500})}{Y(c_{200})} \right)^{1/3} \left(\frac{200}{500} \right)^{1/3} , \tag{4.38}$$

which can be approximated numerically to derive a conversion between c_{500} and c_{200},

$$c_{500} = 0.7027 c_{200} - 0.0245 . \tag{4.39}$$

Inserting 4.37 in 4.39 one can derive a relation between c_{500} and M_{500}, which I again approximate numerically,

$$c_{500} = 0.056 \left(\log_{10} M_{500} \right)^2 - 2.18 \log_{10} M_{500} + 22.566 . \tag{4.40}$$

By applying 4.40 to 4.36 the only free parameter is r_{500}. These mass estimates are used as the default to derive cosmological parameters.

Figure 4.15 shows the determined total masses for the different extrapolation methods. *kT extrapolate* and *NFW Freeze* masses (red and gray datapoints) give realistic mass estimates, i.e. not too many masses above $10^{15}\,\mathrm{M}_\odot$, non of them above $10^{16}\,\mathrm{M}_\odot$, and also no mass estimate below $10^{13}\,\mathrm{M}_\odot$. *NFW Hudson* and *NFW All* (green and blue) give in very few cases unrealistically high masses (in two cases $> 10^{16}\,\mathrm{M}_\odot$, one of them Coma), while one case (NGC4636) is suspiciously low mass. The average uncertainty estimates are 14% (kT extrapolate), 13% (NFW All), 11% (NFW Hudson), and 11% (NFW Freeze). Most likely this is due to the degrees of freedom that the different cases imply: The NFW model in general puts constraints and leaves less possibilities for scatter as the extrapolated temperatures. NFW Hudson excludes the cool core and reduces the scatter. The NFW Freeze model first introduces more uncertainty for M_{500} by just using the outermost mass measurements for the extrapolation, but also restricts the concentration parameter, so the final uncertainty is comparable to the other methods.

Figure 4.16 shows the kT extrapolated masses compared to the other three estimates. It is clear that the NFW Freeze masses show best agreement and smallest scatter, while the other two methods give on average higher masses. Moreover, NFW Freeze (the default in the following) approach the kT extrapolated masses when the extrapolation is small or non existing (Fig. 4.16, bottom right). This is a consistency check that the measured hydrostatic masses (without extrapolation) more or less match the NFW Freeze masses. Note that the point with a measured r_{500} fraction ≈ 1.7 is A2244. The temperature could be constrained to far outer regions (see also Fig. A.30), because the ACIS-S observations covers the $15'$ offset with the S1 chip (BI).

HIFLUGCS luminosities

Many studies show that there is a correlation between the X-ray luminosity L_x and the total mass of a galaxy cluster that can be described by a powerlaw (e.g., Reiprich and Böhringer, 2002; Pratt et al., 2009; Vikhlinin et al., 2009a; Mantz et al., 2010a; Zhang et al., 2011a; Reichert et al., 2011). Also other quantities like the temperature of the gas or its mass show a correlation with the total mass and can be used as tracers for the total mass. Here I will focus on the luminosity, since it is the most simple quantity that can be derived for any galaxy cluster with known redshift. Especially for the all-sky survey by eROSITA (Merloni et al., 2012) most of the expected 100 000 galaxy clusters will only have a luminosity (with the redshift coming from optical follow-up observations). So this quantity is crucial and it needs to be understood in detail. The relation between the cluster mass and its luminosity can also be predicted

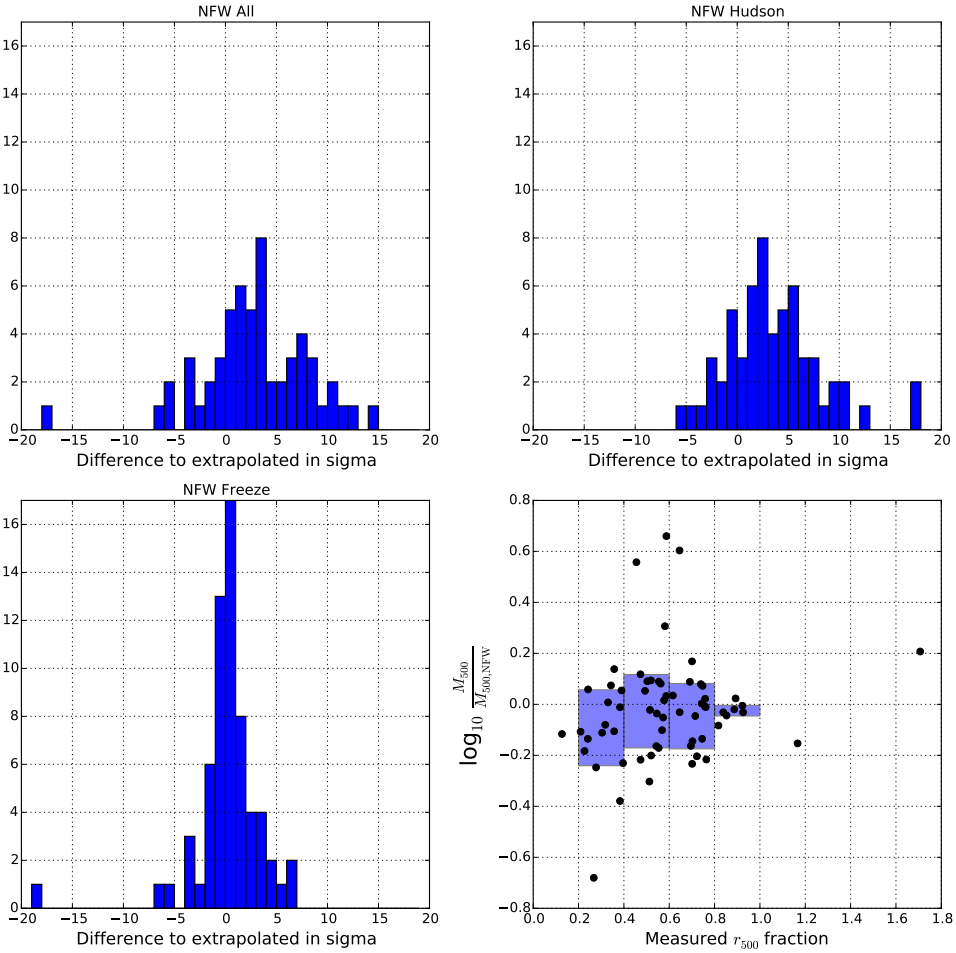

Figure 4.16: Comparison of the derived masses for HIFLUGCS. The top left, top right and bottom left panel show the difference in σ between kT extrapolated and NFW All, NFW Hudson and NFW Freeze masses, respectively. A negative significance means the kT extrapolated mass is larger. The bottom right panel shows the ratio of the kT extrapolated and NFW Freeze masses as a function of the largest radius that has temperature measurements (r_{500} from the NFW Freeze method). Blue shaded areas show the median and standard deviation.

from simple self-similar relations (Arnaud and Evrard (1999); Reiprich and Böhringer (2002); Pratt et al. (2009)): Following Arnaud and Evrard (1999) the luminosity can be written as

$$L(T) = f_{\mathrm{gas}}^2(T) \cdot M_{\mathrm{tot}}(T) \cdot \frac{< \rho_{\mathrm{gas}}^2 >}{< \rho_{\mathrm{gas}} >^2} \cdot \Lambda(T) \ , \tag{4.41}$$

where $<>$ denotes the volume average. Using virial equilibrium, $2E_{\mathrm{kin}} = -E_{\mathrm{pot}}$, and the isothermal β model, $\beta = \frac{\mu m_{\mathrm{p}} \sigma^2}{k_{\mathrm{B}} T}$, one gets $M \propto T\, R^{-1}$, where R is the virial radius. Since $R \propto M^{\frac{1}{3}}$ one concludes

$$M \propto T^{\frac{3}{2}} \ . \tag{4.42}$$

From the free-free emission it follows that $\Lambda_{\mathrm{bolo}} \propto T^{\frac{1}{2}}$, while in the ROSAT band the cooling function does not depend strongly on T for $T > 2\,\mathrm{keV}$. For the $0.5 - 2.0\,\mathrm{keV}$ band a similar behavior as in the ROSAT band is expected. If the gas mass fraction in 4.41 is constant and the fraction $\frac{<\rho_{\mathrm{gas}}^2>}{<\rho_{\mathrm{gas}}>^2}$, which describes internal substructure or clumping, is assumed to be independent of temperature, one immediately can

conclude

$$L_{\rm bolo} \propto M^{\frac{4}{3}} , \tag{4.43}$$

$$L_{0.1-2.4{\rm keV}} \propto M \tag{4.44}$$

As indicated in Pratt et al. (2009) observed slopes of the $L_{\rm bolo} - M$ as well as the $L_{0.1-2.4{\rm keV}} - M$ relation (1.8 for the bolometric case, 1.5 for the $0.1 - 2.4\,{\rm keV}$ case) are much steeper than expected from the self-similar prediction.

Furthermore, the luminosities are import for the cosmological analysis, since the cluster masses from the mass function need to have assigned a flux in order to follow the selection function (flux limit). A way to do this is to use a scaling relation. In Mantz et al. (2010a) it is demonstrated how the selection effects can bias the slope and normalization of the $L_X - M$ relation of a luminosity limited sample: Due to the intrinsic scatter fainter objects get detected with a lower probability, which makes the observed $L_x - M$ relation shallower. The prediction on how the $L_x - M$ relation of a flux limited sample would be affected is not trivial, but since the most clusters of the HIFLUGCS sample have a redshift around 0.05, one could first start with the simple assumption of a luminosity limited sample and expect the same trend of a steepening in the bias corrected $L_x - M$ relation. It has been shown in the past that the scatter in the $L_x - M$ relation is diminished significantly if the core region of clusters is excised or not accounted for (Pratt et al., 2009; Zhang et al., 2011a). So a smaller scatter is favored since selection effects should be minimized. But several remarks have to be made on the luminosities that were used in the end (Reiprich and Böhringer, 2002):

- The cosmological analysis requires consistency between the selection of objects and the assigned luminosities in the $L_x - M$ relation. The HIFLUGCS clusters were selected based on redetermined fluxes of a bigger sample with a lower flux limit, which ensures a homogeneous selection instead of just using fluxes from the catalogs. So the only way to stay consistent with the selection function is to use the luminosities from Reiprich and Böhringer (2002). Those luminosities are tabulated for the $(0.1 - 2.4)\,{\rm keV}$ band (source rest frame) and using a flat Universe with $H_0 = 50\,{\rm km\,s^{-1}\,Mpc^{-1}}$ and $\Omega_{\rm m} = 1$. So every time the cosmological parameters are varied the luminosities have to be recalculated. Additionally a K-correction has to be performed to account for the difference between the observed and the emitted energy band due to the redshift (see e.g., Jones et al., 1998, App. B).
- The Chandra FOV is too small to directly measure the luminosity of the clusters from the observed counts rates, especially for the low redshift objects.
- After more detailed X-ray data was available, RXCJ1504 was added later to the sample, since it was first falsely classified to have a strong AGN boosting the X-ray luminosity just above the flux limit.

4.4 Cosmology

4.4.1 Likelihood Function

As pointed out in the previous section, luminosities and the $L_x - M$ relation,

$$\log_{10}\left(\frac{L_x}{h^{-2}\,10^{44}\,{\rm erg\,s^{-1}}}\right) = A_{\rm LM} + B_{\rm LM}\cdot\log_{10}\left(\frac{M}{h^{-1}\,10^{15}\,{\rm M_\odot}}\right) \tag{4.45}$$

play a crucial role for the cosmological constraints. It is either possible that an external or a self consistently computed scaling relation (Reiprich and Böhringer, 2002) is used but fixed for the cosmological analysis. Although Mantz et al. (2010b) state that for low redshift, high X-ray flux samples the selection biases in scaling relations are small, this statement is not obvious and selection effects are taken into account in the following. A simultaneous fit of the $L_x - M$ relation in a cosmological analysis has been shown before, e.g., Allen et al. (2003). The cosmological analysis of the HIFLUGCS cluster sample follows the description of the likelihood function in Mantz et al. (2010b), Mantz et al. (2015) and Pacaud et al. (submitted), where selection effects are taken into account in simultaneous fit of the scaling relations. I summarize the important steps in this section.

In order to get grid of biases arising from binning the clusters in mass, flux, luminosity and/or redshift, one can do the transition to make this volume bins as small as possible, as done, e.g., by Mantz et al. (2008); Vikhlinin et al. (2009a). A corresponding likelihood function would then comprise a simple source counting within a Bayesian regression model:

$$\mathcal{L}(\hat{M},\hat{L},N_{\rm det}) = \underbrace{\frac{\langle N\rangle^N\, e^{-\langle N\rangle}}{N!}}_{\text{Poisson}} \cdot \underbrace{\frac{N!}{N_{\rm det}!\,N_{\rm mis}!}\, p^{N_{\rm det}}\,(1-p)^{N_{\rm mis}}}_{\text{Binomial}} \cdot \underbrace{\prod_{i=1}^{N_{\rm det}} \tilde{P}_i}_{\text{observational probability}} \quad . \tag{4.46}$$

The hat, $\hat{x}$, on parameters marks observed quantities. The first part is the Poisson likelihood for predicting $\langle N\rangle$ clusters with the halo mass function (without selection) while having N clusters in the Universe. The second term is a Binomial likelihood for detecting $N_{\rm det}$ clusters using the selection function out of the N clusters and missing $N_{\rm mis} = N - N_{\rm det}$ clusters in the sample. p is the probability for all the detected sources to be detected within the current constraints on the cosmology, scaling relation and selection function, while $(1-p)$ is the probability to miss $N_{\rm mis}$ sources. The last term is the probability for observing each individual cluster with its properties like mass and luminosity, so $\tilde{P}_i$ depends on the $\hat{M}$, $\hat{L}$, the parameters of the scaling relation and the selection criteria. Following the derivations in Mantz et al. (2010b), one can rewrite the parameters in the following:

$$\langle N\rangle = \int {\rm d}z\, \frac{{\rm d}V}{{\rm d}z} \cdot \int {\rm d}M\, \Omega_{\rm frac}(z,M) \cdot \frac{{\rm d}n}{{\rm d}M}\ , \tag{4.47}$$

where $\langle N\rangle$, as mentioned before, is the total number of predicted clusters and

$$\langle N_{\rm det}\rangle = \int {\rm d}z\, \frac{{\rm d}V}{{\rm d}z} \int {\rm d}M\, \Omega_{\rm frac}(z,M) \cdot \frac{{\rm d}n}{{\rm d}M} \int {\rm d}L \int {\rm d}\hat{L} \cdot \mathcal{N}(L,\hat{L},\sigma_{\hat{L}}) \cdot \mathcal{N}(L,L_{\rm LM},\sigma_{\rm LM}) \cdot P_I\ , \tag{4.48}$$

is the number of predicted clusters accounting for the selection function, where $\frac{{\rm d}V}{{\rm d}z}$ is the comoving volume element at redshift z, $\Omega_{\rm frac}(z,M)$ is the covered sky fraction (which is assumed to be constant for HIFLUGCS, but will be tested to depend on redshift or mass) and $\frac{{\rm d}n}{{\rm d}M}$ is the halo mass function (halo number density per mass, e.g., by Tinker et al., 2008). The fact that the sky fraction can depend on parameters like redshift or mass is a way to include a more complicated selection function without changing the luminosity integrals. L and $\hat{L}$ are "real" and observed luminosities, respectively. $\sigma_{\hat{L}}$ is the uncertainty (model) of the measured luminosities, which could in principle depend on flux or solid angle. $L_{\rm LM}$ is the luminosity coming from the $L-M$ relation and $\sigma_{\rm LM}$ is the scatter of the mass-luminosity function that is being used, which can also be variable during the cosmological fit. P_I is the selection function and in the most simple case considered here it can be identified with a heavyside step function (1 for clusters above the flux limit and 0 below), so here it will just depend on $\hat{L}$ and z. $\mathcal{N}(x,y,z)$ denotes the normal distribution probability density function at $x-y$ and with a standard deviation z. The probability function p in Eq. 4.46 can be identified by

$$p = \frac{\langle N_{\rm det}\rangle}{\langle N\rangle}\ , \tag{4.49}$$

where $P_{i,\,\rm det}$ is the probability to detect a cluster with certain *observed* quantities ($\hat{M},\hat{L},\hat{z}$,...),

$$\tilde{P}_i = \frac{1}{\langle N_{\rm det}\rangle} \int {\rm d}z\, \delta(\hat{z}_i) \cdot \frac{{\rm d}V}{{\rm d}z} \int {\rm d}M\, \Omega_{\rm frac}(z,M) \cdot \frac{{\rm d}n}{{\rm d}M} \int {\rm d}L\, \mathcal{N}(L,\hat{L}_i,\sigma_{\hat{L}_i}) \cdot \mathcal{N}(M,\hat{M}_i,\sigma_{\hat{M}_i}) \cdot \mathcal{N}(L,L_{\rm LM},\sigma_{\rm LM}) \cdot P_I\ , \tag{4.50}$$

where the redshift is assumed to be perfectly known (modeled by a delta function). $\hat{M}_i$ and $\sigma_{\hat{M}_i}$ are the measured total mass and its standard deviation, respectively. The probability for the missed sources is simply

$$(1-p) = \frac{\langle N_{\rm mis}\rangle}{\langle N\rangle}\ . \tag{4.51}$$

Putting all these derivations together one simplifies Eq. 4.46 to,

$$\mathcal{L} = \underbrace{\frac{\langle N\rangle^N}{\langle N\rangle^{N_{\rm det}}\langle N\rangle^{N_{\rm mis}}}}_{1}\ \underbrace{\frac{1}{N_{\rm det}!}}_{\text{constant}}\ \underbrace{\frac{\langle N_{\rm mis}\rangle^{N_{\rm mis}}\, e^{-\langle N_{\rm mis}\rangle}}{N_{\rm mis}!}}_{\text{for } N_{\rm mis}\in[0,\infty]=1} \cdot e^{-\langle N_{\rm det}\rangle} \prod_{i=1}^{N_{\rm det}} \langle N_{\rm det}\rangle \cdot \tilde{P}_i \ . \tag{4.52}$$

The third term is a Poisson likelihood which is equal to unity when marginalizing over $N_{\rm mis}$ from 0 to ∞. As indicated, only the last term depends on model parameters which gives the likelihood as in Mantz et al. (2010b, 2015),

$$\mathcal{L} \propto e^{-\langle N_{\rm det}\rangle} \prod_{i=1}^{N_{\rm det}} \langle N_{\rm det}\rangle \cdot \tilde{P}_i \ . \tag{4.53}$$

The implementation of this code is in `C` comprising also the CLASS source code (Lesgourgues, 2011a) to recalculate the transfer function for each cosmology. Most integrals are performed using the adaptive integration routines of `GSL` by Galassi et al.. Since the selection function is in the most simple case just a pure flux limit, one can rewrite the $\hat{L}$ integration in Eq. 4.48 and 4.50 into a complementary error function,

$$\mathrm{erfc}(x) = \frac{2}{\sqrt{\pi}} \int_x^\infty e^{-\tau^2}\, \mathrm{d}\tau \ , \tag{4.54}$$

$$\int_{L_{\rm min}}^{\infty} \mathcal{N}(L, \hat{L}, \sigma_{\hat{L}})\, \mathrm{d}\hat{L} = \frac{1}{2}\mathrm{erfc}\left(\frac{L - L_{\rm min}}{\sqrt{2}\sigma_{\hat{L}}}\right) \ . \tag{4.55}$$

The product of two normal distributions (both depending on L) can be expressed as a scaled normal distribution (see, e.e., Bromiley, 2003),

$$\mathcal{N}(L, \hat{L}, \sigma_{\hat{L}}) \cdot \mathcal{N}(L, L_{\rm LM}, \sigma_{\rm LM}) = \mathcal{N}(L, L', \sigma') \cdot \mathcal{N}\left(\hat{L}, L_{\rm LM}, \sqrt{\sigma_{\hat{L}}^2 + \sigma_{\rm LM}^2}\right) \ , \tag{4.56}$$

where

$$\begin{aligned} L' &= \frac{\hat{L}\sigma_{\rm LM}^2 + L_{\rm LM}\sigma_{\hat{L}}^2}{\sigma_{\hat{L}}^2 + \sigma_{\rm LM}^2} \ , \\ \sigma' &= \sqrt{\frac{\sigma_{\rm LM}^2\sigma_{\hat{L}}^2}{\sigma_{\rm LM}^2 + \sigma_{\hat{L}}^2}} \ . \end{aligned}$$

Since the nested integrals in 4.48 and 4.50 are computationally expensive, these simplifications to the luminosity integral make the code much more efficient. Furthermore, the computation of the likelihood was implemented using OpenMP[3] to run several threads in parallel.

4.4.2 MCMC and the Metropolis Algorithm

Markov chain Monte Carlo (MCMC, sometimes also called Markov Chain simulation) is a powerful tool to calculate the posterior distribution of a target. The posterior is the conditional probability distribution of the model parameters given the observed data. In Bayesian theory the posterior probability, $P(\theta|Y)$ can be written as

$$P(\theta|Y) = \frac{P(Y|\theta) \cdot P(\theta)}{P(Y)} \ , \tag{4.57}$$

where θ is the model, Y are the observations, $P(Y|\theta)$ is the likelihood, i.e. the probability for the observations given some model parameters, $P(\theta)$ are the priors, i.e. any restrictions on the model parameters and $P(Y)$ is a normalization constant. Equation 4.57 is also called Bayes' formula. The

[3] `www.openmp.org`

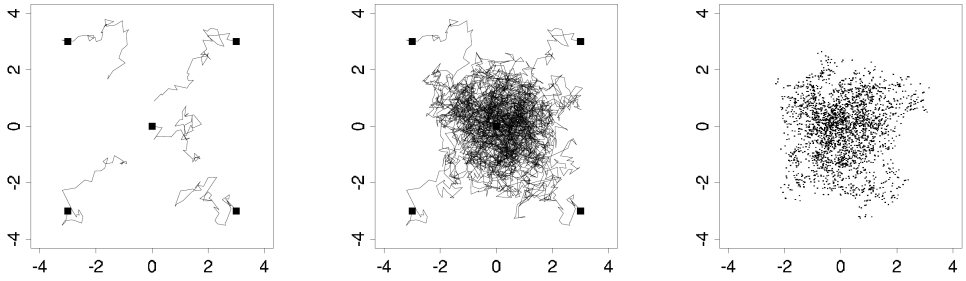

Figure 4.17: Example for an MCMC with five independent sequences. *Left:* After 50 iterations. *Center:* After 1000 iterations. *Right:* Second half of the samples shown in the center image. Taken from Gelman et al. (2013).

priors summarize the knowledge on the model before the data is known. When there is no further information, a simple prior could be a uniform distribution, but it can also comprise previous experiments and measurements. Simple examples for the likelihoods are a Poisson probability density for counting experiments or Binomial distribution for repeated binary experiments. In a Markov chain one starts a stochastic process, where the future state depends on the current state of the system, but not on past states. The random variables in the Markov Chain give a distribution that, with every new step, approximates the target distribution better. Markov chains generated by a Monte Carlo simulation are then called MCMCs.

The concept of MCMC is especially superior to time consuming methods, such as the evaluation of the parameter space on a grid, as soon as many (more than 2) parameters are involved, or to the Fisher matrix approach (which computes the Hessian at the maximum likelihood point in the parameter space) when the likelihood is not Gaussian near its maximum, i.e. parameters have complicated degeneracies. Useful references for Bayesian statistics and MCMC are Pawitan (2001); Gamerman and Lopes (2006); Gelman et al. (2013). In general an MCMC uses an algorithm to iteratively draw samples in order to approach the posterior distribution. Figure 4.17 shows an example with five independent samplers exploring the two dimensional parameter space. The starting points are indicated by squares and one can see that with more samples convergence can be achieved. Famous algorithms for a Markov chain Monte Carlo are the Gibbs sampler and the Metropolis-Hastings algorithm. In this work I focus on the *Metropolis* algorithm (Metropolis et al., 1953), which is a simple and powerful MCMC sampler. The idea behind the Metropolis algorithm is a random walk in the parameter space with an acceptance and rejection criterion for the new proposed points in order to reach convergence. The important steps are:

1. Choose a starting point θ_0 in the parameter space and calculate its posterior probability.

2. Generate a new proposal point θ_1 from a symmetric "jumping" distribution $\mathcal{J}$. This distribution should on the one hand give points at a reasonable distance in the parameter space so the chain does not evolve too slow, on the other hand jumps should not be rejected too often. In order to achieve a faster exploration of the parameter space allowed by the posterior distribution I use a multivariate Gaussian distribution for $\mathcal{J}$ with a covariance matrix calculated from a number of previous steps (usually 200). This procedure does not change the posterior distribution, but only increases the acceptance rate (see below). Another possibility to speed up the convergence is to use an adaptive algorithm, where the variance of $\mathcal{J}$ is tuned according to the current acceptance rate.

3. Calculate the posterior of the new point and compare it with the previous:

$$r = \frac{P(\theta_1|Y)}{P(\theta_0|Y)} \tag{4.58}$$

4. The new point θ_1 gets accepted if $r > 1$, i.e. the new point is more likely than the one before. If $r < 1$, the new point can still be accepted, if a uniform random variable $k \in [0, 1]$ is smaller than r. If $k > r$ the new point gets rejected and $\theta_1 = \theta_0$. Note that k changes with every sample and that even if a new point gets rejected, a new step is created which is identical to the previous point in the parameter space, i.e. it is possible that the chain is constant on one point in the parameter space for some time.

5. Continue with step 2.

So the Metropolis algorithm always accepts new points that increase and sometimes points that decrease the posterior, but in every step a new point in the chain is generated, even if it is identical to the previous point. The acceptance rate is the number of unique points within the chain divided by the total number of points.

For the cosmological application the metropolis algorithm was also implemented in `C`. The most time consuming part is obviously the calculation of the likelihood for every new set of parameters. In the following I describe the free parameters and their priors:

- Ω_m, the normalized matter density of today's Universe. It is set to a (flat) uniform probability distribution as prior with 0.05 and 0.5 as the lower and upper limits.
- σ_8, the amplitude of density fluctuations in the initial density field: Uniform prior with 0.3 and 1.2 as boundaries.
- A_LM, the intercept of the $L_x - M$ relation (see Eq. 4.45): Uniform prior with 0 and 2.8 as boundaries.
- B_LM, the slope of the $L_x - M$ relation (see Eq. 4.45): Uniform prior with 0.8 and 2.5 as boundaries.
- σ_LM, the scatter of the $L_x - M$ relation: Usually frozen to the scatter of the observed sample, but in some cases variable between 0.1 and 0.5 with a uniform prior.
- $(1 - b)$, the hydrostatic bias: Usually frozen to 1 (no bias), but in some cases variable between 0.5 and 1.1 with a uniform prior (see Section 4.5.3).

The following parameters were not variable during the cosmological analysis, because either the local halo mass function is not sensitive to them, or they are highly degenerate with other parameters for any galaxy cluster sample and need supplementary methods (e.g., primary CMB anisotropies) to be determined:

- H_0, the Hubble constant. It enters only for the calculation of the transfer function and is set to $70\,\mathrm{km\,s^{-1}\,Mpc^{-1}}$.
- Ω_b, the normalized baryon density of today's Universe. It is set to 0.0464.
- Ω_k, the spatial curvature parameter. It is set to 0, which implies a flat Universe.
- Ω_r, the radiation density of today's Universe, which is set to 0 for all calculations except the transfer function.
- w, the equation of state parameter for the Dark Energy. This is set to a constant value (no evolution term w_a) of -1 (Cosmological Constant).
- n_s, the scalar spectral index. It is set to 0.971.
- N_eff, the effective number of neutrino species. This is by default set to 3.046 (Dicus et al., 1982; Mangano et al., 2002; Lesgourgues and Pastor, 2006). One massive neutrino with $m_\nu = 0.06\,\mathrm{eV}$ enters in the calculation of the transfer function (Lesgourgues and Pastor, 2012, 2014).
- T_0, the CMB temperature. It is set to $2.725\,48\,\mathrm{K}$ (Fixsen, 2009). For the given parameters this means that the photon energy density $\Omega_\gamma = 5.0 \times 10^{-5}$ and the neutrino density $\Omega_\nu = 3.5 \times 10^{-5}$, so the total radiation density used for the transfer function is $\Omega_\mathrm{r} = 8.5 \times 10^{-5}$. More details are also given in Section 4.5.5.

The values are adopted from WMAP9 data (Hinshaw et al., 2013), unless stated otherwise.

The convergence of the chains was usually achieved after 500 to 3000 steps, so any setup was run for at least 15 000 steps. The first 3000 are usually classified as burn-in and deleted.

4.4.3 Cosmology from total Masses

As mentioned in the previous section, the default setup of the cosmological analysis is using the HIFLUGCS M_{500} masses extrapolated by an NFW model and freezing the concentration parameter c ("NFW Freeze", see Section 4.3.6). Luminosities are taken from Reiprich and Böhringer (2002) and accounted for the K-correction. The scatter of the $L_x - M$ relation is frozen to the observed value, 0.26 (more details see Section 4.4.4). The results for the four free parameters, $\Omega_\mathrm{m}, \sigma_8, A_\mathrm{LM}, B_\mathrm{LM}$, are shown in Fig. 4.18 and Tab. 4.1. One can see a high degeneracy between Ω_m and σ_8, which is very slightly deviating from

Setup	Ω_m	σ_8	A_LM	B_LM	σ_LM
default	$0.168^{+0.021}_{-0.019}$	$0.898^{+0.051}_{-0.048}$	$0.835^{+0.059}_{-0.059}$	$1.358^{+0.075}_{-0.073}$	0.26
σ_LM free	$0.166^{+0.022}_{-0.019}$	$0.903^{+0.054}_{-0.050}$	$0.836^{+0.064}_{-0.069}$	$1.331^{+0.067}_{-0.064}$	$0.248^{+0.025}_{-0.023}$
external $L_x - M$	$0.247^{+0.027}_{-0.025}$	$0.771^{+0.038}_{-0.037}$	0.99	1.62	0.178
Vikhlinin+09	$0.243^{+0.040}_{-0.036}$	$0.830^{+0.057}_{-0.054}$	$0.698^{+0.042}_{-0.043}$	$1.525^{+0.083}_{-0.081}$	0.18

Table 4.1: MCMC results for the free parameters from the cosmological pipeline for the different setups. Uncertainties are marginalized 68.3%.

an elliptical shape. The Pearson correlation coefficient (Pearson, 1896), is -0.89. The definition of σ_8 forces this degeneracy, since the RMS amplitude of fluctuations at a given mass, $\sigma(M)$, enters in the mass function and depends on Ω_m, the limit to a certain scale, σ_8, still depends on Ω_m (see also White et al., 1993a; Vikhlinin et al., 2009b).

Also a correlation between the slope and normalization of the $L_x - M$ relation (the larger the slope, the higher the normalization) can be detected (Pearson 0.81). A smaller degeneracy exists between Ω_m and the slope of the $L_x - M$ relation, B_LM, as well as for σ_8 and the slope or normalization (all three have a Pearson coefficient absolute value between 0.5 and 0.66). No degeneracy (Pearson 0.28) is found for Ω_m and the normalization. The chains (Fig. 4.18, bottom) show a very stable behavior where one can assume that convergence is found very fast. Testing the chains with different initial values (also far away from the potential best-fit) produces the same results, which indicates that one is not just mapping a local minimum of the likelihood function. Details on the $L_x - M$ relation are discussed in Section 4.4.4.

Another setup (also shown in Tab. 4.1 and Fig. 4.19) is to leave the scatter σ_LM free to vary. This introduces an additional degree of freedom, but does not change results. The uncertainties increase slightly in this case, but the best-fit scatter is in perfect agreement with the observed scatter, which was used in the default setup.

I perform one more test by fixing the $L_x - M$ relation, in this case to the bias-corrected one from Pratt et al. (2009), where luminosities were also calculated in the same energy band. In the $\Omega_\mathrm{m} - \sigma_8$ plane the confidence regions follow the main degeneracy of the default case, but shifted toward higher Ω_m.

A general sanity check for the analysis strategy was done by using the sample of Vikhlinin et al. (2009a,b) and compare the results on the cosmological parameters. The sample consists of a low and a high-redshift subsample: The low redshift sample has broad overlap with the HIFLUGCS sample and was constructed using the BCS, REFLEX and HIFLUGCS samples with the same criterion on the survey area as in HIFLUGCS. Fluxes have been redetermined in the $(0.5 - 2)\,\mathrm{keV}$ band using pointed ROSAT observations. The final fluxlimit is $1.3 \times 10^{-11}\,\mathrm{erg\,s^{-1}\,cm^{-2}}$ in this band and additionally a lower redshift limit of 0.025 was applied. This results in 49 galaxy clusters in this low redshift subsample. The high-redshift sample comprises 36 clusters from the 400d survey (Burenin et al., 2007) above redshift 0.35. In the following I only test the low redshift sample. Masses have been obtained by using either the gas mass M_gas, temperature kT, or $Y_x = kT \times M_\mathrm{gas}$ as a proxy. Scaling relations between these quantities and the hydrostatic mass have been calibrated using a low redshift, relaxed sample of 10 clusters (Vikhlinin et al., 2006). While the actual results on Ω_m or σ_8 do not depend on the choice of the mass proxy, Y_x is chosen as default. The cluster masses M_{Y_X} and luminosities of the low redshift subsample have been taken from this reference and tested with the cosmological analysis pipeline, accounting for the new selection and a new K-correction due to the changed energy band. As it can be seen in Fig. 4.19 and Fig. 3 in Vikhlinin et al. (2009b), the

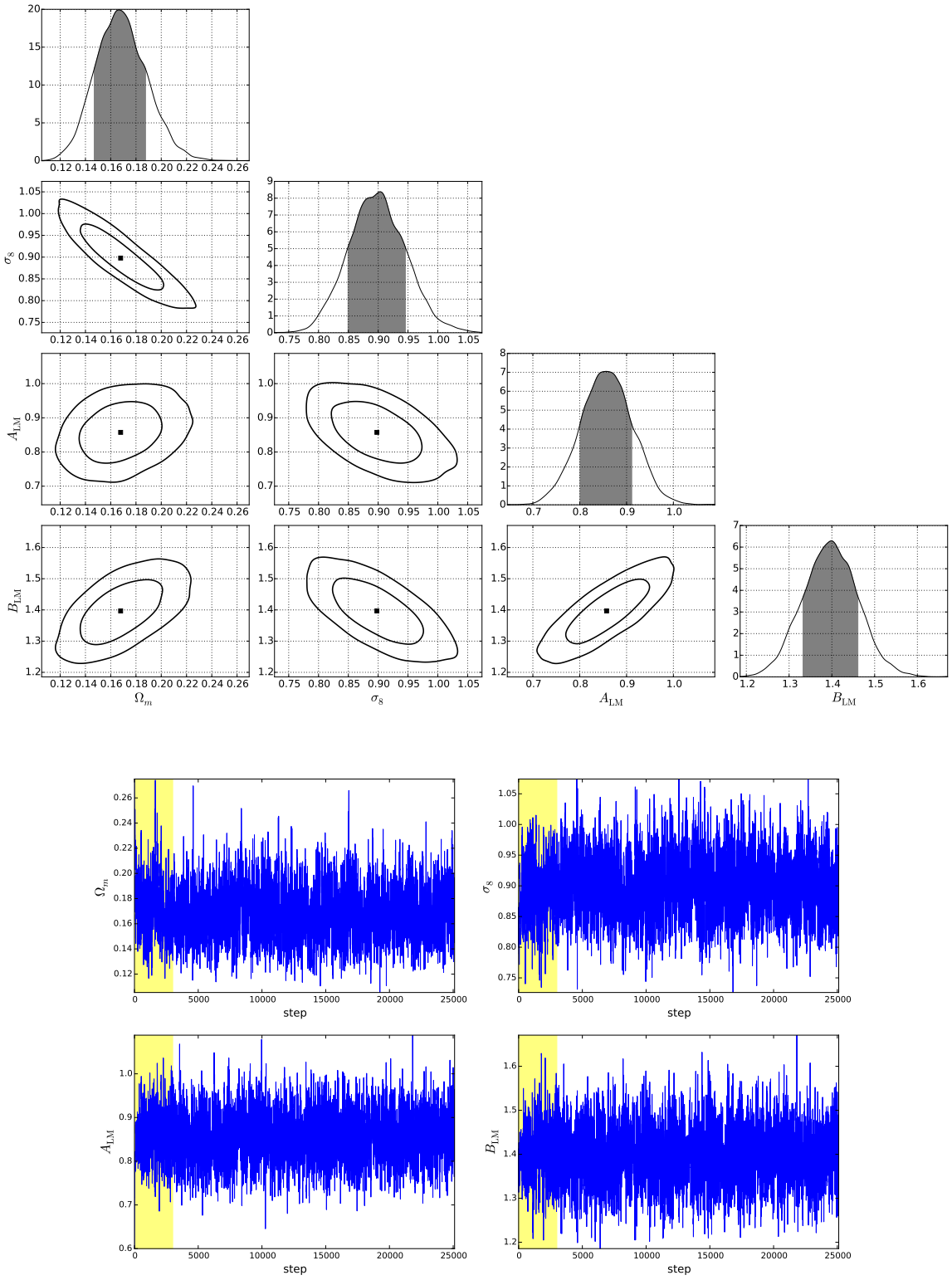

Figure 4.18: Results of the cosmology fit for the default setup: M_{500} with the "NFW Freeze" extrapolation. $\sigma_{\rm LM}$ is frozen to 0.26 (observed value of the scatter). The upper plot shows the degeneracy between and distribution of the four free parameters, $\Omega_{\rm m}, \sigma_8, A_{\rm LM}, B_{\rm LM}$. Below is shown the MCMC chain, with the burn-in phase marked in yellow. See text for more details.

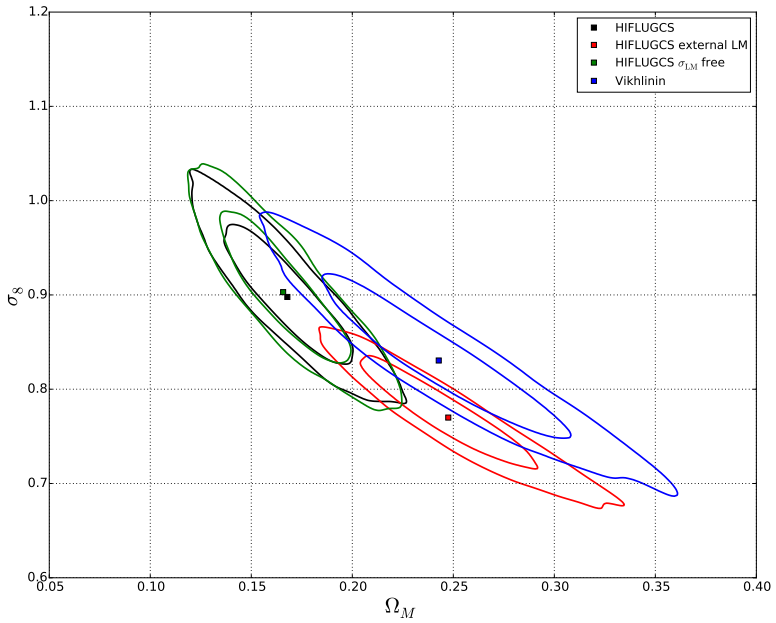

Figure 4.19: 68.3% and 95.4% confidence regions for $\Omega_{\rm M}$ and σ_8 for various analysis setups (see text for details).

results are in good agreement. Note that only the combination of both samples is shown in the reference figure, so perfect agreement is not expected, despite the differences in the analysis strategy. The reference results for the low redshift sample only are $\Omega_{\rm m} = 0.255 \pm 0.043$ and $\sigma_8 = 0.813 \pm 0.013$ at $\Omega_{\rm m} = 0.25$. Marginalization of σ_8 gives comparable uncertainties as quoted in Tab. 4.1.

4.4.4 $L_x - M$ relation

The results of the $L_x - M$ relation are of particular interest since they do not only enter in the cosmological analysis, but can be compared directly with references. Furthermore, the $L_x - M$ relation is an important tracer for total masses and cosmological results of, for example, eROSITA (Merloni et al., 2012), will rely it. Indications for a steepening at the galaxy groups scale have been raised in the past (e.g., Lovisari et al. (2015), but usually this is not modeled in a cosmological context. First I will start with a simple powerlaw description, also to be consistent with what has been done before (Reiprich and Böhringer, 2002; Vikhlinin et al., 2009b; Mantz et al., 2010a).

Equation 4.45 describes the relation between mass and luminosity. I do not include a redshift evolution term ($\propto E(z)$) since I am dealing with a low-redshift sample and any external constraints still exhibit huge scatter (e.g., Reichert et al., 2011). The observed distribution of mass and luminosity can easily be fit using a linear regression code that accounts for intrinsic scatter like BCES (Akritas and Bershady, 1996) or the Bayesian code by Kelly (2007). Furthermore, these algorithms take (symmetric) uncertainties of both parameters (x and y) into account. To minimize the bias when turning the original probability distribution of each mass and luminosity into logspace and identify it with a normal distribution (for symmetric errorbars), I first calculate the values in logspace of the upper and lower boundary and assign then the logspace uncertainty by taking the arithmetic mean of the individual uncertainties. In case of the luminosity, $y = \log_{10} L_x$, and L_x^u and L_x^l as the upper and lower boundaries, respectively, the following is done:

$$\Delta y = 0.5 \cdot (\log_{10} L_x^u - \log_{10} L_x^l) \ ., \tag{4.59}$$

and for the mass, x, accordingly. The intrinsic scatter is always measured according to y, $\sigma^y_{\rm intr} = \sqrt{(\sigma^y_{\rm tot})^2 - (\sigma^y_{\rm stat})^2 - B^2(\sigma^x_{\rm stat})^2}$, where $\sigma^y_{\rm stat} = \langle \Delta y \rangle$, $\sigma^x_{\rm stat} = \langle \Delta x \rangle$ and $\sigma^y_{\rm tot} = \sqrt{\langle y - A - B \cdot x \rangle}$, A and

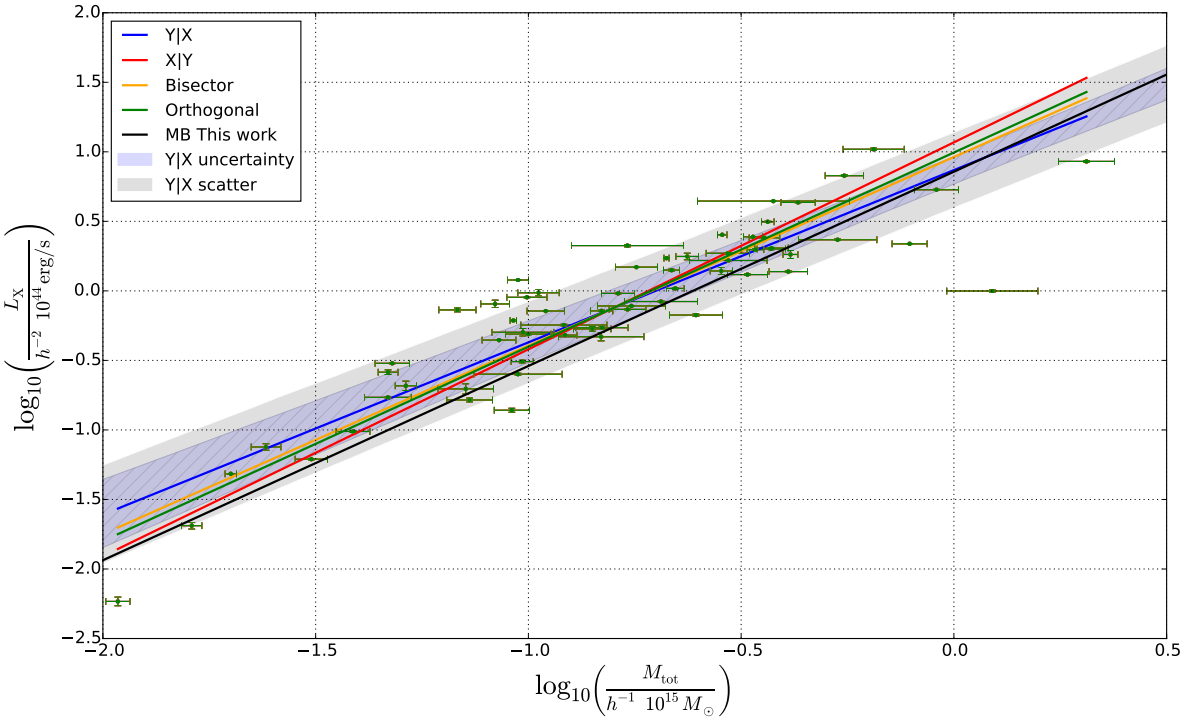

Figure 4.20: Comparison of the different BCES minimization methods for the observed $L_x - M$ relation. The blue shaded area (with hatching) shows the 68% uncertainty region for the Y|X method using only the normalization and slope uncertainties, while the gray shaded uncertainty regions includes the scatter.

B are the intercept and slope, respectively. So the scatter is assumed to be normal distributed in logspace.
The BCES code includes four different minimization schemes:

- $Y|X$: Regression of y on x, i.e. minimization in y direction.
- $X|Y$: Minimization in x direction.
- Bisector: Taking the linear relation that bisects the functions from $Y|X$ and $X|Y$.
- Orthogonal: Minimization in orthogonal direction on the best fit relation.

BCES	Slope	Norm	σ^y_{tot}	σ^y_{intr}
Y|X	1.24 ± 0.11	0.87 ± 0.10	0.26	0.25
X|Y	1.49 ± 0.09	1.07 ± 0.08	0.28	0.27
Bisector	1.36 ± 0.10	0.96 ± 0.09	0.26	0.25
Orthogonal	1.40 ± 0.10	1.00 ± 0.09	0.27	0.26
Kelly	1.26 ± 0.08	0.89 ± 0.07	0.26	0.25

Table 4.2: Values for the $L_x - M$ BCES fits using the default setup.

All these methods take into account the errors of both parameters and intrinsic scatter. For any linear regression of the $L_x - M$ relation I assume the uncertainties of the luminosity and mass to be uncorrelated.

Uncertainties on the best fit slope and intercept are taken from 10 000 bootstrap realizations[4]. Figure 4.20 and Tab. 4.2 show that the different minimization methods can give different results. The regression of y on x gives slightly shallower slopes than the minimization in x. These two methods mark the two extremes in terms of slopes and normalizations, the bisector (by definition) and the orthogonal method are in between and very similar. The uncertainty range based on the slope and intercept errors of the $Y|X$ minimization is shown in Fig. 4.20 by the blue hatched area, which slightly includes the bisector and orthogonal methods but not the $X|Y$ case. The gray shaded area represents the uncertainty of the best fit $L_x - M$ relation including the intrinsic scatter, which is so large that all other best fit relations are within this region.

I also tested the Bayesian linear regression code by Kelly (2007) which was implemented in python by Josh Meyers[5]. Andreon and Hurn (2012) have shown that a Bayesian regression seems to be more unbiased than least square methods like BCES. Table 4.2 also contains the results of this method using 50 000 MCMC steps, which show very good agreement with the BCES $Y|X$ method. The $Y|X$ regression will be chosen as default in the following, because it is frequently used in literature and the likelihood model also minimizes the luminosity deviation from the $L_x - M$ relation. The performance of the BCES code is clearly superior to the Bayesian method which requires an MCMC chain.

Compared to the observed $L_x - M$ relation the bias corrected one (both shown in Fig. 4.21) is slightly steeper, while the normalizations are in agreement. This is in agreement with the naive expectations of a Malmquist and Eddington bias for luminosity cut. As described in Mantz et al. (2010a) the Malmquist bias (intrinsic scatter leading to a higher probability of detecting brighter objects) lowers the observed slope. Since the mass function predicts more fainter objects, the Eddington bias (non-uniform distribution of objects) can lead to an increased slope. A flux limit instead of a pure luminosity cut and the combining the Malmquist and Eddington bias make predictions not straight forward, but usually a steeper slope is expected for the bias corrected relation. The bias corrected $L_x - M$ relation is in agreement with what is published in Reiprich and Böhringer (2002); Mantz et al. (2010a) (Fig. 4.21), while Vikhlinin et al. (2009a); Pratt et al. (2009) find significantly steeper relations. The lower normalization of the Vikhlinin et al. (2009a) $L_x - M$ relation in Fig. 4.21 is due to the slightly different energy band, $(0.5 - 2)$ keV, used therein, which should not affect constraints on the slope.

Since the Bayesian code runs an MCMC, parameter confidence levels can be plotted, as shown in Fig. 4.22. The center and right panel of this figure demonstrate that the scatter is perfectly consistent between the observed and bias corrected sample, which is also found, e.g., by Lovisari et al. (2015) for galaxy groups. The slope and normalization are not in agreement within the 68.3% range (left panel).

[4] The bootstrap methods picks N elements randomly out of a dataset of length N, so the distribution function of the dataset is not necessary.

[5] `https://github.com/jmeyers314/linmix`

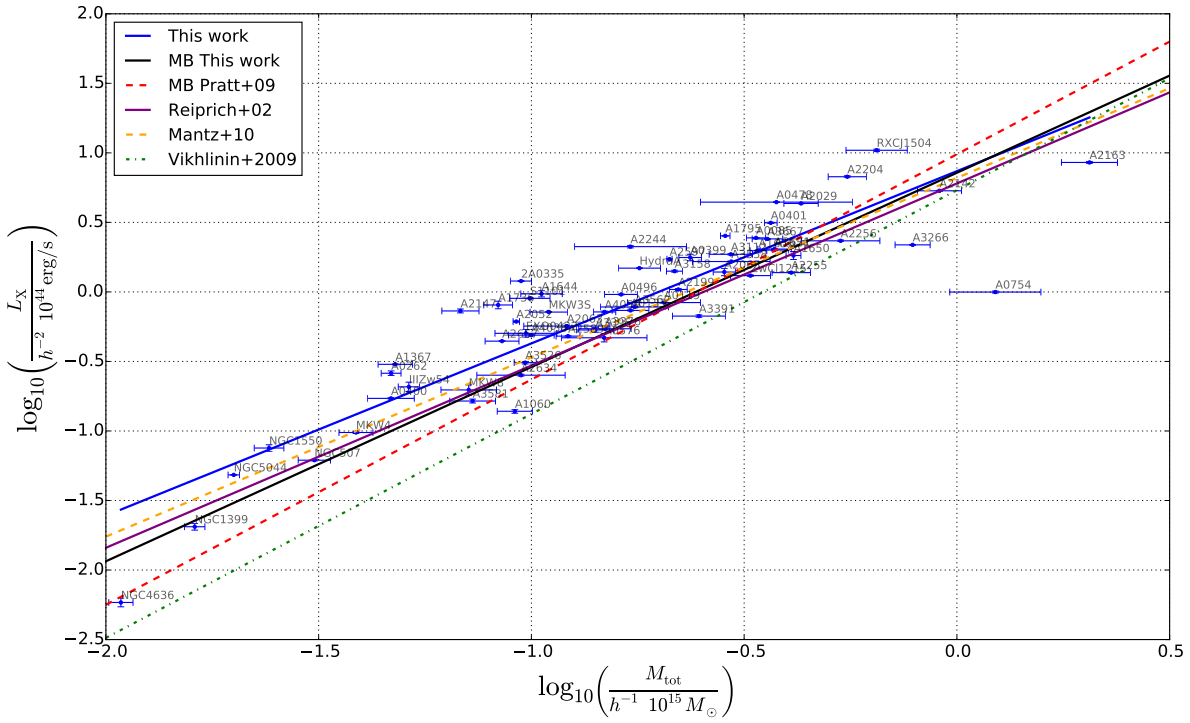

Figure 4.21: $L_x - M_{500}$ scaling relation, observed (blue) and bias corrected (black). Some scaling relations from references are also shown. "MB" indicates bias corrected relations. BCES fits (blue, red, purple) are done with the $Y|X$ minimization method.

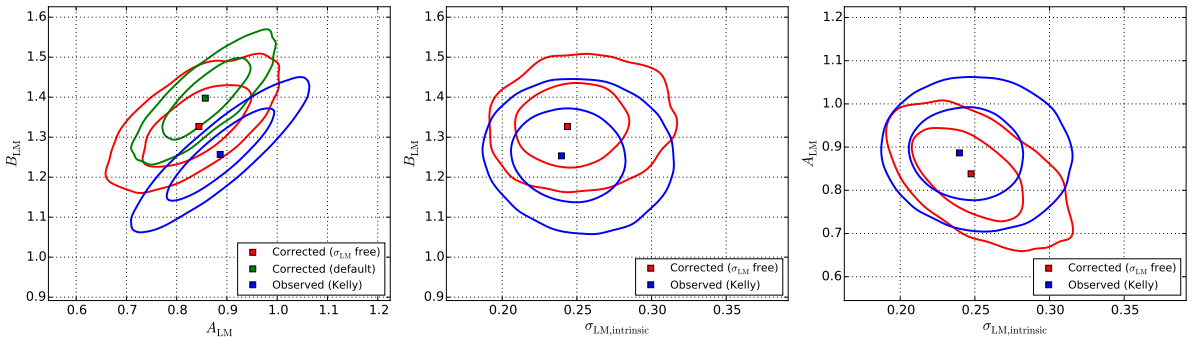

Figure 4.22: 68.3% and 95.4% confidence regions for the $L_x - M$ parameters of the observed (using Kelly (2007) algorithm) and corrected $L_x - M$ relation. *Left:* Slope vs. normalization for the observed and corrected (also with scatter free to vary) scaling relation. *Center/Right:* Slope/Normalization vs. scatter only for the cases with variable scatter.

4.4.5 Cosmology from Gas Masses

In Section 4.3.4 it has been shown that the cluster ICM mass (called gas mass) can be easily extracted from X-ray observations. Using both quantities, the total and gas mass, one can directly draw conclusions on the baryon fraction in the Universe (e.g., White et al., 1993b):

$$\frac{M_{\rm gas} + M_{\rm stars}}{M_{\rm tot}} \approx \frac{\Omega_{\rm b}}{\Omega_{\rm m}} \ , \tag{4.60}$$

where $M_{\rm stars}$ is the total stellar mass, which also contributes to the baryon budget. Observations (e.g., Ettori, 2003; Ettori et al., 2003) have shown that there exists a baryon deficit in clusters, which may be interpreted as undetected baryons or underestimated $\Omega_{\rm m}$. But equation 4.60 only holds, if the gas is distributed in clusters in the same way as in the Universe. Furthermore, the radius at which the masses are measured should not change the the gas mass fraction $f_{\rm gas}$. In reality processes like AGN feedback, cooling and star formation cause the gas to be pushed outside the potential wells. These effects are more dominant in galaxy groups than in clusters, so there might be a mass dependence of the potential baryon deficit.

Non-radiative simulations, including gravity, pressure gradiants and hydrodynamical shocks, by Eke et al. (1998) or Crain et al. (2007) predict that the baryon fraction within the virial radius of galaxy clusters is equal or close to the cosmic mean value inferred from CMB experiments. At smaller radii (e.g., r_{2500}) a depletion factor can be calculated. These correction factors have been used for cosmology, e.g., by Allen et al., 2002, 2008. As mentioned before, other physical effects like AGN feedback, can introduce an additional bias, which has been implemented in more realistic simulations, e.g., by Planelles et al. (2013) and Battaglia et al. (2013), used, e.g., by Mantz et al. (2014), who find $\Omega_{\rm m} = 0.29 \pm 0.04$ and consistency with a flat Universe.

From the CMB power spectrum one has a very precise measurement on the baryon density, $\Omega_{\rm b} = 0.022\,22\,h^{-2}$ (Planck Collaboration et al., 2015c). Due to the lack of appropriate simulations, Allen et al. (2008) modeled the stellar baryon fraction separately, which is now not necessary any more: Planelles et al. (2013) provide estimates for the gas mass fraction of galaxy clusters from simulations. They also modeled the radial, redshift and mass dependence,

$$f_{\rm gas}^{\Lambda{\rm CDM}} = Y_{\rm g}\, A^{\Lambda{\rm CDM}}\, \frac{\Omega_{\rm b}}{\Omega_{\rm m}} \left(\frac{d_{\rm A}^{\Lambda{\rm CDM}}(z)}{d_{\rm A}(z)} \right)^{1.5} \ , \tag{4.61}$$

where ΛCDM refers to the reference cosmology used for the gas and total mass calculation (flat ΛCDM model with $h = 0.71$ and $\Omega_{\rm m} = 0.3$). The ratio of angular diameter distances reflects the mass dependence on cosmology[6]. A is a correction factor to account for the fact that not a fixed radius but an overdensity is used to compute the masses, which changes according to cosmology,

$$A^{\Lambda{\rm CDM}} = \left(\frac{\theta_{2500}^{\Lambda{\rm CDM}}}{\theta_{2500}} \right)^{\eta} \approx \left(\frac{H(z)\, d_{\rm A}}{[H(z)\, d_{\rm A}]^{\Lambda{\rm CDM}}} \right)^{\eta} \ . \tag{4.62}$$

Allen et al. (2008) used this factor with a power $\eta = 0.214 \pm 0.022$, which is also applied here, although the influence is very small, i.e. $A \approx 1$. $Y_{\rm g} = \frac{f_{\rm gas}}{0.167}$ is the gas depletion factor. Planelles et al. (2013) used the WMAP7 (Komatsu et al., 2011) cosmology, which implies to $\frac{\Omega_{\rm b}}{\Omega_{\rm m}} = 0.167$. Following their description, the gas depletion factor can be written as,

$$Y_{\rm g} = Y_{0,{\rm g}}(1 + \alpha z) \left(\frac{M_{500}}{5 \times 10^{14}\,{\rm h^{-1}\,M_\odot}} \right)^{\beta} \left(\frac{\Delta}{500} \right)^{\gamma} \ , \tag{4.63}$$

where $Y_{0,{\rm g}}$ is the normalization, α the redshift dependence, β the mass dependence and γ the radial dependence. Priors on these parameters are adopted from their simulations (see Tab. 4.3). Note that I do not introduce any non-thermal pressure or mass calibration correction factors (like in Allen et al., 2008; Mantz et al., 2014), since this was also not done for the default mass function analysis and any comparison

[6] The power of 1.5 comes from the dependences $M_{\rm gas} \propto h^{-\frac{5}{2}}$ and $M_{\rm tot} \propto h^{-1}$.

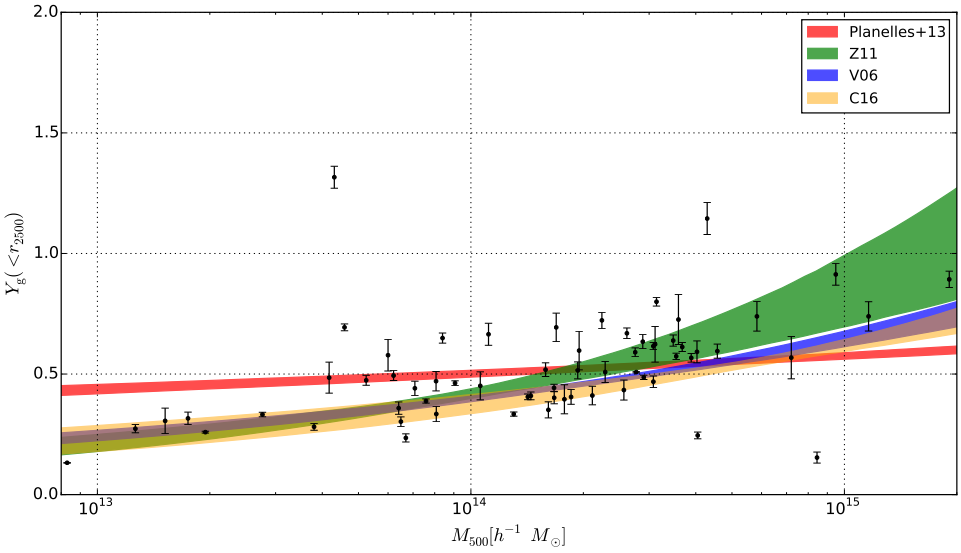

Figure 4.23: Mass dependence of th gas depletion factor ($\propto f_{\rm gas}$). 68% regions of hydrodynamical simulations including AGN feedback (red), observed samples by Vikhlinin et al. (2006); Arnaud et al. (2007); Sun et al. (2009) (blue), Sun et al. (2009); Zhang et al. (2011b) (green), Chiu et al. (2016) (yellow).

of results requires consistency.

I chose to measure the gas mass at overdensity 2500, which makes it necessary to extrapolate profiles for only less than half of the clusters. Furthermore, the total mass is measured from direct temperature profile extrapolation ("kT extrapolate"), to minimize the model influence which might enter with an NFW model. Figure 4.23 shows the measured $Y_{\rm g}$, i.e. the gas mass fraction diveded by 0.167 against the total mass at r_{500}. Despite the scatter there is general agreement with what was found by Sun et al. (2009); Zhang et al. (2011b)(Z11), also Vikhlinin et al. (2006); Arnaud et al. (2007); Sun et al. (2009)(V06) and Chiu et al. (2016)(C16), but disagreement at the group regime with the simulations by Planelles et al. (2013). Therefore I compute the cosmology from the gas mass measurements also with a mass cut of $M_{500} > 2 \times 10^{14}\, h^{-1}\, {\rm M}_\odot$. As mentioned in Planelles et al. (2013), physical processes become less important for rich clusters. The fit was performed using an MCMC with priors on 7 variables and leaving only $\Omega_{\rm m}$ with a uniform prior (see Tab. 4.3). The posterior results for the sample with mass cut (comprising 28

Parameter	Prior	Posterior	
		$M_{500} > 2 \times 10^{14}\, h^{-1}\, {\rm M}_\odot$	All clusters
$\Omega_{\rm m}$	$U(0.05, 0.8)$	$0.277^{+0.008}_{-0.008}$	$0.246^{+0.007}_{-0.007}$
h	$N(0.70, 0.022)$	$0.706^{+0.022}_{-0.021}$	$0.703^{+0.023}_{-0.022}$
$Y_{0,\rm g}$	$N(0.67, 0.01)$	$0.668^{+0.010}_{-0.010}$	$0.669^{+0.010}_{-0.010}$
α	$N(0.02, 0.02)$	$-0.002^{+0.020}_{-0.020}$	$0.010^{+0.020}_{-0.020}$
β	$N(0.06, 0.01)$	$0.057^{+0.009}_{-0.009}$	$0.310^{+0.003}_{-0.003}$
γ	$N(-0.12, 0.01)$	$-0.123^{+0.010}_{-0.010}$	$-0.121^{+0.010}_{-0.011}$
η	$N(0.214, 0.022)$	$0.214^{+0.022}_{-0.022}$	$0.214^{+0.022}_{-0.022}$

Table 4.3: 7 free parameters (with priors) for the $f_{\rm gas}$ test. $N(x, y)$ is a normal distributed prior with mean x and standard deviation y, while $U(v, w)$ is a uniform distributed prior with v and w as the lower and upper boundary.

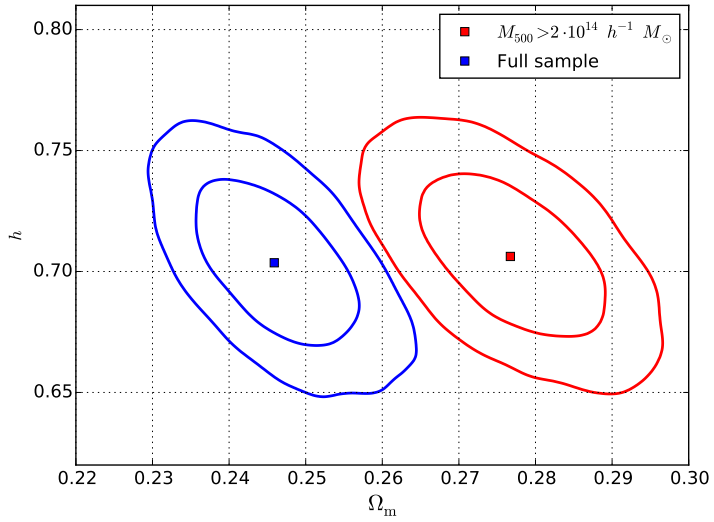

Figure 4.24: 68.3% and 95.4% confidence levels of the f_{gas} tests for Ω_m and h for the HIFLUGCS sample (with and without mass cut). f_{gas} was calculated at r_{2500}.

objects), shows excellent agreement with the priors, while Ω_m is significantly higher than in mass function cosmological analysis. Without the mass cut Ω_m is roughly 10% lower and the mass dependence of the depletion, β, is in strong tension with the prior input, but in agreement with Z11 ($\beta_{Z11} = 0.30 \pm 0.07$). There exist correlations (absolute of Pearson coefficient larger than 0.5) for Ω_m and h, Ω_m and γ, and Ω_m and $Y_{0,g}$. The first correlation is negative (the larger Ω_m, the smaller becomes h), while the latter are positive. I also tested the algorithm by artificially multiplying all f_{gas} values by 2 or 0.5. This leads to roughly halved or doubled Ω_m values, respectively, while the change for the other parameters is very small. This test was performed for both cases, with or without the mass cut and indicates that the best-fit determination of Ω_m is not biased by the priors on the other parameters.

4.5 Discussion

In this section I will discuss the main results I have presented before: The cosmological results of the HIFLUGCS galaxy cluster sample from the mass function and gas mass analyses as well as the $L_x - M$ relation. I will compare the results and draw conclusions for the possible differences.

4.5.1 Difference to WMAP9/Planck

As mentioned in Section 1.3, the CMB radiation originates from the recombination at a redshift ≈ 1100. Comprehensive summaries are, e.g., by White et al. (1994); Hu et al. (1997); Challinor (2013). Temperature fluctuations in the CMB originate from

- the earths movement relative to the CMB rest from (dipole anisotropy),
- the gravitational potential in which the electrons are located at last scattering (Sachs-Wolfe effect),
- Doppler shifts of the photons at last scattering,
- the fact that intrinsically hotter regions recombine later,
- Sunyaev-Zeldovich fluctuations.

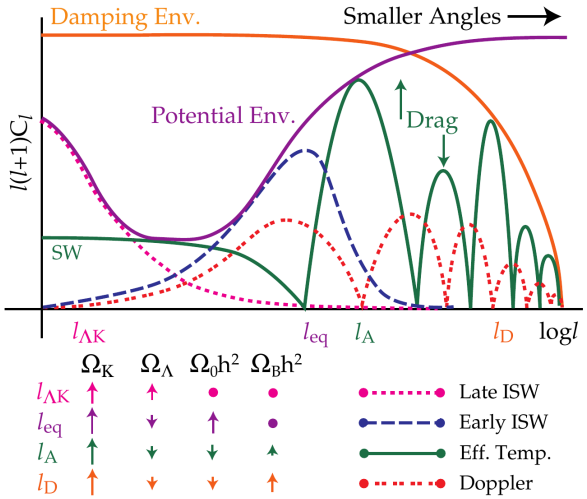

Figure 4.25: The CMB power spectrum showing different aniotropies in the CMB and their sensitivity to cosmological parameters. Note that here Ω_0 is the normalized matter density today (Ω_m). Taken from Hu et al. (1996).

After expanding the temperature fluctuations into spherical harmonics (Rich, 2001),

$$T(\theta,\phi) = 2.725 \pm 0.010\,\mathrm{K} + 3.358 \pm 0.020\,\mathrm{mK} \cdot \cos(\theta) + \sum_{l\geq 2,m} a_{l,m} Y_{l,m}(\theta,\phi)\ , \tag{4.64}$$

where the second term corresponds to the dipole anisotropy and l gives the temperature fluctuations on angular scales,

$$l \sim \frac{\pi}{\Delta\theta}\ , \tag{4.65}$$

one is able to identify the structures in this power spectrum with physical effects (see Fig. 4.25): At large angular scales (small l), the Sachs-Wolfe plateau sensitive to the curvature, Ω_k, and the matter density; the acoustic spacing l_A which provides the most precise constrain on the curvature; the Silk Damping at small scales (large l) which is sensitive to the baryon density.

So CMB experiments which measure temperature fluctuations at a large variety of angular scales can constrain several cosmological parameters with great precision and provide, additionally to galaxy clusters, another reference for the composition and evolution of the Universe. The two latest all-sky CMB temperature fluctuation measurements come from the WMAP satellite (9 year data; Hinshaw et al., 2013) and the Planck Satellite (Planck Collaboration et al., 2015c) and are compared to the HIFLUGCS cosmological results in Fig. 4.26. One great advantage of combining different measurements is to eleminate the degeneracy, e.g., of Ω_m and σ_8. The WMAP9 and HIFLUGCS (default) results exhibit small overlap, while the Planck 2015 results are shifted toward larger Ω_m. In the following I focus on a comparison with the WMAP9 results, since one can raise doubts on the Planck results: A Planck cosmology would predict slightly too many galaxy cluster (e.g., Pacaud et al., submitted) and there is some tension with the Planck SZ results, which predict smaller Ω_m. The latter problem could be solved at least partially by using a particular weak lensing mass calibration (Planck Collaboration et al., 2015b, Fig. 7). Furthermore, the Planck CMB result itself is not consistent between the low and high multipole constraints (Addison et al., 2015). For example the low multipole constraints on Ω_m are in agreement with WMAP, while the for $l > 1000$ the value Hubble constant, $H_0 = 64.1 \pm 1.7\,\mathrm{km\,s^{-1}\,Mpc^{-1}}$ is in strong tension with any measurements from the local distance ladder.

The results of the combined WMAP+HIFLUGCS analysis, which is the default setup with the WMAP9 constraints as priors on Ω_m and σ_8, are also shown in Tab. 4.4. The uncertainties of σ_8 decrease by more than 70% and in Ω_m by 50%. Now, these two parameters show almost no correlation any more. While the uncertainties on the $L_x - M$ parameters decrease as well, the degeneracy between slope and normalization cannot be broken (Pearson coefficient 0.79) by including CMB data. This is also expected, since WMAP

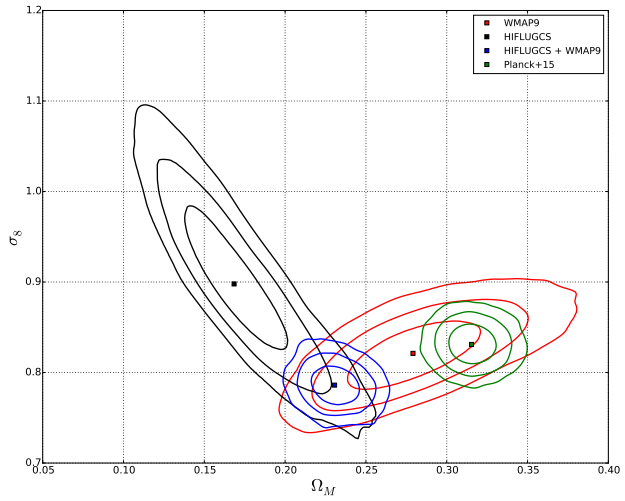

Figure 4.26: HIFLUGCS cosmology results compared to WMAP9 (Hinshaw et al., 2013) and Planck 2015 (Planck Collaboration et al., 2015c) results in the Ω_m-σ_8 plane. The contours correspond to 68.3%, 95.4% and 99.73% confidence regions.

Setup	Ω_m	σ_8	A_LM	B_LM	σ_LM
HIFLUGCS + WMAP9	$0.231^{+0.010}_{-0.009}$	$0.786^{+0.013}_{-0.013}$	$0.863^{+0.051}_{-0.051}$	$1.439^{+0.056}_{-0.055}$	0.26

Table 4.4: MCMC results for the free parameters from the cosmological pipeline for the default setup including WMAP9 priors. Uncertainties are marginalized 68.3%.

does not measure any X-ray luminosities and puts no direct prior on it.

4.5.2 Systematics of the mass determination

It is of crucial importance to take all possible effect into account, which could systematically bias the results. In the following I will discuss the influence of the extrapolation methods, instrumental calibration effects and the use of a different overdensity than the default $500\rho_\mathrm{crit}$. The physical effects of individual clusters, like a strong AGN feedback process, and modifications to the cosmological model are discussed at the end of this section.

One general concern connected with the likelihood function and the sample selection is, that a few clusters are very close to the flux limit. There is a chance that these clusters might slip, due to the variable K-correction, slightly below the flux limit, which results in a very small value of the likelihood. By excluding[7] these clusters from the analysis it was ensured that the cosmological results do not get biased by a very small number of clusters at the flux limit.

A similar effect could also happen, if a cluster is far away from the best fit $L_x - M$ relation. Usually the luminosity uncertainties are very small and the probability could essentially be 0 or very close to it. Excluding these objects as well ensures that far outliers are not influencing the results too much. As with the lowest flux objects, here I also conclude that $L_x - M$ relation outliers are not biasing the results.

[7] In order to not change the statistics these clusters were not really excluded, but just given much larger uncertainties on the luminosity.

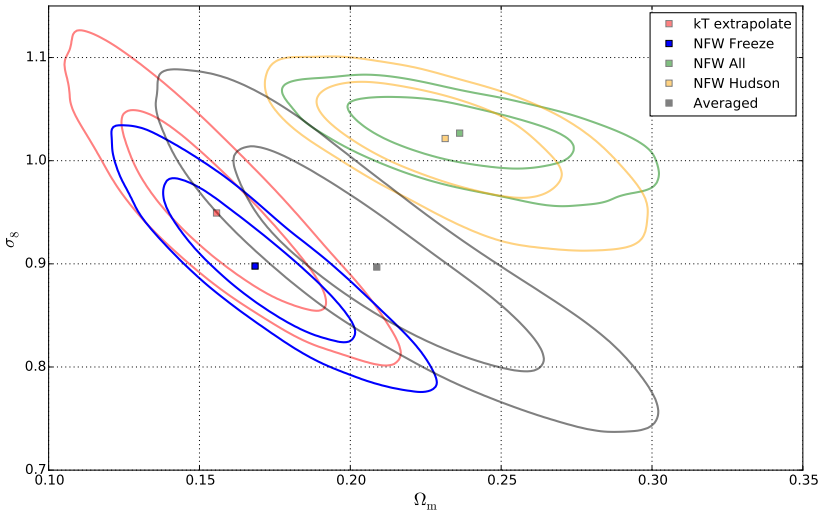

Figure 4.27: 68.3% and 95.4% confidence levels for Ω_m and σ_8 of the different extrapolation method, plus an additional mass estimated from an averaged cluster mass (see text for details).

Impact of different extrapolation methods

In Section 4.3.6 four different total mass estimates were introduced, of which the "NFW Freeze" method was chosen as default and used up to now. Although the default method should give the most robust mass estimates for large extrapolations, I show the cosmological results using the other mass estimates as well. Since some of the "NFW All" or "NFW Hudson" masses are unphysically high ($> 10^{16}\,M_\odot$), the results might give biases σ_8 values, which is sensitive to the high mass end of the mass function.

To take into account the scatter among the different methods I create a new mass estimate for each cluster (called "averaged"): The 4 masses of each cluster are sorted and the arithmetic mean of the two intermediate mass estimates is taken as the new mass for each cluster. The upper and lower errorbars are given by the other two extreme estimates. Note that this method uses only the mass estimates of the other extrapolation methods and does not take any of their uncertainties into account. Figure 4.27 shows the cosmological constraints of these 5 different methods to obtain masses. The temperature profile extrapolation method (red) seems to be almost in agreement with constraints of the default method (blue) and gives very similar results in the $\Omega_m - \sigma_8$ plane. The uncertainties (see Tab. 4.5) are slightly larger for "kT extrapolate", since the default method has only one free parameter for the extrapolation.

Setup	Ω_m	σ_8	A_{LM}	B_{LM}	σ_{LM}
NFW All	$0.237^{+0.026}_{-0.021}$	$1.026^{+0.019}_{-0.024}$	$0.123^{+0.057}_{-0.055}$	$1.244^{+0.049}_{-0.047}$	0.42
NFW Hudson	$0.231^{+0.026}_{-0.024}$	$1.021^{+0.028}_{-0.039}$	$0.161^{+0.059}_{-0.060}$	$1.267^{+0.059}_{-0.053}$	0.42
NFW Freeze	$0.168^{+0.021}_{-0.019}$	$0.898^{+0.051}_{-0.048}$	$0.835^{+0.059}_{-0.059}$	$1.358^{+0.075}_{-0.073}$	0.26
kT extrapolate	$0.156^{+0.021}_{-0.020}$	$0.949^{+0.063}_{-0.057}$	$0.694^{+0.061}_{-0.062}$	$1.229^{+0.070}_{-0.072}$	0.30
Averaged	$0.209^{+0.035}_{-0.030}$	$0.897^{+0.070}_{-0.064}$	$0.623^{+0.082}_{-0.077}$	$1.398^{+0.101}_{-0.101}$	0.32

Table 4.5: MCMC results for the free parameters from the cosmological pipeline for the different setups. Uncertainties are marginalized 68.3%.

The results of "NFW All" and "NFW Hudson" are in very good agreement. Both methods use also inner parts of the mass profile (Hudson excludes the central cool core region, if present) for the extrapolation.

The inner regions might not follow an NFW profile, but show a steeper slope of the profile. This causes some cluster masses to be biased high, since the concentration parameter of the NFW profile becomes unrealistically small (< 1) to fit the profile. Especially a mass biases high at the high mass end will force larger σ_8, which can be seen in Fig. 4.27. The mass uncertainties of the "averaged" method (black contour), which reflect the scatter of the different methods, are on average five times larger than the uncertainties of the default method, independent of mass. The "averaged" constraints do not reflect all possible systematics that enter in a galaxy cluster mass determination, because the extrapolation methods are chosen more or less arbitrary. So the position of this contour should not be taken too serious, but the uncertainties of the parameters are roughly 30% larger than for the default method.

XMM-Newton Masses

In Section 3.7.3 (also published in Schellenberger et al., 2015) the impact of instrumental cross calibration uncertainties on the cosmological constraints from the mass function have been evaluated. The temperature scaling shown in Tab. 3.2 was used to convert Chandra derived temperature profiles into XMM-Newton profiles, which work as input for the mass determination and cosmological analysis. The main result was a shift toward slightly smaller Ω_m for the XMM-Newton masses. While in Section 3.7.3 galaxy clusters have been binned in mass and an external $L_x - M$ relation from Reiprich and Böhringer (2002) was used to calculate the volumes, here I re-evaluate this effect using the derived masses for HIFLUGCS and the likelihood approach including the simultaneous fit of the $L_x - M$ relation. For the scaling of the temperature profiles I again use the "ACIS–Combined XMM" relation for the full energy band. I do point out that the Chandra calibration is different here, it now includes the new contamination model vN0008, but the since the effect is rather small ($< 2\%$) it should be negligible. Here the temperature extrapolation method is used to calculate the masses, because the purpose is to study the effects of calibration uncertainties (entering in the temperature profile) and NFW fits would possibly introduce an additional bias.

Figure 4.28 (top panel) shows the Chandra and scaled XMM-Newton masses, which exhibit a different behavior than what was inferred in the previous work: In Schellenberger et al. (2015) the masses were found to have a constant fractional difference ($\sim 14\%$), while now the difference between Chandra and XMM-Newton masses is increasing with mass. This trend is reflected in the lower panel, since XMM-Newton masses show a shift toward lower σ_8 with respect to Chandra. The constraints on the two (Chandra and XMM-Newton) $L_x - M$ relations are clearly not in agreement any more. Still, the overall shift in the $\Omega_\mathrm{m} - \sigma_8$ plane cannot explain the difference between cosmological constraints of Planck primary CMB anisotropies and SZ, as concluded in Schellenberger et al. (2015).

Different overdensities

The ideal halo mass function is a universal parametrization, which applies at all redshifts and cosmologies. Unfortunately, as pointed out in Tinker et al. (2008); Bocquet et al. (2015), not only redshift correction have to be made, but also at overdensities larger than $180\rho_\mathrm{mean}$, deviations from the universality should be expected. As this work, many other cosmological analyses that involve galaxy clusters use $500\rho_\mathrm{crit}$ as an overdensity for the mass calculation. So it is good for comparison reasons to choose the same overdensity. Furthermore, $500\rho_\mathrm{crit}$ seems to be a good compromise for keeping extrapolation to a minimum and not moving to too small radii, where hydrostatic equilibrium might not hold. I now recalculate the masses and extrapolate until $200\rho_\mathrm{crit}$ using the "kT extrapolate" and "NFW Freeze" methods. The change in cosmological parameters in shown in Fig. 4.29. For the pure temperature extrapolation no significant change can be detected, only that the uncertainties increase. For the "NFW Freeze" method, the uncertainties increase as well, but there is also a clear shift toward higher ($\sim 40\%$) Ω_m. This can be explained because the NFW model with a frozen concentration parameter puts more constraints on the shape of the mass profile, which can cause larger biases the more it is extrapolated. The fact that this change is toward larger Ω_m might be just by chance.

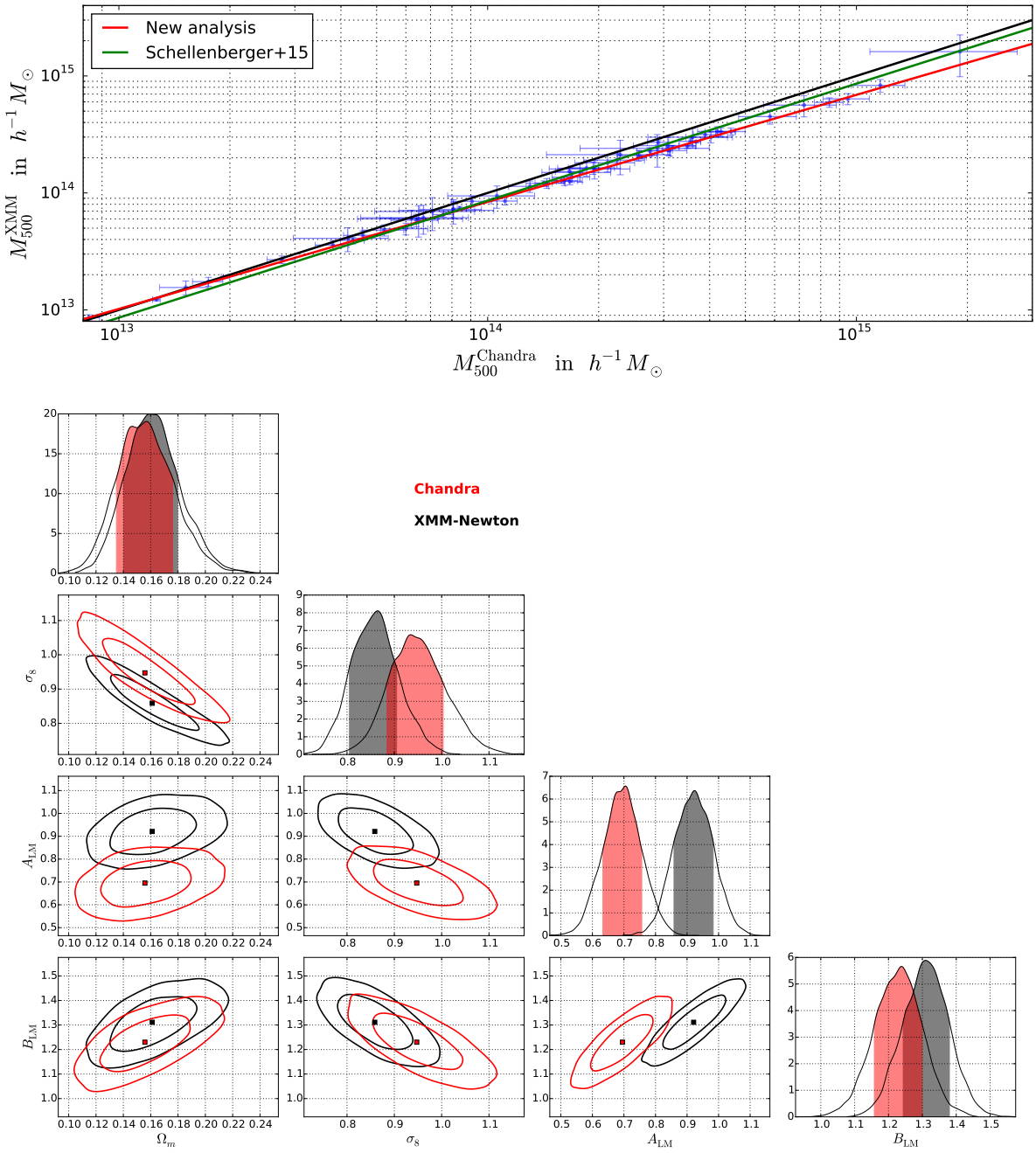

Figure 4.28: *Top:* Chandra vs. XMM-Newton masses (from rescaled Chandra temperatures) for HIFLUGCS using the temperature extrapolation method. The green line corresponds to the best fit relation from Section 3.9.4. *Bottom:* 68.3% and 95.4% confidence levels for the parameters using (exceptionally) the "kT extrapolate" masses for Chandra and XMM-Newton to test the systematics.

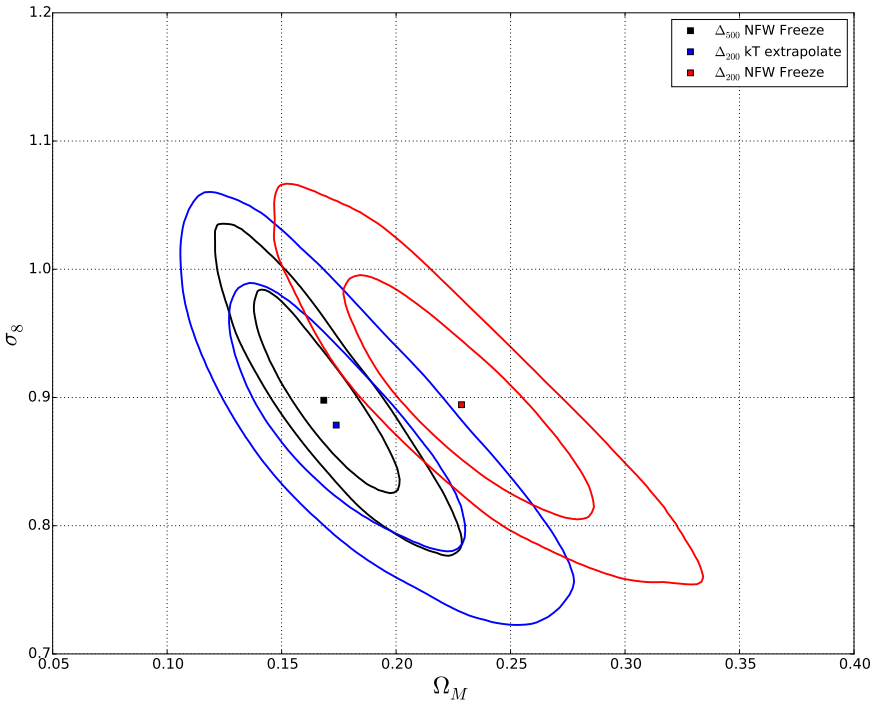

Figure 4.29: 68.3% and 95.4% confidence levels for different overdensities and extrapolation methods. Δ_{500} and Δ_{200} refer to 500 and 200 times the critical density of the Universe, respectively.

4.5.3 Galaxy cluster physics

In previous sections I compared the cosmological results of the HIFLUGCS cluster sample to the results of Vikhlinin et al. (2009b) and the CMB WMAP9 results. In this Section I will discuss various effects and processes that could cause the observed difference in Ω_m and σ_8, but I do point out that the aim is not to reproduce, e.g., the CMB results, but to test several influences that enter in a purely flux limited sample.

Galaxy groups

The first effect to be analyzed here is the sample composition: In contrast to, e.g., Vikhlinin et al. (2009b), HIFLUGCS sample consists of several galaxy groups. In the following I consider every object with $M_{500} < 10^{14}\,h^{-1}\,\mathrm{M}_\odot$ as galaxy group, since there is not a well defined threshold to separate groups from clusters (Sun et al., 2009). As shown, e.g., in Sun et al. (2009); Eckmiller et al. (2011); Bharadwaj et al. (2014); Lovisari et al. (2015) these objects have different scaling properties than galaxy clusters. One simple powerlaw to describe the $L_x - M$ relation for the full sample might not be enough. One first approach is here to exclude the galaxy groups by introducing a lower redshift cut (like in Vikhlinin et al., 2009b). I decided to use 0.05 as the redshift threshold, this will almost split the sample into two equal sized subsamples and the minimum mass of the high redshift samples is roughly $10^{14}\,h^{-1}\,\mathrm{M}_\odot$ (see Fig 4.30). Already the observed $L_x - M$ relations of these subsamples show a clear break with the high redshift (and high mass) sample to be significantly flatter. This is also seen in the corrected relation (Fig. 4.31), which shows a similar break between the two subsamples. Ω_m and σ_8 can also be seen in Fig. 4.31: The high redshift sample gives larger constraints on Ω_m, which cannot be explained by the degeneracy between the $L_x - M$ slope and Ω_m, which gives larger matter densities for increasing slopes. The $\Omega_\mathrm{m} - \sigma_8$ constraints are in perfect agreement with Vikhlinin et al. (2009b), but have larger uncertainties.

To test in more detail the effect on the mass function of galaxy groups in the sample I introduced a

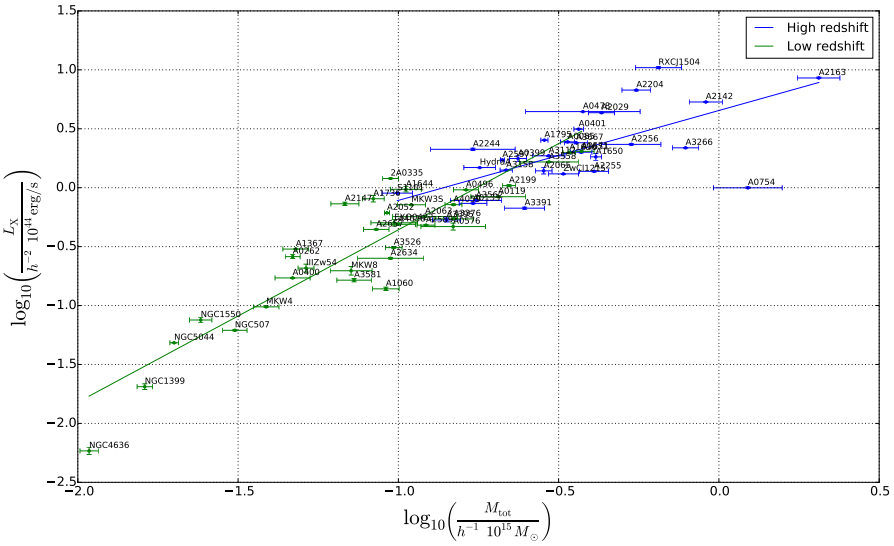

Figure 4.30: $L_x - M$ relations for the low ($z < 0.05$) and high redshift ($z \geq 0.05$) sample.

scaling factor x for the skyfraction for objects with a mass lower than $10^{14}\,\mathrm{M}_\odot$ (for $h = 0.71$). This should mimic the increasing incompleteness of ROSAT catalogs on galaxy group scale. In, e.g., Lovisari et al. (2015), a higher luminosity for low mass systems was detected than what is given in the ROSAT catalogs. The authors argue that ROSAT was not able to detect the emission out to large radii for these faint objects. In order not to have discontinuities I model this change in the skyfraction by a sigmoid function, where 99% of the final skyfraction is reached at mass of $1.7 \times 10^{14}\,\mathrm{M}_\odot$. I set x to 25%, 50% and 80%.

Setup	Ω_m	σ_8	A_LM	B_LM	σ_LM
High-z	$0.226^{+0.068}_{-0.052}$	$0.859^{+0.089}_{-0.086}$	$0.689^{+0.072}_{-0.074}$	$1.200^{+0.139}_{-0.138}$	0.24
Low-z	$0.149^{+0.037}_{-0.028}$	$0.920^{+0.131}_{-0.121}$	$1.239^{+0.108}_{-0.109}$	$1.624^{+0.105}_{-0.100}$	0.22
25% Groups	$0.233^{+0.039}_{-0.032}$	$0.787^{+0.052}_{-0.056}$	$0.791^{+0.058}_{-0.062}$	$1.298^{+0.061}_{-0.068}$	0.26
50% Groups	$0.189^{+0.025}_{-0.024}$	$0.845^{+0.051}_{-0.045}$	$0.813^{+0.047}_{-0.049}$	$1.341^{+0.054}_{-0.054}$	0.26
80% Groups	$0.183^{+0.023}_{-0.020}$	$0.858^{+0.042}_{-0.047}$	$0.832^{+0.057}_{-0.063}$	$1.373^{+0.071}_{-0.060}$	0.26
Broken Powerlaw	$0.133^{+0.021}_{-0.020}$	$0.993^{+0.092}_{-0.075}$	$1.389^{+0.163}_{-0.109}$	$1.842^{+0.153}_{-0.099}$	$^{\mathrm{a}}0.943^{+0.109}_{-0.167}$

Table 4.6: MCMC results for the free parameters from the cosmological pipeline for the different setups (x% Groups refer to the normal skyfraction multiplied by $x/100$ for all objects with $M < 10^{14}\,\mathrm{M}_\odot$). Uncertainties are marginalized 68.3%. a: The high mass slope for the broken powerlaw instead of the scatter, which is 0.26.

For 80% and 50% I do not detect any significant change in the cosmological parameters, while for 25% of the original skyfraction there is a clear shift toward higher Ω_m (see Tab. 4.6), which seems to be in rough agreement with WMAP9 results. Unfortunately, detecting only a quarter of the existing galaxy groups is quite unrealistic, given the high flux limit, where even low mass objects should be detected quite reliably (e.g., Böhringer et al., 2001, Fig. 23).

Another approach to model the different behavior of galaxy groups is to use a broken powerlaw for the $L_x - M$ relation (Tab. 4.6). The point where the slope changes is again at $10^{14}\,\mathrm{M}_\odot$. As expected a much flatter slope is detected for the high mass objects, which is only about 50% of the slope for the low mass objects. The result for Ω_m and σ_8 is only shifted along the degeneracy toward lower Ω_m. But in case groups are missed in the sample due to selection effects or catalog incompleteness a broken powerlaw

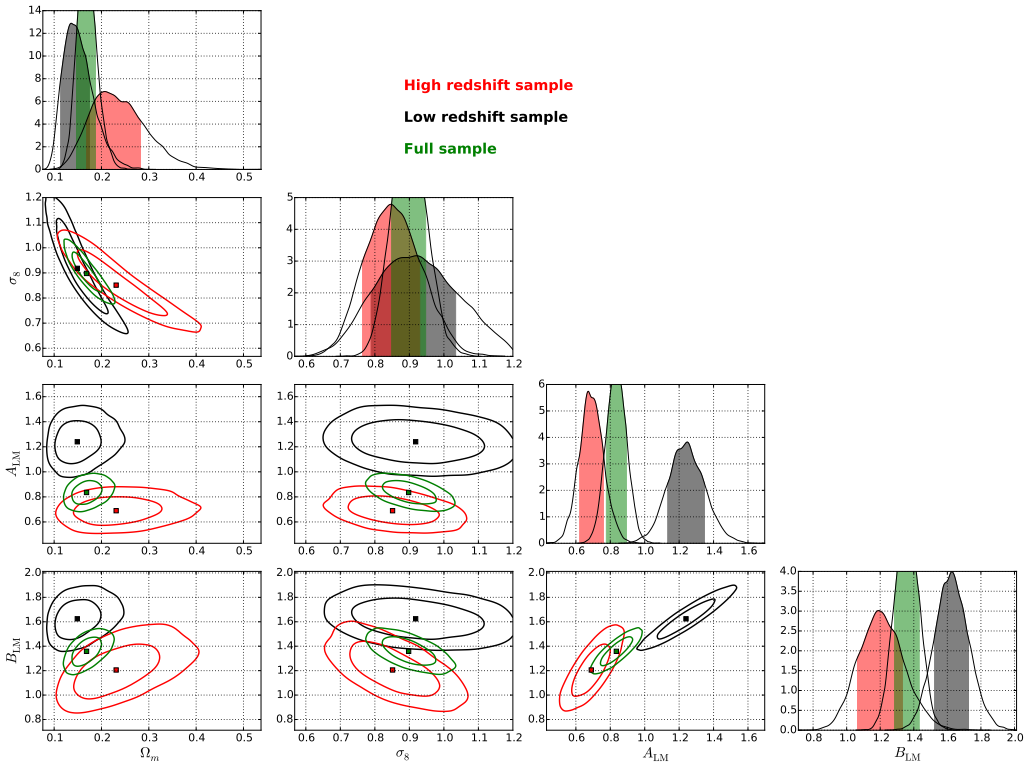

Figure 4.31: 68.3% and 95.4% confidence levels for the full sample (green), the high redshift sample ($z \geq 0.05$, red) and the low redshift sample ($z < 0.05$, black).

would just model the observed behavior and neglect these effects. The real distribution of galaxy clusters and groups in the $L_x - M$ plane could look different, and unknown effects push the groups toward lower luminosities, which cause the observed steepening. So a lower $\Omega_{\rm m}$, mostly driven by the lower number of groups that has to be matched, is the expected trend for this setup. The split into a high and low redshift sample seems to be more justified than to just treat groups differently, since the low redshift objects require more extrapolation due to their larger apparent extend.

Hydrostatic bias

Several effects can lead to systematically biased cosmological results, such as instrumental calibrations (see Chapter 3 and Section 4.5.2, substructure (Section 4.3.3), clumping, major merger events or non-thermal pressure which is not accounted in the hydrostatic equation. In Nagai et al. (2007) the authors estimate that Chandra mass measurements are biased by 10% to 20% low with the respect to the "true" masses found in simulations of relaxed clusters. This can for example originate from subsonic turbulent gas motion (Evrard et al., 1996), which will be measured in detail by the future Astro-H mission (Kitayama et al., 2014; Ota et al., 2015; ZuHone et al., 2015). With hydrodynamic simulations it is possible to derive hydrostatic equilibrium correction factors for clusters (e.g., Nelson et al., 2014; Shi et al., 2015; Avestruz et al., 2015), but individual clusters might deviate from this trend because of asphericity or clumping. Also the mass accretion rate (i.e. the dynamical state of the cluster) plays an important role. Typically, the unrelaxed clusters show a larger hydrostatic bias.

Observationally there have been studies finding agreement with the predictions on the hydrostatic bias, e.g., by comparing Planck SZ masses derived from XMM-Newton scaling relations with weak-lensing masses (von der Linden et al., 2014). Other studies find agreement of X-ray masses (mostly from Chandra) with weak-lensing masses (Gruen et al., 2014; Israel et al., 2014b; Applegate et al., 2015; Smith et al., 2015), and also of X-ray with caustic masses from galaxy dynamics (Maughan et al., 2015), implying that the hydrostatic bias is negligible. In a provocative way, one could conclude that if the hydrostatic

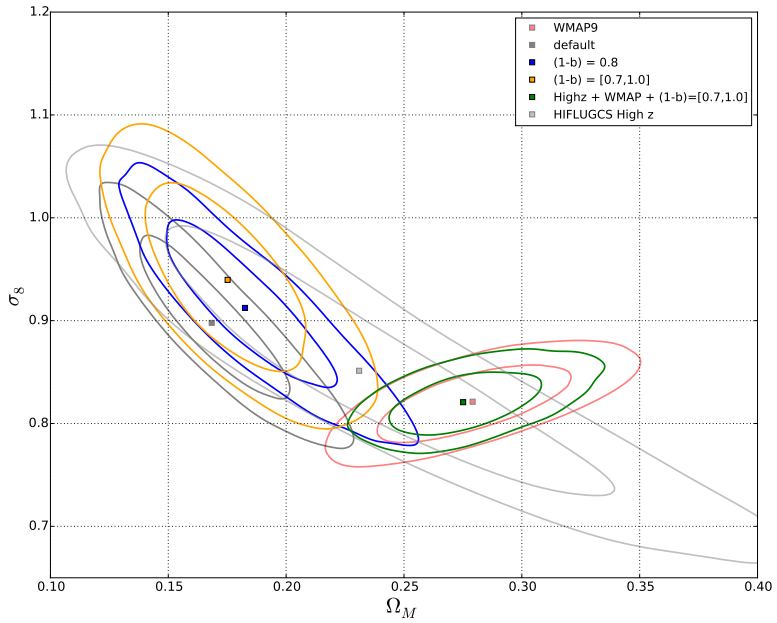

Figure 4.32: 68.3% and 95.4% confidence levels for various setups including a hydrostatic mass bias $(1-b) = \frac{M_{\rm hydro}}{M_{\rm true}}$. See text for details.

mass bias is significant, XMM-Newton might be a well calibrated instrument, because mass constraints using its data are lower than weak lensing masses, while Chandra might be the more reliable instrument if there is no hydrostatic bias. In reality, of course, the situation is more complicated since the procedure of estimating a mass matters as well as the weak lensing masses can be biased. Furthermore, in earlier XMM-Newton studies (Zhang et al., 2008, 2010; Foëx et al., 2012) a vanishing hydrostatic bias has been found as well.

Here I first model the hydrostatic bias,

$$(1-b) = \frac{M_{\rm hydro}}{M_{\rm true}} \ , \tag{4.66}$$

by increasing the mass by a fixed factor of 1.25, which corresponds to $(1-b) = 0.8$. Furthermore, one can marginalize over a uniformly distributed bias, $(1-b) = [0.7, 1.0]$. The shift (see Fig. 4.32) is in both cases toward higher $\Omega_{\rm m}$ and higher σ_8 values. For the marginalized bias the uncertainties are slightly larger.

Setup	$\Omega_{\rm m}$	σ_8	$A_{\rm LM}$	$B_{\rm LM}$	$\sigma_{\rm LM}$
$(1-b) = [0.7, 1]$	$0.175^{+0.017}_{-0.017}$	$0.938^{+0.043}_{-0.042}$	$0.725^{+0.063}_{-0.072}$	$1.338^{+0.058}_{-0.070}$	0.26
$(1-b) = 0.8$	$0.182^{+0.011}_{-0.009}$	$0.912^{+0.026}_{-0.024}$	$0.705^{+0.032}_{-0.032}$	$1.385^{+0.041}_{-0.039}$	0.26
High-z + varbias + WMAP9	$0.275^{+0.022}_{-0.018}$	$0.821^{+0.020}_{-0.018}$	$0.619^{+0.082}_{-0.084}$	$1.302^{+0.113}_{-0.109}$	0.26

Table 4.7: MCMC results for the free parameters from the cosmological pipeline for the different setups including a hydrostatic bias. Uncertainties are marginalized 68.3%.

If one would use the large confidence intervals of the high redshift sample from the previous section together with the WMAP9 priors, it is possible to constrain the bias since the $\Omega_{\rm m}$ and σ_8 values are determined almost entirely by WMAP9 (Fig. 4.32). The result is $(1-b) = 0.83^{+0.11}_{-0.12}$, which is in agreement

with simulations and shows overlap with weak lensing studies comparing their masses to Planck SZ masses, like Weighing the Giants ($1-b = 0.70 \pm 0.06$; von der Linden et al., 2014) or CCCP ($1-b = 0.76 \pm 0.05$ with only statistical uncertainties; Hoekstra et al., 2015). This is a different way of predicting a hydrostatic bias than illustrated before, where masses have been compared to reference values (weak or strong lensing), since now cosmological constraints are compared to a reference (CMB). Since many effects can bias cosmological constraints, this should not be seen as a solid determination of the bias, but as one way of interpreting the HIFLUGCS cosmology results.

Relaxed clusters

Many studies require dynamically relaxed clusters (i.e., shape close to spherical, no substructure or major merger) to calibrate their scaling relations. Consequently the cosmological results of the full sample is influenced.

Up to now I used the pure flux cut which creates a sample of relaxed and unrelaxed objects. Unfortunately, there is no general criterion to define relaxed clusters: Vikhlinin et al. (2009a) classify clusters with a second emission maximum, filamentary structure or significant centroid shifts as unrelaxed, while Hudson et al. (2010) call clusters with round or elliptical isophote and the emission peak in the center of all isophotes relaxed. Zhang et al. (2011a) find that clusters with a large offset between the BCG position and the X-ray emission weighted center are often disturbed. A clearer distinction of clusters can be made via the central cooling time, which splits clusters into cool core or non cool core clusters[8]. Although the cool core criterion seems to be more objective, there are several disturbed clusters with short cooling times (see Hudson et al., 2010, Fig. 19). I decide to take the disturbed-undisturbed classification from Tab. 2 in Zhang et al. (2011a), which is based on the visual inspection of the X-ray flux images as also done in Vikhlinin et al. (2009a). Disturbed clusters are: A0119, A0399, A0400, A0754, A1367, A1644, A1656, A1736, A2065, A2147, A2163, A2255, A2256, A3266, A3376, A3395, A3526, A3558, A3667, MKW8, NGC507. Note that the studies by Zhang et al. (2011a) misses 2A0355 and RXCJ1504, but both of them are strong cool core clusters (Hudson et al., 2010), so I assume that they are relaxed as well.

Setup	Ω_m	σ_8	A_LM	B_LM	σ_LM
No disturbed	$0.214^{+0.032}_{-0.028}$	$0.782^{+0.052}_{-0.050}$	$0.982^{+0.071}_{-0.071}$	$1.524^{+0.085}_{-0.083}$	0.26
No disturbed + $(1-b) = 0.8$	$0.165^{+0.022}_{-0.019}$	$0.937^{+0.055}_{-0.052}$	$0.756^{+0.054}_{-0.049}$	$1.303^{+0.068}_{-0.060}$	0.26
No disturbed + varbias + WMAP9	$0.267^{+0.021}_{-0.021}$	$0.815^{+0.020}_{-0.021}$	$0.735^{+0.105}_{-0.096}$	$1.574^{+0.067}_{-0.060}$	0.26

Table 4.8: MCMC results for the free parameters from the cosmological pipeline for the different setups excluding disturbed clusters. Uncertainties are marginalized 68.3%.

Figure 4.33 shows that when one leaves the mass of unrelaxed clusters unconstrained, i.e. very large errorbars, these clusters have no weight and the mass is constrained mainly by the $L_x - M$ relation which itself is determined by the remaining, relaxed clusters, the constraints of Ω_m are shifted toward larger values along the degeneracy with σ_8. Adding a hydrostatic bias on this shifts the contours toward higher Ω_m and σ_8 (as shown in the previous section), which will exhibit broad overlap with WMAP9. So I put a uniform prior on the hydrostatic bias and added WMAP9 priors on the two variable cosmological parameters. The resulting bias (Fig. 4.33) is $(1-b) = 0.66^{+0.10}_{-0.12}$, which slightly overlaps with the 68.3% uncertainties of the bias constraints from the high redshift subsample combined with WMAP9.

4.5.4 Additional mass tracers

In this section I test other available quantities that are connected to the total cluster mass. From the virial theorem it follows that the optical velocity dispersion, σ_v, of the member galaxies is a direct measure of the total mass. Also the integrated Comptonization parameter Y_SZ, which is proportional to the gas pressure, is often used to constrain cluster masses. These two quantities are used as independent mass

[8] One can also split clusters into three classes, strong-, weak-, and non-cool core clusters as demonstrated in Hudson et al. (2010)

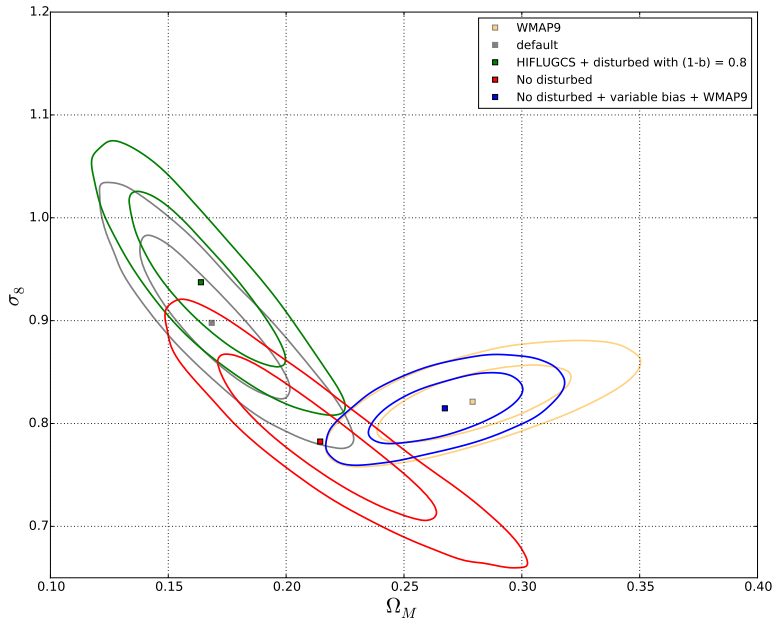

Figure 4.33: 68.3% and 95.4% confidence levels for various setups to demonstrate the effect of dynamically disturbed clusters.

estimators in the second paragraph, while first I focus on adding further constraints using the gas mass and the pure $Y_{\rm SZ}$ parameter on my total mass estimates.

Additional scaling relations

In Vikhlinin et al. (2009a,b) several mass proxies are discussed in detail: The gas mass $M_{\rm gas}$, the overall cluster temperature $T_{\rm gas}$ and the product of the two, Y_X. Here I will show cosmological constraints by using the gas mass $M_{\rm gas}$ of all clusters as additional constraint, which means, the deviation from a self calibrated $M_{\rm gas} - M_{\rm tot}$ scaling relation enters in the likelihood function. I do not detect any significant changes to the default results, only that the slope and normalization of the $L_x - M$ relation are shifted by 3-4% toward lower values (not significant). With this setup I am able to give a (corrected) $M_{\rm gas}$ scaling relation:

$$\log_{10}\left(\frac{M_{\rm gas}}{10^{13}\,h^{-2.5}\,{\rm M}_\odot}\right) = 1.223^{+0.047}_{-0.050} + 1.140^{+0.060}_{-0.063}\cdot\log_{10}\left(\frac{M_{\rm tot}}{10^{15}\,h^{-1}\,{\rm M}_\odot}\right) \pm 0.228^{+0.021}_{-0.017}\ . \qquad (4.67)$$

The observed relation deviates only slightly: The observed slope is 1.113 ± 0.056, the observed normalization 1.368 ± 0.072 and the observed intrinsic scatter 0.237. One needs to consider that this procedure is not identical to what was done in Vikhlinin et al. (2009b), where masses are not determined independently but through a scaling relation calibrated by a small subsample of relaxed clusters: Here are the full sample is used to constrain the scaling relation, which enters in the likelihood function, but is not dominating it.

Independent mass estimates

The $M_{\rm gas}$ constraints did not have a significant effect on the cosmological parameter estimation. So here I explore the use of independent masses of the HIFLUGCS sample, in particular the mass from the velocity dispersion $\sigma_{\rm v}$ and the mass from the Planck SZ measurements. Described in Section 1.3 the $Y_{\rm SZ}$ parameter can be extracted from the y maps provided by Planck. Using a scaling relation calibrated with XMM-Newton data by Arnaud et al. (2010), total masses are calculated for the galaxy clusters.

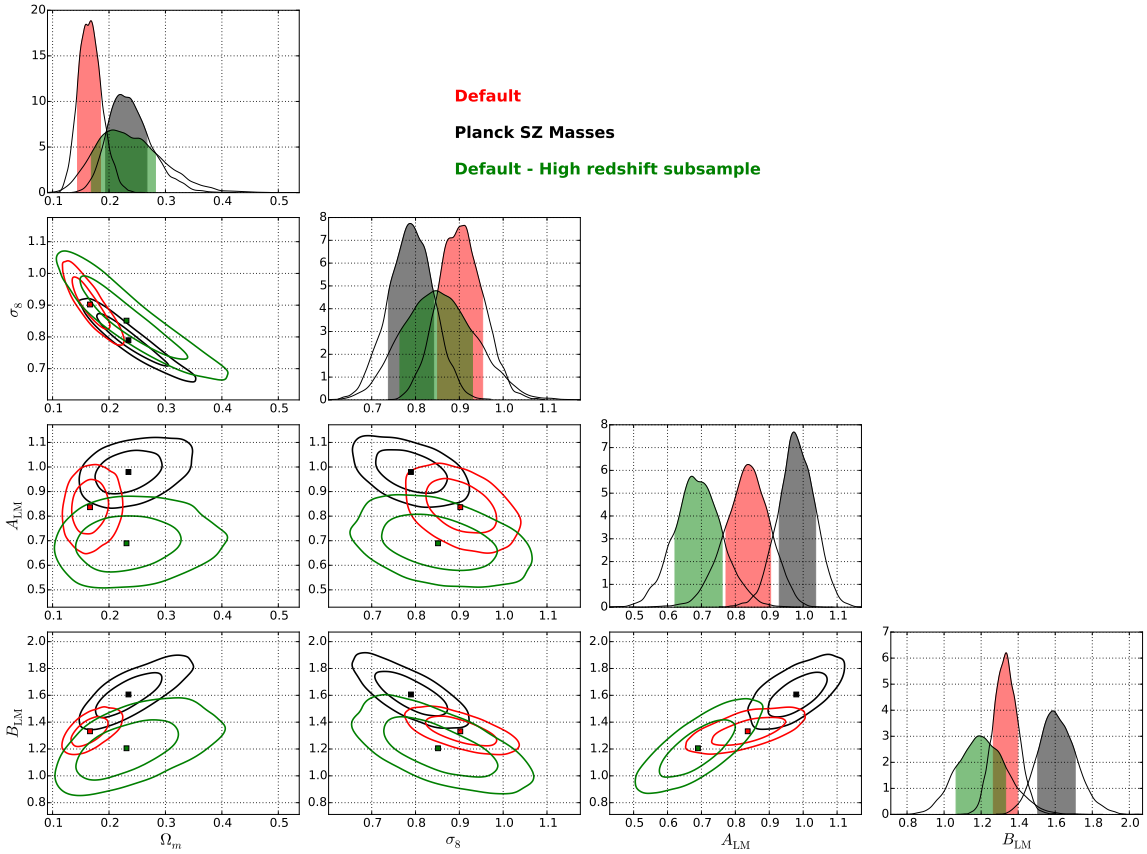

Figure 4.34: 68.3% and 95.4% confidence levels for the analysis of the Planck SZ masses of HIFLUGCS (black), compared to the default analysis procedure (red) and the high redshift subsample (green).

From three different pipelines (Matched Multi-Filter MMF1, MMF3 and PowellSnakes, PwS) clusters are detected in the Planck maps. All detections including integrated Y parameters and total masses, M_{500}, are summarized in the "union catalogue" (Planck Collaboration et al., 2015a,b,d, which is available on the Planck website[9].

I compared this catalog with HIFLUGCS and found 50 out of the 64 objects. The missing ones are mainly low mass objects: NGC1399, A2052, A3581, EXO0422, NGC1550, MKW4, NGC4636, A0400, ZwCl1215, NGC5044, NGC507, A1060, HydraA, and IIIZw54. 90% of the detected objects have an SZ signal-to-noise ratio (SNR) above 6, which was used for the Planck SZ study. Here I use all detected objects (minimum SNR is 4.5) and set the mass uncertainties of the undetected objects to a very broad range, which again gives them no weight. Out of this 14 undetected clusters, 12 are in the low redshift subsample of HIFLUGCS. Figure 4.34 shows that for the Planck SZ masses of HIFLUGCS, there exists overlap for $\Omega_{\rm m}$ and σ_8 with the high redshift subsample of the default analysis procedure, as expected since 12 low redshift clusters are already excluded. The $L_x - M$ relation constrained from the Planck masses (of course using the same luminosities) deviates strongly from the default or high redshift sample: The slope and normalization are about 30% larger than the high redshift subsample constraints. A higher normalization of the $L_x - M$ relation could be due to a systematic bias that lowers all Planck masses. Following the degeneracy between slope and normalization, the slope has to increase as well. The Chandra−XMM-Newton cross calibration could contribute to this effect, but it is unlikely that it is fully attributed to calibration uncertainties, which would not cause such a strong deviation (see 4.5.2). Looking at Fig. 4.35 (right panel) reveals, that Planck masses are slightly larger for the lower masses ($\sim 10^{14}\,M_\odot$) and smaller at the high mass end, which will steepen the $L_x - M$ relation and increase the normalization. But it is not clear why the Planck masses are larger at the low mass end. One could guess, that the $Y - M_{500}$ scaling relation from Arnaud et al.

[9] `http://wiki.cosmos.esa.int/planckpla2015/index.php/Catalogues`

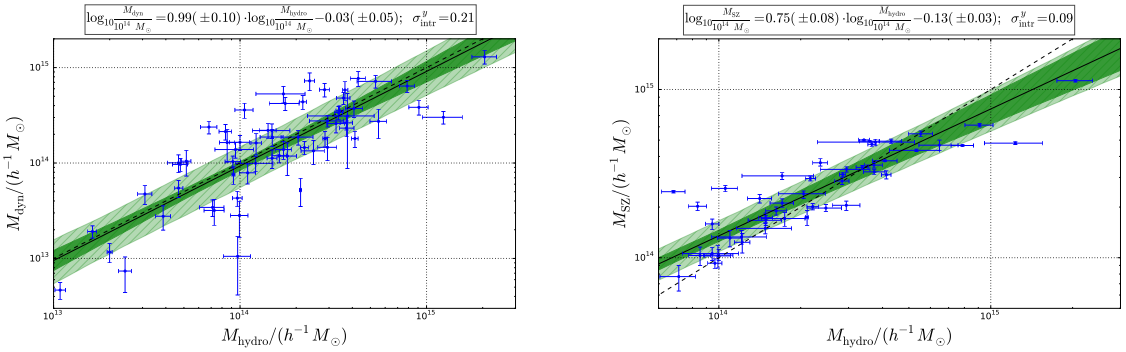

Figure 4.35: Direct comparison of the hydrostatic X-ray masses (default) and 62 dynamical mass estimates (left; Zhang et al., in prep.), and the hydrostatic masses and 50 Planck SZ masses (right). The dark green region is the 68.3% uncertainty region of the scaling relation (the light green region including the intrinsic scatter). The black dashed line is equality of masses. The best fit relations above each graph are calculated using the BCES Y|X estimator.

(2010), which is not corrected for selection effects, does not reflect the real behavior. Furthermore, the uncertainties of the Planck masses are much smaller than the X-ray constraints, because no uncertainties on the pressure profile and no uncertainties or scatter of the $Y - M_{500}$ enter in the calculation and the errorbars represent only statistical uncertainties (Planck Collaboration et al., 2015a).

The connection between the galaxy velocity dispersion and the total mass follows from simple considerations of the virial theorem,

$$\sigma_{\rm v} = \sqrt{\frac{MG}{r}}\ , \tag{4.68}$$

where r is the virial radius and M is called the dynamic mass. Since this radius is usually unknown, one can use an NFW model to describe the density distribution, as done by Biviano et al. (2006). Saro et al. (2013) use simulations to calibrate the dynamic mass. I use the mass estimates by Zhang et al. (in preparation; private communication) based on the velocity dispersion of the HIFLUGCS sample from Zhang et al. (2011a) with some updates.

Setup	$\Omega_{\rm m}$	σ_8	$A_{\rm LM}$	$B_{\rm LM}$	$\sigma_{\rm LM}$
Planck SZ Masses	$0.234^{+0.042}_{-0.033}$	$0.790^{+0.051}_{-0.052}$	$0.980^{+0.055}_{-0.053}$	$1.606^{+0.107}_{-0.095}$	$0.197^{+0.025}_{-0.021}$
Dynamical Masses	$0.171^{+0.027}_{-0.021}$	$0.944^{+0.063}_{-0.062}$	$0.573^{+0.068}_{-0.072}$	$1.236^{+0.079}_{-0.078}$	0.35

Table 4.9: MCMC results for the free parameters from the cosmological pipeline for alternative mass estimates. Uncertainties are marginalized 68.3%.

The two missing clusters (2A0355 and RXCJ1504) get very large uncertainties so their mass is determined by the $L_x - M$ relation. The direct comparison to the (default) hydrostatic masses in Fig. 4.35(left) shows that despite the scatter the dynamic and hydrostatic masses are in prefect agreement, so it is no surprise the cosmological results are also matching very well (Fig. 4.36) with larger uncertainties. As indicated in Fig. 4.36 adding a hydrostatic bias $(1 - b) = 0.8$ to the default masses gives even better agreement with the dynamic mass cosmology. This independent mass estimator shows that the hydrostatic masses derived here are robust: First, there is no mass dependency between the Chandra derived hydrostatic masses and the dynamic mass estimates, which can give a hint that the Chandra instrumental calibration is reliable. Second, the offset is consistent with zero (-0.03 ± 0.05), which also makes the existence of unaccounted non-thermal pressure less likely.

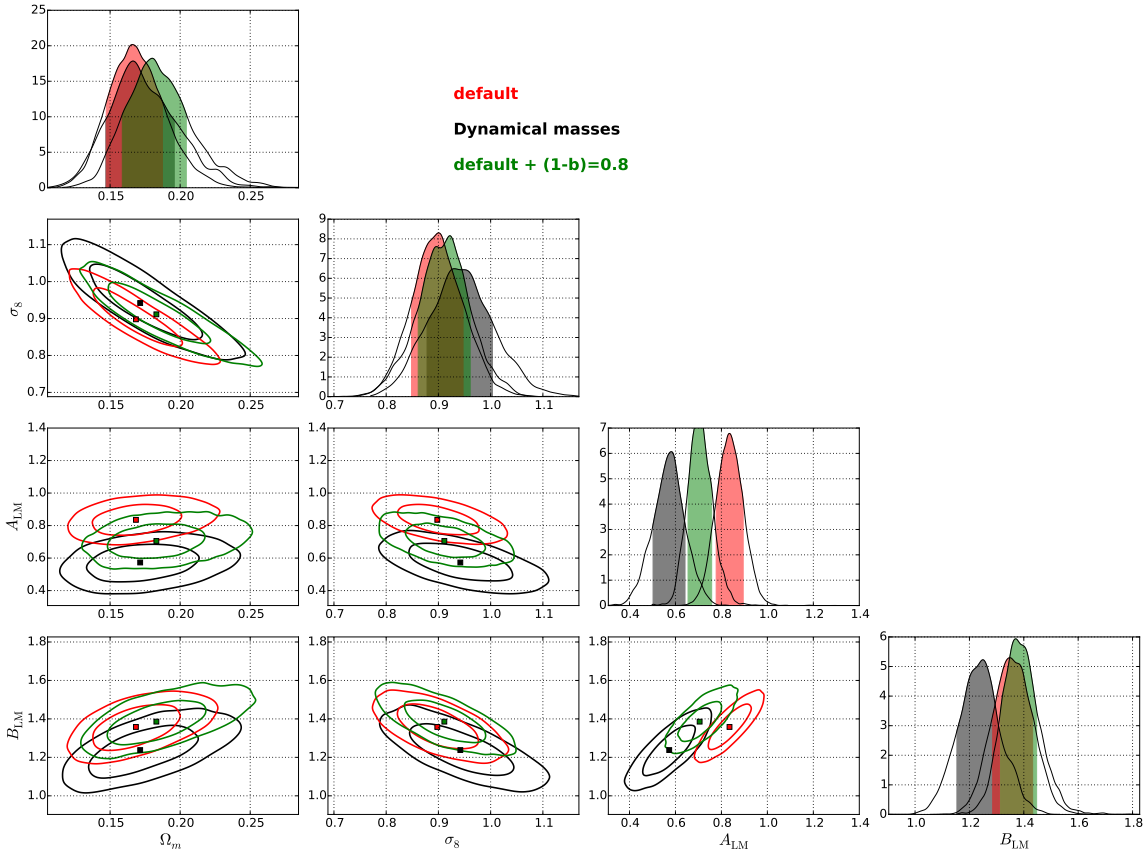

Figure 4.36: 68.3% and 95.4% confidence levels for the analysis of the dynamic masses of HIFLUGCS (black; Zhang et al., in prep.), compared to the default analysis procedure (red) and the default setup plus a fixed hydrostatic bias of $(1 - b) = 0.8$ (green).

4.5.5 Reference model validity

In this final part of the discussion on the HIFLUGCS cosmology results of the mass function analysis I focus on the mass function itself. For the construction of the Tinker et al. (2008) halo mass function Dark Matter simulations without baryons were used. Furthermore, simplistic assumptions like a negligible neutrino mass or non existing coupling between the Dark Energy and Dark Matter have been made which will be tested here. I do point out that these tests are used to demonstrate the impact of these components, but not to put any constraints on them. This is not easily possible with galaxy clusters alone, especially not with a low redshift sample.

Impact of baryons

The clear difference between baryonic matter and Dark Matter is the fact that Dark Matter only interacts gravitationally. Dark Matter is seen as collisionless and so does not have pressure. Obviously the Universe consists of baryonic matter, but due to its interaction simplicity and the much higher energy density in the Universe, simulations in the past were often performed using Dark Matter particles and neglect baryons.

Up to now the properties of the baryonic matter entered only in the matter power spectrum (or matter transfer function): The interaction of the baryons and the tightly coupled photons in the early Universe led to oscillations (Baryonic acoustic oscillations, e.g., Eisenstein, 2005). These are imprinted on the matter power spectrum, since baryons change the total gravitational potential. Apart from the oscillations also a damping can be observed due to photons smoothing out the small scale temperature fluctuations at the epoch of recombination. More details are given in Eisenstein and Hu (1998); Eisenstein (2005). The effect of baryons on the transfer function is fully accounted by the CLASS algorithms.

For the mass function the situation is the following: Baryons force by adiabatic contraction a larger halo concentration, which leads to a uniform shift of halo masses toward larger values (e.g., Cui et al., 2012b). Furthermore, baryons cause several physical effects that are accounted in current hydrodynamic simulations (Cui et al., 2014; Bocquet et al., 2015), such as gas heating, radiative cooling, star formation and feedback processes from active galactic nuclei(AGN) and galactic winds driven by supernovae. It was found that the impact of baryons is much larger at inner regions (e.g., r_{2500}) and almost negligible at the virial radius. Cooling and star formation lead to a slightly larger halo density (i.e. increase of the mass function with respect to Dark Matter only derived mass functions), while adding AGN feedback on top can result in a suppression of the mass function (Cui et al., 2014).

Here I adopt the mass function from Bocquet et al. (2015), which includes stellar evolution, chemical enrichment, star formation and feedback processes (AGN and SNe). The simulations are based on three different box sizes of the Magneticum simulation with an input cosmology $\Omega_\mathrm{m} = 0.272, \Omega_\mathrm{b} = 0.0456, \sigma_8 = 0.809$ and $h = 0.704$. The mass function including baryonic effects is explicitly given for an overdensity $\Delta_{500\mathrm{c}}$:

$$\frac{\mathrm{d}n}{\mathrm{d}M_{500\mathrm{c}}} = f(\sigma)\frac{\bar{\rho_\mathrm{m}}}{M_{500\mathrm{c}}}\frac{\mathrm{d}\sigma^{-1}}{\mathrm{d}M_{500\mathrm{c}}} \times \frac{M_{500\mathrm{c}}}{M_{200\mathrm{m}}} \ , \tag{4.69}$$

where $f(\sigma)$ defined as in Eq. 2.52 with new parameters including a covariance matrix given in Bocquet et al. (2015)[10]. The last factor in Eq. 4.69 accounts for the increase of baryonic effects toward inner cluster regions and depends on redshift and Ω_m. Bocquet et al. (2015) predict for $z < 0.3$ that the mass function from hydrodynamic simulations (including the baryonic effects, HydroMF in the following) will be smaller than Tinker et al. (2008) at all masses, while the difference seems to be minimal around $10^{15}\,\mathrm{M}_\odot$. Naively that would mean that the HydroMF gives larger Ω_m than Tinker et al. (2008). Of course the impact will depend on the individual sample selection. For example for an eROSITA like sample (X-ray flux selected) the Tinker et al. (2008) mass function would predict lower Ω_m and smaller σ_8. Note that the input cosmology for this tests in Bocquet et al. (2015) was close to the cosmology used in the simulations.

Setup	Ω_m	σ_8	A_LM	B_LM	σ_LM
Bocquet DM	$0.156^{+0.022}_{-0.019}$	$0.870^{+0.036}_{-0.036}$	$0.853^{+0.058}_{-0.056}$	$1.389^{+0.065}_{-0.067}$	0.26
Bocquet Hydro	$0.165^{+0.024}_{-0.020}$	$0.864^{+0.035}_{-0.038}$	$0.850^{+0.057}_{-0.051}$	$1.377^{+0.070}_{-0.054}$	0.26

Table 4.10: MCMC results for the free parameters from the cosmological pipeline for different halo mass functions. Uncertainties are marginalized 68.3%.

Applying the Bocquet et al. (2015) mass function to HIFLUGCS (default) results in a different trend (see Fig. 4.37): I detect no change in Ω_m and a lower σ_8 when using the HydroMF, which is not expected. The Dark Matter only mass function from Bocquet et al. (2015) gives results which are in perfect agreement with the HydroMF, which is also not expected. The uncertainties of the HydroMF are larger, mostly because the covariance matrix enters and puts uncertainties on the parameters in $f(\sigma)$, which was not done for the Dark Matter only mass function of Tinker et al. (2008) and Bocquet et al. (2015). Directly comparing the HydroMF mass function against Tinker et al. (2008) reveals that for $\Omega_\mathrm{m} \approx 0.17$ the situation is reverse than described in Bocquet et al. (2015): Tinker et al. (2008) gives a lower halo density than HydroMF for high masses and shows agreement for low masses, which is locally equivalent to a change in σ_8 as observed. This behavior raises doubts that one (or both) mass functions compared here are not universal at $\Delta_{500\mathrm{c}}$. As indicated already in Bocquet et al. (2015) the best universality is given at an overdensity of $\Delta_{200\mathrm{m}}$, but usually it is assumed that deviations from universality are compensated by the redshift dependent factors in $f(\sigma)$. Despite these doubts it seems that for HIFLUGCS the effects of baryons in the mass function is negligible (if HydroMF is correct), especially if one compares the tiny difference between the Dark Matter only (orange) and HydroMF (green) constraints of the Bocquet et al. (2015) mass functions in Fig. 4.37. The differences between different Dark Matter only simulation setups on the other hand can be significant, as in the described case there is only small overlap of the 68.3% confidence regions.

[10] arXiv version v3, private communication

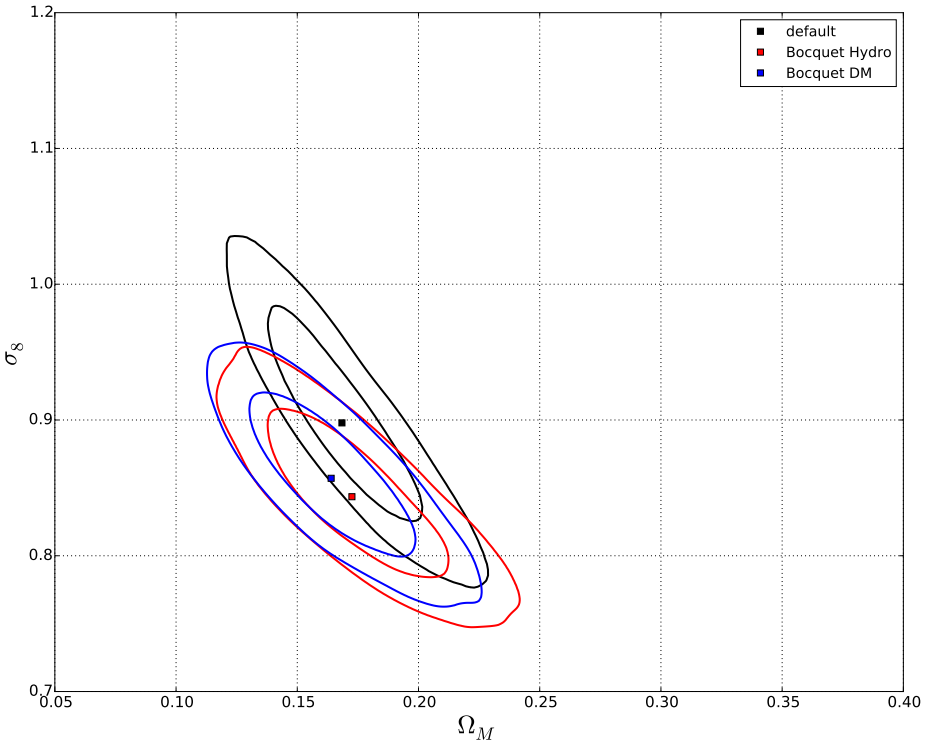

Figure 4.37: 68.3% and 95.4% constraints on Ω_m and σ_8 from the mass functions by Bocquet et al. (2015) (Version v3, private communication). Red ellipses are from hydrodynamical simulations, while the blue contours are Dark Matter only simulations. The Tinker et al. (2008) constraints ("default") are shown in black.

Neutrinos

The normalized energy density of photons Ω_γ can be easily derived from the temperature, since it is a blackbody spectrum,

$$\Omega_\gamma = \frac{4\sigma_\mathrm{SB} T_0^4}{\rho_\mathrm{crit} c^3} \approx 5.0 \times 10^{-5} \ , \tag{4.70}$$

where σ_SB is the Stefan-Boltzmann-constant, T_0 the photon (CMB) temperature and c the speed of light.

Energy conservation forced Pauli in 1930 to postulate neutrinos for particle decaying processes. For example in the Sun, the dominating process is the pp cycle,

$$4p \rightarrow {}^4\mathrm{He} + 2e^+ + 2\nu_e \ , \tag{4.71}$$

where 2 electron neutrinos per Helium nucleus are produced. This results in a total neutrino flux of $6.6 \times 10^{10}\,\mathrm{cm}^{-2}\,\mathrm{s}^{-1}$ (BOREXINO Collaboration et al., 2014).

The current neutrino density is now given by

$$\Omega_\nu = N_\mathrm{eff} \cdot \frac{7}{8} \cdot \frac{4\sigma_\mathrm{SB} T_\nu^4}{\rho_\mathrm{crit} c^3} \approx 3.5 \times 10^{-5} \ , \tag{4.72}$$

where the factor $\frac{7}{8}$ accounts for the Pauli exclusion principle (neutrinos are Fermions) and the neutrino

temperature is

$$T_\nu = \left(\frac{4}{11}\right)^{\frac{1}{3}} T_0 \approx 1.945\,39\,\mathrm{K}\ , \tag{4.73}$$

where the factor $\frac{4}{11}$ characterizes the higher temperatures of photons with respect to neutrinos: Since in the early Universe neutrinos decouple from baryons before the pair production is stopped, only the photons gain energy from the electron-positron annihilation (see also Bilenky, 2010) and their temperature jumps $\propto \left(\frac{11}{4}\right)^{\frac{1}{3}}$. After decoupling, neutrinos expand adiabatically and create the cosmic neutrino background (CNB).

In the standard model of particle physics neutrinos are considered as massless particles without charge, although there are suggestions for non-zero mass (e.g., Kamionkowski and Kosowsky, 1999; Hirsch and Valle, 2004; Fogli et al., 2012; Burenin, 2013). Very recently, the Nobel Prize in Physics 2015 was attributed to the discovery of neutrino oscillations by Takaaki Kajita (Super-Kamiokande Collaboration, University of Tokyo, Kashiwa, Japan) and Arthur B. McDonald (Sudbury Neutrino Observatory Collaboration, Queen's University, Kingston, Canada). Their measurements suggest that, while before $\frac{2}{3}$ of the neutrinos in observations were missing compared to theoretical predictions, neutrinos can change their flavor. This means, e.g., an electron neutrino can turn into a muon or tau neutrino and the probability for these flavors oscillates, which in turn means that neutrinos cannot be massless.

A massive neutrino will have an effect on the large scale structure that can be seen in the matter power spectrum (e.g., Lesgourgues and Pastor, 2006, 2012, 2014): On sub-free-streaming-scales neutrinos will smooth the density field, which makes the gravitational potential shallower and slows down structure growth (Agarwal and Feldman, 2011). The distribution of masses among the neutrino species is uncertain, but important here is the sum of the masses of the three species, $\sum m_\nu$. From CMB observations one knows that there are around 339 neutrinos and anti-neutrinos per cm^3 in the Universe (Lesgourgues and Pastor, 2012). An additional hypothetical particle with a finite mass, which interacts (almost) only gravitationally, has been suggested (Dodelson and Widrow, 1994; Boyarsky et al., 2009). These sterile neutrinos might be a candidate for Dark Matter and there are claims that a decay line at $\sim 3.5\,\mathrm{keV}$ was observed in X-rays (Boyarsky et al., 2014; Bulbul et al., 2014). Here I consider only the normal types of neutrinos.

The neutrino mass enters in the calculation of the matter power spectrum and it is taken into account by CLASS (Lesgourgues, 2011a,b; Lesgourgues and Tram, 2011). Massive neutrinos are no longer in the relativistic regime, but can be described by a Fermi-Dirac distribution. The mass can be translated into an energy density,

$$\Omega_\nu = \frac{\sum m_\nu}{93.14\,\mathrm{eV}\,h^2}\ , \tag{4.74}$$

which is taken into account when calculating the total matter density. The oscillation experiments now determine three neutrino mass states, and each mass corresponds to a superposition of the three different neutrino flavors. Theory now predicts two different scenarios, how these mass states are distributed: The normal and inverse hierarchy (see also Cahn et al., 2013), with each having different implications on standard model of particle physics. But for cosmological application, the sum of neutrino masses is important.

The results for the REFLEX2 galaxy cluster sample (Böhringer and Chon, 2015) suggest a smaller σ_8 and larger Ω_m, when increasing the neutrino mass. This is in good agreement with what is obtained for HIFLUGCS (see Fig. 4.38).

Setup	Ω_m	σ_8	A_LM	B_LM	σ_LM
$\sum m_\nu = 0.5\,\mathrm{eV}$	$0.196^{+0.024}_{-0.020}$	$0.814^{+0.039}_{-0.044}$	$0.845^{+0.070}_{-0.059}$	$1.392^{+0.082}_{-0.065}$	0.26
$\sum m_\nu = 1.0\,\mathrm{eV}$	$0.223^{+0.027}_{-0.022}$	$0.761^{+0.034}_{-0.036}$	$0.856^{+0.060}_{-0.053}$	$1.402^{+0.071}_{-0.055}$	0.26

Table 4.11: MCMC results for the free parameters from the cosmological pipeline for the different neutrino masses. Uncertainties are marginalized 68.3%.

The cases shown here ($\sum m_\nu$ up to 1 eV) are unrealistically high, current upper limits from Planck

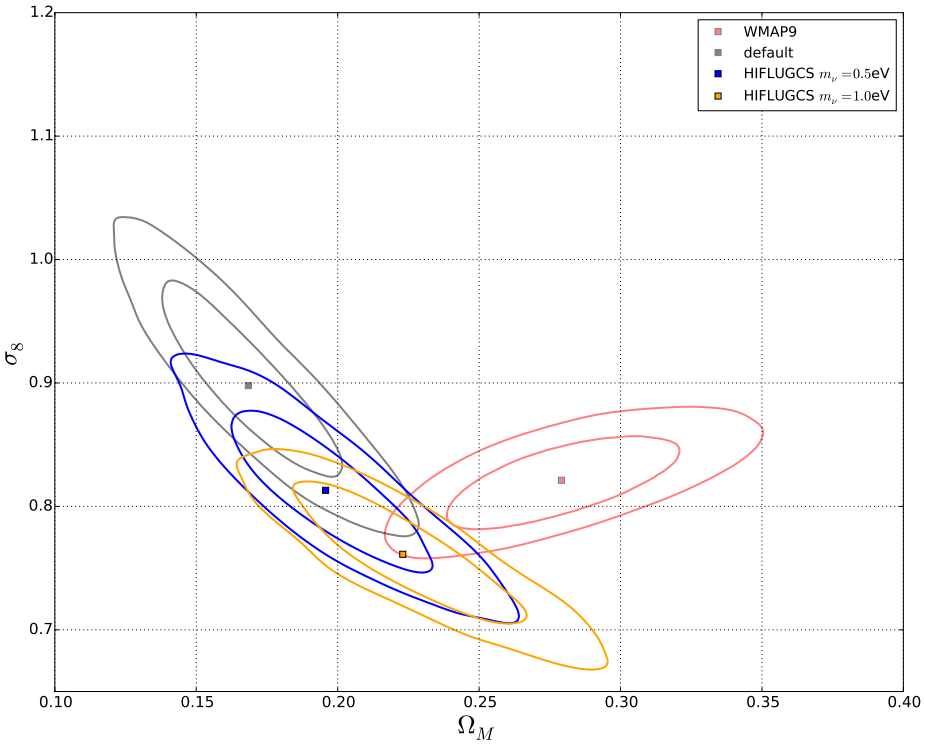

Figure 4.38: 68.3% and 95.4% constraints on Ω_m and σ_8 for an increased (summed) mass of neutrinos (default: $\sum m_\nu = 0.06\,\mathrm{eV}$).

(Lesgourgues and Pastor, 2014) are 0.23 eV at 95% confidence level, but it is shown here to demonstrate when the effect would be significant. The constraints on the $L_x - M$ relation are unchanged for any high neutrino mass tested here. The effect in the Ω_m-σ_8 plane is perpendicular to the hydrostatic bias, so in principle one could reproduce the WMAP9 results by adding a sufficiently high bias and neutrino mass, which both would be unphysical, and, as stated before, it is not the aim to reproduce CMB results.

Coupled Dark Matter - Dark Energy

Dark Matter and Dark Energy are both unknown constituents of our Universe and account for roughly 95% of the energy content. A self-interaction or coupling between these two components, as it has been suggested, e.g., in Amendola (2000); Schuecker (2005); Tarrant et al. (2012); Baldi (2014), would have effects on cosmological observables. But unfortunately, they are degenerate with other effects, so a distinction in order to falsify the ΛCDM model is very hard. One example, how distinguish interacting Dark Energy from cosmologies with a variable Dark Energy equation of state parameter w, is given in Väliviita and Palmgren (2015). The authors use several probes (Planck CMB, CMB lensing and baryonic acoustic oscillations) to determine an energy transfer between Dark Matter and Dark Energy and find that for $w < -1$ an interacting Dark Energy is favored.

The effect of a self-interacting or coupled Dark Energy on the halo mass function is studied in Cui et al. (2012a) for several different scenarios. Most of them show a larger halo abundance for high mass objects, which seems to be completely degenerate with σ_8 for a local sample like HIFLUGCS. The more interaction is assumed between Dark Energy and Dark Matter, the higher will be the local (z=0) σ_8. This effect is seen for a constant and an exponentially growing coupling. With a cluster sample that covers a large redshift and mass range, it might be possible to break the degeneracy.

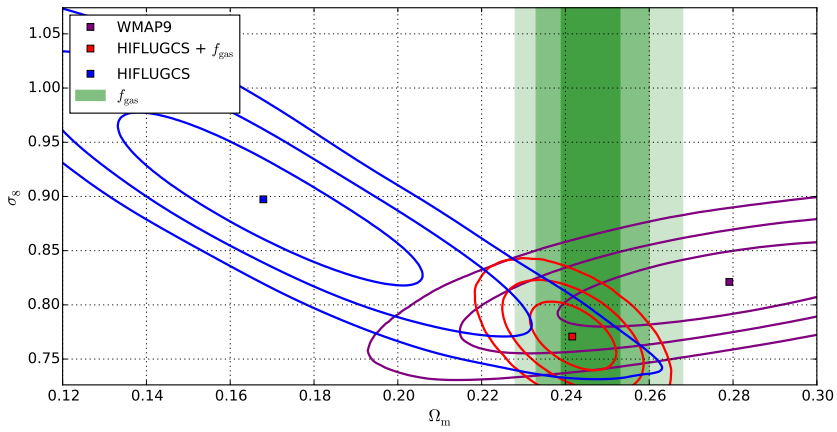

Figure 4.39: The elliptical regions and the green shaded area ($f_{\rm gas}$) correspond to the 68.3%, 95.4% and 99.7% confidence levels for a comparison that includes the gas mass fraction results on $\Omega_{\rm m}$ as a prior.

Interestingly, a discovery of possible self-interaction of Dark Matter has been made very recently (Massey et al., 2015): An offset (3.3σ significance) between the weak lensing mass peak and the optical galaxy distribution in a merging galaxy cluster can be interpreted in a way that the Dark Matter halos of the two merging systems interact also non-gravitationally (similar like the intracluster gas would do), while the galaxies are unaffected and are ahead of the Dark Matter peak. If it can be confirmed that this offset cannot be caused by other astrophysical effects (differential tidal forces or dynamical friction), this result would observationally discard the general idea that Dark Matter only interacts gravitationally and of course change the halo mass function models.

4.5.6 Gas Mass measurements

The results of the $f_{\rm gas}$ test (Section 4.4.5) alone can only constrain $\Omega_{\rm m}$, but not σ_8. The derived constraints on $\Omega_{\rm m}$ of the full sample is now added as a prior on the default setup of the halo mass function analysis. As shown in Fig. 4.39 this additional information eliminates the degeneracy between $\Omega_{\rm m}$ and σ_8 and the results seem to be very similar as if one would add the WMAP9 constraints as priors. For the setup including the $f_{\rm gas}$ priors one cannot detect any significant difference of the $L_x - M$ relation compared to the default setup. The different $\Omega_{\rm m}$ constraints of these two analysis procedures (halo mass function and $f_{\rm gas}$ test) of the same sample can probably be explained by the sensitivities of the test: $f_{\rm gas}$ is compared to hydrodynamic simulations with many degrees of freedom in the fit. Especially the mass dependence modeled by β in Eq. 4.61 gives flexibility to account for the different behavior of galaxy groups. The values of β in Table 4.3 show that when including groups the simulations clearly don't reproduce the observed behavior (high values of β), but since this parameter is free, the fit is able to account for the observed lower gas mass fractions in groups (which is also supported by other studies, see Fig. 4.23). This flexibility is not given in the mass function fit, even not when using the Bocquet et al. (2015) mass function.

Recently, Main et al. (2015) derive 45 gas mass fractions for an overdensity Δ_{2500c} for a sample that comprises some 21 strong cool core clusters from HIFLUGCS with central radio cavities, i.e. strong AGN feedback processes. Other 24 clusters are added, which also have radio cavities present. I use their Chandra derived gas mass estimates to compute $\Omega_{\rm m}$ with the same method as for HIFLUGCS. The result (Fig. 4.40) shows a much higher $\Omega_{\rm m}$, clearly not in agreement with my results. One reason could be the higher redshift range, that is covered by the Main et al. (2015) sample, which constraints $\alpha = 0.09 \pm 0.02$ (the prior is 0.02 ± 0.02). The higher redshift (> 0.3) results are not in agreement with the simulations and maybe then other parameters get biased as well, leading to the larger $\Omega_{\rm m}$ to balance out the inconsistencies. Another possibility is the selection of clusters with X-ray cavities: These clusters with strong AGN activity could have pushed out more gas than average clusters, leading to a larger $\Omega_{\rm m}$ in the fit.

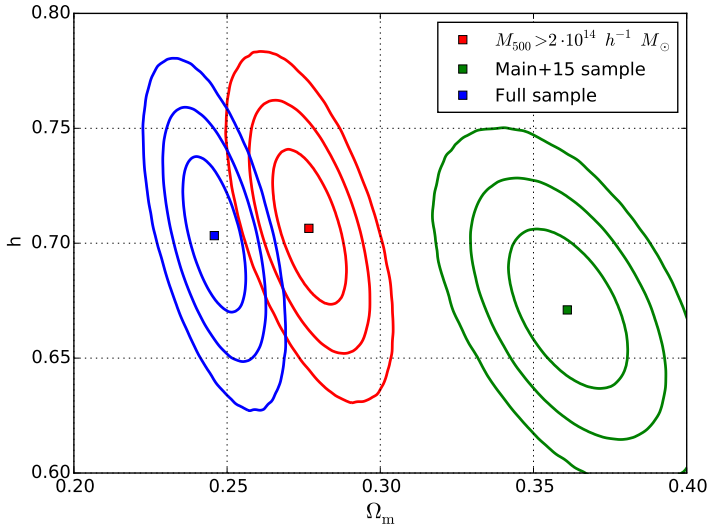

Figure 4.40: 68.3%, 95.4% and 99.7% confidence levels of the f_{gas} tests for Ω_m and h for the HIFLUGCS sample (with and without mass cut) and the Main et al. (2015) sample. f_{gas} was calculated at r_{2500}.

4.6 Conclusion

In this chapter I showed a detailed analysis of the HIFLUGCS galaxy clusters in a cosmological context, by estimating their total and hydrostatic masses individually. The focus is set on the evaluation of systematics, which can bias results. The default analysis results in $\Omega_m = 0.168^{+0.021}_{-0.019}$ and $\sigma_8 = 0.898^{+0.051}_{-0.048}$. The gas mass fraction of each galaxy cluster is also compared with simulations, which constrain $\Omega_m = 0.246^{+0.007}_{-0.007}$. The subsamples containing only the high redshift clusters ($z > 0.05$) or relaxed objects seem to show more agreement with WMAP9 results A hydrostatic bias between 10-30% on these subsamples gives excellent agreement with WMAP9. Finally, the analysis shows good agreement with independently derived dynamical mass estimates. Since the f_{gas} test shows deviations from simulations on the group scale, galaxy groups might not be modeled well by current hydrostatic simulations and this aspect needs further attention in the future.

For a detailed outlook I refer to Chapter 6.

CHAPTER 5

Substructure in Galaxy clusters: The long X-ray tail in Zwicky 8338

The previous chapters were focused on technical aspects and the cosmological conclusions that can be drawn from X-ray observations of galaxy clusters. Often there enters the assumption that galaxy clusters are ideal objects which can be described in a general way. Point sources and substructure that could bias results was excluded before. The main purpose of this chapter is to present a case of substructure within a Chandra observation of a galaxy cluster, which is in the extended HIFLUGCS sample (eHIFLUGCS), Zwicky 8338. Since no pointed X-ray observation was available before the recent Chandra observation was performed within the successful eHIFLUGCS proposal, this surprising and interesting case of galaxy and ICM interaction process was a very nice discovery. It seems to be a unique case to study X-ray tails disconnected from the host galaxy in a galaxy clusters and compare this new scenario to simulations.

This chapter has been published in Schellenberger and Reiprich, 2015 (Schellenberger, G. and Reiprich, T. H.: 2015, A&A 583, L2).

Abstract

The interaction processes in galaxy clusters between the hot ionized gas (ICM) and the member galaxies are of crucial importance to understand the dynamics in galaxy clusters, the chemical enrichment processes, and the validity of their hydrostatic mass estimates. Recently, several X-ray tails associated with gas that was partly stripped of galaxies have been discovered. We report on the X-ray tail in the 3 keV galaxy cluster Zwicky 8338, which might be the longest galaxy-scale stripping process ever observed. We derive the properties of the galaxy cluster environment and give hints on the substructure present in this X-ray tail, which is very likely associated with the galaxy CGCG254-021. The X-ray tail is extraordinarily luminous ($2 \times 10^{42}\,\mathrm{erg\,s^{-1}}$), the thermal emission has a temperature of 0.8 keV, and the X-ray luminous gas might be stripped off completely from the galaxy. From assumptions about the 3D geometry, we estimate the gas mass fraction ($< 0.1\%$) and conclude that the gas has been compressed and/or heated.

5.1 Introduction

Galaxy clusters are important tools for cosmology. They consist of galaxies, the intracluster medium (ICM), which is a very hot plasma (several 10^7 K), and dark matter. This hot gas is emitting mainly line and free-free emission in X-rays. Although the ICM undergoes many processes that affect the composition and thermal structure, a simplistic assumption is to treat galaxy clusters as relaxed objects. Understanding all these processes, which play a key role in the evolution, is essential to obtain robust constraints on parameters, such as, gas and total mass. One important process to look at is the infall and dynamics of member galaxies as initially described by Gunn and Gott (1972). Halo gas and the cold inter stellar medium (ISM) from the galaxy can then be stripped off and interact with the ICM. Part of the gas from the galaxy is then used for new stars, either in the galactic halo or outside the galaxy in the ICM (see,

e.g., Sun et al., 2007). Simulations of the interaction between ISM and ICM (e.g., Stevens et al., 1999; Kapferer et al., 2009; Steinhauser et al., 2012; Roediger et al., 2015) predict a leading bow shock and tail behind the galaxy, which are both visible in X-rays. The highest chance to find these structures is in cool nearby clusters with blue galaxies. Since an X-ray counterpart is not always found when, e.g., an HI tail is detected (see Oosterloo and van Gorkom, 2005), the process of stripping off gas from the host galaxy is still not understood completely and should be analyzed in more detail. Unfortunately only very few detections in X-rays have been made so far (e.g., Wang et al., 2004; Sun and Vikhlinin, 2005; Machacek et al., 2005; Sun et al., 2006; Randall et al., 2008; Kim et al., 2008). The interaction of the ICM with subclusters or galaxy groups can also produce X-ray bright and long tails (e.g., Reiprich et al., 2004; Eckert et al., 2014).

In our short Chandra observation of the galaxy cluster Z8338, we identify a member galaxy exhibiting a very long X-ray tail (at least 76 kpc length). It turns out that this object is already listed in the ROSAT catalog (Voges et al., 1999) as *1RXSJ181030.0+495615*. The projected distance of this galaxy from the main cluster center is 310 kpc. Surprisingly, the galaxy has probably lost all of its X-ray emitting gas very recently. The peak of the emission is 40 kpc offset from the galaxy center, so clearly this has never been seen before. Moreover, we see hints of a bow shock because of an increased temperature in a region in front of the X-ray tail. Here, we present the parameters, such as the thermodynamic structure, derived from the short observation of this very long and bright tail. It is likely the longest X-ray tail associated with a stripping process from a galaxy with the largest separation from the host galaxy ever detected. We assume a ΛCDM cosmology, with $\Omega_\mathrm{m} = 0.3$, $\Omega_\Lambda = 0.7$ and $H_0 = 71\,\mathrm{km\,s^{-1}\,Mpc^{-1}}$, to be consistent with Piffaretti et al., 2011(P11). All uncertainties are at the 68% confidence level.

5.2 Data analysis and results

For the following analysis, the CIAO Software package 4.7 and CALDB 4.6.7, as well as the HEASOFT tools 6.17 including Xspec 12.9 (Arnaud, 1996), were used. Since we are dealing with regions of few counts, we use the Xspec implemented C-statistics (Cash, 1979). For each spectral fit, we verified our parameter estimates and degeneracies by performing an MCMC within Xspec, so all derived quantities, such as the luminosity, were calculated using the distributions of the source parameters (temperature, abundance, normalization, and in some cases redshift). The steps for the data reduction follow the same structure as described in Schellenberger et al. (2015). The solar abundances are set to the values given by Asplund et al. (2009). The influence of the abundance table, especially at lower plasma temperatures on the best-fit parameters, are shown, e.g., in Lovisari et al. (2015).

5.2.1 The cluster

The galaxy cluster of interest for this work is listed in P11 with the following basic properties:

- The name is given as ZwCl8338 or MCXC J1811.0+4954.
- The equatorial coordinates are
  RA = 272.7504°, DEC = 49.9111° (J2000).
- $L_{500} = 5.3 \times 10^{43}\,\mathrm{erg\,s^{-1}}$ in the $0.1 - 2.4\,\mathrm{keV}$ energy band, which corresponds to $3.4 \times 10^{43}\,\mathrm{erg\,s^{-1}}$ in $0.5 - 2\mathrm{keV}$ band.
- $M_{500} = 1.3 \times 10^{14}\,\mathrm{M_\odot}$.
- $R_{500} = 0.767\,\mathrm{Mpc}$.
- Redshift $z = 0.0501$ (as given in Böhringer et al., 2000).

While analyzing our 8 ks Chandra observation from Observation Cycle 14 (OBSID 15163) pointed at this cluster, we discovered a comet-like structure to the west (Fig. 5.1).

Analyzing the cluster Z8338 itself by extracting spectra reveals some details about the ICM environment. In the following, the ICM emission is described by an `apec`-model (AtomDB 2.0.2) combined with a `phabs`-model to account for the Galactic absorption ($N_\mathrm{H} = 4.8 \times 10^{20}\,\mathrm{cm^{-2}}$, Willingale et al., 2013).

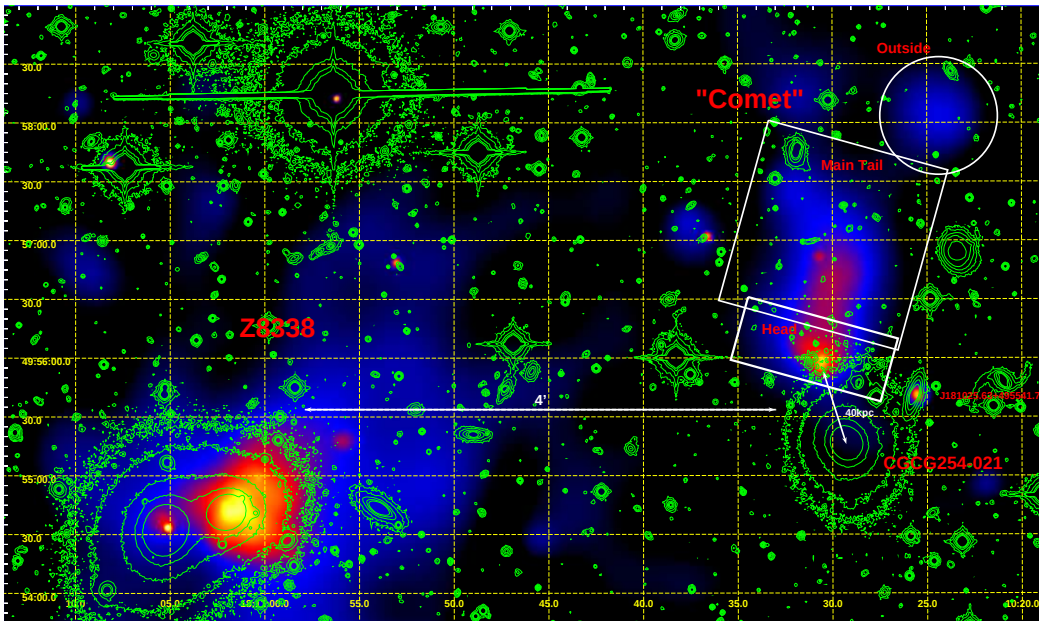

Figure 5.1: Adaptively smoothed X-ray image with V-band contours from WINGS (Fasano et al., 2006) in green. The distance of the "Comet" from the cluster center (Z8338) is 5.3′ (310 kpc). The tail of the "Comet" has roughly a length of 1.3′ (76 kpc). Two close member galaxies (CGCG254-021 and J181025.63) are labeled as well; we assume that the comet-shaped X-ray emission is due to gas stripped from CGCG254-021.

Region	kT [keV]	Z $Z_\odot$	$L_{0.5-2}$ $10^{43}\,\mathrm{erg\,s^{-1}}$
$(0-0.5)'$	$1.89^{+0.09}_{-0.10}$	$0.94^{+0.34}_{-0.25}$	$0.40^{+0.02}_{-0.02}$
$(0-4)'$	$3.09^{+0.16}_{-0.15}$	$0.64^{+0.17}_{-0.14}$	$1.48^{+0.03}_{-0.04}$
$(4-7)'$	$3.61^{+0.42}_{-0.37}$	$0.35^{+0.26}_{-0.19}$	$0.84^{+0.03}_{-0.04}$
$(0-10)'$	$2.98^{+0.17}_{-0.16}$	$0.43^{+0.13}_{-0.11}$	$2.84^{+0.06}_{-0.05}$

Table 5.1: Temperature, abundance of heavy elements, and luminosity for the cluster in different regions using a redshift of 0.05.

Several regions around the cluster center (excluding point sources and the Comet) are fitted (see Table 5.1).

Leaving the redshift free to vary in a region with high signal-to-noise, we constrain $z = 0.060^{+0.011}_{-0.022}$, which is consistent with P11. Also, the calculated luminosity within 77% R_{500} deviates by only 17% from the value in P11. For the calculation of our luminosities point sources and the Comet structure have been excluded, while this is not the case in P11. The core region of the cluster shows a significant drop in temperature. We find a cluster temperature in the annulus, which comprises the "Comet", of 3.6 ± 0.4 keV. Compared with the inner and outer regions of the cluster, this seems to be significantly higher. If one splits this annulus into one east and one west sector, the latter including the region around the Comet, we detect consistent temperatures and abundances in these two sectors.

5.2.2 The "Comet"

The structure to the west (referred to as Comet) consists of a brighter spot to the south (referred to as Head) and an elongated structure of diffuse emission (referred to as Main tail). Estimating the length of the structure by eye from the smoothed image shown in Fig. 5.1, we conclude a size of 1.2′, which corresponds to 70.5 kpc using the cluster redshift of 0.05. By extracting a profile (from equal sized boxes of 10″ width) along the tail from the (unsmoothed) exposure corrected counts image (Fig. 5.2), we are

able to fit the function

$$F(r) = \begin{cases} c + a \cdot r^{-b} \text{ , for } r > r_0 \\ c \text{ , for } r < r_0 \end{cases} \tag{5.1}$$

to the photon flux, where a, b, c, and r_0 are free parameters. With the same redshift, we find a length of 143, 98 or 76 kpc when the function reaches at c plus 1σ, 2σ, or 3σ, respectively. The flux increase in Fig. 5.2 at around $(260 - 280)$ arcsec (the red dashed line) corresponds to the light peak labeled "Outside" in Fig. 5.1. This could imply that the Comet consists of substructure and its total length extends beyond 150 kpc. In this region outside the main tail (Outside in Fig. 5.1) the temperature seems to be significantly higher than any part of the tail (Table 5.2), but still much lower than in the surrounding cluster region.

Unfortunately this structure has only around 300 source counts in this observation, so it is hard to derive any detailed properties. Still we are able to obtain rough estimates for the properties of the Comet, given in Table 5.2. As a result of the lower temperature, we decided to perform the spectral fits related to the Comet in the $(0.5 - 3)$ keV band. It turns out that the head is (with low significance) cooler than the tail, possibly due to a dense cool core. Overall, when accounting for the projected cluster emission, the Comet exhibits a temperature 0.77 ± 0.08 keV and a luminosity in the $(0.5 - 2)$ keV band of $2.0 \pm 0.2 \times 10^{42}\,\mathrm{erg\,s^{-1}}$. These properties are consistent with the expectations for X-ray tails (e.g., Sun et al., 2006), only the luminosity is almost one order of magnitude higher. Despite the large uncertainties, there might be indications that the tail has a much lower abundance of heavy elements than the head of the Comet, which is again consistent with the head being the remnant of a cool core.

We tried to determine the redshift from the spectrum with the highest count number and got a value $(0.062^{+0.028}_{-0.047})$ consistent with that from the cluster spectrum, so we assume that the Comet is interacting with the ICM of Z8338. Also, comparing the measured X-ray flux of the Comet with those of small galaxy groups using the L-T relation from Lovisari et al. (2015), we conclude a redshift range $z = 0.036^{+0.021}_{-0.012}$, which also excludes this structure from being a background cluster.

Having the gas properties, such as X-ray luminosity and temperature as well as the redshift of the Comet in hand, one can calculate the gas mass assuming a 3D shape. Since the information on the properties has large uncertainties and to obtain a rough estimate, we assume a cylindrical shape with $1.2'$ height and $0.15'$ radius. We calculate $M_{\mathrm{gas}}^{\mathrm{Comet}} = 1 \times 10^{10}\,\mathrm{M_\odot}$. Assuming the Comet is a small galaxy group, one can use a scaling relation to convert the X-ray luminosity into the total mass at the structure the Comet used to reside in, assuming it has been stripped. With the bias corrected $L - M$ relation for galaxy groups from Lovisari et al. (2015), we estimate a total mass for the Comet structure of $M_{\mathrm{tot,LM}}^{\mathrm{Comet}} = 2 \times 10^{13}\,\mathrm{M_\odot}$ and a gas mass fraction of 0.04%. We estimate $M_{\mathrm{tot,MT}}^{\mathrm{Comet}} = 1.6 \times 10^{13}\,\mathrm{M_\odot}$ and a gas mass fraction of 0.06% with the $M - T$ relation from the same reference. For a total mass in this range, a gas mass fraction of $3 - 7\%$ is expected (Lovisari et al., 2015). Even when we dramatically increase our rough estimates for the cylinder (radius $\times 2$, height $\times 1.5$), we still get an upper limit for the gas mass fraction of $\sim 0.1\%$. These values indicate that this object is far too luminous and hot than what is expected for its size. This could indicate that the gas is compressed, e.g., by tidal ram pressure stripping processes, or heated by shocks or compression. However, assuming that the gas originally was attached to a small galaxy group and now almost completely left the gravitational potential, it is expected that at least the outer parts of it undergo adiabatic expansion. This would not only cool down the gas, but also lower its density, making it more difficult to detect X-rays resulting in both an underestimated gas mass and underestimated luminosity and total mass.

With the use of the spectrum of our observation of the cluster in the $(4 - 7)'$ annulus, we can roughly estimate the pressure, $5.4 \pm 0.6 \times 10^{-12}\,\mathrm{erg\,cm^{-3}}$, and density, $8.0 \pm 0.3 \times 10^{-28}\,\mathrm{g\,cm^{-3}}$, around the Comet. Simulations in Kapferer et al. (2009) show that for a relative velocity between the surrounding gas and the galaxy of $v_{\mathrm{rel}} = 1000\,\mathrm{km\,s^{-1}}$ and pressure that is eight times higher and surrounding density that is six times higher, the scenario of a completely stripped gaseous disk can be explained. This might be a hint that the relative velocity of the galaxy is significantly larger. Owing to the very low number of counts, we find an interesting but weak hint from a spectral analysis that there might be a high temperature region in front of the Comet. A test to mirror the same region on the other side of the cluster strengthens this hypothesis since there we measure a temperature consistent with that in this cluster annulus (Table 5.1). Unfortunately, we are not able to detect a surface brightness enhancement connected to the hypothesized bow shock region, which in turn weakens this idea.

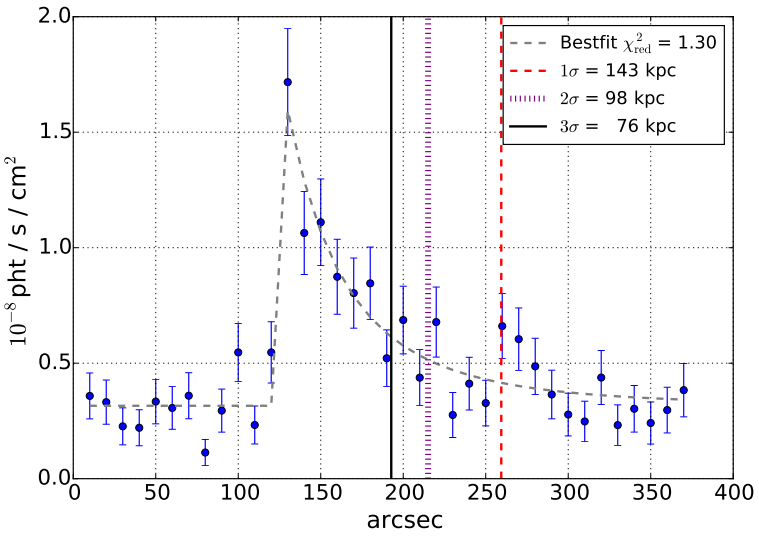

Figure 5.2: Photon flux profile across the Comet structure from south to north.

Region	kT keV	Z $Z_\odot$	$L_{0.5-2}$ $10^{43}\,\mathrm{erg\,s^{-1}}$	S/N
Head	$0.72^{+0.09}_{-0.09}$	$0.25^{+0.22}_{-0.12}$	$0.13^{+0.02}_{-0.02}$	
Tail	$0.93^{+0.16}_{-0.13}$	$0.05^{+0.05}_{-0.03}$	$0.17^{+0.02}_{-0.02}$	
Full Comet	$0.81^{+0.08}_{-0.07}$	$0.09^{+0.04}_{-0.03}$	$0.28^{+0.02}_{-0.02}$	
Head*	$0.68^{+0.11}_{-0.17}$	$0.32^{+0.93}_{-0.24}$	$0.10^{+0.02}_{-0.01}$	10
Main Tail*	$0.80^{+0.12}_{-0.11}$	$0.06^{+0.04}_{-0.03}$	$0.13^{+0.02}_{-0.01}$	11
Full Comet*	$0.77^{+0.08}_{-0.07}$	$0.14^{+0.08}_{-0.06}$	$0.20^{+0.02}_{-0.01}$	14
Outside*	$1.17^{+0.14}_{-0.18}$	0.05 fixed	$0.04^{+0.02}_{-0.01}$	5

Table 5.2: Best-fit temperature, relative abundance of heavy elements, X-ray luminosity, and signal-to-noise ratio using a redshift of 0.0501. The * marks fits, where the cluster emission in $(4-7)'$ was simultaneously fitted and accounted for (the S/N could only in these cases be calculated properly, since the cluster emission is accounted for in the noise).

5.3 Counterparts in other wavelengths

We find galaxies in the vicinity of this structure with publicly available image data from the Wide-field Infrared Survey Explorer (WISE, Wright et al., 2010) and the WINGS survey (Fasano et al., 2006; Varela et al., 2009; Valentinuzzi et al., 2009) : To the south we can identify the 14.126 $\mathrm{mag_V}$ galaxy CGCG254-021 (also called J181029.20+495517.0; Fritz et al., 2011, F11) with a stellar mass of $1.36 \pm 0.01 \times 10^{12}\,\mathrm{M_\odot}$, which seems unusually high. This galaxy is listed as a member galaxy of Z8338 (Smith et al., 2004; and a spectroscopic redshift of 0.0511 in Cava et al. (2009), in agreement with the cluster redshift in P11). According to F11, this is the galaxy with the highest mass, by far the highest star formation (SF) rate in the past ($5.5\,\mathrm{M_\odot/yr}$, while no SF is detected in current age), and the highest age within Z8338. Hence, this galaxy was a large starburst galaxy and is now clearly dominant over other objects in Z8338 in the region around the Comet.

With the colors $(\mathrm{B-V}) = 1.1$ and $(\mathrm{U-B}) = 0.95$ (Varela et al., 2009; Omizzolo et al., 2014) the galaxy CGCG254 is clearly an early-type galaxy (de Vaucouleurs, 1961). Since the bolometric X-ray luminosity compared to the B-band luminosity seems to agree with what is expected for BCGs, as shown by O'Sullivan et al. (2001), one can raise the assumption that the galaxy was the BCG of a galaxy group. Jeltema et al. (2008) have shown that also the X-ray and near-infrared (K-band) luminosity of early-type galaxies in clusters and groups are correlated. Applying their relation for clusters and using infrared data

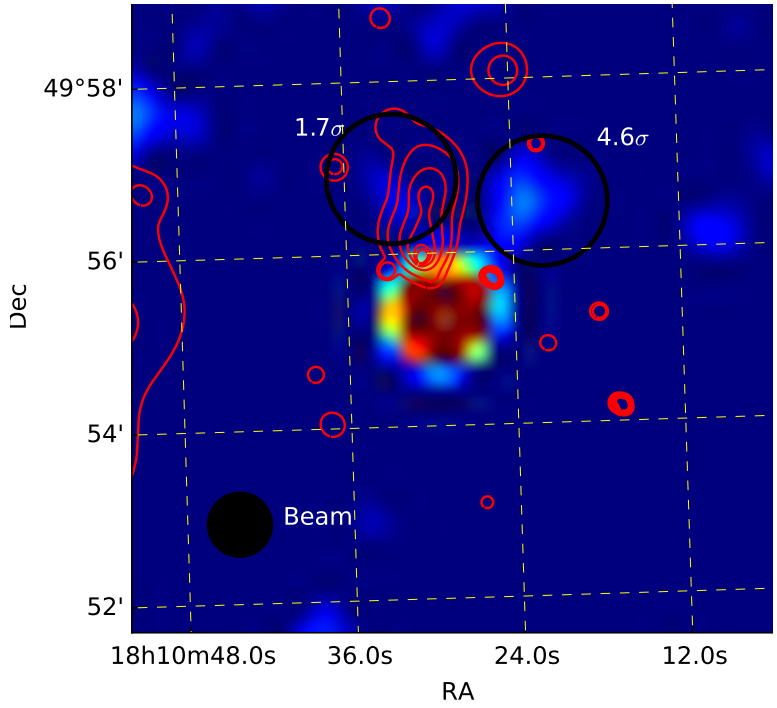

Figure 5.3: The 21 cm-Radio continuum from NVSS showing two possible bent radio lobes qualitatively, which follow the expected direction of motion from the X-ray morphology (red). The significance of the possible detections are indicated.

from 2MASS (Skrutskie et al., 2006) we find a predicted $L_X = 3.7^{+0.8}_{-0.7} \times 10^{40}\,\mathrm{erg\,s^{-1}}$, which is almost two orders of magnitude lower than measured. Instead, the predicted and measured X-ray luminosities are almost consistent when assuming that the galaxy is a field galaxy, which has not lost gas from the interaction with the cluster ICM.

In Fig. 5.1 we can also see that a cone at the end of the head (region "Head" in Fig. 5.1) of the structure is pointing toward the galaxy. The galaxy has a radio counterpart visible in the NVSS image (Condon et al., 1998, Fig. 5.3). Interpreting qualitatively the radio morphology as due to bent lobes of the radio AGN at the center of CGCG254, the inferred direction of motion (south) is consistent with that inferred from the X-ray morphology at the Comet. Unfortunately, the radio signal is very weak (1.7 and 4.6 σ), so this assertion needs a deeper radio observation to be confirmed. The optical/N-IR source to the south west of the Comet is a galaxy (J181025.63+495541.7) with a V-band magnitude of 16.6 (see Varela et al., 2009) and a redshift of $z = 0.051$ (Smith et al., 2004), so this galaxy most likely belongs to the cluster but we see no indications of interaction with it or the Comet or CGCG254.

Compared to the 70 kpc X-ray tail of a galaxy analyzed in Sun et al. (2006), this X-ray tail is about 20 times more luminous. The Chandra ACIS-I count-rate for our object is 40% higher than that of the X-ray tail in Sun et al. (2006), while the two objects have a very similar temperature structure. This means the amount of gas that apparently has been stripped of the galaxy is very high, or the galaxy lost almost all of its gas to the ICM. If this scenario was confirmed by the analysis of a longer observation, one would have the chance to study in detail the properties of this interaction for such a luminous and massive object.

5.4 Conclusion

In our short Chandra observation of Zwicky 8338, we identify a long X-ray tail, of which we study the properties. We measure the surrounding ICM to have a temperature of 3.6 ± 0.4 keV. The X-ray tail itself shows thermal emission with a temperature of 0.77 keV. Indications point to a head-tail structure within the X-ray tail: A cooler, but more metal rich part has a very peaked brightness distribution, while

the other part is more diffuse. The 14 $\mathrm{mag_V}$ galaxy CGCG254-021 is very close to this X-ray object and several indications point to the scenario that the X-ray tail is stripped gas from this galaxy or from a small galaxy group with this galaxy as its BCG:

- The projected distance between the peak of the X-ray tail and the galaxy center is only 40 kpc.
- The redshift of galaxy and X-ray tail are consistent with the cluster redshift.
- The apparently bent radio lobes from the galaxy's AGN are consistent with the inferred direction of motion.
- The galaxy is the brightest galaxy within this region with the highest star formation rate in the past.
- The tail's gas mass inferred from the X-ray luminosity is far too low for its estimated total mass, if one compares these values with galaxy group scaling relations.
- The stellar mass of the galaxy is consistent with those of BCGs in galaxy groups.

With a deeper X-ray observation, it would be possible to characterize more detailed properties as well as a definite scenario for the interaction history.

CHAPTER 6

Conclusion and outlook

In the past chapters I showed a detailed analysis of the HIFLUGCS galaxy cluster sample, which explores several aspects: A local sample of galaxy clusters used for cosmology and the evaluation of systematic effects, such as the instrumental calibration uncertainties, selection effects or the influence of physical effects. Here, I will summarize and give future prospects.

6.1 Calibration

Galaxy clusters are excellent targets to perform a cross calibration between X-ray instruments, such as Chandra and XMM-Netwon, because they are bright, extended and not time variable. I showed that using the X-ray brightest galaxy clusters, I can quantify with high precision the energy dependency of the normalized residuals of Chandra ACIS and XMM-Newton EPIC. These residuals are model independent and show directly the calibration uncertainties between two instruments. The result can be summarized as a significant, energy dependent flux difference between ACIS and any EPIC instrument in a soft energy band until 3 keV, where ACIS fluxes are higher with increasing energy. Due to this energy dependence the best-fit temperatures for the ICM emission are affected and Chandra ACIS gives higher temperatures than any XMM detector. The high energy band is much less affected and the conclusion on the temperature difference also holds when the fit is performed in a broad energy band. Tests and simulations have been carried out to confirm that the measured temperature differences are due to calibration uncertainties of the effective area and cannot be explained by multitemperature structure of the gas or the different spatial resolutions of the instruments. Although a final conclusion on which instrument is correct cannot be drawn, two tests show that with larger samples and longer observation times implying better knowledge on the multitemperature structure, it is in principle possible to give an absolute calibration: The free-$N_{\rm H}$ test constraints the Hydrogen column density from the X-ray spectra and compares it to reference values (e.g., from radio HI). Although at first Chandra shows better agreement, uncertainties in the relative solar abundance table lower the significance of this result drastically. By comparing the soft and hard band temperatures of the same instrument, a similar picture can be drawn: Chandra shows acceptable agreement while XMM-Newton EPIC-PN does not. But in the latter test the multitemperature structure has a big impact on the agreement of temperatures measured in different bands, independently of the calibration uncertainties. Unless the detailed temperature structure is known, this test remains inconclusive as well.

Outlook

In the future I am able to combine the HIFLUGCS deprojected temperature and density profiles to model the structure and re-test soft vs. hard band temperatures of each instrument. Furthermore, the $N_{\rm H}$ test might improve by adding statistical power using more galaxy clusters, increasing the extraction regions to shrink the uncertainties and using a more recent abundance table, like Lodders and Palme (2009). Also the uncertainties of the reference $N_{\rm H}$ values need to be accounted for. One possibility to achieve an absolute calibration is to add more instruments to the cross calibration (see Burrows et al., 2014, Sec. 1.3) and check where most of them show agreement with each other (assuming the instruments give independent

measurements of the same source quantity, such as flux). For future instruments, like eROSITA, this is of special interest since for some clusters temperature estimates will come directly from the survey data and enter in the cosmological analysis. One very important test that can point toward an absolute calibration of ICM temperatures is the emission line ratio temperature, that I will describe in more detail in the following.

Line ratio temperatures

Emission lines from heavy elements are induced when an atom is in an excited state and a photon is emitted with the energy difference between the initial and final state (see also Section 1.1.4). The probability to emit the photon, which is proportional to the intensity of the line, depends on the temperature of the gas, and reaches a peak value at a transition specific temperature T_p. Under the assumption of collisional ionization equilibrium one could precisely determine the gas temperature just by measuring the line intensity and knowing the number of atoms of the specific element in the gas. This temperature estimate would be independent of effective area calibration uncertainties since these do not vary much within the width of the line. By comparing two different emission lines of the same element, which have different peak temperatures, one does not even have to know the number of atoms. The ratio of these two line intensities only depends on the plasma temperature. This method was used, e.g., by Gastaldello and Molendi (2004) and used for cross calibration in Nevalainen et al. (2010). Elements which are well suited for this exercise are for example the Helium-like and Hydrogen-like Iron atoms (FeXXV, FeXXVI), or the Sulfur S-XV and S-XVI emission lines. Some important lines are summarized in Tab. 6.1. To identify the

Element	Ion	Transition	Line energy	T_p
			keV	keV
Iron	XXV	$7 \rightarrow 1$	6.7	5.4
	XXVI	$4 \rightarrow 1$	7.0	10.9
Sulfur	XV	$7 \rightarrow 1$	2.5	1.4
	XVI	$3 \rightarrow 1$	2.6	2.2
Silicon	XIII	$7 \rightarrow 1$	1.9	0.9
	XIV	$4 \rightarrow 1$	2.0	1.4

Table 6.1: Important emission lines and the peak temperature T_p of the intensity.

correct plasma temperature and eliminate calibration uncertainties one should use lines which peak at a high temperature ($> 4\,\mathrm{keV}$), where also the calibration uncertainties play a major role. Moreover, for temperature determination, emission lines should contain many counts so they can be well determined. This requires long exposure times on bright, hot clusters. But the emission lines with low T_p, such as Silicon and Sulfur (Tab. 6.1), can still be used to confirm the broad band temperatures and to show that the method works. Practically, one can model the emission lines by Gaussians and add a free-free emission model for the continuum, but since the lines often consist of complexes, this is not a very good model of the data or one would need many Gaussians. Another approach, which I started implementing, is to model the emission by two plasma models, one where the specific element is turned off (e.g., by setting the element abundance to zero), and another where the normalization is fixed to a very small value and the element of interest gets a very large abundance. The temperature of this second plasma model is only determined by the line emission of one specific element. Simulations have shown that by creating fake spectra with an input temperature and fitting the spectra with a modified response (to simulate calibration uncertainties), the input temperature can be recovered from the Iron emission lines. This procedure has been tested on A85 using a recent, very long XMM-Newton observation (see Fig. 6.1). The selected region is an annulus from 80 to 120″ around the emission peak. It seems that the Iron line temperatures are larger than the broad band temperatures, but due to the large uncertainties the significance is small. Also the expected Chandra temperatures can be probably not reached, so in this case the correct temperature might be

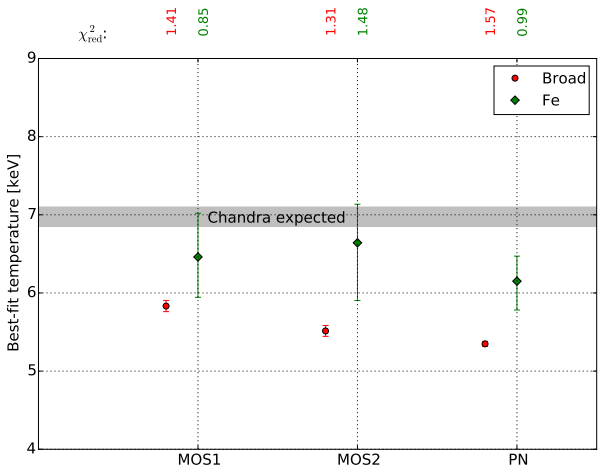

Figure 6.1: Best-fit temperature for Abell85 (XMM-Newton observation 0723802201) from a broad-band fit, $(0.7-7)$ keV, and the line ratio temperatures for the three detectors. The expected Chandra temperature (estimated using the scaling from Schellenberger et al., 2015) is indicated as a gray bar. The reduced χ^2 values indicate the goodness of fit.

between the MOS1 and ACIS. Note that due to the high quality data, the broad band fits are not very good and calibration uncertainties and possible multitemperature structure prevents a single temperature fit to give $\chi^2_{\rm red} \approx 1$. Since in the center of the cluster, the emission is more intense, constraints on the line temperatures improve, but at the same time the temperature drops (since it is a cool core cluster) and effects like resonant scattering (Churazov et al., 2004; Gastaldello and Molendi, 2004) bias results in high density regions. Future work will also comprise a detailed analyis on the effects of multitemperature plasma on the line ratio temperatures.

6.2 HICOSMO

The HIFLUGCS cosmology project uses a complete, X-ray selected, purely flux limited sample of 64 local galaxy clusters to constrain cosmological parameters and calibrate the $L_x - M$ scaling relation simultaneously. Masses of the galaxy clusters have been calculated individually for each cluster from the temperature and surface brightness profiles. A crucial step was to perform the extrapolation of the mass, since the Chandra FOV and, for some clusters, the limited exposure time, does not allow to measure the temperature and its gradient at r_{500}. Several different methods are proposed to perform the extrapolation, either simply by using models for the temperature profiles, which can produce (unphysical) decreasing total mass profiles in the outer regions, or by using an NFW model. The NFW fit with a concentration parameter linked to the total mass, was used as default in the end.

Cosmology was constrained by applying the Tinker et al. (2008) halo mass function. Results suggest a value for $\Omega_{\rm m} = 0.168^{+0.021}_{-0.019}$ and $\sigma_8 = 0.898^{+0.051}_{-0.048}$, which are not in agreement with current reference values from CMB observations. Without implying that the CMB results are perfectly correct, I started several test to measure the robustness of these constraints: Simple tests like excluding some extreme clusters (fluxes which are just at the flux limit, large deviations from the $L_x - M$ relation), did not show a significant effect. Systematic modifications of the sample selection function, like a redshift cut, revealed an interesting trend: The high redshift subsample shows larger uncertainties, as expected, but is also more in agreement with CMB measurements. The low redshift subsample, containing all the groups of the full sample, exhibits a much steeper $L_x - M$ relation and even lower $\Omega_{\rm m}$ values. Since some effects, like the influence of galaxy groups, seems to be important, this was evaluated in more detail:

- The tension between the HIFLUGCS and CMB results could not be solved by using a broken powerlaw to model the $L_x - M$ relation. The shallower behavior at the high-mass scale will not allow many massive clusters to exceed the flux limit. This leads to an increase in σ_8.

- Reducing the predicted number of groups (by using a smaller skyfraction) shifts the constraints toward the CMB results. This means that theory predicts many more groups than measured. But the decrease needed to achieve agreement is too large to be physically motivated (e.g., by the incompleteness of the catalogs).
- Introducing a hydrostatic bias shifts both, Ω_m and σ_8, to higher values. The hydrostatic bias needed for the high redshift subsample to be in perfect agreement with CMB results, is $(1-b) = 0.83^{+0.11}_{-0.12}$.
- Dynamically disturbed clusters, which often violate (to some extend) hydrostatic equilibrium, can bias results, since the exclusion of this subsample leads to higher values of Ω_m and lower values of σ_8. For the relaxed clusters to be in agreement with WMAP9 a bias $(1-b) = 0.66^{+0.10}_{-0.12}$ is needed.
- Baryonic effects (e.g., feedback processes) are expected to play a significant role for low mass systems. Using a mass function which incorporates these effects shows only minor changes: Compared to a consistently derived Dark Matter only mass function, the change is completely insignificant. But also the difference between this more recent Dark Matter only mass function and the default halo mass function used here is small (6% lower σ_8). This is also a reverse trend than what is observed for a WMAP9 cosmology (where the default halo mass function gives smaller σ_8 values), so there might be some small universality problems of one of the mass functions.
- A summed mass of the neutrino species above 0.5 eV shows a significant effect by shifting the Ω_m-σ_8 ellipse along the degeneracy toward higher values of Ω_m. But other measurements, like the Planck Satellite, show that these neutrino masses are too high.
- The dynamical mass estimates (from Zhang et al., in prep.) for HIFLUGCS show broad overlap of the 68.3% regions of Ω_m and σ_8, compared to the default analysis. Introducing a hydrostatic bias $(1-b) = 0.8$ on the default analysis, lowers the discrepancy to the dynamical mass estimates even more.

In sum, the effect of galaxy groups and/or disturbed objects in HIFLUGCS seems to bias results toward lower Ω_m, assuming the CMB values are correct. Due to large uncertainties of the results of subsamples, the changes are often at low significance. The f_gas test also shows, that galaxy groups need to be treated more carefully. Simulations are not able to recover the values of f_gas for low massive system, so the suspicion can be raised that halo mass function simulations can also not reproduce the low massive systems well. Combining the constraints of the f_gas test with the halo mass function, one achieves rough agreement with WMAP9 results.

Outlook

The results reveal several aspects, that can be studied in more detail in future works:

- The halo mass function is still uncertain. At overdensities $> \Delta_{200\mathrm{m}}$ the universality might have to be tested in more detail, since two mass functions evaluated here show different trends at different cosmologies. Furthermore, the effort spend on including ICM feedback in the simulations seems not to have a big effect for the HIFLUGCS sample, although it consists of several galaxy groups. As the f_gas test also showed, these galaxy groups are not well modeled by simulations and need to be investigated further. In the future, the apparent ellipticity of halos can be included, which makes it possible to match better the observed properties of clusters.
- Galaxy clusters are excellent tools to constrain cosmology. Although, a lot of confidence is given to the CMB results (like WMAP or Planck), a disagreement with galaxy cluster cosmology reveals interesting facts about the Universe: Either the cluster physics is not understood well and needs to be studied in more detail, or unknown effects, like massive neutrinos, a coupling between Dark Matter and Dark Energy, or theories of modified gravity can ease the tension. Therefore, larger samples of galaxy clusters are needed, which also cover a wide range of redshifts and masses.
- The extended HIFLUGCS sample, eHIFLUGCS, consists of 183 galaxy clusters, comprising all HIFLUGCS clusters. Naively this would lead to $\sim 41\%$ lower uncertainties. But since also the

$L_x - M$ relation will be constrained better, especially at the low and high mass end, in reality the uncertainties might be even lower. Using the eHIFLUGCS fluxlimit ($9 \times 10^{-12}\,\mathrm{erg\,s^{-1}\,cm^{-2}}$), I created a fake sample with the cosmology and $L_x - M$ relation of from HIFLUGCS. The observed skyfraction was lowered by 8% (to a skyfraction of 59.6%) to match the number of given eHIFLUGCS clusters. The uncertainties on the 4 parameters (Ω_m, σ_8, slope and intercept of the $L_x - M$ relation) for the fake-eHIFLUGCS sample are on average 45% lower than for HIFLUGCS. Some of the clusters of the eHIFLUGCS sample have been analyzed already: A mass determination of the clusters, which only have XMM-Newton observations, was already performed by Florian Käfer (MSc Thesis, 2015). I started also a preliminary analysis of some Chandra observations for eHIFLUGCS and determined

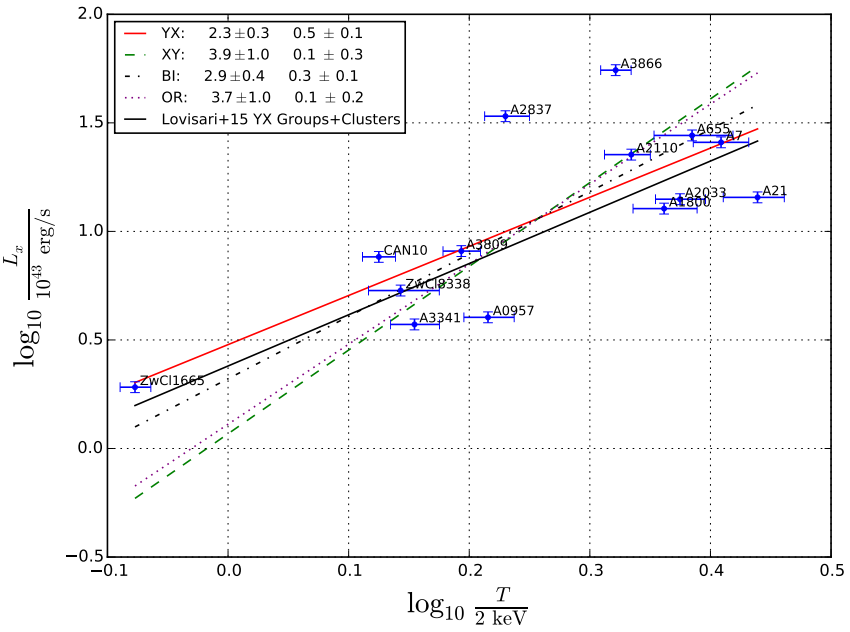

Figure 6.2: Luminosity – temperature relation for 14 eHIFLUGCS clusters observed with Chandra. Luminosities are taken from Piffaretti et al. (2011). The values in the legend represent the slope and intercept for the $L_x - T$ relation, respectively.

the overall temperatures (within an aperture that maximizes the S/N, see Fig. 6.2). This shows good agreement with the results for groups and clusters in Lovisari et al. (2015). In the future eHIFLUGCS will help to solve the questions raised before, e.g., if galaxy groups bias the halo mass function analysis.

6.3 X-ray tail in Z8338

In contrast to the other Chapters, which focused on a systematic analysis of a whole sample in a consistent way, Chapter 5 describes the study of an individual object, which was found a recent Chandra observation of the eHIFLUGCS sample – the X-ray tail in Zwicky 8338. The interesting object, one of the longest X-ray tails ever found with the connection to a galaxy, is an example for the interaction process between the hot ICM, which is of extraordinary importance for the cosmological study, and an infalling galaxy. The indirect relation to cosmology, since this X-ray tail could on the one hand bias results and on the other hand indicate a merging system, is not of primary interest here. Instead I compare an evolutionary step of this cluster with simulations, to see whether to what extend the dynamical and chemical enrichment processes have been understood. It is the first time that an observation of an X-ray tail which is completely disconnected from the host galaxy in a galaxy cluster has been made. I actually showed by estimating the X-ray tail's redshift from the spectra and the X-ray luminosity compared to its temperature, that there is interaction

related to the ICM of Z8338. The X-ray tail originates from the early-type galaxy CGCG254-021, due to the proximity and the inferred direction of motion. This galaxy is very bright and seems to have a high initial star formation rate. Interestingly, the expected X-ray luminosity for a field galaxy is almost consistent with the observation, pointing toward the scenario of stripped gas. Unfortunately, the enrichment of the cluster ICM with heavy elements and a detailed study of the temperature structure can only be achieved with longer observation.

6.4 Final remarks

In sum, I demonstrated how the X-ray analysis of galaxy clusters is important for both, cosmological constraints on our Universe, and the understanding of their evolution and astrophysical interactions. In all cases, systematics can easily bias results and lead to wrong conclusions, so already the comprehensive understanding of the instrument is essential.

APPENDIX A

Temperature and mass profiles

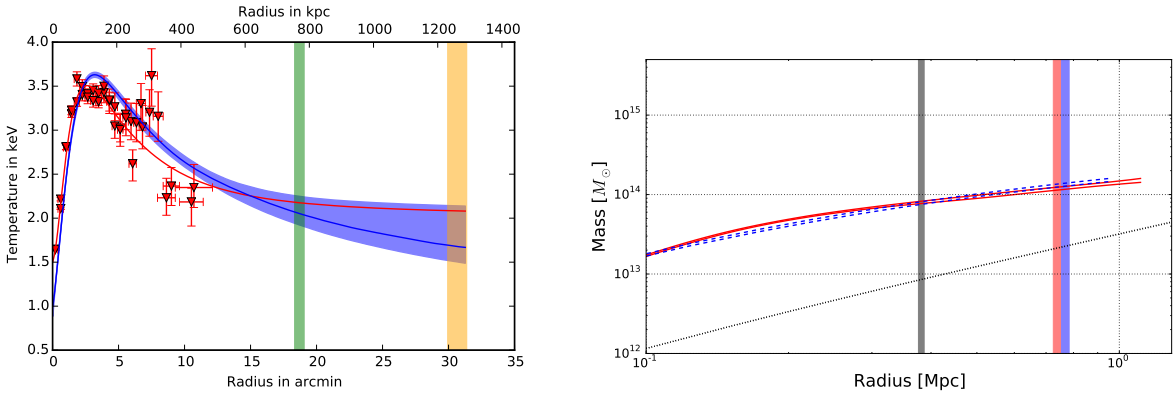

Figure A.1: Temperature and mass profiles for 2A0335. The left panel shows the measured temperatures (red datapoints) and the best fit model (red line), while the deprojected temperature is represented by the blue line. The green and orange regions show r_{500} and r_{200} (from the NFW-Freeze model) estimates, respectively. The right panel shows the total mass of the temperature profile extrapolation (red), and the NFW-Freeze model (blue). The black lines show the gas mass estimates. The red and blue vertical regions represent the corresponding r_{500}, the black region r_{2500} from the temperature extrapolation method. All regions are 68.3% confidence levels.

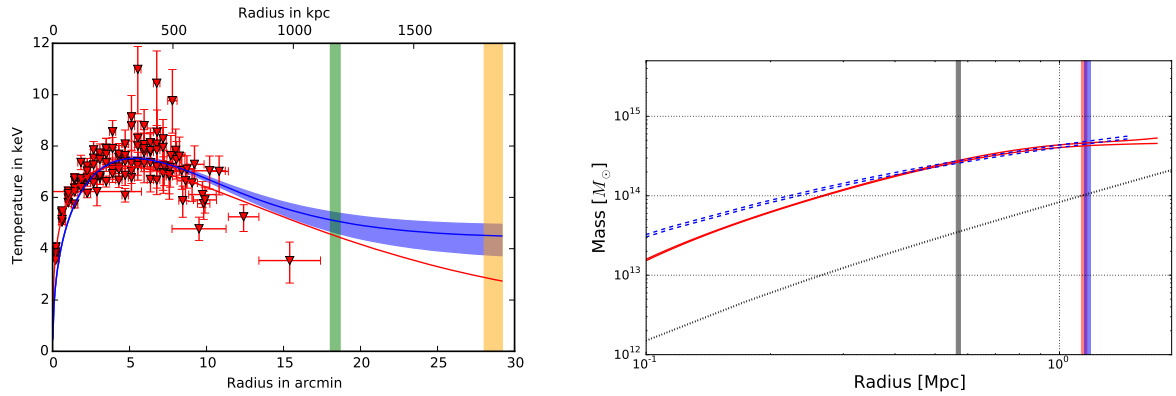

Figure A.2: As Fig. A.1 but for A0085.

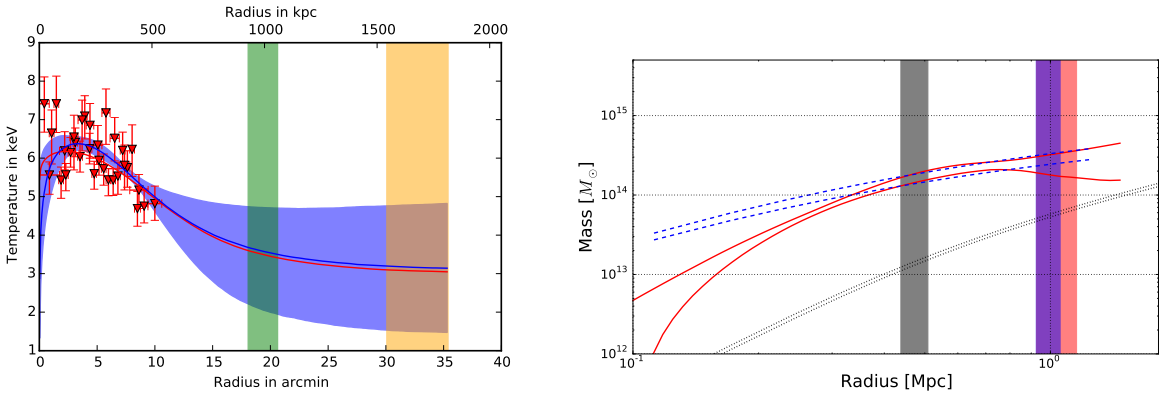

Figure A.3: As Fig. A.1 but for A0119.

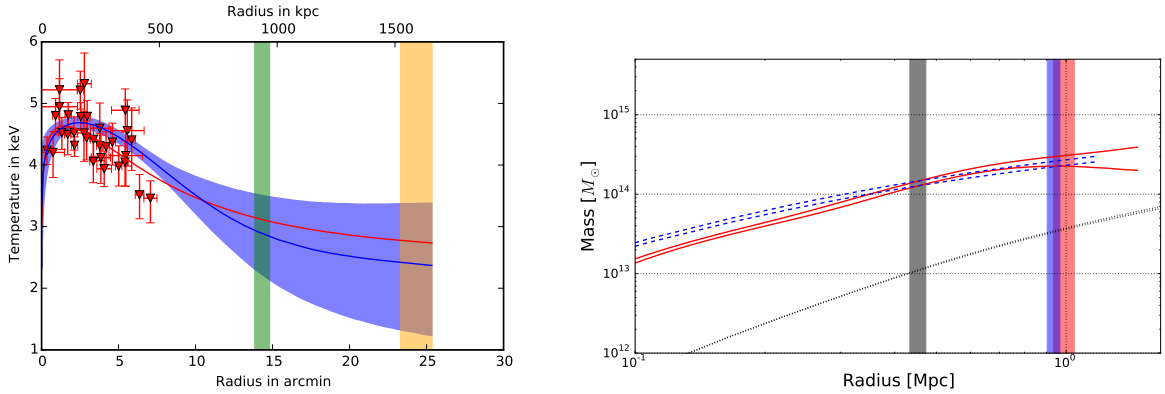

Figure A.4: As Fig. A.1 but for A0133.

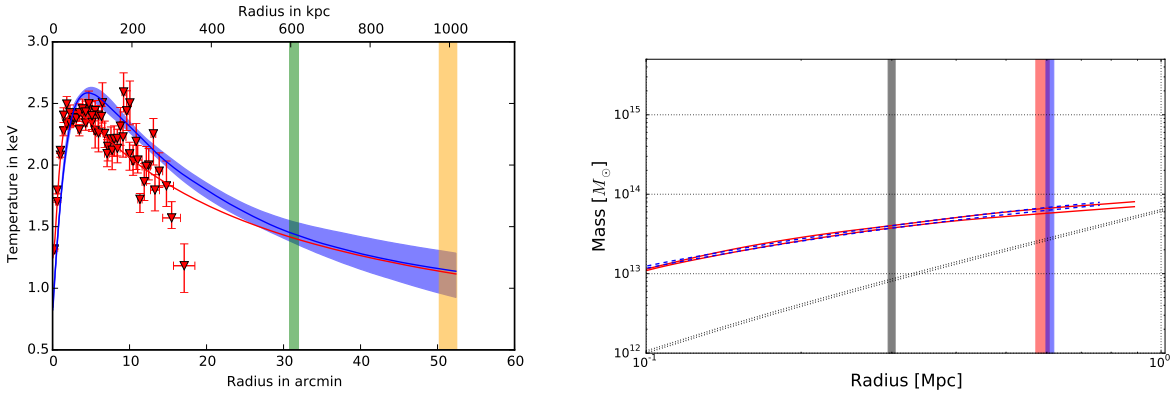

Figure A.5: As Fig. A.1 but for A0262.

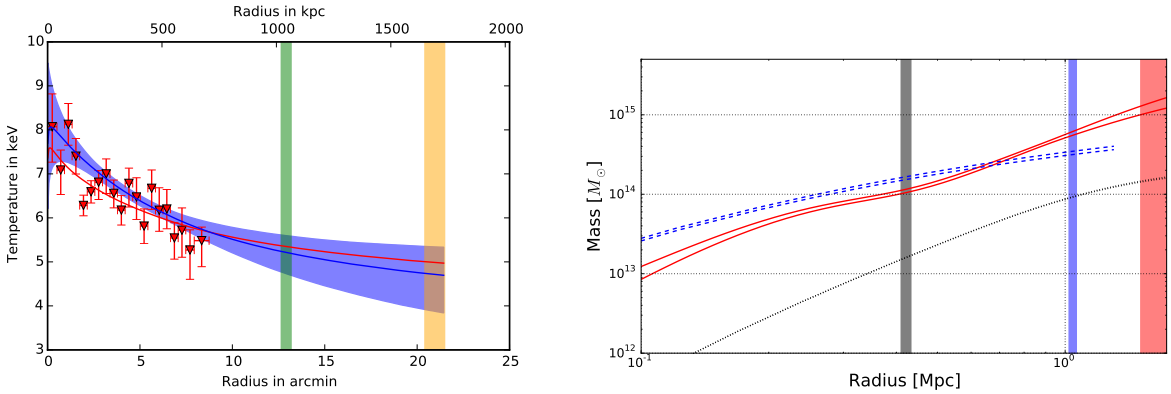

Figure A.6: As Fig. A.1 but for A0399.

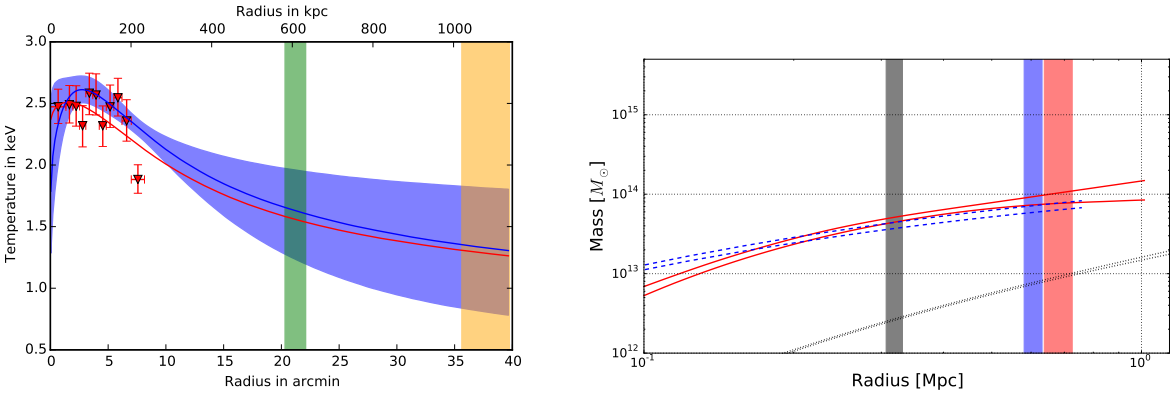

Figure A.7: As Fig. A.1 but for A0400.

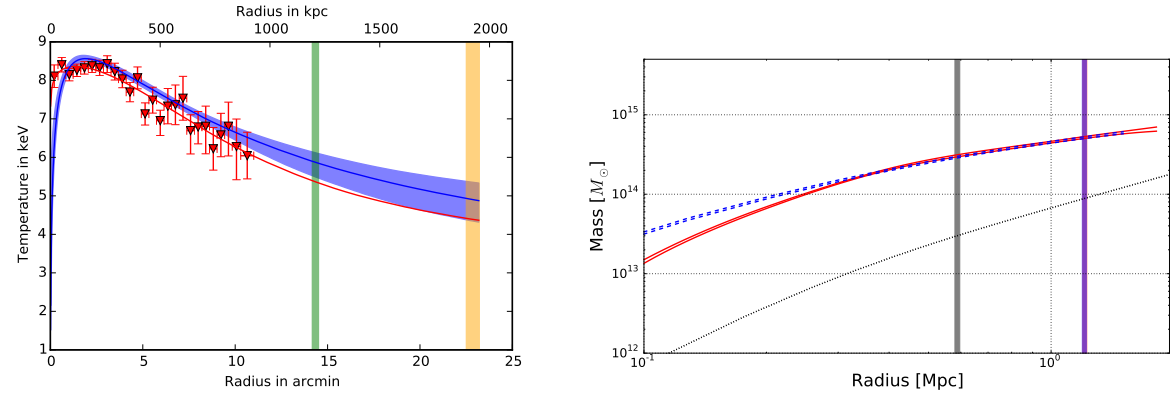

Figure A.8: As Fig. A.1 but for A0401.

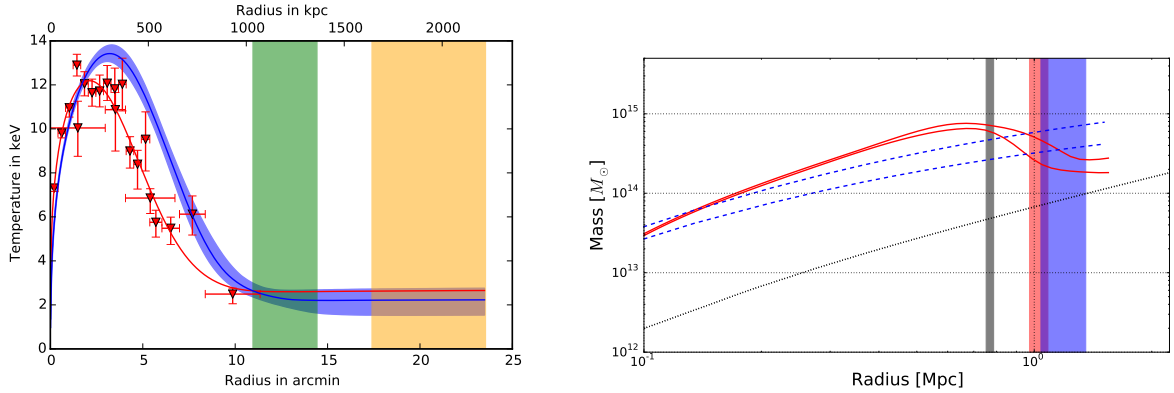

Figure A.9: As Fig. A.1 but for A0478.

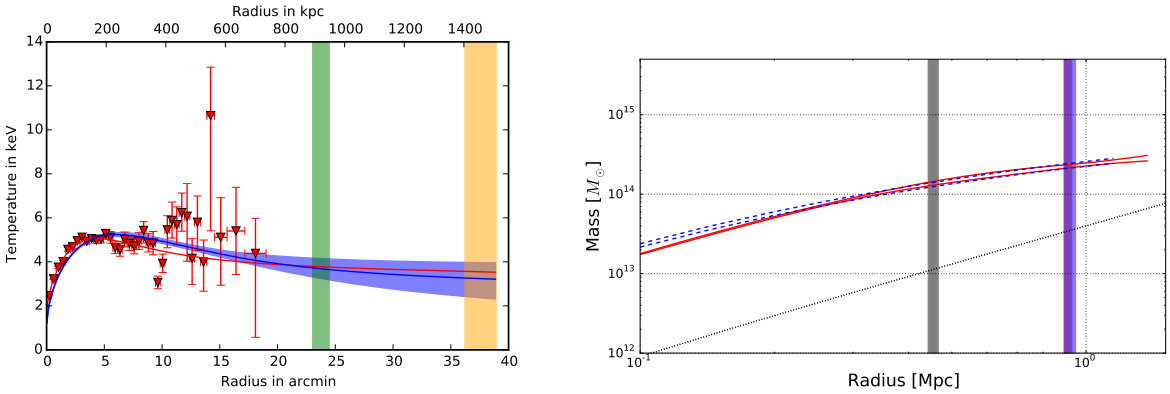

Figure A.10: As Fig. A.1 but for A0496.

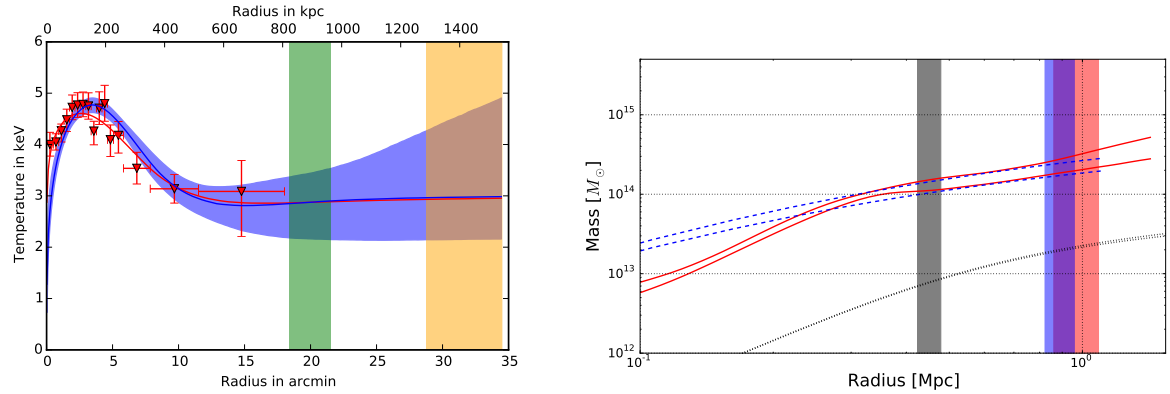

Figure A.11: As Fig. A.1 but for A0576.

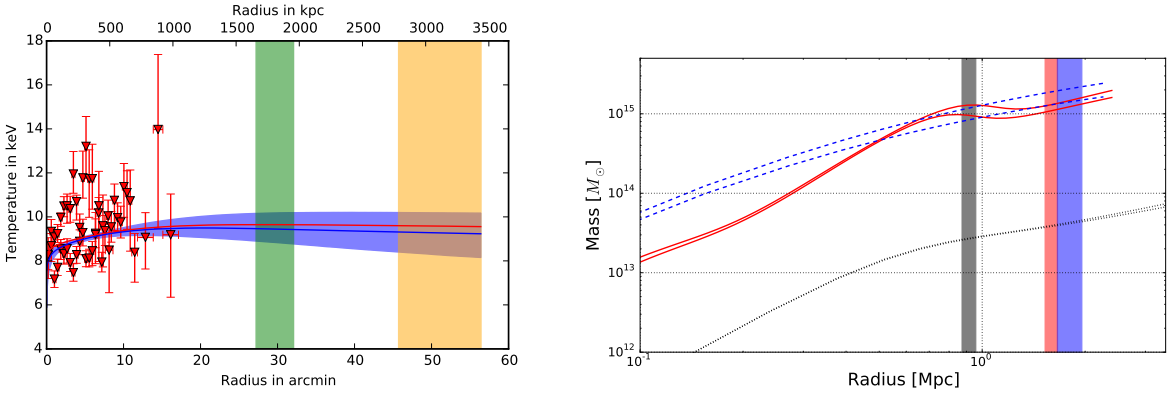

Figure A.12: As Fig. A.1 but for A0754.

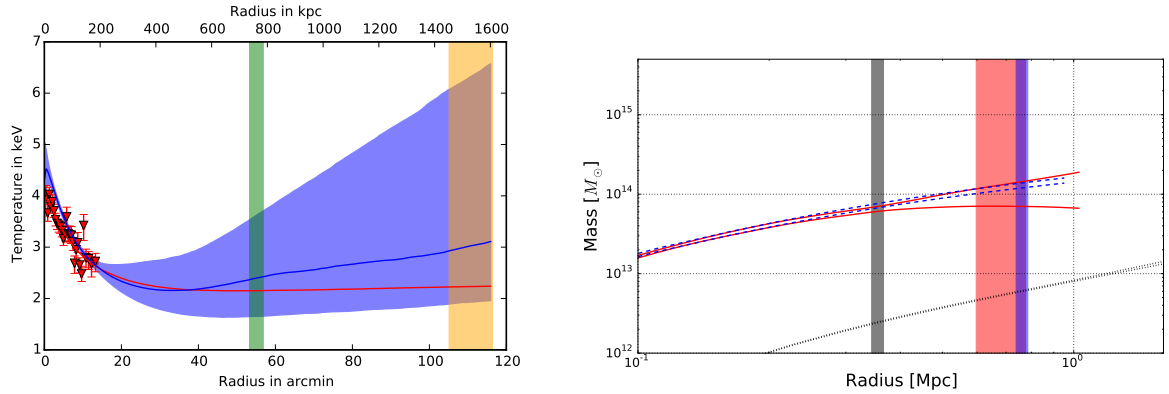

Figure A.13: As Fig. A.1 but for A1060.

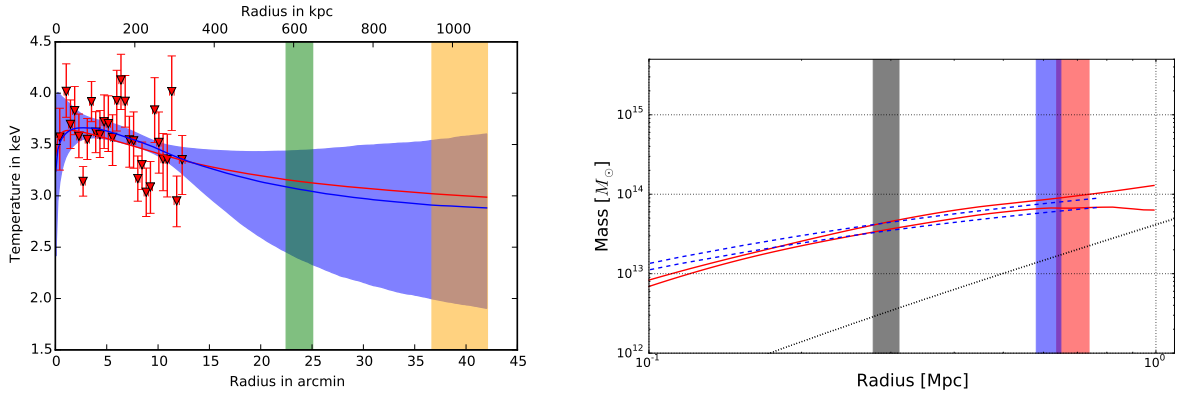

Figure A.14: As Fig. A.1 but for A1367.

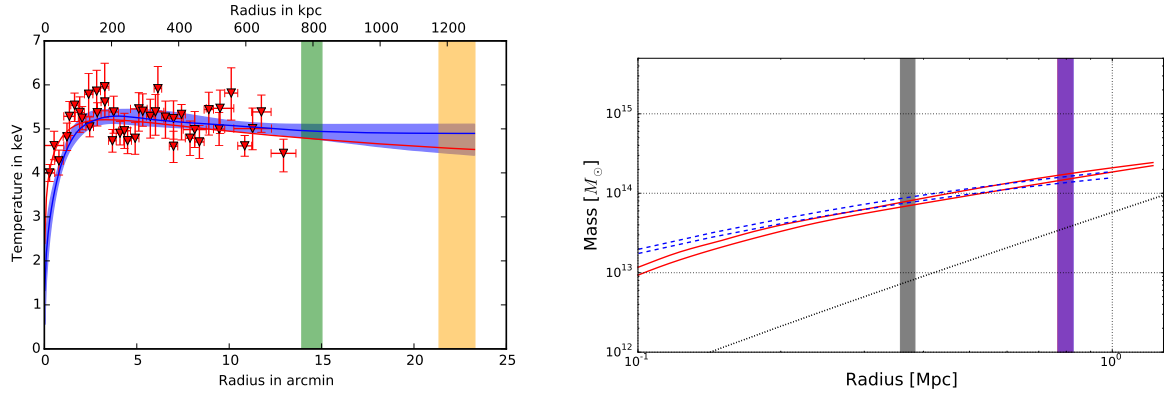

Figure A.15: As Fig. A.1 but for A1644.

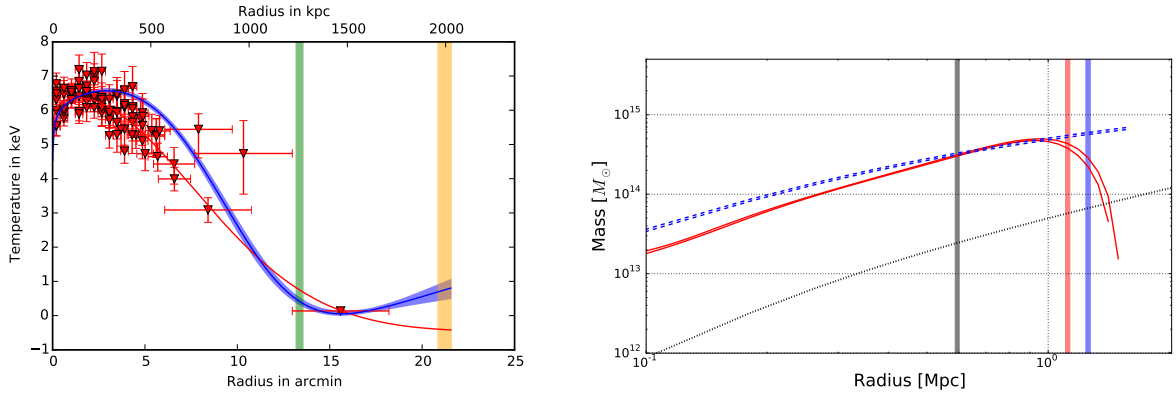

Figure A.16: As Fig. A.1 but for A1650.

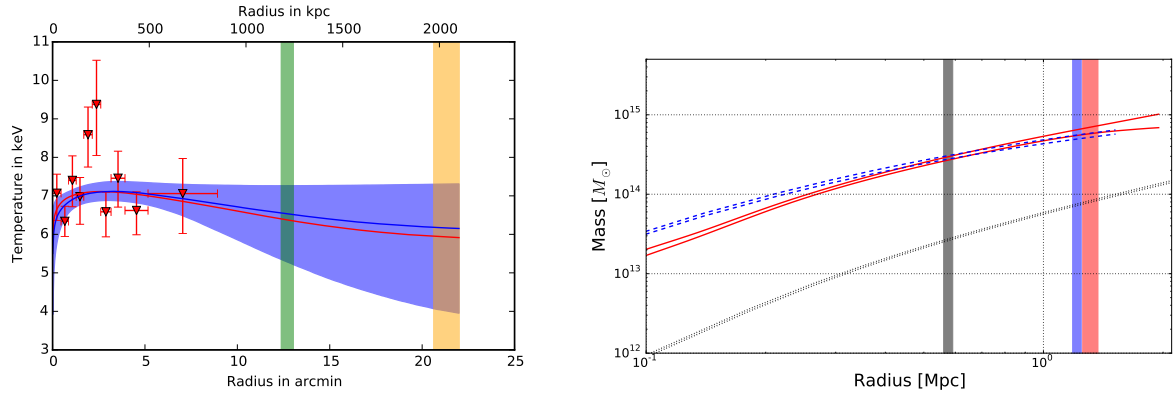

Figure A.17: As Fig. A.1 but for A1651.

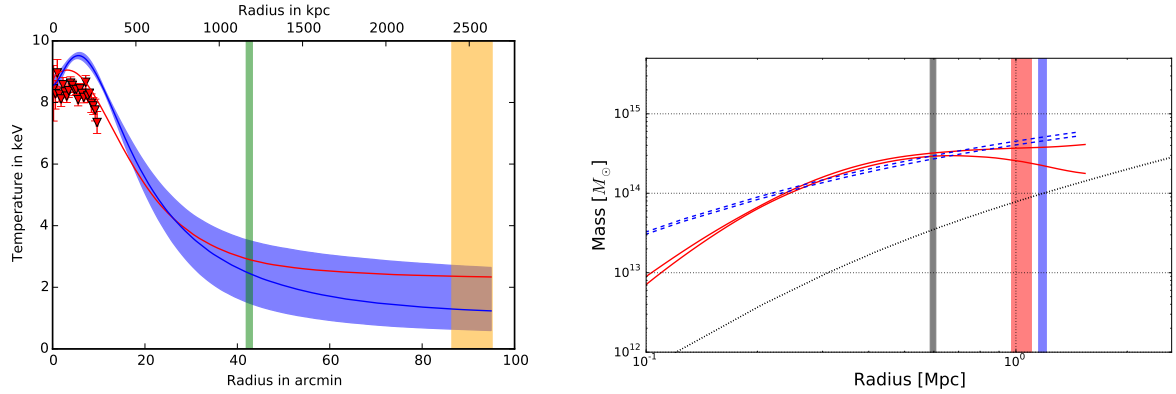

Figure A.18: As Fig. A.1 but for A1656.

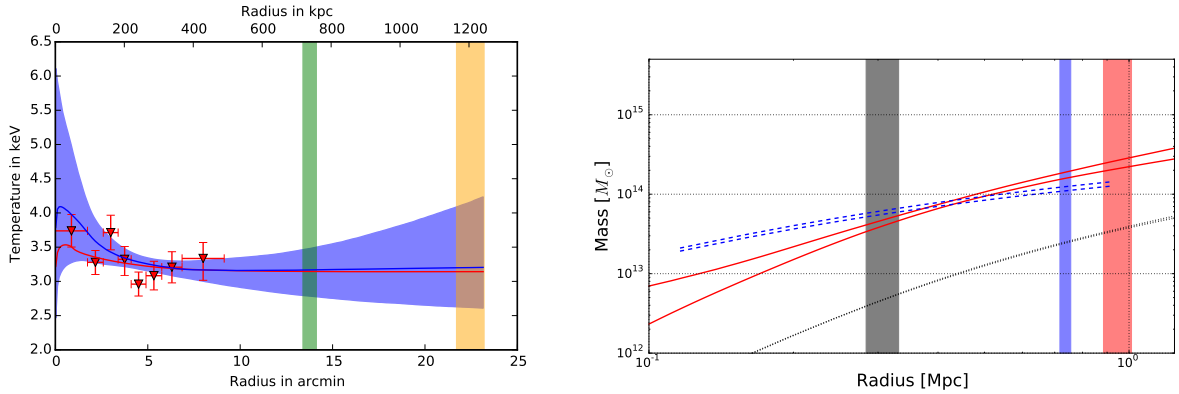

Figure A.19: As Fig. A.1 but for A1736.

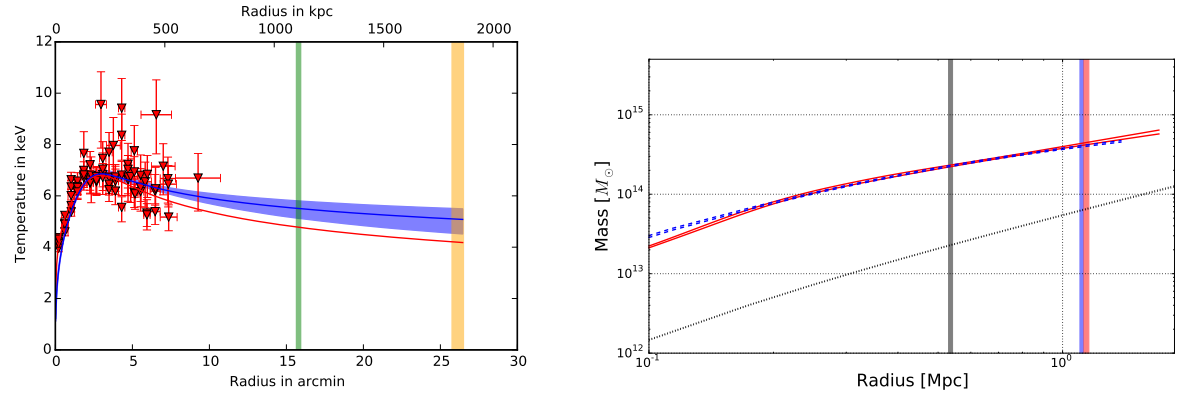

Figure A.20: As Fig. A.1 but for A1795.

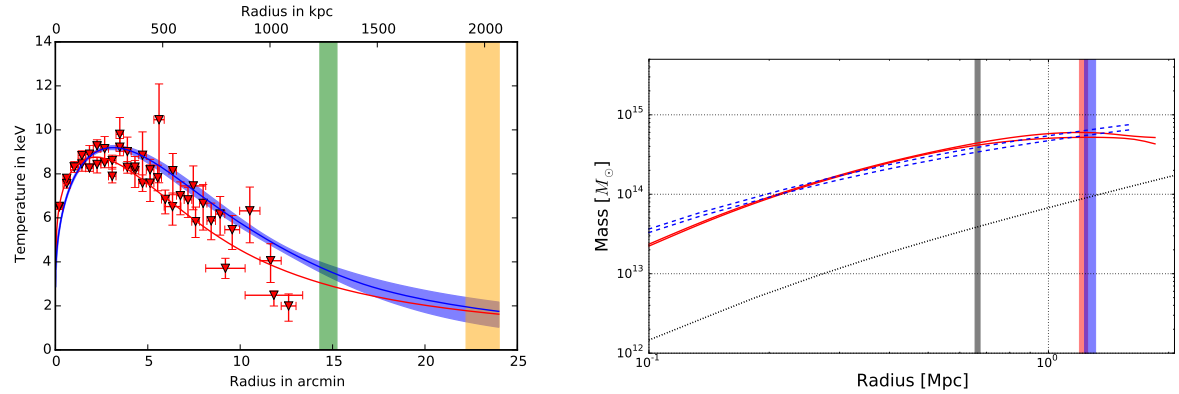

Figure A.21: As Fig. A.1 but for A2029.

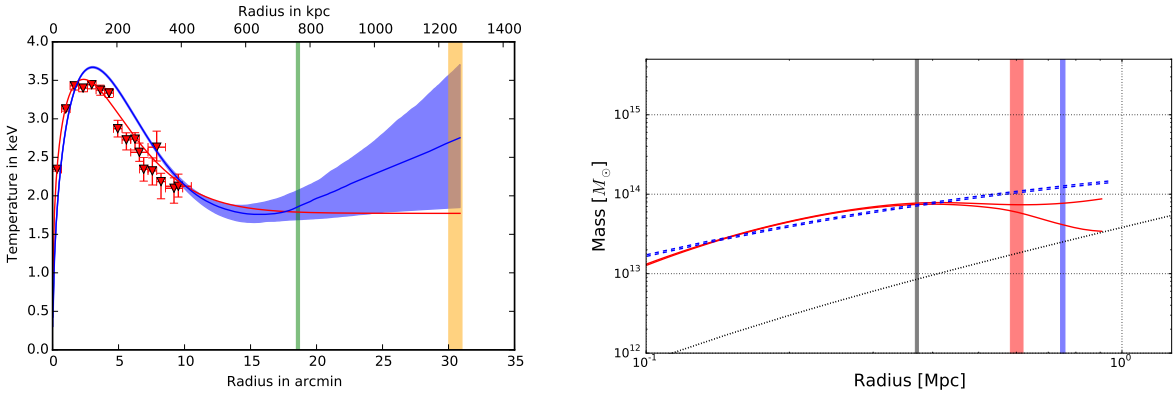

Figure A.22: As Fig. A.1 but for A2052.

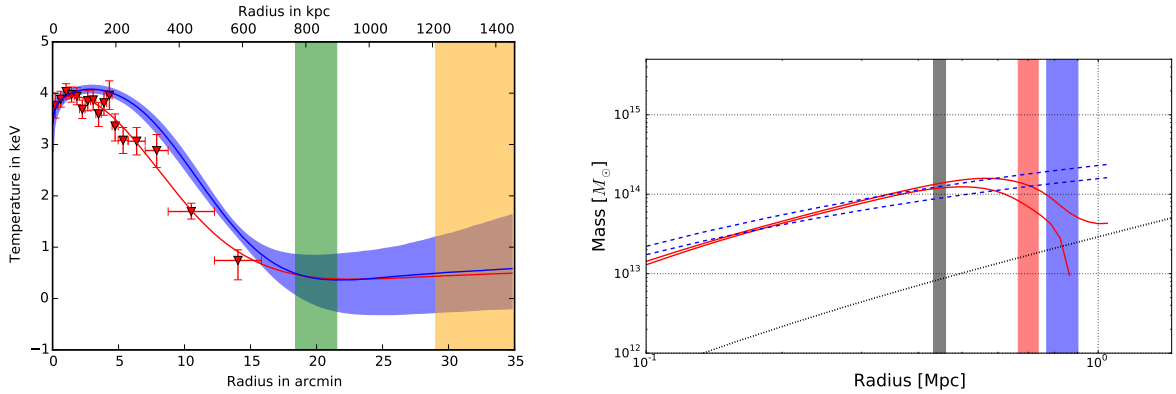

Figure A.23: As Fig. A.1 but for A2063.

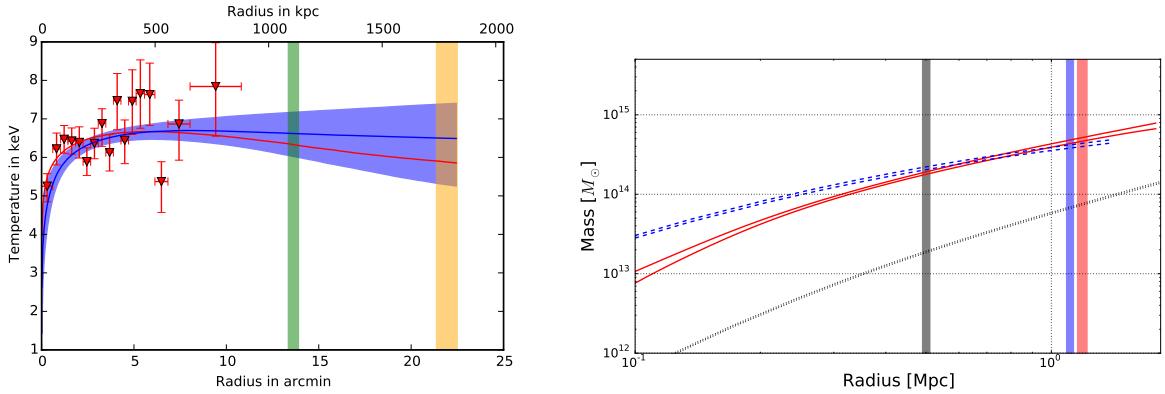

Figure A.24: As Fig. A.1 but for A2065.

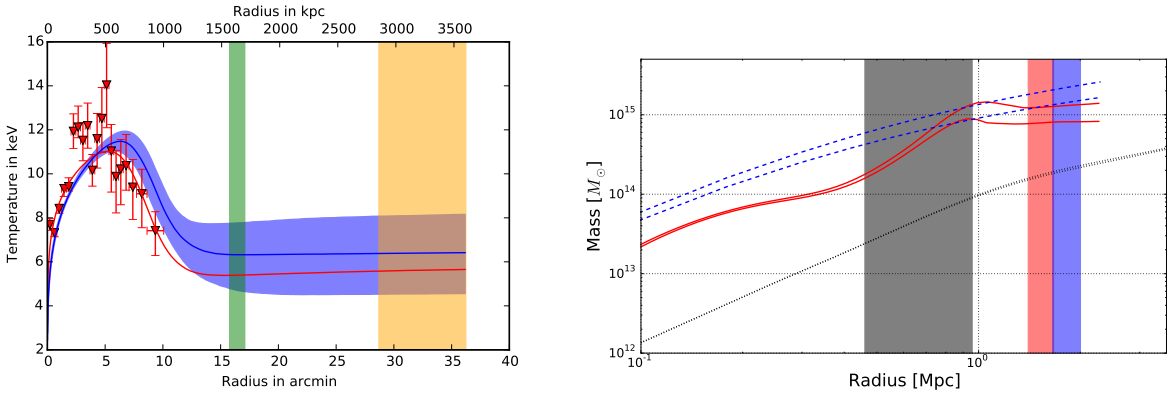

Figure A.25: As Fig. A.1 but for A2142.

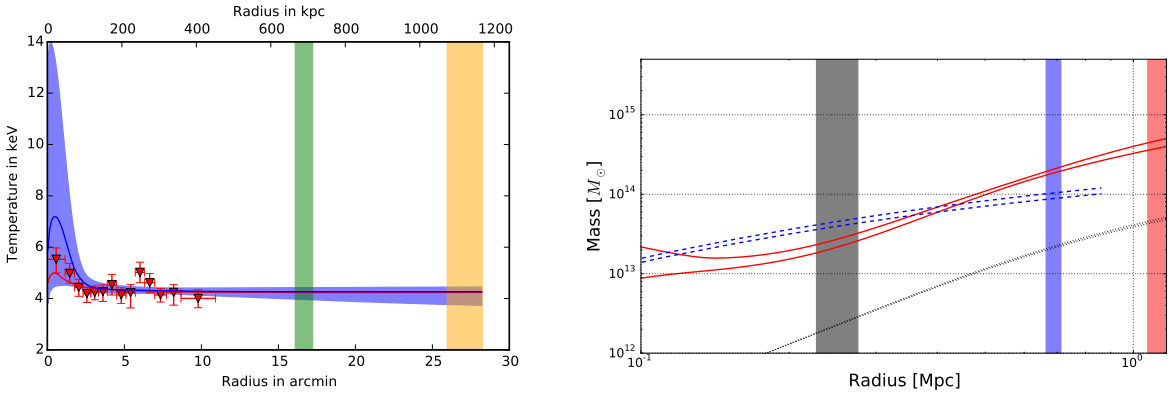

Figure A.26: As Fig. A.1 but for A2147.

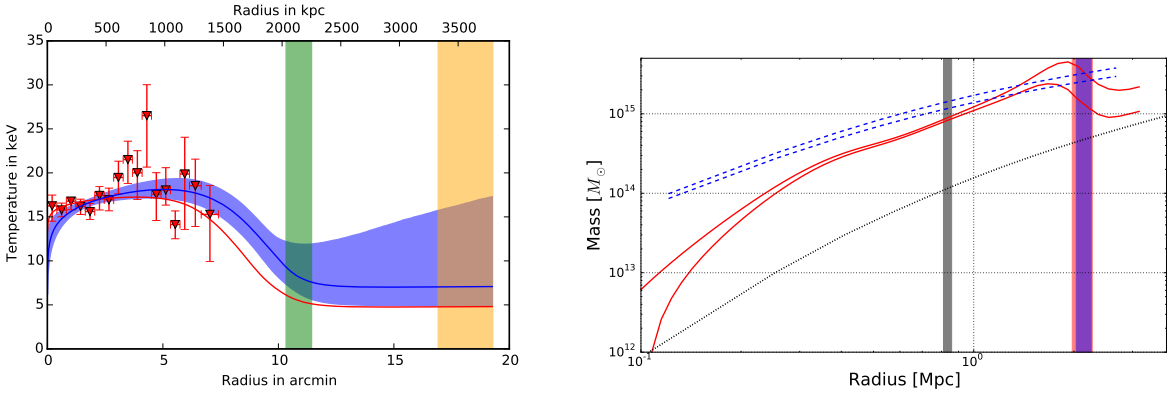

Figure A.27: As Fig. A.1 but for A2163.

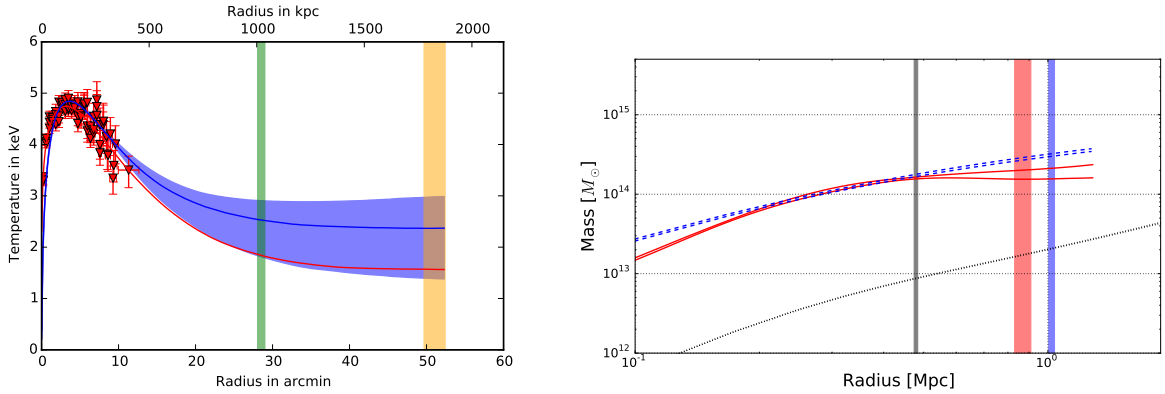

Figure A.28: As Fig. A.1 but for A2199.

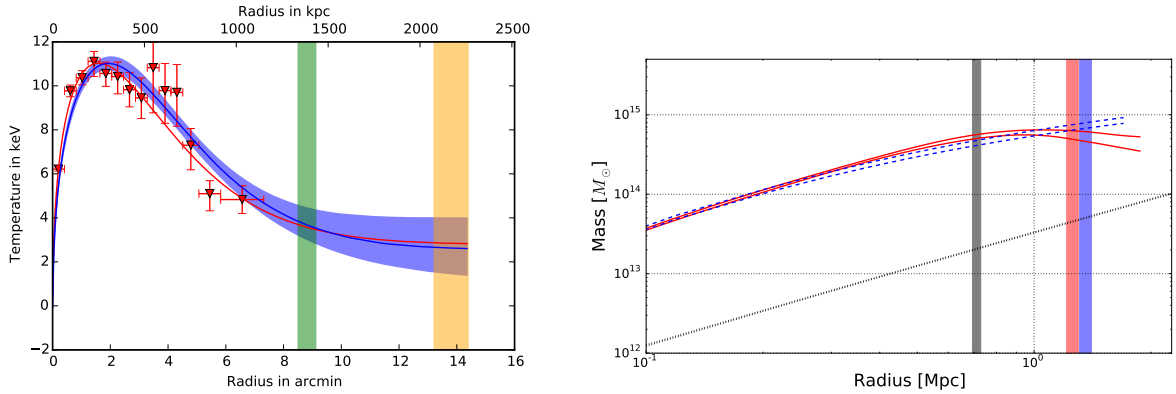

Figure A.29: As Fig. A.1 but for A2204.

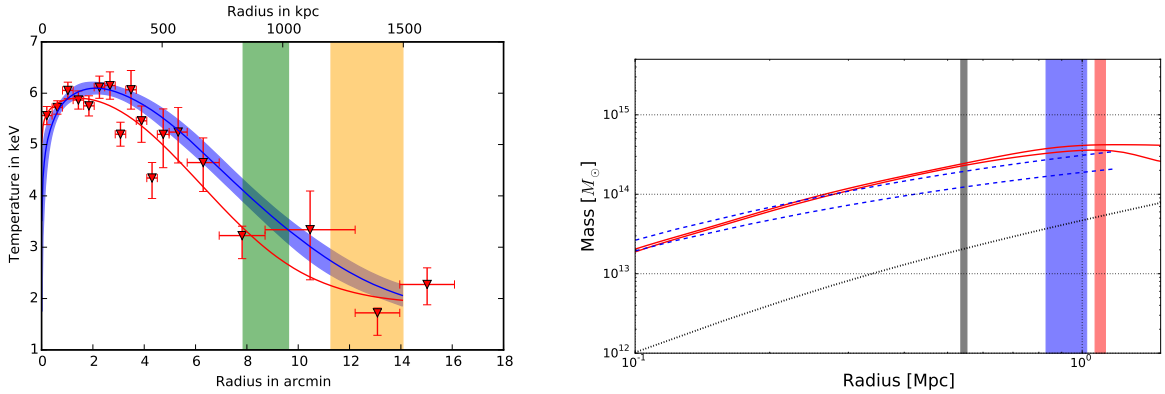

Figure A.30: As Fig. A.1 but for A2244.

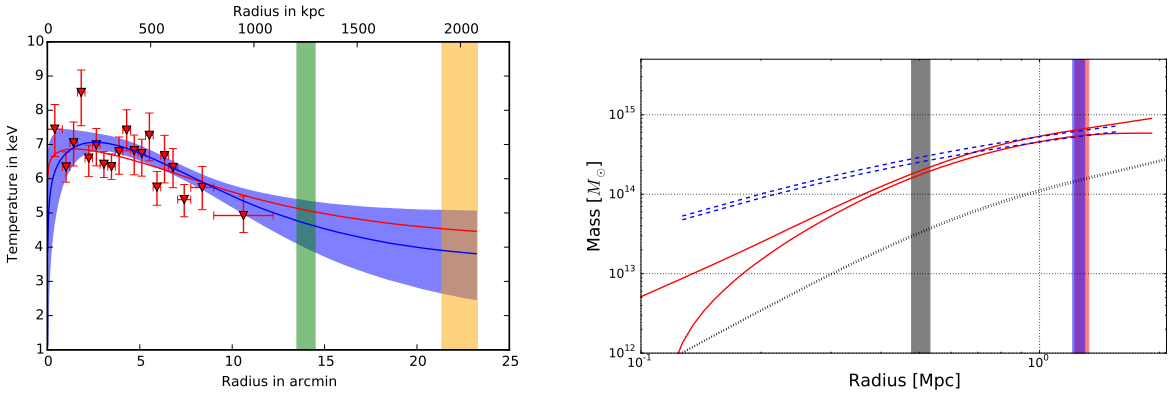

Figure A.31: As Fig. A.1 but for A2255.

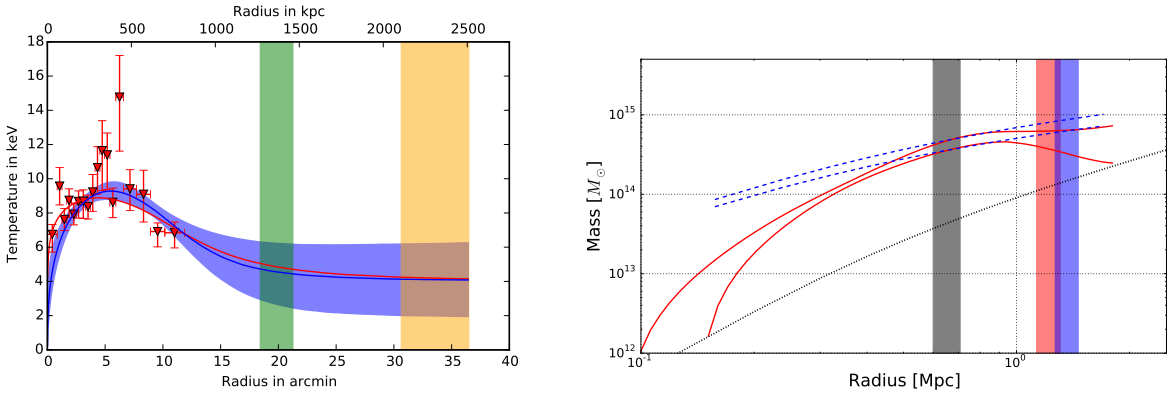

Figure A.32: As Fig. A.1 but for A2256.

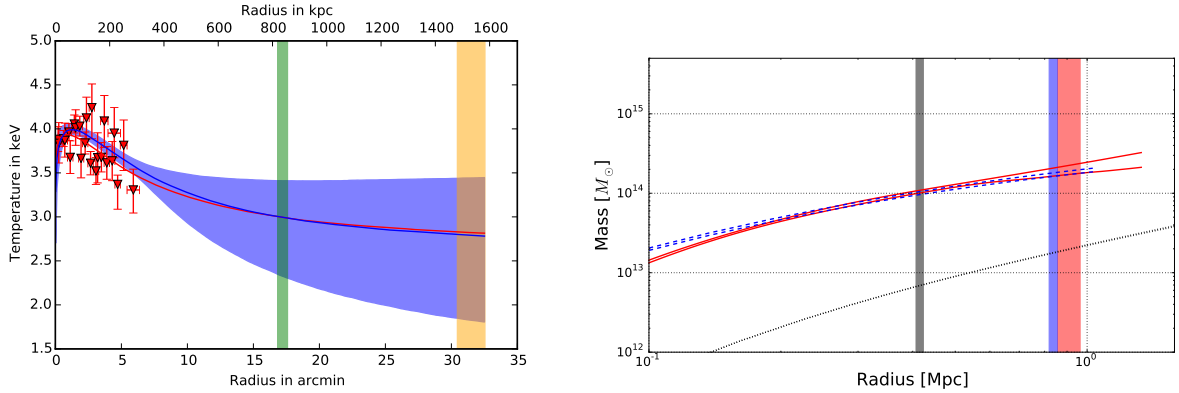

Figure A.33: As Fig. A.1 but for A2589.

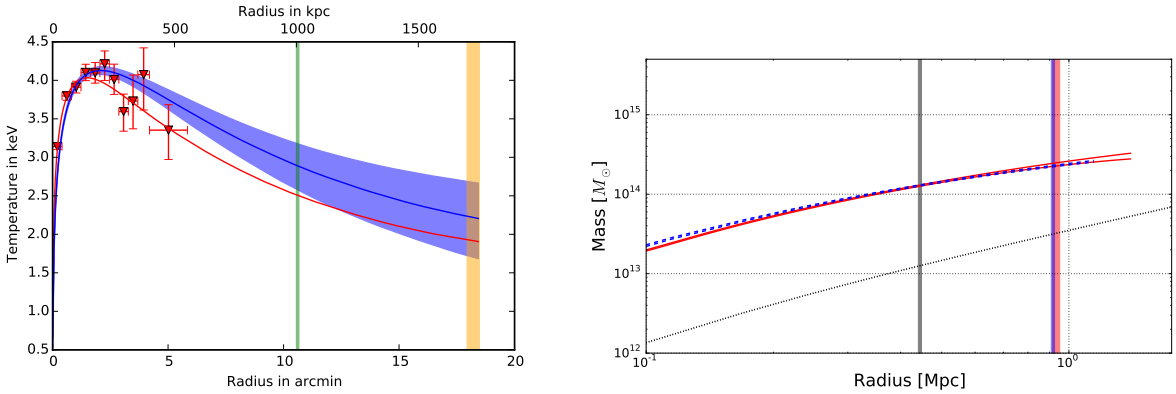

Figure A.34: As Fig. A.1 but for A2597.

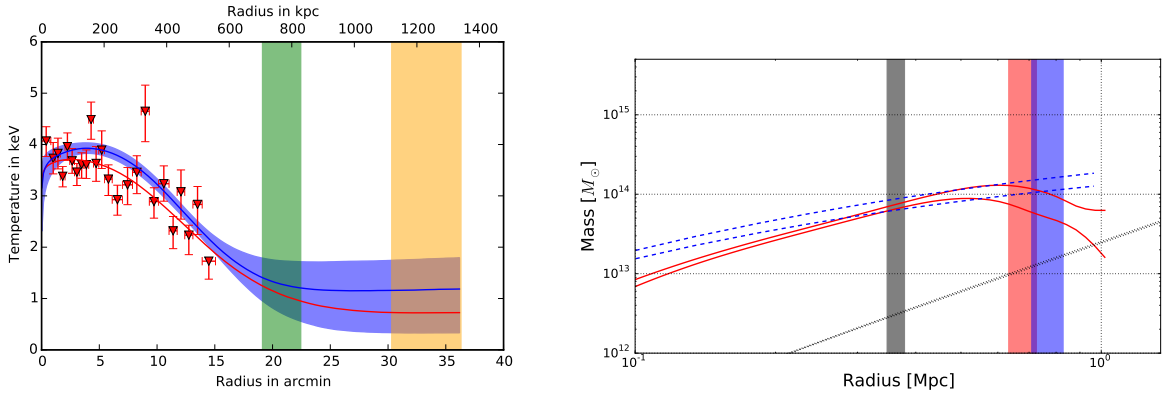

Figure A.35: As Fig. A.1 but for A2634.

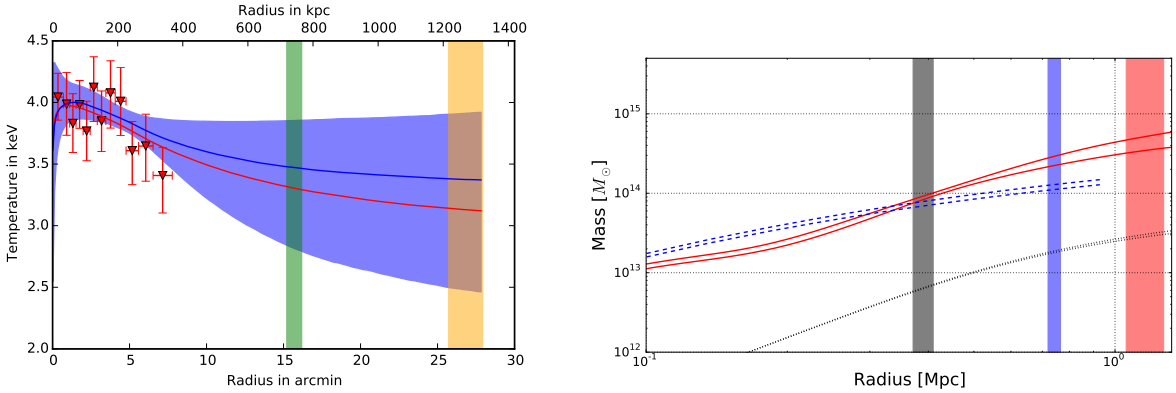

Figure A.36: As Fig. A.1 but for A2657.

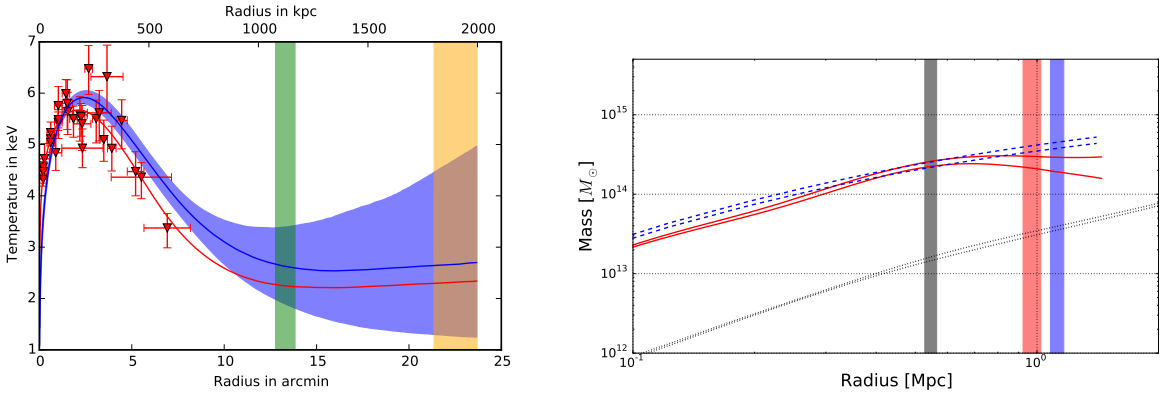

Figure A.37: As Fig. A.1 but for A3112.

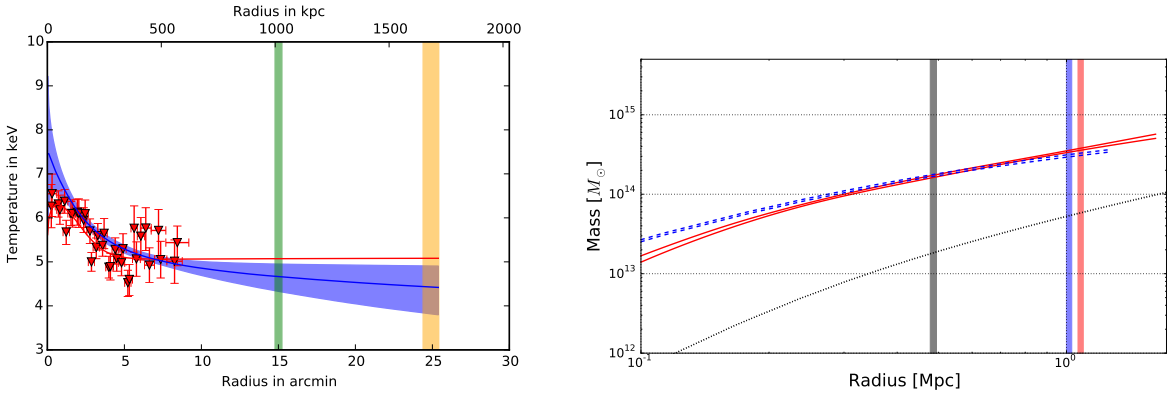

Figure A.38: As Fig. A.1 but for A3158.

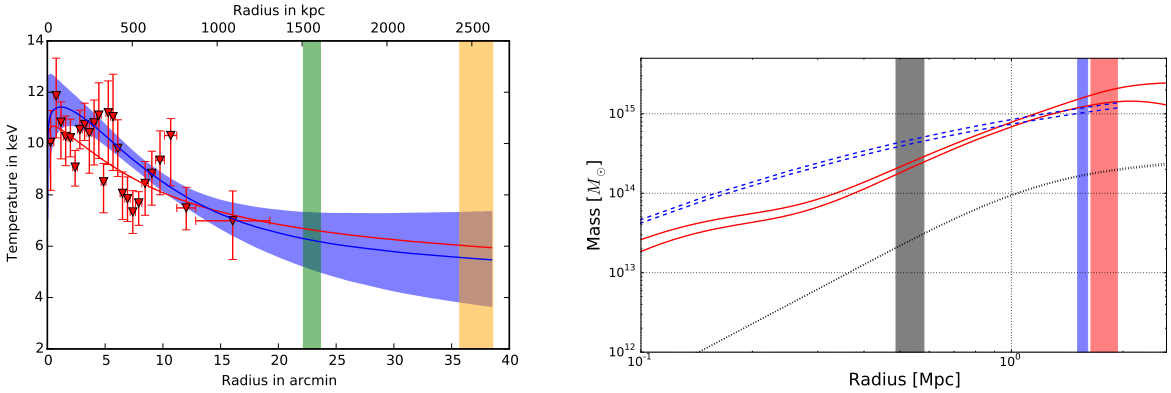

Figure A.39: As Fig. A.1 but for A3266.

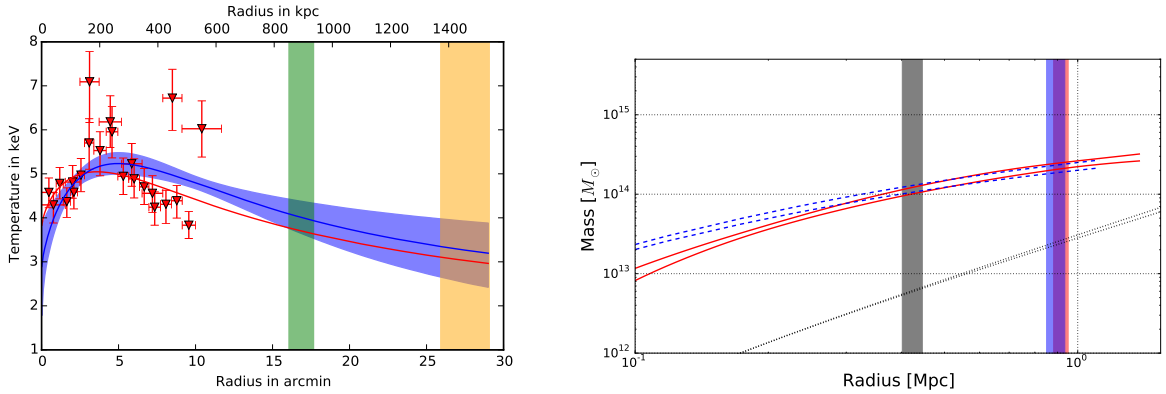

Figure A.40: As Fig. A.1 but for A3376.

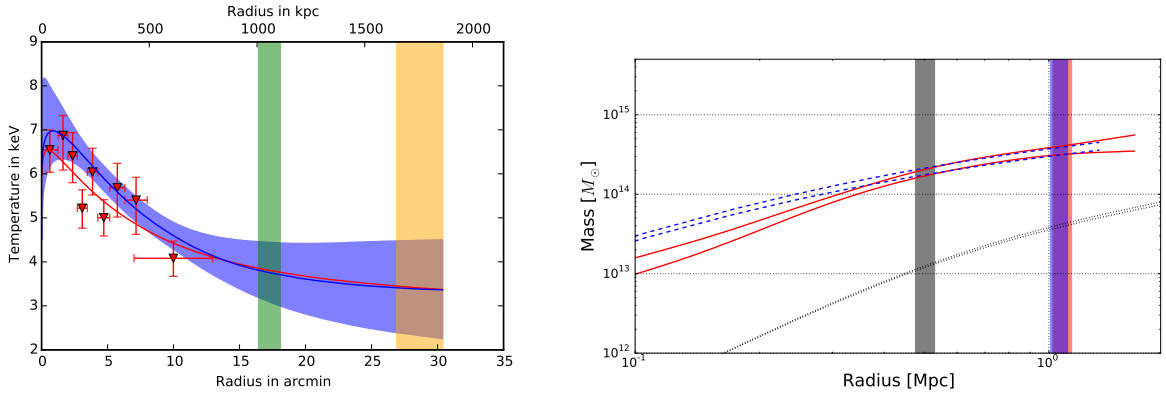

Figure A.41: As Fig. A.1 but for A3391.

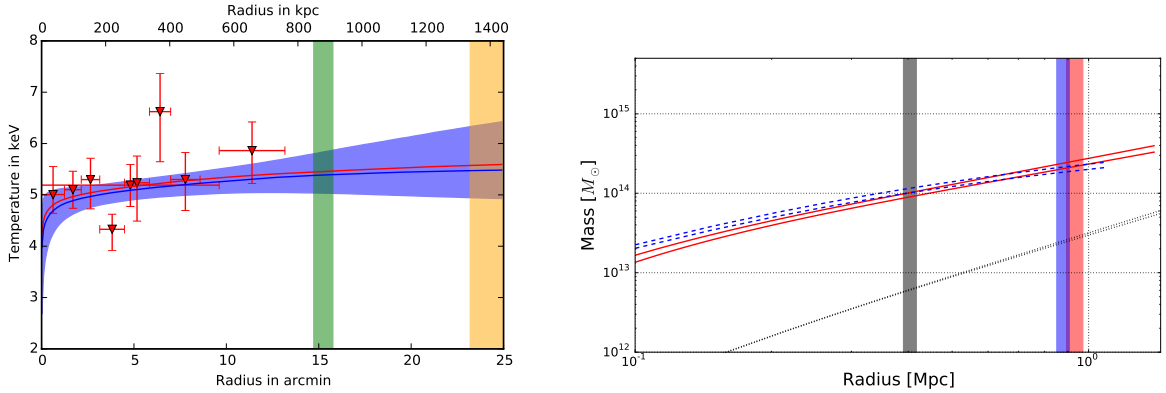

Figure A.42: As Fig. A.1 but for A3395.

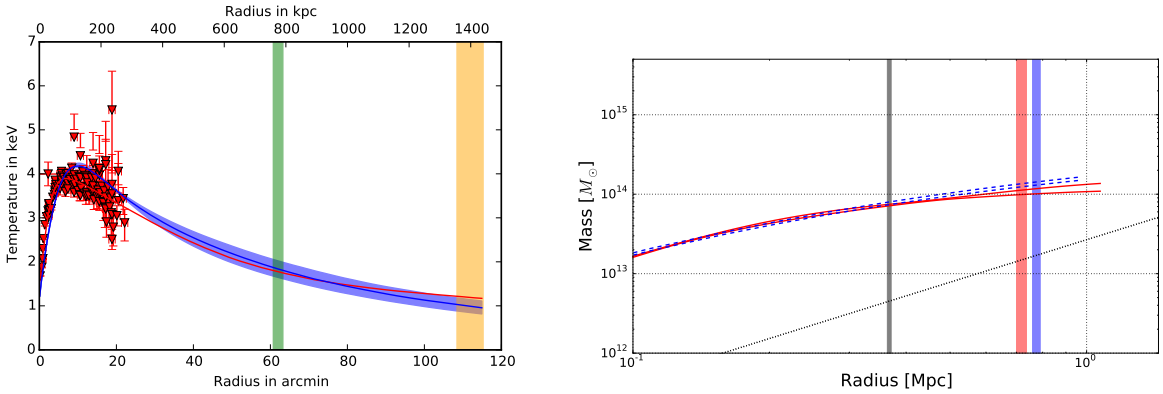

Figure A.43: As Fig. A.1 but for A3526.

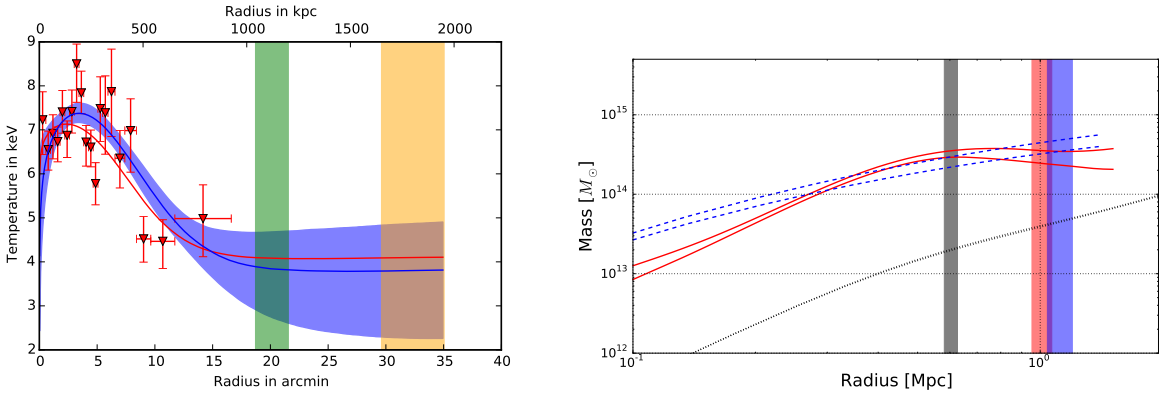

Figure A.44: As Fig. A.1 but for A3558.

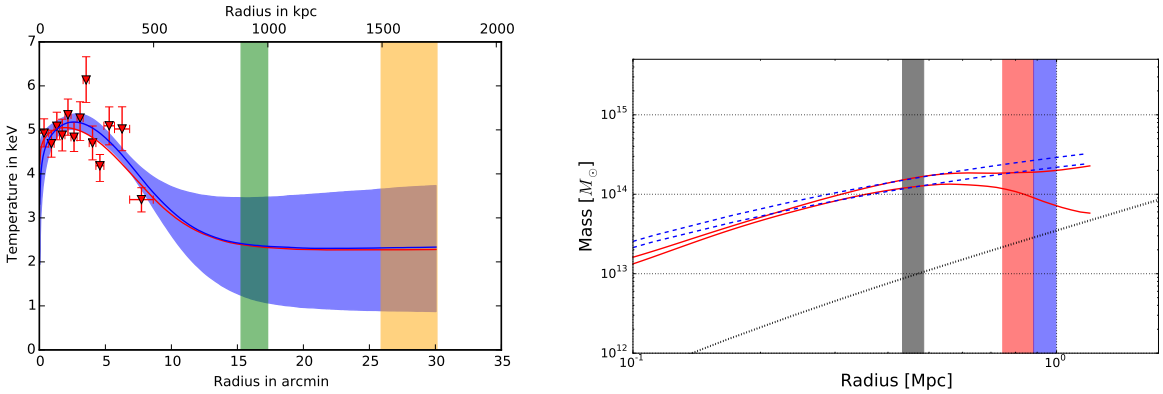

Figure A.45: As Fig. A.1 but for A3562.

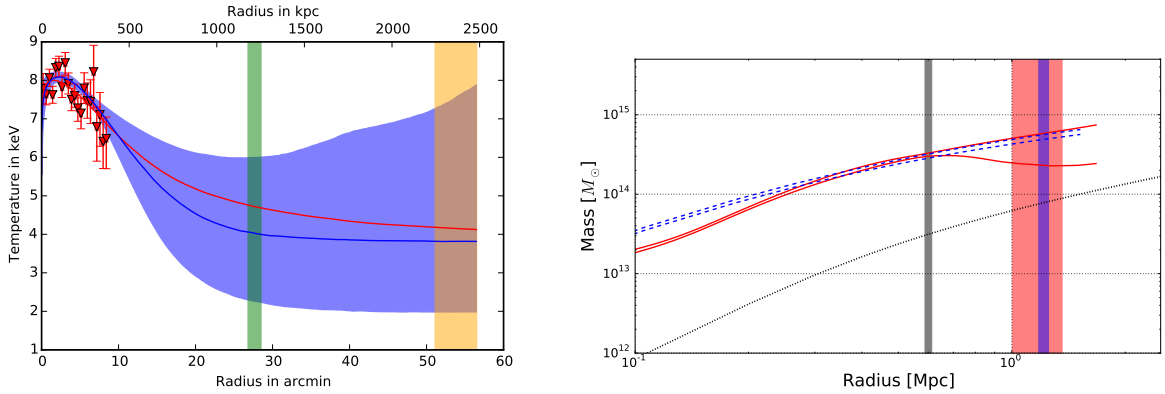

Figure A.46: As Fig. A.1 but for A3571.

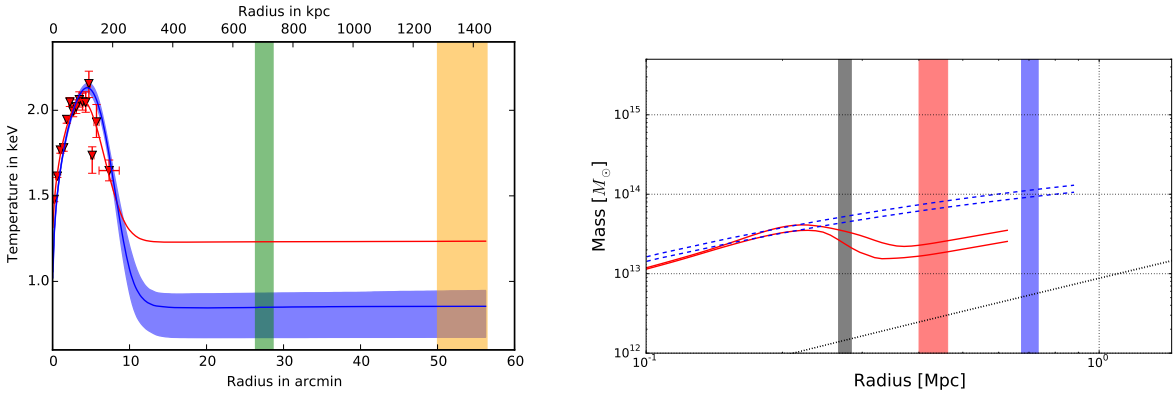

Figure A.47: As Fig. A.1 but for A3581.

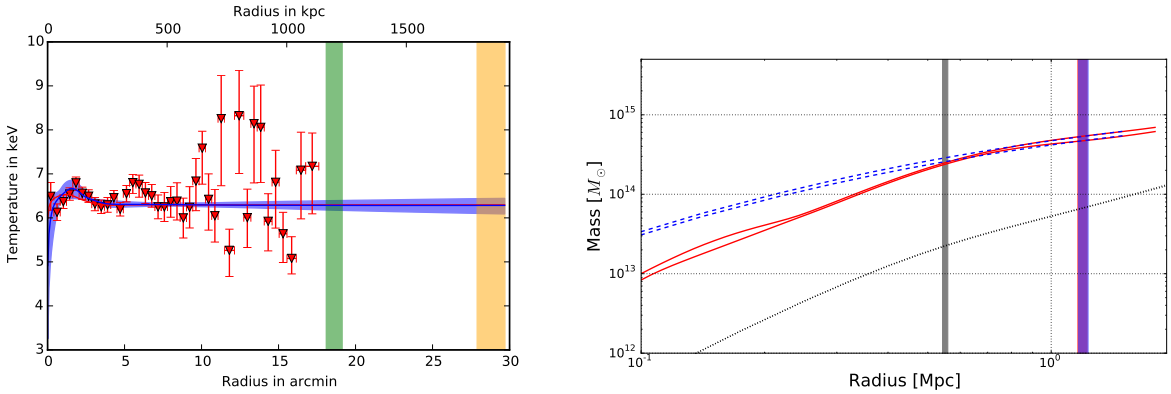

Figure A.48: As Fig. A.1 but for A3667.

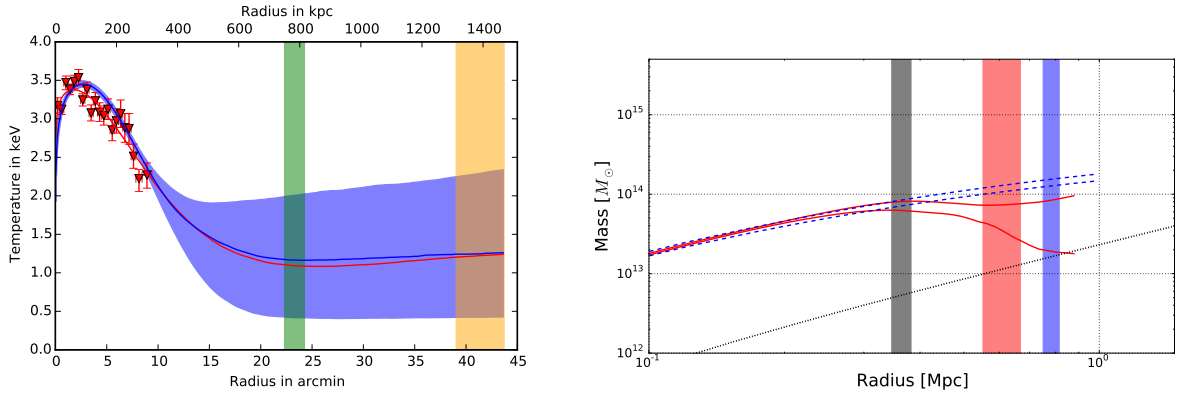

Figure A.49: As Fig. A.1 but for A4038.

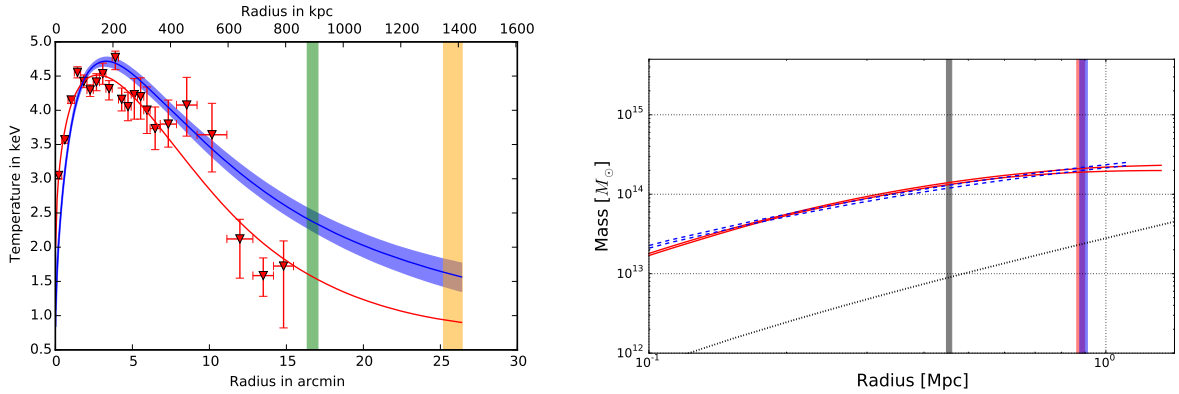

Figure A.50: As Fig. A.1 but for A4059.

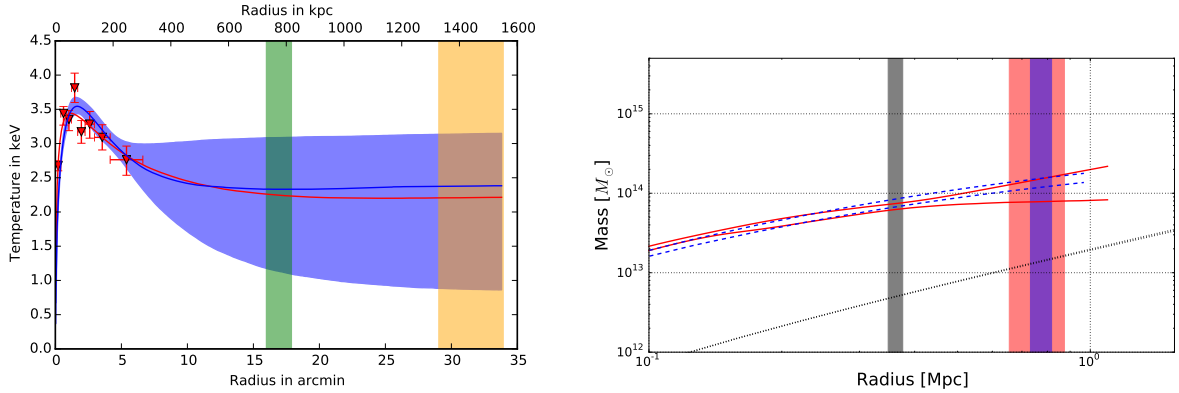

Figure A.51: As Fig. A.1 but for EXO0422.

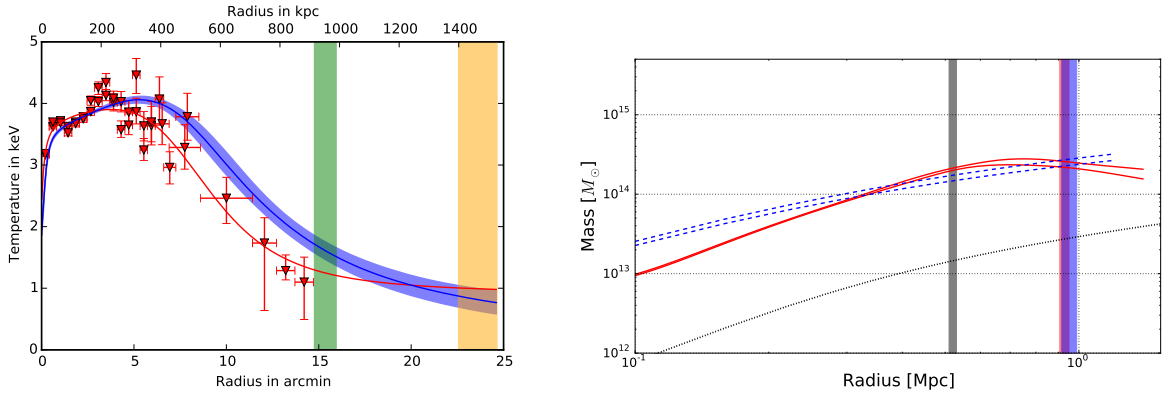

Figure A.52: As Fig. A.1 but for HydraA.

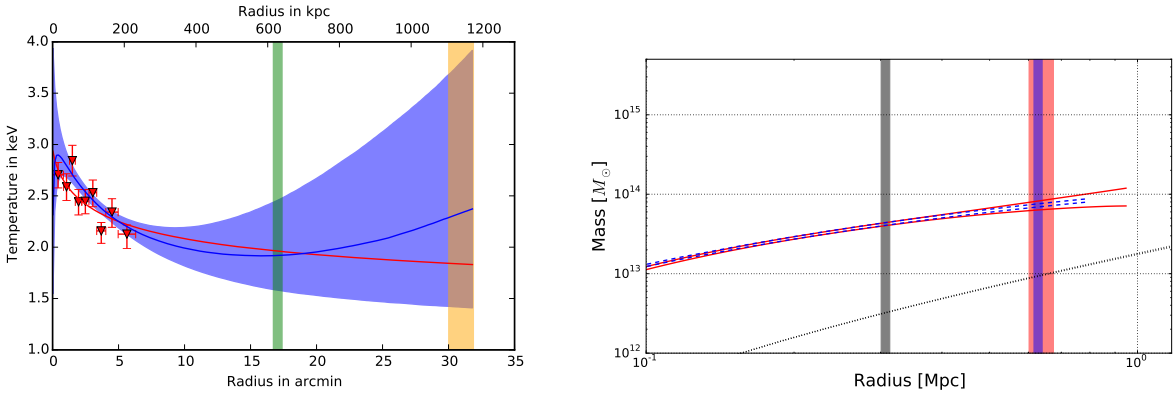

Figure A.53: As Fig. A.1 but for IIIZw54.

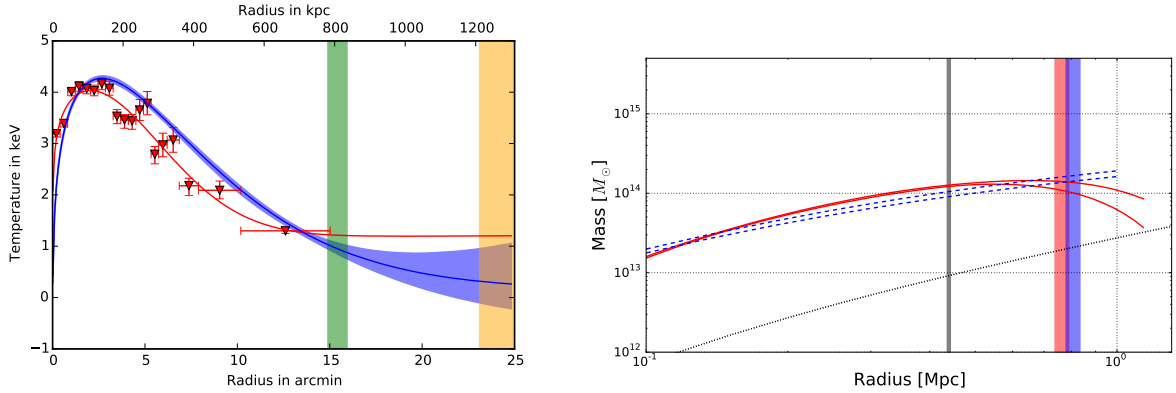

Figure A.54: As Fig. A.1 but for MKW3S.

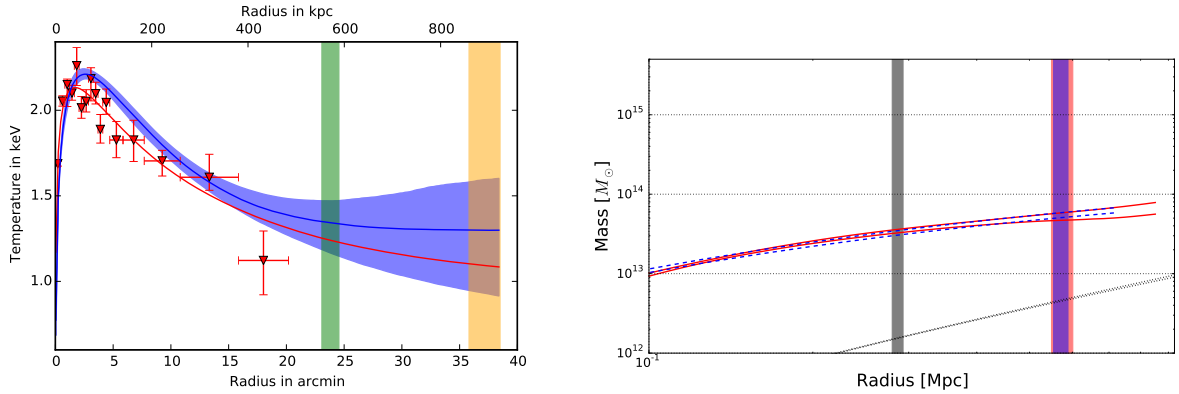

Figure A.55: As Fig. A.1 but for MKW4.

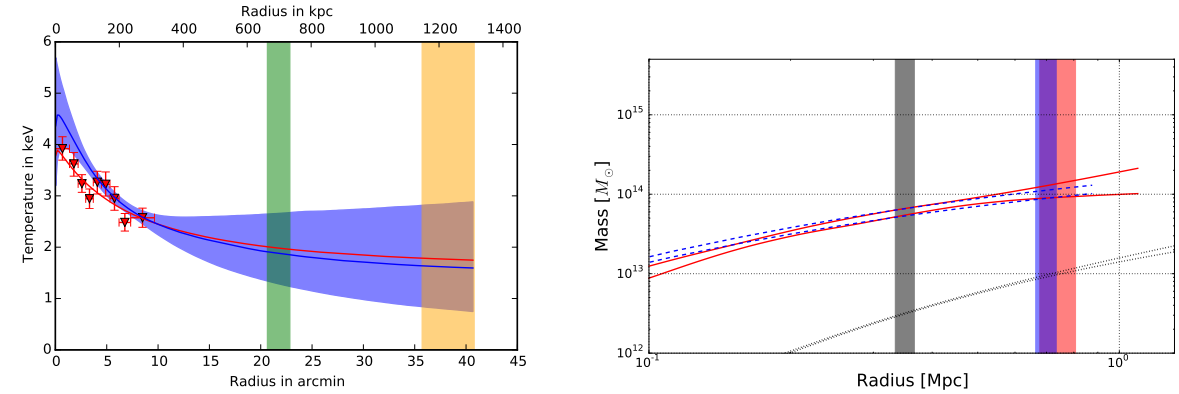

Figure A.56: As Fig. A.1 but for MKW8.

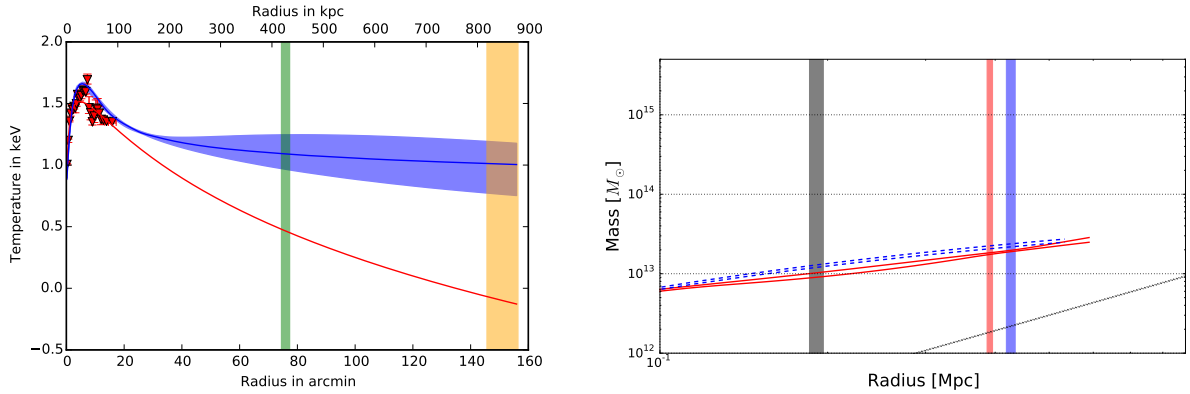

Figure A.57: As Fig. A.1 but for NGC1399.

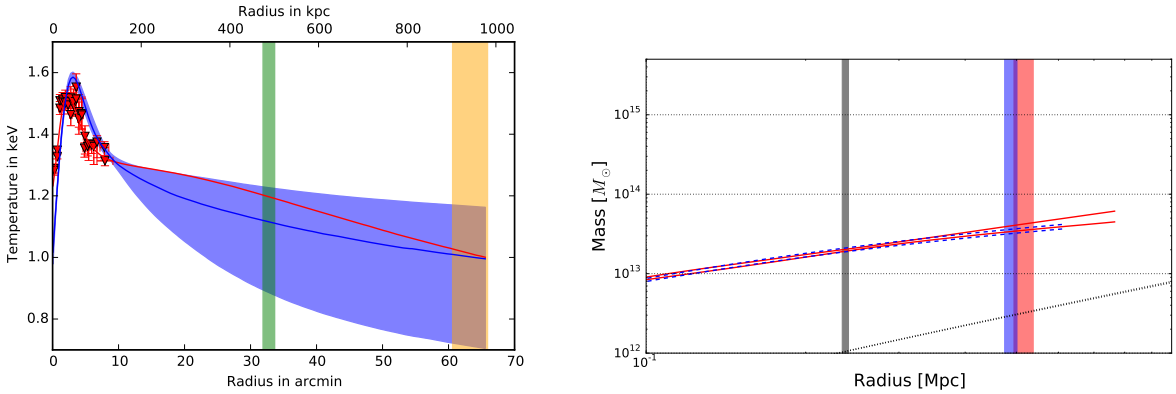

Figure A.58: As Fig. A.1 but for NGC1550.

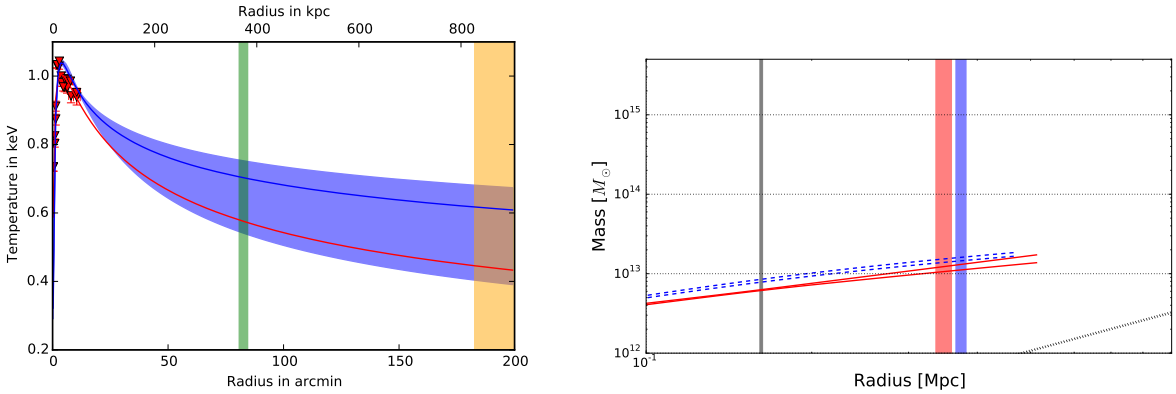

Figure A.59: As Fig. A.1 but for NGC4636.

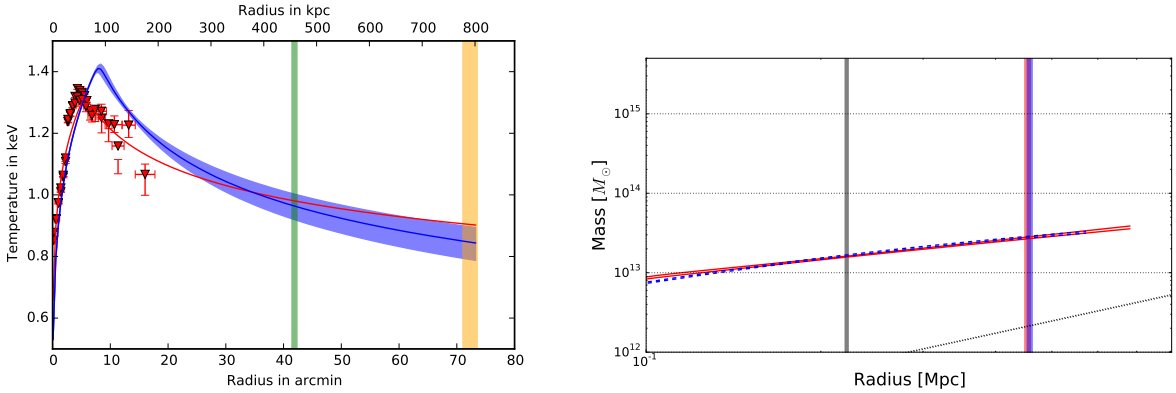

Figure A.60: As Fig. A.1 but for NGC5044.

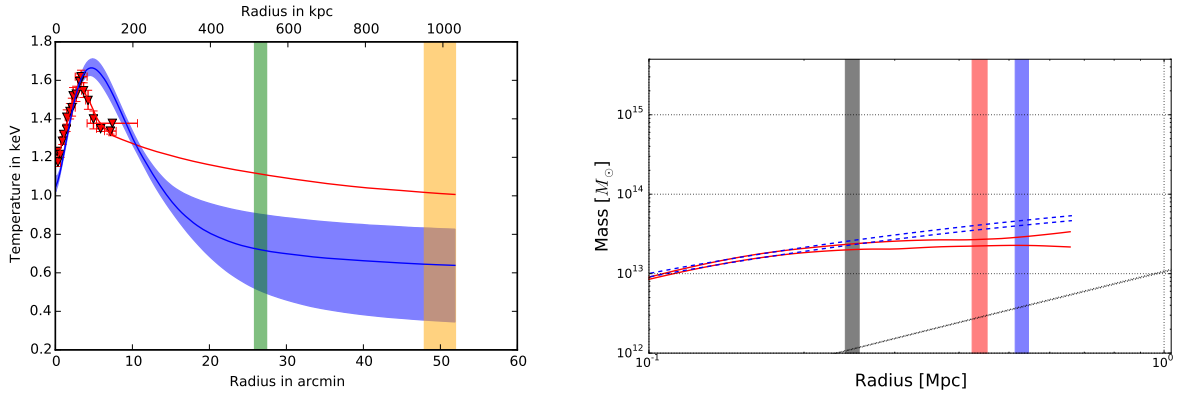

Figure A.61: As Fig. A.1 but for NGC507.

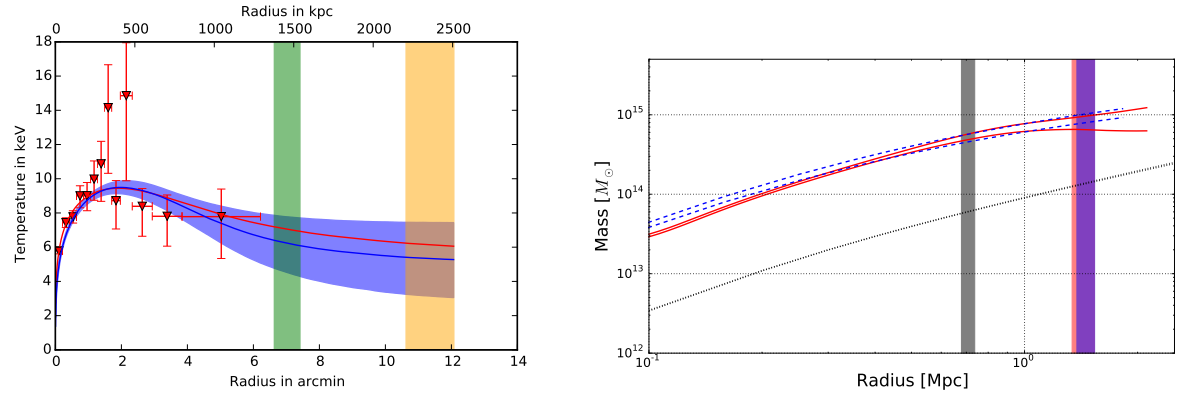

Figure A.62: As Fig. A.1 but for RXCJ1504.

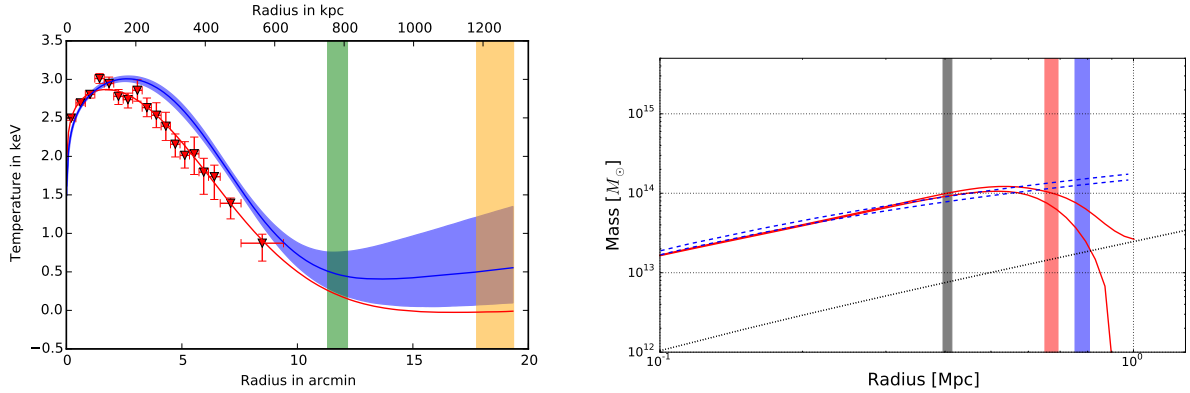

Figure A.63: As Fig. A.1 but for S1101.

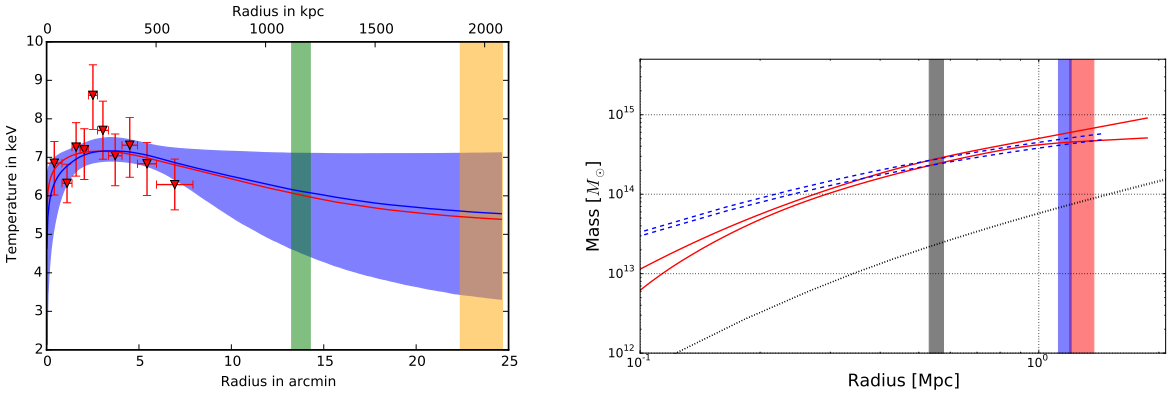

Figure A.64: As Fig. A.1 but for ZwCl1215.

APPENDIX B

Tables

Table B.1: Masses for HIFLUGCS clusters with different extrapolation methods and for two overdensities using $h = 0.7$ and $\Omega_{\rm m} = 0.3$.

Name	$M_{500}^{\text{NFW Freeze}}$ $10^{14}\,\mathrm{M}_\odot$	$M_{500}^{\text{kT extrp}}$ $10^{14}\,\mathrm{M}_\odot$	$M_{500}^{\text{NFW Hudson}}$ $10^{14}\,\mathrm{M}_\odot$	$M_{500}^{\text{NFW All}}$ $10^{14}\,\mathrm{M}_\odot$	$M_{200}^{\text{NFW Freeze}}$ $10^{14}\,\mathrm{M}_\odot$	$M_{200}^{\text{kT extrp}}$ $10^{14}\,\mathrm{M}_\odot$	$M_{500}^{\text{Planck SZ}}$ $10^{14}\,\mathrm{M}_\odot$
2A0335	$0.945^{+0.055}_{-0.052}$	$0.840^{+0.040}_{-0.032}$	$1.137^{+0.018}_{-0.016}$	$2.169^{+0.031}_{-0.031}$	$1.664^{+0.121}_{-0.111}$	$1.062^{+0.053}_{-0.062}$	$1.588^{+0.108}_{-0.122}$
A0085	$3.372^{+0.169}_{-0.174}$	$3.176^{+0.131}_{-0.129}$	$4.788^{+0.043}_{-0.039}$	$6.594^{+0.056}_{-0.057}$	$5.093^{+0.327}_{-0.296}$	$3.494^{+0.208}_{-0.244}$	$3.443^{+0.089}_{-0.102}$
A0119	$2.049^{+0.412}_{-0.390}$	$1.949^{+0.298}_{-0.663}$	$19.029^{+3.937}_{-5.191}$	$20.038^{+3.460}_{-5.080}$	$3.956^{+1.018}_{-0.898}$	$2.378^{+0.713}_{-1.304}$	$2.401^{+0.090}_{-0.152}$
A0133	$1.710^{+0.172}_{-0.167}$	$1.932^{+0.222}_{-0.328}$	$1.881^{+0.135}_{-0.117}$	$1.962^{+0.136}_{-0.134}$	$3.348^{+0.437}_{-0.406}$	$2.105^{+0.541}_{-0.659}$	$2.112^{+0.125}_{-0.115}$
A0262	$0.468^{+0.026}_{-0.025}$	$0.431^{+0.038}_{-0.025}$	$0.777^{+0.019}_{-0.021}$	$0.825^{+0.024}_{-0.023}$	$0.824^{+0.053}_{-0.054}$	$0.520^{+0.041}_{-0.034}$	$0.785^{+0.075}_{-0.080}$
A0399	$2.362^{+0.144}_{-0.146}$	$9.483^{+1.352}_{-1.356}$	$2.174^{+0.117}_{-0.114}$	$2.016^{+0.119}_{-0.111}$	$4.026^{+0.319}_{-0.296}$	$16.629^{+4.071}_{-4.236}$	$3.668^{+0.204}_{-0.162}$
A0400	$0.468^{+0.059}_{-0.059}$	$0.641^{+0.090}_{-0.098}$	$7.614^{+4.272}_{-3.625}$	$7.155^{+4.130}_{-3.900}$	$1.043^{+0.184}_{-0.158}$	$0.843^{+0.204}_{-0.245}$	–
A0401	$3.652^{+0.132}_{-0.119}$	$3.679^{+0.101}_{-0.099}$	$4.385^{+0.065}_{-0.067}$	$4.570^{+0.078}_{-0.083}$	$5.922^{+0.278}_{-0.264}$	$4.792^{+0.146}_{-0.400}$	$4.722^{+0.155}_{-0.121}$
A0478	$3.765^{+1.473}_{-1.463}$	$2.288^{+1.083}_{-0.606}$	$18.653^{+1.172}_{-1.120}$	$33.115^{+3.289}_{-2.743}$	$6.082^{+3.029}_{-2.398}$	$1.589^{+0.464}_{-0.243}$	$4.867^{+0.198}_{-0.198}$
A0496	$1.625^{+0.146}_{-0.144}$	$1.584^{+0.091}_{-0.062}$	$2.022^{+0.043}_{-0.037}$	$2.152^{+0.037}_{-0.036}$	$2.561^{+0.293}_{-0.260}$	$1.971^{+0.168}_{-0.126}$	$1.900^{+0.102}_{-0.108}$
A0576	$1.483^{+0.366}_{-0.319}$	$1.780^{+0.361}_{-0.392}$	$5.853^{+2.678}_{-1.477}$	$18.127^{+4.981}_{-5.427}$	$2.372^{+0.680}_{-0.594}$	$3.175^{+1.028}_{-1.034}$	$1.494^{+0.103}_{-0.107}$
A0754	$12.312^{+3.220}_{-2.828}$	$8.446^{+0.819}_{-0.678}$	$177.785^{+2.996}_{-3.143}$	$178.124^{+2.969}_{-3.193}$	$24.998^{+8.809}_{-7.010}$	$13.164^{+1.515}_{-1.273}$	$4.798^{+0.087}_{-0.089}$
A1060	$0.914^{+0.091}_{-0.083}$	$0.670^{+0.266}_{-0.169}$	$1.126^{+0.080}_{-0.079}$	$1.129^{+0.105}_{-0.087}$	$2.966^{+0.486}_{-0.417}$	$0.894^{+0.446}_{-0.423}$	–
A1367	$0.479^{+0.044}_{-0.044}$	$0.600^{+0.049}_{-0.127}$	$0.939^{+0.124}_{-0.102}$	$0.969^{+0.126}_{-0.103}$	$0.878^{+0.193}_{-0.168}$	$0.832^{+0.092}_{-0.386}$	$1.167^{+0.075}_{-0.071}$
A1644	$1.056^{+0.118}_{-0.118}$	$1.115^{+0.139}_{-0.038}$	$1.046^{+0.044}_{-0.042}$	$1.133^{+0.046}_{-0.045}$	$1.549^{+0.204}_{-0.197}$	$1.717^{+0.077}_{-0.072}$	$2.582^{+0.110}_{-0.116}$
A1650	$4.130^{+0.166}_{-0.165}$	$2.903^{+0.182}_{-0.205}$	$4.796^{+0.054}_{-0.052}$	$5.107^{+0.058}_{-0.062}$	$6.595^{+0.346}_{-0.311}$	$1.701^{+0.234}_{-0.230}$	$3.113^{+0.169}_{-0.173}$
A1651	$3.721^{+0.287}_{-0.280}$	$4.569^{+0.347}_{-0.490}$	$4.715^{+0.444}_{-0.384}$	$5.313^{+0.894}_{-0.636}$	$7.026^{+0.702}_{-0.657}$	$6.602^{+0.788}_{-1.681}$	$3.552^{+0.124}_{-0.140}$
A1656	$3.417^{+0.161}_{-0.148}$	$2.242^{+0.392}_{-0.449}$	$177.898^{+3.462}_{-4.848}$	$174.502^{+3.330}_{-4.444}$	$13.158^{+2.096}_{-1.711}$	$2.163^{+0.636}_{-0.800}$	$5.016^{+0.047}_{-0.075}$
A1736	$0.835^{+0.066}_{-0.064}$	$1.692^{+0.168}_{-0.227}$	$2.788^{+1.220}_{-0.916}$	$2.285^{+1.585}_{-0.955}$	$1.454^{+0.146}_{-0.141}$	$3.077^{+0.512}_{-0.624}$	$2.022^{+0.117}_{-0.117}$
A1795	$2.855^{+0.072}_{-0.075}$	$3.079^{+0.094}_{-0.102}$	$2.787^{+0.045}_{-0.048}$	$3.982^{+0.064}_{-0.059}$	$5.168^{+0.224}_{-0.214}$	$4.420^{+0.221}_{-0.283}$	$3.126^{+0.099}_{-0.099}$
A2029	$4.303^{+0.389}_{-0.406}$	$3.890^{+0.365}_{-0.193}$	$6.879^{+0.090}_{-0.091}$	$7.286^{+0.094}_{-0.084}$	$6.592^{+0.762}_{-0.757}$	$3.664^{+0.152}_{-0.177}$	$4.928^{+0.139}_{-0.135}$
A2052	$0.922^{+0.016}_{-0.016}$	$0.459^{+0.065}_{-0.040}$	$1.873^{+0.020}_{-0.020}$	$2.080^{+0.027}_{-0.025}$	$1.629^{+0.082}_{-0.075}$	$0.412^{+0.149}_{-0.142}$	–
A2063	$1.212^{+0.289}_{-0.270}$	$0.708^{+0.219}_{-0.209}$	$2.180^{+0.175}_{-0.143}$	$2.270^{+0.186}_{-0.150}$	$1.974^{+0.582}_{-0.499}$	$0.418^{+0.192}_{-0.140}$	$1.329^{+0.122}_{-0.126}$
A2065	$2.841^{+0.170}_{-0.170}$	$3.481^{+0.193}_{-0.177}$	$3.588^{+0.218}_{-0.205}$	$3.974^{+0.291}_{-0.253}$	$4.729^{+0.372}_{-0.353}$	$5.451^{+0.412}_{-0.546}$	$2.857^{+0.130}_{-0.133}$
A2142	$9.101^{+1.094}_{-1.064}$	$7.207^{+1.588}_{-1.630}$	$38.608^{+14.517}_{-15.795}$	$2.759^{+0.120}_{-0.121}$	$28.030^{+10.835}_{-8.686}$	$7.928^{+1.755}_{-2.120}$	$6.140^{+0.130}_{-0.147}$
A2147	$0.681^{+0.070}_{-0.067}$	$3.113^{+0.359}_{-0.357}$	$1.337^{+0.759}_{-0.380}$	$0.690^{+0.492}_{-0.217}$	$1.172^{+0.153}_{-0.141}$	$5.164^{+0.798}_{-0.791}$	$2.469^{+0.036}_{-0.041}$
A2163	$20.490^{+3.220}_{-2.984}$	$19.085^{+7.270}_{-9.143}$	$18.567^{+1.724}_{-1.516}$	$18.014^{+1.722}_{-1.525}$	$37.413^{+8.051}_{-6.685}$	$10.768^{+6.350}_{-3.668}$	$11.282^{+0.208}_{-0.205}$
A2199	$2.214^{+0.107}_{-0.106}$	$1.302^{+0.117}_{-0.208}$	$9.979^{+0.623}_{-0.490}$	$15.446^{+1.301}_{-1.160}$	$5.070^{+0.417}_{-0.394}$	$1.397^{+0.210}_{-0.268}$	$2.011^{+0.087}_{-0.085}$
A2204	$5.525^{+0.586}_{-0.554}$	$4.200^{+0.441}_{-0.540}$	$6.491^{+0.271}_{-0.277}$	$8.352^{+0.341}_{-0.352}$	$8.508^{+1.119}_{-1.053}$	$3.583^{+0.571}_{-0.607}$	$5.452^{+0.210}_{-0.211}$
A2244	$1.709^{+0.523}_{-0.492}$	$2.753^{+0.224}_{-0.204}$	$3.145^{+0.088}_{-0.092}$	$3.205^{+0.100}_{-0.098}$	$2.084^{+0.712}_{-0.645}$	$2.595^{+0.355}_{-0.701}$	$3.066^{+0.133}_{-0.151}$
A2255	$4.081^{+0.442}_{-0.405}$	$4.292^{+0.394}_{-0.414}$	$11.023^{+2.544}_{-2.080}$	$14.749^{+1.863}_{-2.685}$	$6.603^{+0.898}_{-0.796}$	$5.264^{+0.975}_{-1.107}$	$3.768^{+0.041}_{-0.043}$
A2256	$5.330^{+1.160}_{-1.087}$	$3.595^{+0.839}_{-0.912}$	$13.717^{+13.803}_{-4.604}$	$38.248^{+7.943}_{-10.702}$	$10.172^{+2.962}_{-2.383}$	$3.424^{+1.386}_{-1.528}$	$4.348^{+0.071}_{-0.064}$

continued on the next page

Name	$M_{500}^{\mathrm{NFW\ Freeze}}$ $10^{14}\,\mathrm{M}_\odot$	$M_{500}^{\mathrm{kT\ extrp}}$ $10^{14}\,\mathrm{M}_\odot$	$M_{500}^{\mathrm{NFW\ Hudson}}$ $10^{14}\,\mathrm{M}_\odot$	$M_{500}^{\mathrm{NFW\ All}}$ $10^{14}\,\mathrm{M}_\odot$	$M_{200}^{\mathrm{NFW\ Freeze}}$ $10^{14}\,\mathrm{M}_\odot$	$M_{200}^{\mathrm{kT\ extrp}}$ $10^{14}\,\mathrm{M}_\odot$	$M_{500}^{\mathrm{Planck\ SZ}}$ $10^{14}\,\mathrm{M}_\odot$
A2589	$1.219^{+0.081}_{-0.076}$	$1.447^{+0.107}_{-0.244}$	$2.756^{+0.186}_{-0.205}$	$2.930^{+0.262}_{-0.216}$	$2.994^{+0.303}_{-0.290}$	$2.058^{+0.291}_{-0.543}$	$1.235^{+0.158}_{-0.169}$
A2597	$2.111^{+0.029}_{-0.028}$	$2.771^{+0.017}_{-0.019}$	$1.944^{+0.013}_{-0.013}$	$2.352^{+0.015}_{-0.014}$	$4.259^{+0.198}_{-0.169}$	$4.247^{+0.027}_{-0.030}$	$1.738^{+0.169}_{-0.180}$
A2634	$0.945^{+0.237}_{-0.212}$	$0.649^{+0.224}_{-0.187}$	$1.809^{+0.189}_{-0.166}$	$1.875^{+0.203}_{-0.193}$	$1.554^{+0.452}_{-0.386}$	$0.432^{+0.227}_{-0.103}$	$1.058^{+0.088}_{-0.095}$
A2657	$0.853^{+0.078}_{-0.078}$	$3.080^{+0.526}_{-0.663}$	$0.654^{+0.085}_{-0.067}$	$0.491^{+0.058}_{-0.047}$	$1.691^{+0.225}_{-0.192}$	$4.062^{+1.161}_{-1.061}$	$1.030^{+0.126}_{-0.132}$
A3112	$2.943^{+0.359}_{-0.332}$	$1.854^{+0.277}_{-0.335}$	$2.760^{+0.176}_{-0.152}$	$3.179^{+0.211}_{-0.177}$	$5.733^{+0.901}_{-0.857}$	$1.679^{+0.379}_{-0.435}$	$2.049^{+0.120}_{-0.138}$
A3158	$2.170^{+0.098}_{-0.093}$	$2.616^{+0.078}_{-0.076}$	$2.559^{+0.071}_{-0.072}$	$2.600^{+0.081}_{-0.075}$	$3.971^{+0.246}_{-0.237}$	$3.970^{+0.236}_{-0.277}$	$2.957^{+0.103}_{-0.093}$
A3266	$7.869^{+0.772}_{-0.721}$	$11.606^{+1.912}_{-1.944}$	$10.513^{+2.067}_{-1.773}$	$8.137^{+1.750}_{-1.407}$	$13.440^{+1.554}_{-1.516}$	$13.080^{+4.147}_{-3.547}$	$4.646^{+0.080}_{-0.081}$
A3376	$1.488^{+0.213}_{-0.207}$	$1.612^{+0.157}_{-0.127}$	$2.170^{+0.225}_{-0.207}$	$2.255^{+0.286}_{-0.241}$	$2.582^{+0.453}_{-0.430}$	$2.055^{+0.195}_{-0.208}$	$1.669^{+0.111}_{-0.114}$
A3391	$2.476^{+0.350}_{-0.352}$	$2.568^{+0.307}_{-0.327}$	$4.115^{+1.490}_{-0.851}$	$5.590^{+4.604}_{-1.865}$	$4.514^{+0.860}_{-0.789}$	$3.167^{+0.692}_{-0.705}$	$1.973^{+0.100}_{-0.094}$
A3395	$1.413^{+0.148}_{-0.137}$	$1.671^{+0.133}_{-0.137}$	$1.426^{+0.122}_{-0.100}$	$1.431^{+0.161}_{-0.125}$	$2.236^{+0.256}_{-0.243}$	$2.755^{+0.276}_{-0.250}$	$2.248^{+0.129}_{-0.135}$
A3526	$0.967^{+0.059}_{-0.057}$	$0.758^{+0.038}_{-0.057}$	$1.755^{+0.026}_{-0.028}$	$1.946^{+0.019}_{-0.021}$	$2.266^{+0.220}_{-0.194}$	$0.865^{+0.085}_{-0.098}$	$0.927^{+0.057}_{-0.061}$
A3558	$2.950^{+0.644}_{-0.590}$	$2.114^{+0.401}_{-0.378}$	$12.844^{+3.220}_{-2.033}$	$42.808^{+23.284}_{-17.987}$	$4.886^{+1.296}_{-1.146}$	$2.063^{+0.463}_{-0.570}$	$3.350^{+0.116}_{-0.122}$
A3562	$1.747^{+0.326}_{-0.314}$	$1.059^{+0.269}_{-0.292}$	$2.709^{+0.464}_{-0.378}$	$2.876^{+0.600}_{-0.451}$	$3.534^{+0.849}_{-0.747}$	$1.047^{+0.446}_{-0.597}$	$1.710^{+0.149}_{-0.171}$
A3571	$3.727^{+0.354}_{-0.321}$	$2.885^{+1.005}_{-1.204}$	$12.317^{+2.717}_{-1.940}$	$14.332^{+4.163}_{-3.347}$	$10.904^{+1.825}_{-1.476}$	$3.345^{+1.733}_{-1.672}$	$3.239^{+0.097}_{-0.104}$
A3581	$0.728^{+0.094}_{-0.086}$	$0.152^{+0.016}_{-0.030}$	$0.589^{+0.022}_{-0.020}$	$0.718^{+0.023}_{-0.023}$	$2.114^{+0.399}_{-0.364}$	$0.235^{+0.026}_{-0.046}$	–
A3667	$3.588^{+0.297}_{-0.295}$	$3.545^{+0.275}_{-0.203}$	$5.312^{+0.121}_{-0.115}$	$5.439^{+0.139}_{-0.124}$	$5.301^{+0.516}_{-0.479}$	$4.503^{+0.359}_{-0.205}$	$4.925^{+0.036}_{-0.037}$
A4038	$0.999^{+0.127}_{-0.120}$	$0.417^{+0.100}_{-0.140}$	$1.313^{+0.046}_{-0.049}$	$1.330^{+0.054}_{-0.053}$	$2.231^{+0.405}_{-0.351}$	$0.433^{+0.183}_{-0.302}$	$1.036^{+0.080}_{-0.075}$
A4059	$1.486^{+0.090}_{-0.090}$	$1.420^{+0.077}_{-0.076}$	$1.996^{+0.037}_{-0.038}$	$2.074^{+0.044}_{-0.040}$	$2.194^{+0.153}_{-0.152}$	$1.511^{+0.113}_{-0.103}$	$1.728^{+0.114}_{-0.104}$
EXO0422	$0.971^{+0.166}_{-0.157}$	$0.807^{+0.208}_{-0.256}$	$1.434^{+0.251}_{-0.203}$	$2.047^{+0.724}_{-0.461}$	$2.492^{+0.615}_{-0.540}$	$1.227^{+0.389}_{-0.637}$	–
HydraA	$1.794^{+0.215}_{-0.196}$	$1.669^{+0.161}_{-0.124}$	$4.052^{+0.195}_{-0.210}$	$3.874^{+0.127}_{-0.124}$	$2.604^{+0.366}_{-0.323}$	$1.430^{+0.154}_{-0.155}$	–
IIIZw54	$0.515^{+0.030}_{-0.029}$	$0.524^{+0.063}_{-0.073}$	$0.737^{+0.080}_{-0.077}$	$0.875^{+0.202}_{-0.117}$	$1.229^{+0.115}_{-0.107}$	$0.690^{+0.150}_{-0.186}$	–
MKW3S	$1.098^{+0.113}_{-0.108}$	$0.907^{+0.092}_{-0.128}$	$1.946^{+0.043}_{-0.041}$	$2.473^{+0.059}_{-0.051}$	$1.659^{+0.195}_{-0.182}$	$0.722^{+0.110}_{-0.217}$	$1.309^{+0.141}_{-0.148}$
MKW4	$0.387^{+0.037}_{-0.034}$	$0.380^{+0.032}_{-0.048}$	$0.510^{+0.024}_{-0.024}$	$0.414^{+0.020}_{-0.020}$	$0.589^{+0.066}_{-0.061}$	$0.483^{+0.065}_{-0.092}$	–
MKW8	$0.712^{+0.107}_{-0.105}$	$0.808^{+0.145}_{-0.164}$	$1.104^{+0.466}_{-0.259}$	$1.210^{+2.200}_{-0.387}$	$1.549^{+0.321}_{-0.292}$	$1.097^{+0.413}_{-0.376}$	$0.772^{+0.127}_{-0.139}$
NGC1399	$0.162^{+0.009}_{-0.009}$	$0.126^{+0.004}_{-0.002}$	$0.113^{+0.004}_{-0.004}$	$0.114^{+0.003}_{-0.002}$	$0.506^{+0.058}_{-0.050}$	$0.184^{+0.025}_{-0.004}$	–
NGC1550	$0.242^{+0.020}_{-0.019}$	$0.277^{+0.020}_{-0.029}$	$1.416^{+0.217}_{-0.160}$	$1.107^{+0.150}_{-0.113}$	$0.693^{+0.093}_{-0.081}$	$0.402^{+0.043}_{-0.079}$	–
NGC4636	$0.108^{+0.007}_{-0.007}$	$0.083^{+0.003}_{-0.008}$	$0.048^{+0.002}_{-0.002}$	$0.033^{+0.001}_{-0.001}$	$0.534^{+0.077}_{-0.064}$	$0.119^{+0.006}_{-0.020}$	–
NGC5044	$0.200^{+0.006}_{-0.006}$	$0.195^{+0.005}_{-0.005}$	$0.244^{+0.008}_{-0.007}$	$0.154^{+0.003}_{-0.002}$	$0.411^{+0.022}_{-0.021}$	$0.265^{+0.010}_{-0.011}$	–
NGC507	$0.309^{+0.028}_{-0.026}$	$0.175^{+0.017}_{-0.016}$	$0.717^{+0.100}_{-0.077}$	$0.715^{+0.094}_{-0.072}$	$0.815^{+0.100}_{-0.096}$	$0.185^{+0.040}_{-0.028}$	–
RXCJ1504	$6.477^{+1.104}_{-1.035}$	$5.831^{+0.879}_{-1.202}$	$5.383^{+0.707}_{-0.578}$	$5.691^{+0.372}_{-0.366}$	$10.844^{+2.272}_{-1.899}$	$6.632^{+1.741}_{-2.202}$	$4.666^{+0.336}_{-0.338}$
S1101	$0.992^{+0.110}_{-0.105}$	$0.621^{+0.101}_{-0.121}$	$1.053^{+0.021}_{-0.020}$	$1.006^{+0.014}_{-0.014}$	$1.568^{+0.209}_{-0.194}$	$0.369^{+0.154}_{-0.126}$	$1.025^{+0.154}_{-0.157}$
ZwCl1215	$3.272^{+0.353}_{-0.352}$	$4.030^{+0.384}_{-0.781}$	$6.395^{+1.485}_{-1.057}$	$10.006^{+5.437}_{-2.614}$	$6.538^{+0.956}_{-0.925}$	$5.579^{+0.936}_{-1.958}$	–

Table B.2: Properties of the 64 HIFLUGCS clusters. The last column is the average radius of the largest annulus for the temperature measurements.

Name	Emission weighted center		Redshift	$N_{\rm H}$	L_x	$R_{\rm kT}^{\rm max}$
	RA [h:m:s]	DEC [d:m:s]		$10^{22}\,{\rm cm}^{-2}$	$10^{43}\,{\rm erg\,s}^{-1}\,{\rm cm}^{-2}$	arcmin
2A0335	3:38:40.2941	9:58:4.7892	0.035	0.307	$11.972^{+0.090}_{-0.090}$	10.7
A0085	0:41:50.3064	-9:18:11.1240	0.056	0.031	$24.472^{+0.150}_{-0.150}$	15.4
A0119	0:56:16.0400	-1:15:20.6000	0.044	0.033	$8.384^{+0.076}_{-0.076}$	10.0
A0133	1:2:43.1400	-21:52:47.0280	0.057	0.017	$7.360^{+0.062}_{-0.062}$	7.1
A0262	1:52:45.6096	36:9:3.9240	0.016	0.071	$2.601^{+0.100}_{-0.100}$	17.1
A0399	2:57:51.6360	13:2:49.5240	0.071	0.171	$17.675^{+0.956}_{-0.956}$	8.3
A0400	2:57:41.3496	6:1:36.9480	0.024	0.131	$1.716^{+0.019}_{-0.019}$	7.6
A0401	2:58:57.2160	13:34:46.5600	0.075	0.152	$31.383^{+0.338}_{-0.338}$	10.7
A0478	4:13:25.2960	10:27:57.9600	0.085	0.257	$44.225^{+0.252}_{-0.252}$	9.9
A0496	4:33:37.8192	-13:15:38.5560	0.033	0.060	$9.591^{+0.071}_{-0.071}$	18.1
A0576	7:21:26.1144	55:45:34.2360	0.038	0.071	$4.679^{+0.319}_{-0.319}$	14.8
A0754	9:9:18.1872	-9:41:15.9360	0.053	0.058	$9.975^{+0.162}_{-0.162}$	16.1
A1060	10:36:42.8592	-27:31:42.0960	0.011	0.062	$1.386^{+0.045}_{-0.045}$	13.3
A1367	11:44:44.5008	19:43:55.8120	0.022	0.020	$3.015^{+0.023}_{-0.023}$	12.3
A1644	12:57:10.7352	-17:24:10.2960	0.047	0.051	$9.690^{+0.496}_{-0.496}$	12.9
A1650	12:58:41.8848	-1:45:32.9040	0.085	0.014	$18.270^{+1.205}_{-1.205}$	15.6
A1651	12:59:22.3512	-4:11:46.6080	0.086	0.016	$20.000^{+0.239}_{-0.239}$	7.0
A1656	12:59:45.3408	27:57:5.6160	0.023	0.009	$19.791^{+0.272}_{-0.272}$	9.6
A1736	13:26:53.7120	-27:10:35.4000	0.046	0.055	$8.056^{+0.504}_{-0.504}$	8.0
A1795	13:48:52.7904	26:35:34.3680	0.062	0.012	$25.310^{+0.086}_{-0.086}$	9.3
A2029	15:10:55.9896	5:44:33.6480	0.077	0.037	$43.282^{+0.262}_{-0.262}$	12.6
A2052	15:16:43.5100	7:1:19.8000	0.035	0.027	$6.123^{+0.063}_{-0.063}$	9.5
A2063	15:23:5.7720	8:36:25.3800	0.035	0.030	$5.681^{+0.073}_{-0.073}$	14.0
A2065	15:22:29.0832	27:43:14.3760	0.072	0.030	$13.901^{+0.848}_{-0.848}$	9.4
A2142	15:58:19.7760	27:14:0.9600	0.090	0.044	$53.363^{+0.463}_{-0.463}$	9.3
A2147	16:2:16.3056	15:58:18.4440	0.035	0.034	$7.297^{+0.237}_{-0.237}$	9.8
A2163	16:15:46.3920	-6:8:36.9600	0.201	0.205	$85.320^{+1.316}_{-1.316}$	7.0
A2199	16:28:37.1256	39:32:53.3040	0.030	0.009	$10.412^{+0.190}_{-0.190}$	11.3
A2204	16:32:47.0592	5:34:32.0160	0.152	0.073	$67.345^{+1.092}_{-1.092}$	6.6
A2244	17:2:41.9760	34:3:28.0800	0.097	0.020	$21.171^{+0.454}_{-0.454}$	15.0
A2255	17:12:54.5376	64:3:51.4440	0.080	0.027	$13.765^{+0.166}_{-0.166}$	10.6
A2256	17:3:52.4688	78:40:19.1280	0.060	0.050	$23.304^{+0.320}_{-0.320}$	11.0
A2589	23:23:56.7720	16:46:33.2040	0.042	0.035	$4.809^{+0.063}_{-0.063}$	5.9
A2597	23:25:20.0088	-12:7:27.1920	0.085	0.028	$17.206^{+0.210}_{-0.210}$	5.0
A2634	23:38:29.0448	27:1:51.6720	0.031	0.062	$2.519^{+0.039}_{-0.039}$	14.5
A2657	23:44:56.7432	9:11:52.9440	0.040	0.084	$4.426^{+0.039}_{-0.039}$	7.2
A3112	3:17:58.7136	-44:14:8.3760	0.075	0.014	$18.640^{+0.205}_{-0.205}$	6.9
A3158	3:42:53.5824	-53:37:51.7080	0.059	0.014	$14.095^{+0.214}_{-0.214}$	8.4
A3266	4:31:14.9088	-61:26:54.1320	0.059	0.017	$21.794^{+0.144}_{-0.144}$	16.0
A3376	6:2:10.1088	-39:57:35.7480	0.045	0.058	$5.435^{+0.079}_{-0.079}$	10.4
A3391	6:26:24.2232	-53:41:24.0360	0.053	0.076	$6.702^{+0.129}_{-0.129}$	10.0
A3395	6:26:46.0800	-54:32:43.0800	0.050	0.098	$5.327^{+0.204}_{-0.204}$	11.4
A3526	12:48:50.6424	-41:18:15.2640	0.010	0.122	$3.102^{+0.068}_{-0.068}$	22.1
A3558	13:28:0.4104	-31:30:0.7920	0.048	0.049	$16.539^{+0.076}_{-0.076}$	14.2
A3562	13:33:36.4872	-31:40:25.5360	0.050	0.045	$7.792^{+0.073}_{-0.073}$	7.7
A3571	13:47:27.8688	-32:51:37.6560	0.037	0.051	$20.330^{+0.151}_{-0.151}$	8.4
A3581	14:7:30.6264	-27:0:47.3400	0.021	0.053	$1.642^{+0.053}_{-0.053}$	7.3

continued on the next page

Name	Emission weighted center		Redshift	$N_{\rm H}$	L_x	$R_{\rm kT}^{\rm max}$
	RA [h:m:s]	DEC [d:m:s]		$10^{22}\,{\rm cm}^{-2}$	$10^{43}\,{\rm erg\,s}^{-1}\,{\rm cm}^{-2}$	arcmin
A3667	20:12:40.7088	-56:50:27.0600	0.056	0.052	$24.059^{+0.164}_{-0.164}$	17.2
A4038	23:47:44.6520	-28:8:42.4680	0.028	0.016	$4.889^{+0.062}_{-0.062}$	8.9
A4059	23:57:1.6992	-34:45:29.1240	0.046	0.013	$7.180^{+0.095}_{-0.095}$	14.8
EXO0422	4:25:51.2232	-8:33:40.3560	0.039	0.124	$5.037^{+0.311}_{-0.311}$	5.4
HydraA	9:18:5.9880	-12:5:36.1680	0.054	0.055	$14.824^{+0.083}_{-0.083}$	14.2
IIIZw54	3:41:18.7296	15:24:13.8960	0.031	0.267	$2.077^{+0.160}_{-0.160}$	5.6
MKW3S	15:21:50.2776	7:42:11.7720	0.045	0.030	$7.162^{+0.074}_{-0.074}$	12.6
MKW4	12:4:27.6600	1:53:41.4960	0.020	0.019	$0.975^{+0.016}_{-0.016}$	18.0
MKW8	14:40:42.1512	3:28:17.8680	0.027	0.027	$1.974^{+0.165}_{-0.165}$	8.5
NGC1399	3:38:28.7904	-35:27:4.5000	0.005	0.016	$0.205^{+0.011}_{-0.011}$	15.9
NGC1550	4:19:38.0208	2:24:33.3720	0.012	0.162	$0.754^{+0.041}_{-0.041}$	7.9
NGC4636	12:42:50.2656	2:41:30.6240	0.004	0.021	$0.058^{+0.004}_{-0.004}$	10.5
NGC5044	13:15:23.7816	-16:23:11.6880	0.009	0.062	$0.483^{+0.002}_{-0.002}$	16.0
NGC507	1:23:38.5680	33:15:2.0880	0.017	0.064	$0.617^{+0.008}_{-0.008}$	7.4
RXCJ1504	15:4:7.8024	-2:48:10.2892	0.215	0.084	$104.370^{+1.960}_{-1.960}$	5.0
S1101	23:13:58.3128	-42:43:36.1200	0.058	0.012	$8.992^{+0.082}_{-0.082}$	8.5
ZwCl1215	12:17:40.6368	3:39:29.6640	0.075	0.019	$13.100^{+0.166}_{-0.166}$	6.9

Table B.3: List of Chandra observations of the HIFLUGCS clusters, in green the observations that were used for the analysis. The main observations that is used for substructure determination is printed in boldface. Below each cluster is a summary over the number of observation and their summed raw exposure time for the available observations and those which were used (including a fraction of the used exposure time).

Cluster	Observation ID	Detector	Exposure ks	Cycle	Offset arcmin	Comment
2A0335						
	7939	**ACIS-S**	**50.18**	**8**	**0.10**	
	9792	ACIS-S	34.18	8	0.10	
	919	ACIS-S	19.98	1	0.23	
Total	Observations	3	Exposure	104.34ks		
Used	Observations	3	Exposure	104.34ks	100%	
A0085						
	15173	**ACIS-I**	**43.08**	**14**	**3.39**	
	15174	ACIS-I	40.08	14	6.42	
	904	ACIS-I	38.91	1	4.71	
	16263	ACIS-I	38.66	14	6.42	
	16264	ACIS-I	37.08	14	3.39	
	4887	ACIS-I	10.18	5	11.49	
	4884	ACIS-I	9.76	5	15.56	
	4885	ACIS-I	9.76	5	17.74	
	4882	ACIS-I	9.75	5	20.60	
	4888	ACIS-I	9.75	5	20.61	
	4886	ACIS-I	9.74	5	18.77	
Total	Observations	11	Exposure	256.75ks		
Used	Observations	6	Exposure	207.99ks	81%	
A0119						
	7918	**ACIS-I**	**45.63**	**8**	**0.04**	
	4180	ACIS-I	12.09	4	0.04	
Total	Observations	2	Exposure	57.72ks		
Used	Observations	2	Exposure	57.72ks	100%	
A0133						
	13442	ACIS-I	179.02	13	18.45	
	13448	ACIS-I	148.05	13	20.54	
	13452	ACIS-I	143.95	13	23.22	
	13456	ACIS-I	137.43	13	16.08	
	14333	ACIS-I	136.54	13	17.07	
	14338	ACIS-I	119.06	13	20.75	
	13450	ACIS-I	109.61	13	23.67	
	13454	ACIS-I	93.00	13	19.85	
	14346	ACIS-I	87.04	13	19.85	
	13451	ACIS-I	71.05	13	24.18	
	13443	ACIS-I	70.60	13	18.07	
	13455	ACIS-I	70.55	13	17.33	
	9897	**ACIS-I**	**70.13**	**10**	**0.10**	
	13447	ACIS-I	70.05	13	19.07	
	13457	ACIS-I	70.04	13	22.23	
	13453	ACIS-I	69.86	13	19.10	

continued on the next page

Cluster	OBSID	Detector	Exposure ks	Cycle	Offset arcmin	Comment
	14347	ACIS-I	69.60	13	23.67	
	13449	ACIS-I	69.06	13	19.20	
	13445	ACIS-I	66.04	13	20.66	
	13446	ACIS-I	59.19	13	20.75	
	12179	ACIS-I	51.77	12	15.86	
	12177	ACIS-I	50.77	12	16.35	
	13392	ACIS-I	50.55	13	19.26	
	13518	ACIS-I	50.26	13	3.79	
	12178	ACIS-I	47.45	12	19.47	
	13391	ACIS-I	47.05	13	21.55	
	3710	ACIS-I	45.18	3	0.34	
	3183	ACIS-I	45.11	3	0.34	
	14354	ACIS-I	39.16	13	16.08	
	13444	ACIS-I	38.76	13	17.07	
	2203	ACIS-S	35.91	2	0.29	
	14343	ACIS-I	35.77	13	20.54	
	14345	ACIS-I	34.19	13	23.22	
Total	Observations	33	Exposure	2481.80ks		
Used	Observations	6	Exposure	527.39ks	21%	
A0262						
	7921	**ACIS-S**	**112.14**	**8**	**0.13**	
	2215	ACIS-S	29.12	2	0.13	
Total	Observations	2	Exposure	141.26ks		
Used	Observations	2	Exposure	141.26ks	100%	
A0399						
	3230	**ACIS-I**	**49.28**	**3**	**0.47**	
Total	Observations	1	Exposure	49.28ks		
Used	Observations	1	Exposure	49.28ks	100%	
A0400						
	4181	**ACIS-I**	**21.78**	**4**	**0.14**	
Total	Observations	1	Exposure	21.78ks		
Used	Observations	1	Exposure	21.78ks	100%	
A0401						
	14024	**ACIS-I**	**136.86**	**13**	**0.20**	
	518	ACIS-I	18.24	1	0.40	
	2309	ACIS-I	11.72	1	0.40	
Total	Observations	3	Exposure	166.82ks		
Used	Observations	1	Exposure	136.86ks	82%	
A0478						
	1669	**ACIS-S**	**42.94**	**2**	**0.08**	
	7217	ACIS-I	18.56	7	10.65	
	7231	ACIS-I	17.55	7	11.15	
	7232	ACIS-I	16.13	7	11.15	
	6102	ACIS-I	10.13	5	0.04	
	7233	ACIS-I	9.14	7	11.15	
Total	Observations	6	Exposure	114.45ks		
Used	Observations	2	Exposure	60.49ks	53%	

continued on the next page

Cluster	OBSID	Detector	Exposure ks	Cycle	Offset arcmin	Comment
A0496						
	4976	**ACIS-S**	**76.08**	**5**	**1.40**	
	931	ACIS-S	19.16	1	0.06	
	3361	ACIS-S	10.13	1	0.06	
Total	Observations	3	Exposure	105.37ks		
Used	Observations	1	Exposure	76.08ks	72%	
A0576						
	3289	**ACIS-S**	**39.10**	**3**	**0.29**	
Total	Observations	1	Exposure	39.10ks		
Used	Observations	1	Exposure	39.10ks	100%	
A0754						
	10743	**ACIS-I**	**95.36**	**10**	**6.99**	
	577	ACIS-I	44.77	0	2.54	
	6797	ACIS-I	10.16	7	17.96	
	6798	ACIS-I	10.16	7	22.63	
	6793	ACIS-I	10.07	7	20.09	
	6794	ACIS-I	10.05	7	14.43	
	6795	ACIS-I	9.77	7	22.89	
	6796	ACIS-I	9.77	7	14.21	
	6799	ACIS-I	9.77	7	17.80	
Total	Observations	9	Exposure	209.88ks		
Used	Observations	2	Exposure	140.13ks	67%	
A1060						
	2220	**ACIS-I**	**32.32**	**2**	**0.17**	
Total	Observations	1	Exposure	32.32ks		
Used	Observations	1	Exposure	32.32ks	100%	
A1367						
	4189	ACIS-S	48.11	4	22.19	
	514	**ACIS-S**	**41.05**	**1**	**7.05**	
	4916	ACIS-S	38.33	5	4.27	
Total	Observations	3	Exposure	127.49ks		
Used	Observations	1	Exposure	41.05ks	32%	
A1644						
	7922	**ACIS-I**	**52.17**	**8**	**6.50**	
	2206	ACIS-I	18.96	2	0.53	
Total	Observations	2	Exposure	71.13ks		
Used	Observations	2	Exposure	71.13ks	100%	
A1650						
	5823	**ACIS-I**	**40.13**	**6**	**0.05**	
	7242	ACIS-I	37.67	6	0.05	
	6356	ACIS-I	37.04	6	0.05	
	6357	ACIS-I	33.09	6	0.05	
	6358	ACIS-I	32.22	6	0.05	
	4178	ACIS-S	27.62	4	0.03	
	5822	ACIS-I	20.15	6	0.05	

continued on the next page

Cluster	OBSID	Detector	Exposure ks	Cycle	Offset arcmin	Comment
Total	Observations	7	Exposure	227.92ks		
Used	Observations	7	Exposure	227.92ks	100%	
A1651						
	4185	**ACIS-I**	**9.77**	**4**	**0.09**	
Total	Observations	1	Exposure	9.77ks		
Used	Observations	1	Exposure	9.77ks	100%	
A1656						
	13996	**ACIS-I**	**124.68**	**13**	**3.53**	
	13994	ACIS-I	83.08	13	3.21	
	14410	ACIS-I	79.57	13	4.86	
	13995	ACIS-I	63.82	13	5.84	
	2941	ACIS-I	63.74	3	20.46	
	13993	ACIS-I	40.08	13	4.86	
	14415	ACIS-I	34.97	13	5.84	
	14411	ACIS-I	34.08	13	3.21	
	9714	ACIS-I	30.04	9	2.74	
	10672	ACIS-S	28.91	10	2.74	
	14406	ACIS-I	25.09	13	5.84	
	1112	ACIS-I	9.78	0	2.74	
	556	ACIS-S	9.77	1	2.74	
	1113	ACIS-I	9.77	0	2.74	
	1086	ACIS-S	9.66	0	2.74	
	1114	ACIS-I	9.17	0	2.74	
Total	Observations	16	Exposure	656.21ks		
Used	Observations	4	Exposure	351.15ks	54%	
A1736						
	4186	**ACIS-I**	**15.12**	**4**	**0.43**	
Total	Observations	1	Exposure	15.12ks		
Used	Observations	1	Exposure	15.12ks	100%	
A1795						
	17230	ACIS-I	59.04	16	24.96	
	17226	ACIS-I	58.45	16	24.40	
	493	ACIS-S	19.88	1	0.10	
	494	ACIS-S	19.77	1	0.10	
	10900	ACIS-S	16.03	11	0.10	
	10898	ACIS-I	15.95	11	0.10	
	10901	ACIS-S	15.67	11	0.10	
	12028	ACIS-S	15.17	11	0.10	
	5289	ACIS-I	15.15	5	0.10	
	5290	ACIS-I	15.14	5	0.10	
	10899	**ACIS-I**	**15.12**	**11**	**0.10**	
	12026	ACIS-I	15.12	11	0.10	
	14274	ACIS-I	15.08	13	0.10	
	14275	ACIS-I	15.08	13	0.10	
	15487	ACIS-I	15.08	14	0.10	
	15490	ACIS-I	15.08	14	0.10	
	15491	ACIS-I	15.08	14	0.10	
	16434	ACIS-I	15.08	15	0.10	

continued on the next page

Cluster	OBSID	Detector	Exposure ks	Cycle	Offset arcmin	Comment
	16468	ACIS-I	15.08	15	0.10	
	16469	ACIS-I	15.08	15	0.10	
	16471	ACIS-I	15.08	15	0.10	
	16472	ACIS-I	15.08	15	0.10	
	17399	ACIS-I	15.08	16	0.10	
	17404	ACIS-I	15.08	16	0.10	
	17407	ACIS-I	15.08	16	0.10	
	17684	ACIS-I	15.08	17	0.10	
	16466	ACIS-S	15.07	15	0.10	
	6159	ACIS-I	15.05	5	0.10	
	6163	ACIS-I	15.05	5	0.10	
	13108	ACIS-I	15.05	12	0.10	
	13412	ACIS-I	15.05	13	0.09	
	13413	ACIS-I	15.05	13	0.09	
	13417	ACIS-I	15.05	13	0.09	
	6160	ACIS-S	15.04	5	0.10	
	12027	ACIS-I	15.04	11	0.10	
	12029	ACIS-S	14.89	11	0.10	
	16438	ACIS-I	14.89	15	0.10	
	17406	ACIS-I	14.89	16	0.10	
	13111	ACIS-I	14.78	12	0.10	
	13113	ACIS-I	14.78	12	0.10	
	14272	ACIS-I	14.78	13	0.10	
	14273	ACIS-I	14.78	13	0.10	
	16437	ACIS-I	14.78	15	0.10	
	17401	ACIS-I	14.78	16	0.10	
	17402	ACIS-I	14.78	16	0.10	
	17403	ACIS-I	14.78	16	0.10	
	17409	ACIS-I	14.78	16	0.10	
	17410	ACIS-I	14.78	16	0.10	
	13415	ACIS-I	14.78	13	0.09	
	13109	ACIS-I	14.77	12	0.10	
	13110	ACIS-I	14.77	12	0.10	
	13112	ACIS-I	14.77	12	0.10	
	13416	ACIS-I	14.77	13	0.10	
	15488	ACIS-I	14.77	14	0.10	
	15489	ACIS-I	14.77	14	0.10	
	15492	ACIS-I	14.77	14	0.10	
	16435	ACIS-I	14.77	15	0.10	
	16436	ACIS-I	14.77	15	0.10	
	16439	ACIS-I	14.77	15	0.10	
	16467	ACIS-I	14.77	15	0.10	
	16470	ACIS-I	14.77	15	0.10	
	17400	ACIS-I	14.77	16	0.10	
	17408	ACIS-I	14.77	16	0.10	
	13414	ACIS-I	14.77	13	0.09	
	5288	ACIS-S	14.76	5	0.10	
	3666	ACIS-S	14.61	3	0.10	
	5286	ACIS-S	14.49	5	0.10	
	5287	ACIS-S	14.49	5	0.10	
	14270	ACIS-I	14.47	13	0.10	
	14271	ACIS-I	14.16	13	0.10	

continued on the next page

Cluster	OBSID	Detector	Exposure ks	Cycle	Offset arcmin	Comment
	17411	ACIS-I	14.08	16	0.10	
	17683	ACIS-I	14.02	17	0.10	
	6162	ACIS-I	13.78	5	0.10	
	6161	ACIS-I	13.77	5	0.10	
	14269	ACIS-S	10.07	13	0.10	
	15485	ACIS-S	10.07	14	0.10	
	16432	ACIS-S	10.07	15	0.10	
	14268	ACIS-S	10.06	13	0.10	
	16433	ACIS-S	10.06	15	0.10	
	17397	ACIS-S	10.06	16	0.10	
	17405	ACIS-S	10.06	16	0.10	
	17686	ACIS-S	10.06	17	0.10	
	17398	ACIS-S	10.05	16	0.10	
	13106	ACIS-S	10.04	12	0.10	
	17685	ACIS-S	10.03	17	0.10	
	15486	ACIS-S	9.81	14	0.10	
	13107	ACIS-S	9.77	12	0.10	
	16465	ACIS-S	9.77	15	0.10	
Total	Observations	88	Exposure	1338.47ks		
Used	Observations	58	Exposure	874.25ks	65%	
A2029						
	4977	**ACIS-S**	**78.91**	**5**	**0.06**	
	891	ACIS-S	20.07	1	0.06	
	6101	ACIS-I	10.05	5	0.04	
Total	Observations	3	Exposure	109.03ks		
Used	Observations	2	Exposure	98.98ks	91%	
A2052						
	5807	ACIS-S	128.63	6	0.25	
	10478	**ACIS-S**	**120.67**	**10**	**0.25**	
	10879	ACIS-S	82.21	10	0.25	
	10479	ACIS-S	65.76	10	0.25	
	10477	ACIS-S	62.03	10	0.25	
	10917	ACIS-S	55.99	10	0.25	
	10914	ACIS-S	39.36	10	0.25	
	890	ACIS-S	37.23	1	0.22	
	10916	ACIS-S	35.47	10	0.25	
	10480	ACIS-S	20.15	10	0.25	
	10915	ACIS-S	15.16	10	0.25	
Total	Observations	11	Exposure	662.66ks		
Used	Observations	1	Exposure	120.67ks	18%	
A2063						
	6263	**ACIS-S**	**17.04**	**6**	**0.10**	
	6262	ACIS-S	14.35	6	0.10	
	5795	ACIS-S	10.04	6	0.10	
Total	Observations	3	Exposure	41.43ks		
Used	Observations	2	Exposure	31.39ks	76%	
A2065						
	3182	**ACIS-I**	**50.09**	**3**	**0.15**	

continued on the next page

Cluster	OBSID	Detector	Exposure ks	Cycle	Offset arcmin	Comment
Total	Observations	1	Exposure	50.09ks		
Used	Observations	1	Exposure	50.09ks	100%	
A2142						
	15186	ACIS-S	91.07	14	0.34	
	5005	**ACIS-I**	**45.15**	**5**	**1.52**	
	16564	ACIS-S	45.06	14	0.34	
	16565	ACIS-S	21.07	14	0.34	
	1228	ACIS-S	12.26	0	0.20	
	1196	ACIS-S	11.54	0	0.20	
Total	Observations	6	Exposure	226.15ks		
Used	Observations	1	Exposure	45.15ks	20%	
A2147						
	3211	**ACIS-I**	**18.12**	**3**	**2.45**	
Total	Observations	1	Exposure	18.12ks		
Used	Observations	1	Exposure	18.12ks	100%	
A2163						
	1653	**ACIS-I**	**72.09**	**2**	**0.25**	
	545	ACIS-I	9.57	1	0.25	
Total	Observations	2	Exposure	81.66ks		
Used	Observations	1	Exposure	72.09ks	88%	
A2199						
	10748	**ACIS-I**	**41.11**	**10**	**0.05**	
	10805	ACIS-I	30.73	10	0.05	
	10803	ACIS-I	30.56	10	0.05	
	497	ACIS-S	19.72	1	0.05	
	498	ACIS-S	19.16	1	0.05	
	10804	ACIS-I	19.04	10	0.05	
Total	Observations	6	Exposure	160.32ks		
Used	Observations	3	Exposure	102.40ks	64%	
A2204						
	7940	**ACIS-I**	**78.16**	**8**	**0.07**	
	499	ACIS-S	10.20	1	0.03	
	6104	ACIS-I	9.74	5	0.07	
Total	Observations	3	Exposure	98.10ks		
Used	Observations	1	Exposure	78.16ks	80%	
A2244						
	4179	**ACIS-S**	**57.72**	**4**	**0.04**	
Total	Observations	1	Exposure	57.72ks		
Used	Observations	1	Exposure	57.72ks	100%	
A2255						
	894	**ACIS-I**	**39.94**	**1**	**0.81**	
Total	Observations	1	Exposure	39.94ks		
Used	Observations	1	Exposure	39.94ks	100%	
A2256						

continued on the next page

Cluster	OBSID	Detector	Exposure ks	Cycle	Offset arcmin	Comment
	1386	ACIS-I	12.53	1	3.01	
	2419	**ACIS-S**	**12.02**	**1**	**3.01**	
	965	ACIS-S	11.22	1	3.01	
Total	Observations	3	Exposure	35.77ks		
Used	Observations	1	Exposure	12.02ks	34%	
A2589						
	7190	**ACIS-S**	**54.13**	**7**	**0.02**	
	7340	ACIS-S	15.11	7	0.02	
	3210	ACIS-S	13.86	3	0.10	Flared
	6948	ACIS-S	10.47	7	0.02	
Total	Observations	4	Exposure	93.57ks		
Used	Observations	2	Exposure	69.24ks	74%	
A2597						
	7329	**ACIS-S**	**60.90**	**7**	**0.06**	
	6934	ACIS-S	52.88	7	0.06	
	922	ACIS-S	39.86	1	0.08	Problem with Background Files
Total	Observations	3	Exposure	153.64ks		
Used	Observations	2	Exposure	113.78ks	74%	
A2634						
	4816	**ACIS-S**	**50.16**	**5**	**0.04**	
Total	Observations	1	Exposure	50.16ks		
Used	Observations	1	Exposure	50.16ks	100%	
A2657						
	4941	**ACIS-I**	**16.36**	**5**	**0.41**	
Total	Observations	1	Exposure	16.36ks		
Used	Observations	1	Exposure	16.36ks	100%	
A3112						
	13135	**ACIS-I**	**42.80**	**12**	**0.02**	
	6972	ACIS-I	30.16	7	0.02	
	7323	ACIS-I	28.81	7	0.02	
	7324	ACIS-I	25.77	7	0.02	
	2516	ACIS-S	17.14	2	0.02	
Total	Observations	5	Exposure	144.68ks		
Used	Observations	4	Exposure	127.54ks	88%	
A3158						
	3712	**ACIS-I**	**31.35**	**3**	**1.35**	
	3201	ACIS-I	25.12	3	1.35	
Total	Observations	2	Exposure	56.47ks		
Used	Observations	2	Exposure	56.47ks	100%	
A3266						
	899	**ACIS-I**	**30.14**	**1**	**0.26**	
Total	Observations	1	Exposure	30.14ks		
Used	Observations	1	Exposure	30.14ks	100%	
A3376						

continued on the next page

Cluster	OBSID	Detector	Exposure ks	Cycle	Offset arcmin	Comment
	3202	**ACIS-I**	**44.85**	**3**	**0.60**	
	3450	ACIS-I	20.11	3	0.60	
Total	Observations	2	Exposure	64.96ks		
Used	Observations	2	Exposure	64.96ks	100%	
A3391						
	13525	ACIS-I	49.08	13	14.97	
	13519	ACIS-I	48.08	13	23.57	
	4943	**ACIS-I**	**18.69**	**5**	**0.25**	
Total	Observations	3	Exposure	115.85ks		
Used	Observations	2	Exposure	67.77ks	58%	
A3395						
	13522	ACIS-I	50.08	13	15.47	
	4944	**ACIS-I**	**22.17**	**5**	**0.04**	
Total	Observations	2	Exposure	72.25ks		
Used	Observations	2	Exposure	72.25ks	100%	
A3526						
	16223	ACIS-S	181.33	15	0.01	
	4954	**ACIS-S**	**90.19**	**5**	**0.01**	
	16609	ACIS-S	83.42	15	0.01	
	16534	ACIS-S	56.18	15	0.01	
	5310	ACIS-S	49.96	5	0.01	
	16607	ACIS-S	46.28	15	0.01	
	4955	ACIS-S	45.26	5	0.01	
	16224	ACIS-S	42.85	15	0.01	
	4190	ACIS-S	34.72	4	3.90	
	16608	ACIS-S	34.56	15	0.01	
	4191	ACIS-S	34.47	4	4.14	
	504	ACIS-S	32.12	1	0.03	
	16225	ACIS-S	30.50	15	0.01	
	8179	ACIS-S	30.18	8	14.70	
	16610	ACIS-S	17.56	15	0.01	
	505	ACIS-S	10.08	1	0.03	
Total	Observations	16	Exposure	819.66ks		
Used	Observations	7	Exposure	316.90ks	39%	
A3558						
	4165	ACIS-I	18.61	4	24.08	
	1646	**ACIS-S**	**14.61**	**2**	**0.01**	
Total	Observations	2	Exposure	33.22ks		
Used	Observations	1	Exposure	14.61ks	44%	
A3562						
	4167	**ACIS-I**	**19.54**	**4**	**0.32**	
Total	Observations	1	Exposure	19.54ks		
Used	Observations	1	Exposure	19.54ks	100%	
A3571						
	4203	**ACIS-S**	**34.44**	**4**	**0.85**	
Total	Observations	1	Exposure	34.44ks		

continued on the next page

Cluster	OBSID	Detector	Exposure ks	Cycle	Offset arcmin	Comment
Used	Observations	1	Exposure	34.44ks	100%	
A3581						
	12884	**ACIS-S**	**85.66**	**12**	**0.15**	
Total	Observations	1	Exposure	85.66ks		
Used	Observations	1	Exposure	85.66ks	100%	
A3667						
	5751	**ACIS-I**	**130.60**	**6**	**4.24**	
	5753	ACIS-I	105.01	6	4.24	
	5752	ACIS-I	61.20	6	4.24	
	889	ACIS-I	50.96	1	8.91	
	6295	ACIS-I	50.15	6	4.24	
	6296	ACIS-I	50.04	6	4.24	
	6292	ACIS-I	47.29	6	4.24	
	513	ACIS-I	45.41	1	1.05	
Total	Observations	8	Exposure	540.66ks		
Used	Observations	6	Exposure	444.29ks	82%	
A4038						
	4992	**ACIS-I**	**33.97**	**5**	**0.12**	
Total	Observations	1	Exposure	33.97ks		
Used	Observations	1	Exposure	33.97ks	100%	
A4059						
	5785	**ACIS-S**	**93.34**	**6**	**0.05**	
	897	ACIS-S	41.19	1	0.20	Observation split
Total	Observations	2	Exposure	134.53ks		
Used	Observations	1	Exposure	93.34ks	69%	
EXO0422						
	3970	ACIS-S	15.75	4	0.16	not in full frame
	4183	**ACIS-I**	**10.14**	**4**	**0.01**	
Total	Observations	2	Exposure	25.89ks		
Used	Observations	1	Exposure	10.14ks	39%	
HydraA						
	4970	ACIS-S	100.13	5	0.10	
	4969	**ACIS-S**	**98.20**	**5**	**0.10**	
	575	ACIS-I	24.10	0	0.10	
	576	ACIS-S	19.78	0	0.10	
Total	Observations	4	Exposure	242.21ks		
Used	Observations	2	Exposure	198.33ks	82%	
IIIZw54						
	4182	**ACIS-I**	**23.76**	**4**	**0.17**	
Total	Observations	1	Exposure	23.76ks		
Used	Observations	1	Exposure	23.76ks	100%	
MKW3S						
	900	**ACIS-I**	**58.03**	**1**	**0.07**	
Total	Observations	1	Exposure	58.03ks		

continued on the next page

Cluster	OBSID	Detector	Exposure ks	Cycle	Offset arcmin	Comment
Used	Observations	1	Exposure	58.03ks	100%	
MKW4						
	3234	**ACIS-S**	**30.36**	**3**	**0.11**	
Total	Observations	1	Exposure	30.36ks		
Used	Observations	1	Exposure	30.36ks	100%	
MKW8						
	4942	**ACIS-I**	**23.45**	**5**	**1.24**	
Total	Observations	1	Exposure	23.45ks		
Used	Observations	1	Exposure	23.45ks	100%	
NGC1399						
	3949	ACIS-S	66.33	4	23.20	
	4175	ACIS-I	63.73	4	22.20	
	9530	**ACIS-S**	**60.11**	**9**	**0.02**	
	319	ACIS-S	56.66	1	0.06	
	4177	ACIS-I	47.58	4	22.60	
	4176	ACIS-I	46.64	4	15.52	
	4174	ACIS-I	46.27	4	8.66	
	4168	ACIS-I	46.24	4	18.36	
	4169	ACIS-I	45.88	4	23.46	
	4173	ACIS-I	45.68	4	17.63	
	4171	ACIS-I	45.55	4	15.33	
	4170	ACIS-I	45.18	4	20.39	
	4172	ACIS-I	45.09	4	1.49	
	624	ACIS-S	44.17	1	13.41	
	2942	ACIS-S	29.62	3	9.74	
	14527	ACIS-S	28.16	14	0.04	
	9799	ACIS-S	21.57	9	8.73	
	9798	ACIS-S	18.54	9	8.73	
Total	Observations	18	Exposure	803.00ks		
Used	Observations	8	Exposure	363.74ks	45%	
NGC1550						
	5800	**ACIS-S**	**45.13**	**6**	**3.93**	
	5801	ACIS-S	45.04	6	4.17	
	3186	ACIS-I	10.12	3	0.91	
	3187	ACIS-I	9.77	3	0.91	
Total	Observations	4	Exposure	110.06ks		
Used	Observations	2	Exposure	90.17ks	82%	
NGC4636						
	3926	**ACIS-I**	**75.69**	**4**	**0.08**	
	4415	ACIS-I	75.34	4	0.08	
	323	ACIS-S	53.05	1	0.09	
Total	Observations	3	Exposure	204.08ks		
Used	Observations	2	Exposure	151.03ks	74%	
NGC5044						
	9399	**ACIS-S**	**83.78**	**9**	**0.03**	
	798	ACIS-S	20.73	1	0.03	

continued on the next page

Cluster	OBSID	Detector	Exposure ks	Cycle	Offset arcmin	Comment
Total	Observations	2	Exposure	104.51ks		
Used	Observations	2	Exposure	104.51ks	100%	
NGC507						
	2882	**ACIS-I**	**44.21**	**3**	**0.38**	
	317	ACIS-S	27.19	1	0.18	
	10536	ACIS-S	18.64	10	13.62	
Total	Observations	3	Exposure	90.04ks		
Used	Observations	2	Exposure	62.85ks	70%	
RXCJ1504						
	5793	**ACIS-I**	**39.67**	**6**	**0.05**	
	4935	ACIS-I	13.47	5	0.28	
Total	Observations	2	Exposure	53.14ks		
Used	Observations	1	Exposure	39.67ks	75%	
S1101						
	11758	**ACIS-I**	**99.03**	**11**	**0.14**	
	1668	ACIS-S	10.08	2	0.07	
Total	Observations	2	Exposure	109.11ks		
Used	Observations	1	Exposure	99.03ks	91%	
ZwCl1215						
	4184	**ACIS-I**	**12.22**	**4**	**0.34**	
Total	Observations	1	Exposure	12.22ks		
Used	Observations	1	Exposure	12.22ks	100%	

Bibliography

Abell, G. O.: 1958, *ApJS* **3**, 211

Addison, G. E., Huang, Y., Watts, D. J., Bennett, C. L., Halpern, M., Hinshaw, G., and Weiland, J. L.: 2015, *ArXiv e-prints 1511.00055v1*

Agarwal, S. and Feldman, H. A.: 2011, *MNRAS* **410**, 1647

Akritas, M. G. and Bershady, M. A.: 1996, *ApJ* **470**, 706

Alcock, C., Allsman, R. A., Axelrod, T. S., Bennett, D. P., Cook, K. H., Park, H. S., Marshall, S. L., Stubbs, C. W., Griest, K., Perlmutter, S., Sutherland, W., Freeman, K. C., Peterson, B. A., Quinn, P. J., and Rodgers, A. W.: 1993, in B. T. Soifer (ed.), *Sky Surveys. Protostars to Protogalaxies*, Vol. 43 of *Astronomical Society of the Pacific Conference Series*, p. 291

Allen, S. W., Rapetti, D. A., Schmidt, R. W., Ebeling, H., Morris, R. G., and Fabian, A. C.: 2008, *MNRAS* **383**, 879

Allen, S. W., Schmidt, R. W., and Fabian, A. C.: 2001, *MNRAS* **328**, L37

Allen, S. W., Schmidt, R. W., and Fabian, A. C.: 2002, *MNRAS* **334**, L11

Allen, S. W., Schmidt, R. W., Fabian, A. C., and Ebeling, H.: 2003, *MNRAS* **342**, 287

Amendola, L.: 2000, *Phys. Rev. D* **62(4)**, 043511

Anders, E. and Ebihara, M.: 1982, *Geochim. Cosmochim. Acta* **46**, 2363

Anders, E. and Grevesse, N.: 1989, *Geochim. Cosmochim. Acta* **53**, 197

Andreon, S. and Hurn, M. A.: 2012, *ArXiv e-prints 1210.6232v1*

Applegate, D. E., Mantz, A., Allen, S. W., von der Linden, A., Morris, R. G., Hilbert, S., Kelly, P. L., Burke, D. L., Ebeling, H., Rapetti, D. A., and Schmidt, R. W.: 2015, *ArXiv e-prints 1509.02162v1*

Arnaud, K. A.: 1996, in G. H. Jacoby & J. Barnes (ed.), *Astronomical Data Analysis Software and Systems V*, Vol. 101 of *Astronomical Society of the Pacific Conference Series*, p. 17

Arnaud, M. and Evrard, A. E.: 1999, *MNRAS* **305**, 631

Arnaud, M., Pointecouteau, E., and Pratt, G. W.: 2007, *A&A* **474**, L37

Arnaud, M., Pratt, G. W., Piffaretti, R., Böhringer, H., Croston, J. H., and Pointecouteau, E.: 2010, *A&A* **517**, A92

Aschenbach, B.: 1985, *Reports on Progress in Physics* **48**, 579

Asplund, M., Grevesse, N., Sauval, A. J., and Scott, P.: 2009, *ARA&A* **47**, 481

Avestruz, C., Nagai, D., Lau, E. T., and Nelson, K.: 2015, *ApJ* **808**, 176

Baldi, M.: 2014, *Physics of the Dark Universe* **3**, 4

Balucinska-Church, M. and McCammon, D.: 1992, *ApJ* **400**, 699

Battaglia, N., Bond, J. R., Pfrommer, C., and Sievers, J. L.: 2013, *ApJ* **777**, 123

Bernardeau, F.: 2009, in M. Novello and S. Perez (eds.), *American Institute of Physics Conference Series*, Vol. 1132 of *American Institute of Physics Conference Series*, pp 42–85

Bharadwaj, V., Reiprich, T. H., Schellenberger, G., Eckmiller, H. J., Mittal, R., and Israel, H.: 2014, *A&A* **572**, A46

Bhattacharya, S., Habib, S., Heitmann, K., and Vikhlinin, A.: 2013, *ApJ* **766**, 32

Bhattacharya, S., Heitmann, K., White, M., Lukić, Z., Wagner, C., and Habib, S.: 2011, *ApJ* **732**, 122

Bilenky, S.: 2010, *Introduction to the physics of massive and mixed neutrinos*, Springer-Verlag Berlin Heidelberg, Lecture Notes in Physics, Volume 817; ISBN 978-3-642-14042-6

Birkinshaw, M.: 1999, *Phys. Rep.* **310**, 97

Biviano, A., Murante, G., Borgani, S., Diaferio, A., Dolag, K., and Girardi, M.: 2006, *A&A* **456**, 23

Blumenthal, G. R., Faber, S. M., Primack, J. R., and Rees, M. J.: 1984, *Nature* **311**, 517

Bocquet, S., Saro, A., Dolag, K., and Mohr, J. J.: 2015, *ArXiv e-prints 1502.07357v2*

Boella, G., Butler, R. C., Perola, G. C., Piro, L., Scarsi, L., and Bleeker, J. A. M.: 1997, *A&AS* **122**, 299

Boggess, N. W., Mather, J. C., Weiss, R., Bennett, C. L., Cheng, E. S., Dwek, E., Gulkis, S., Hauser, M. G., Janssen, M. A., Kelsall, T., Meyer, S. S., Moseley, S. H., Murdock, T. L., Shafer, R. A., Silverberg, R. F., Smoot, G. F., Wilkinson, D. T., and Wright, E. L.: 1992, *ApJ* **397**, 420

Böhringer, H. and Chon, G.: 2015, *A&A* **574**, L8

Böhringer, H., Schuecker, P., Guzzo, L., Collins, C. A., Voges, W., Schindler, S., Neumann, D. M., Cruddace, R. G., De Grandi, S., Chincarini, G., Edge, A. C., MacGillivray, H. T., and Shaver, P.: 2001, *A&A* **369**, 826

Böhringer, H., Voges, W., Huchra, J. P., McLean, B., Giacconi, R., Rosati, P., Burg, R., Mader, J., Schuecker, P., Simiç, D., Komossa, S., Reiprich, T. H., Retzlaff, J., and Trümper, J.: 2000, *ApJS* **129**, 435

BOREXINO Collaboration, Bellini, G., Benziger, J., Bick, D., Bonfini, G., Bravo, D., Caccianiga, B., Cadonati, L., Calaprice, F., Caminata, A., Cavalcante, P., Chavarria, A., Chepurnov, A., D'Angelo, D., Davini, S., Derbin, A., Empl, A., Etenko, A., Fomenko, K., Franco, D., Gabriele, F., Galbiati, C., Gazzana, S., Ghiano, C., Giammarchi, M., Göger-Neff, M., Goretti, A., Gromov, M., Hagner, C., Hungerford, E., Ianni, A., Ianni, A., Kobychev, V., Korablev, D., Korga, G., Kryn, D., Laubenstein, M., Lehnert, B., Lewke, T., Litvinovich, E., Lombardi, F., Lombardi, P., Ludhova, L., Lukyanchenko, G., Machulin, I., Manecki, S., Maneschg, W., Marcocci, S., Meindl, Q., Meroni, E., Meyer, M., Miramonti, L., Misiaszek, M., Montuschi, M., Mosteiro, P., Muratova, V., Oberauer, L., Obolensky, M., Ortica, F., Otis, K., Pallavicini, M., Papp, L., Perasso, L., Pocar, A., Ranucci, G., Razeto, A., Re, A., Romani, A., Rossi, N., Saldanha, R., Salvo, C., Schönert, S., Simgen, H., Skorokhvatov, M., Smirnov, O., Sotnikov, A., Sukhotin, S., Suvorov, Y., Tartaglia, R., Testera, G., Vignaud, D., Vogelaar, R. B., von Feilitzsch, F., Wang, H., Winter, J., Wojcik, M., Wright, A., Wurm, M., Zaimidoroga, O., Zavatarelli, S., Zuber, K., and Zuzel, G.: 2014, *Nature* **512**, 383

Boyarsky, A., Ruchayskiy, O., Iakubovskyi, D., and Franse, J.: 2014, *Physical Review Letters* **113(25)**, 251301

Boyarsky, A., Ruchayskiy, O., and Shaposhnikov, M.: 2009, *Annual Review of Nuclear and Particle Science* **59**, 191

Bradač, M., Lombardi, M., and Schneider, P.: 2004, *A&A* **424**, 13

Bromiley, P.: 2003, *Products and Convolutions of Gaussian Distributions*, Internal Report 2003-003, TINA Vision

Bulbul, E., Markevitch, M., Foster, A., Smith, R. K., Loewenstein, M., and Randall, S. W.: 2014, *ApJ* **789**, 13

Buote, D. A.: 2000a, *ApJ* **532**, L113

Buote, D. A.: 2000b, *MNRAS* **311**, 176

Burenin, R. A.: 2013, *Astronomy Letters* **39**, 357

Burenin, R. A., Vikhlinin, A., Hornstrup, A., Ebeling, H., Quintana, H., and Mescheryakov, A.: 2007, *ApJS* **172**, 561

Burrows, D., Gastaldello, F., Grant, C. E., Guainazzi, M., Madsen, K., Miller, E., Nevalainen, J., Plucinsky, P. P., and Sembay, S.: 2014, *ArXiv e-prints 1412.6233v1*

Byram, E. T., Chubb, T. A., and Friedman, H.: 1966, *AJ* **71**, 379

Cahn, R. N., Dwyer, D. A., Freedman, S. J., Haxton, W. C., Kadel, R. W., Kolomensky, Y. G., Luk, K. B., McDonald, P., Orebi Gann, G. D., and Poon, A. W. P.: 2013, *ArXiv e-prints*

Carlstrom, J. E., Holder, G. P., and Reese, E. D.: 2002, *ARA&A* **40**, 643

Carroll, S. M.: 2001, *Living Reviews in Relativity* **4**, 1

Cash, W.: 1979, *ApJ* **228**, 939

Cava, A., Bettoni, D., Poggianti, B. M., Couch, W. J., Moles, M., Varela, J., Biviano, A., D'Onofrio, M., Dressler, A., Fasano, G., Fritz, J., Kjærgaard, P., Ramella, M., and Valentinuzzi, T.: 2009, *A&A* **495**, 707

Challinor, A.: 2013, in M. G. Burton, X. Cui, and N. F. H. Tothill (eds.), *IAU Symposium*, Vol. 288 of *IAU Symposium*, pp 42–52

Chandra X-ray Center Chandra Project Science, M. C. I. T.: 2010, *The Chandra Proposers' Observatory Guide*, 13 edition

Chen, Y., Reiprich, T. H., Böhringer, H., Ikebe, Y., and Zhang, Y.-Y.: 2007, *A&A* **466**, 805

Chiu, I., Mohr, J., McDonald, M., Bocquet, S., Ashby, M. L. N., Bayliss, M., Benson, B. A., Bleem, L. E., Brodwin, M., Desai, S., Dietrich, J. P., Forman, W. R., Gangkofner, C., Gonzalez, A. H., Hennig, C., Liu, J., Reichardt, C. L., Saro, A., Stalder, B., Stanford, S. A., Song, J., Schrabback, T., Šuhada, R., Strazzullo, V., and Zenteno, A.: 2016, *MNRAS* **455**, 258

Churazov, E., Forman, W., Jones, C., Sunyaev, R., and Böhringer, H.: 2004, *MNRAS* **347**, 29

Ciotti, L.: 2000, *Astrophysical Letters and Communications* **40**, 85

Clowe, D., Randall, S. W., and Markevitch, M.: 2007, *Nuclear Physics B Proceedings Supplements* **173**, 28

Condon, J. J., Cotton, W. D., Greisen, E. W., Yin, Q. F., Perley, R. A., Taylor, G. B., and Broderick, J. J.: 1998, *AJ* **115**, 1693

Crain, R. A., Eke, V. R., Frenk, C. S., Jenkins, A., McCarthy, I. G., Navarro, J. F., and Pearce, F. R.: 2007, *MNRAS* **377**, 41

Cui, W., Baldi, M., and Borgani, S.: 2012a, *MNRAS* **424**, 993

Cui, W., Borgani, S., Dolag, K., Murante, G., and Tornatore, L.: 2012b, *MNRAS* **423**, 2279

Cui, W., Borgani, S., and Murante, G.: 2014, *MNRAS* **441**, 1769

De Grandi, S. and Molendi, S.: 2002, *ApJ* **567**, 163

de Vaucouleurs, G.: 1961, *ApJS* **5**, 233

Diaferio, A.: 1999, *MNRAS* **309**, 610

Dicus, D. A., Kolb, E. W., Gleeson, A. M., Sudarshan, E. C. G., Teplitz, V. L., and Turner, M. S.: 1982, *Phys. Rev. D* **26**, 2694

Dodelson, S. and Widrow, L. M.: 1994, *Physical Review Letters* **72**, 17

Donahue, M., Voit, G. M., Mahdavi, A., Umetsu, K., Ettori, S., Merten, J., Postman, M., Hoffer, A., Baldi, A., Coe, D., Czakon, N., Bartelmann, M., Benitez, N., Bouwens, R., Bradley, L., Broadhurst, T., Ford, H., Gastaldello, F., Grillo, C., Infante, L., Jouvel, S., Koekemoer, A., Kelson, D., Lahav, O., Lemze, D., Medezinski, E., Melchior, P., Meneghetti, M., Molino, A., Moustakas, J., Moustakas, L. A., Nonino, M., Rosati, P., Sayers, J., Seitz, S., Van der Wel, A., Zheng, W., and Zitrin, A.: 2014, *ArXiv e-prints 1405.7876v2*

Dubinski, J.: 1994, *ApJ* **431**, 617

Dunkley, J., Komatsu, E., Nolta, M. R., Spergel, D. N., Larson, D., Hinshaw, G., Page, L., Bennett, C. L., Gold, B., Jarosik, N., Weiland, J. L., Halpern, M., Hill, R. S., Kogut, A., Limon, M., Meyer, S. S., Tucker, G. S., Wollack, E., and Wright, E. L.: 2009, *ApJS* **180**, 306

Ebeling, H., Edge, A. C., Bohringer, H., Allen, S. W., Crawford, C. S., Fabian, A. C., Voges, W., and Huchra, J. P.: 1998, *MNRAS* **301**, 881

Eckert, D., Molendi, S., Owers, M., Gaspari, M., Venturi, T., Rudnick, L., Ettori, S., Paltani, S., Gastaldello, F., and Rossetti, M.: 2014, *A&A* **570**, A119

Eckert, D., Molendi, S., and Paltani, S.: 2011, *A&A* **526**, A79

Eckmiller, H. J., Hudson, D. S., and Reiprich, T. H.: 2011, *A&A* **535**, A105

Eisenstein, D. J.: 2005, *New A Rev.* **49**, 360

Eisenstein, D. J. and Hu, W.: 1998, *ApJ* **496**, 605

Eke, V. R., Navarro, J. F., and Frenk, C. S.: 1998, *ApJ* **503**, 569

Ettori, S.: 2003, *MNRAS* **344**, L13

Ettori, S., Tozzi, P., and Rosati, P.: 2003, *A&A* **398**, 879

Evrard, A. E., Metzler, C. A., and Navarro, J. F.: 1996, *ApJ* **469**, 494

Fabian, A. C.: 1994, *ARA&A* **32**, 277

Fabian, A. C., Hu, E. M., Cowie, L. L., and Grindlay, J.: 1981, *ApJ* **248**, 47

Fabian, A. C., Sanders, J. S., Taylor, G. B., Allen, S. W., Crawford, C. S., Johnstone, R. M., and Iwasawa, K.: 2006, *MNRAS* **366**, 417

Fasano, G., Marmo, C., Varela, J., D'Onofrio, M., Poggianti, B. M., Moles, M., Pignatelli, E., Bettoni, D., Kjærgaard, P., Rizzi, L., Couch, W. J., and Dressler, A.: 2006, *A&A* **445**, 805

Fath, E. A.: 1909, *Lick Observatory Bulletin* **5**, 71

Fixsen, D. J.: 2009, *ApJ* **707**, 916

Foëx, G., Soucail, G., Pointecouteau, E., Arnaud, M., Limousin, M., and Pratt, G. W.: 2012, *A&A* **546**, A106

Fogli, G. L., Lisi, E., Marrone, A., Montanino, D., Palazzo, A., and Rotunno, A. M.: 2012, *Phys. Rev. D* **86(1)**, 013012

Fonnesbeck, C., Patil, A., Huard, D., and Salvatier, J.: 2015, *PyMC: Bayesian Stochastic Modelling in Python*, Astrophysics Source Code Library

Freese, K.: 1986, *Physics Letters B* **167**, 295

Fritz, J., Poggianti, B. M., Cava, A., Valentinuzzi, T., Moretti, A., Bettoni, D., Bressan, A., Couch, W. J., D'Onofrio, M., Dressler, A., Fasano, G., Kjærgaard, P., Moles, M., Omizzolo, A., and Varela, J.: 2011, *A&A* **526**, A45

Galassi, M., Davies, J., Theiler, J., Gough, B., Jungman, G., Booth, M., and Rossi, F., *GNU Scientific Library Reference Manual (3rd Ed.)*

Gamerman, D. and Lopes, H.: 2006, *Markov Chain Monte Carlo: Stochastic Simulation for Bayesian Inference, Second Edition*, Chapman & Hall/CRC Texts in Statistical Science, Taylor & Francis

Gastaldello, F., Buote, D. A., Humphrey, P. J., Zappacosta, L., Bullock, J. S., Brighenti, F., and Mathews, W. G.: 2007, *ApJ* **669**, 158

Gastaldello, F., Ettori, S., Balestra, I., Brighenti, F., Buote, D. A., de Grandi, S., Ghizzardi, S., Gitti, M., and Tozzi, P.: 2010, *A&A* **522**, A34

Gastaldello, F. and Molendi, S.: 2004, *ApJ* **600**, 670

Gelman, A., Carlin, J., Stern, H., Dunson, D., Vehtari, A., and Rubin, D.: 2013, *Bayesian Data Analysis, Third Edition*, Chapman & Hall/CRC Texts in Statistical Science, Taylor & Francis

Giacconi, R. and Burg, R.: 1993, in G. L. Chincarini, A. Iovino, T. Maccacaro, and D. Maccagni (eds.), *Observational Cosmology*, Vol. 51 of *Astronomical Society of the Pacific Conference Series*, p. 342

Giacconi, R., Murray, S., Gursky, H., Kellogg, E., Schreier, E., and Tananbaum, H.: 1972, *ApJ* **178**, 281

Giles, P. A., Maughan, B. J., Hamana, T., Miyazaki, S., Birkinshaw, M., Ellis, R. S., and Massey, R.: 2015, *MNRAS* **447**, 3044

Gorski, K. M., Banday, A. J., Bennett, C. L., Hinshaw, G., Kogut, A., Smoot, G. F., and Wright, E. L.: 1996, *ApJ* **464**, L11

Grant, C. E., Guainazzi, M., Natalucci, L., Nevalainen, J., Plucinsky, P. P., Pollock, A., and Sembay, S.: 2013, *ArXiv e-prints 1305.4480*

Gruen, D., Seitz, S., Brimioulle, F., Kosyra, R., Koppenhoefer, J., Lee, C.-H., Bender, R., Riffeser, A., Eichner, T., Weidinger, T., and Bierschenk, M.: 2014, *MNRAS* **442**, 1507

Gunn, J. E. and Gott, III, J. R.: 1972, *ApJ* **176**, 1

Hasselfield, M., Hilton, M., Marriage, T. A., Addison, G. E., Barrientos, L. F., Battaglia, N., Battistelli, E. S., Bond, J. R., Crichton, D., Das, S., Devlin, M. J., Dicker, S. R., Dunkley, J., Dünner, R., Fowler, J. W., Gralla, M. B., Hajian, A., Halpern, M., Hincks, A. D., Hlozek, R., Hughes, J. P., Infante, L., Irwin, K. D., Kosowsky, A., Marsden, D., Menanteau, F., Moodley, K., Niemack, M. D., Nolta, M. R., Page, L. A., Partridge, B., Reese, E. D., Schmitt, B. L., Sehgal, N., Sherwin, B. D., Sievers, J., Sifón, C., Spergel, D. N., Staggs, S. T., Swetz, D. S., Switzer, E. R., Thornton, R., Trac, H., and Wollack, E. J.: 2013, *J. Cosmology Astropart. Phys.* **7**, 8

Hickox, R. C. and Markevitch, M.: 2006, *ApJ* **645**, 95

Hickson, P.: 1982, *ApJ* **255**, 382

Hinshaw, G., Larson, D., Komatsu, E., Spergel, D. N., Bennett, C. L., Dunkley, J., Nolta, M. R., Halpern, M., Hill, R. S., Odegard, N., Page, L., Smith, K. M., Weiland, J. L., Gold, B., Jarosik, N., Kogut, A., Limon, M., Meyer, S. S., Tucker, G. S., Wollack, E., and Wright, E. L.: 2013, *ApJS* **208**, 19

Hirata, C. and Seljak, U.: 2003, *MNRAS* **343**, 459

Hirsch, M. and Valle, J. W. F.: 2004, *New Journal of Physics* **6**, 76

Hoekstra, H., Herbonnet, R., Muzzin, A., Babul, A., Mahdavi, A., Viola, M., and Cacciato, M.: 2015, *MNRAS* **449**, 685

Hu, W., Sugiyama, N., and Silk, J.: 1996, *ArXiv Astrophysics e-prints 9604166v1*

Hu, W., Sugiyama, N., and Silk, J.: 1997, *Nature* **386**, 37

Hubble, E.: 1936, *ApJ* **84**, 517

Hudson, D. S., Mittal, R., Reiprich, T. H., Nulsen, P. E. J., Andernach, H., and Sarazin, C. L.: 2010, *A&A* **513**, A37

Israel, H., Reiprich, T. H., Erben, T., Massey, R. J., Sarazin, C. L., Schneider, P., and Vikhlinin, A.: 2014a, *A&A* **564**, A129

Israel, H., Schellenberger, G., Nevalainen, J., Massey, R., and Reiprich, T.: 2014b, *ArXiv e-prints 1408.4758*

Jansen, F., Lumb, D., Altieri, B., Clavel, J., Ehle, M., Erd, C., Gabriel, C., Guainazzi, M., Gondoin, P., Much, R., Munoz, R., Santos, M., Schartel, N., Texier, D., and Vacanti, G.: 2001, *A&A* **365**, L1

Jeltema, T. and Profumo, S.: 2015, *MNRAS* **450**, 2143

Jeltema, T. E., Binder, B., and Mulchaey, J. S.: 2008, *ApJ* **679**, 1162

Jenkins, A., Frenk, C. S., White, S. D. M., Colberg, J. M., Cole, S., Evrard, A. E., Couchman, H. M. P., and Yoshida, N.: 2001, *MNRAS* **321**, 372

Jing, Y. P., Mo, H. J., Borner, G., and Fang, L. Z.: 1995, *MNRAS* **276**, 417

Jones, L. R., Scharf, C., Ebeling, H., Perlman, E., Wegner, G., Malkan, M., and Horner, D.: 1998, *ApJ* **495**, 100

Kaiser, N. and Silk, J.: 1986, *Nature* **324**, 529

Kalberla, P. M. W., Burton, W. B., Hartmann, D., Arnal, E. M., Bajaja, E., Morras, R., and Pöppel, W. G. L.: 2005, *A&A* **440**, 775

Kamionkowski, M. and Kosowsky, A.: 1999, *Annual Review of Nuclear and Particle Science* **49**, 77

Kapferer, W., Sluka, C., Schindler, S., Ferrari, C., and Ziegler, B.: 2009, *A&A* **499**, 87

Karzas, W. J. and Latter, R.: 1961, *ApJS* **6**, 167

Kelly, B. C.: 2007, *ApJ* **665**, 1489

Kettula, K., Nevalainen, J., and Miller, E. D.: 2013, *A&A* **552**, A47

Kim, D.-W., Kim, E., Fabbiano, G., and Trinchieri, G.: 2008, *ApJ* **688**, 931

Kitayama, T., Bautz, M., Markevitch, M., Matsushita, K., Allen, S., Kawaharada, M., McNamara, B., Ota, N., Akamatsu, H., de Plaa, J., Galeazzi, M., Madejski, G., Main, R., Miller, E., Nakazawa, K., Russell, H., Sato, K., Sekiya, N., Simionescu, A., Tamura, T., Uchida, Y., Ursino, E., Werner, N., Zhuravleva, I., ZuHone, J., and on behalf of the ASTRO-H Science Working Group: 2014, *ArXiv e-prints 1412.1176v1*

Köhlinger, F., Hoekstra, H., and Eriksen, M.: 2015, *ArXiv e-prints 1508.05308v1*

Kolokotronis, V., Basilakos, S., Plionis, M., and Georgantopoulos, I.: 2001, *MNRAS* **320**, 49

Komatsu, E., Smith, K. M., Dunkley, J., Bennett, C. L., Gold, B., Hinshaw, G., Jarosik, N., Larson, D., Nolta, M. R., Page, L., Spergel, D. N., Halpern, M., Hill, R. S., Kogut, A., Limon, M., Meyer, S. S., Odegard, N., Tucker, G. S., Weiland, J. L., Wollack, E., and Wright, E. L.: 2011, *ApJS* **192**, 18

Koutroumpa, D., Smith, R. K., Edgar, R. J., Kuntz, K. D., Plucinsky, P. P., and Snowden, S. L.: 2011, *ApJ* **726**, 91

Kreye, W. C., Hemsky, J. W., and Andrews, M. L.: 1993, *Journal of Physics D Applied Physics* **26**, 1836

Kriss, G. A., Cioffi, D. F., and Canizares, C. R.: 1983, *ApJ* **272**, 439

Kushino, A., Ishisaki, Y., Morita, U., Yamasaki, N. Y., Ishida, M., Ohashi, T., and Ueda, Y.: 2002, *PASJ* **54**, 327

Leccardi, A. and Molendi, S.: 2008, *A&A* **486**, 359

Lesgourgues, J.: 2011a, *ArXiv e-prints 1104.2932v2*

Lesgourgues, J.: 2011b, *ArXiv e-prints 1104.2934v2*

Lesgourgues, J. and Pastor, S.: 2006, *Phys. Rep.* **429**, 307

Lesgourgues, J. and Pastor, S.: 2012, *ArXiv e-prints 1212.6154v1*

Lesgourgues, J. and Pastor, S.: 2014, *New Journal of Physics* **16(6)**, 065002

Lesgourgues, J. and Tram, T.: 2011, *J. Cosmology Astropart. Phys.* **9**, 32

Lima Neto, G. B.: 2005, *Brazilian Journal of Physics* **35**, 1159

Liu, J., Mohr, J., Saro, A., Aird, K. A., Ashby, M. L. N., Bautz, M., Bayliss, M., Benson, B. A., Bleem, L. E., Bocquet, S., Brodwin, M., Carlstrom, J. E., Chang, C. L., Chiu, I., Cho, H. M., Clocchiatti, A., Crawford, T. M., Crites, A. T., de Haan, T., Desai, S., Dietrich, J. P., Dobbs, M. A., Foley, R. J., Gangkofner, D., George, E. M., Gladders, M. D., Gonzalez, A. H., Halverson, N. W., Hennig, C., Hlavacek-Larrondo, J., Holder, G. P., Holzapfel, W. L., Hrubes, J. D., Jones, C., Keisler, R., Lee, A. T., Leitch, E. M., Lueker, M., Luong-Van, D., McDonald, M., McMahon, J. J., Meyer, S. S., Mocanu, L., Murray, S. S., Padin, S., Pryke, C., Reichardt, C. L., Rest, A., Ruel, J., Ruhl, J. E., Saliwanchik, B. R., Sayre, J. T., Schaffer, K. K., Shirokoff, E., Spieler, H. G., Stalder, B., Staniszewski, Z., Stark, A. A., Story, K., Šuhada, R., Vanderlinde, K., Vieira, J. D., Vikhlinin, A., Williamson, R., Zahn, O., and Zenteno, A.: 2015, *MNRAS* **448**, 2085

Lodders, K. and Palme, H.: 2009, *Meteoritics and Planetary Science Supplement* **72**, 5154

Longinotti, A. L., de La Calle, I., Bianchi, S., Guainazzi, M., and Dovciak, M.: 2008, in *Revista Mexicana de Astronomia y Astrofisica Conference Series*, Vol. 32 of *Revista Mexicana de Astronomia y Astrofisica Conference Series*, pp 62–64

Lovisari, L., Reiprich, T. H., and Schellenberger, G.: 2015, *A&A* **573**, A118

Ludlow, A. D., Navarro, J. F., Angulo, R. E., Boylan-Kolchin, M., Springel, V., Frenk, C., and White, S. D. M.: 2014, *MNRAS* **441**, 378

Ludlow, A. D., Navarro, J. F., Boylan-Kolchin, M., Bett, P. E., Angulo, R. E., Li, M., White, S. D. M., Frenk, C., and Springel, V.: 2013, *MNRAS* **432**, 1103

Machacek, M. E., Nulsen, P., Stirbat, L., Jones, C., and Forman, W. R.: 2005, *ApJ* **630**, 280

Mahdavi, A., Hoekstra, H., Babul, A., Bildfell, C., Jeltema, T., and Henry, J. P.: 2013, *ApJ* **767**, 116

Main, R., McNamara, B., Nulsen, P., Russell, H., and Vantyghem, A.: 2015, *ArXiv e-prints 1510.07046v1*

Mangano, G., Miele, G., Pastor, S., and Peloso, M.: 2002, *Physics Letters B* **534**, 8

Mantz, A., Allen, S. W., Ebeling, H., and Rapetti, D.: 2008, *MNRAS* **387**, 1179

Mantz, A., Allen, S. W., Ebeling, H., Rapetti, D., and Drlica-Wagner, A.: 2010a, *MNRAS* **406**, 1773

Mantz, A., Allen, S. W., Rapetti, D., and Ebeling, H.: 2010b, *MNRAS* **406**, 1759

Mantz, A. B., Allen, S. W., Morris, R. G., Rapetti, D. A., Applegate, D. E., Kelly, P. L., von der Linden, A., and Schmidt, R. W.: 2014, *MNRAS* **440**, 2077

Mantz, A. B., von der Linden, A., Allen, S. W., Applegate, D. E., Kelly, P. L., Morris, R. G., Rapetti, D. A., Schmidt, R. W., Adhikari, S., Allen, M. T., Burchat, P. R., Burke, D. L., Cataneo, M., Donovan, D., Ebeling, H., Shandera, S., and Wright, A.: 2015, *MNRAS* **446**, 2205

Markevitch, M., Bautz, M. W., Biller, B., Butt, Y., Edgar, R., Gaetz, T., Garmire, G., Grant, C. E., Green, P., Juda, M., Plucinsky, P. P., Schwartz, D., Smith, R., Vikhlinin, A., Virani, S., Wargelin, B. J., and Wolk, S.: 2003, *ApJ* **583**, 70

Markevitch, M., Forman, W. R., Sarazin, C. L., and Vikhlinin, A.: 1998, *ApJ* **503**, 77

Martino, R., Mazzotta, P., Bourdin, H., Smith, G. P., Bartalucci, I., Marrone, D. P., Finoguenov, A., and Okabe, N.: 2014, *MNRAS* **443**, 2342

Massey, R., Hoekstra, H., Kitching, T., Rhodes, J., Cropper, M., Amiaux, J., Harvey, D., Mellier, Y., Meneghetti, M., Miller, L., Paulin-Henriksson, S., Pires, S., Scaramella, R., and Schrabback, T.: 2013, *MNRAS* **429**, 661

Massey, R., Williams, L., Smit, R., Swinbank, M., Kitching, T. D., Harvey, D., Jauzac, M., Israel, H., Clowe, D., Edge, A., Hilton, M., Jullo, E., Leonard, A., Liesenborgs, J., Merten, J., Mohammed, I., Nagai, D., Richard, J., Robertson, A., Saha, P., Santana, R., Stott, J., and Tittley, E.: 2015, *MNRAS* **449**, 3393

Maughan, B. J.: 2007, *ApJ* **668**, 772

Maughan, B. J., Giles, P. A., Rines, K. J., Diaferio, A., Geller, M. J., Van Der Pyl, N., and Bonamente, M.: 2015, *ArXiv e-prints 1511.07872v1*

Mazzotta, P., Rasia, E., Moscardini, L., and Tormen, G.: 2004, *MNRAS* **354**, 10

Merloni, A., Predehl, P., Becker, W., Böhringer, H., Boller, T., Brunner, H., Brusa, M., Dennerl, K., Freyberg, M., Friedrich, P., Georgakakis, A., Haberl, F., Hasinger, G., Meidinger, N., Mohr, J., Nandra, K., Rau, A., Reiprich, T. H., Robrade, J., Salvato, M., Santangelo, A., Sasaki, M., Schwope, A., Wilms, J., and German eROSITA Consortium, t.: 2012, *ArXiv e-prints 1209.3114v2*

Metropolis, N., Rosenbluth, A. W., Rosenbluth, M. N., Teller, A. H., and Teller, E.: 1953, *J. Chem. Phys.* **21**, 1087

Mitsuda, K., Bautz, M., Inoue, H., Kelley, R. L., Koyama, K., Kunieda, H., Makishima, K., Ogawara, Y., Petre, R., Takahashi, T., Tsunemi, H., White, N. E., Anabuki, N., Angelini, L., Arnaud, K., Awaki, H., Bamba, A., Boyce, K., Brown, G. V., Chan, K.-W., Cottam, J., Dotani, T., Doty, J., Ebisawa, K., Ezoe, Y., Fabian, A. C., Figueroa, E., Fujimoto, R., Fukazawa, Y., Furusho, T., Furuzawa, A., Gendreau, K., Griffiths, R. E., Haba, Y., Hamaguchi, K., Harrus, I., Hasinger, G., Hatsukade, I., Hayashida, K., Henry, P. J., Hiraga, J. S., Holt, S. S., Hornschemeier, A., Hughes, J. P., Hwang, U., Ishida, M., Ishisaki, Y., Isobe, N., Itoh, M., Iyomoto, N., Kahn, S. M., Kamae, T., Katagiri, H., Kataoka, J., Katayama, H., Kawai, N., Kilbourne, C., Kinugasa, K., Kissel, S., Kitamoto, S., Kohama, M., Kohmura, T., Kokubun, M., Kotani, T., Kotoku, J., Kubota, A., Madejski, G. M., Maeda, Y., Makino, F., Markowitz, A., Matsumoto, C., Matsumoto, H., Matsuoka, M., Matsushita, K., McCammon, D., Mihara, T., Misaki, K., Miyata, E., Mizuno, T., Mori, K., Mori, H., Morii, M., Moseley, H., Mukai, K., Murakami, H., Murakami, T., Mushotzky, R., Nagase, F., Namiki, M., Negoro, H., Nakazawa, K., Nousek, J. A.,

Okajima, T., Ogasaka, Y., Ohashi, T., Oshima, T., Ota, N., Ozaki, M., Ozawa, H., Parmar, A. N., Pence, W. D., Porter, F. S., Reeves, J. N., Ricker, G. R., Sakurai, I., Sanders, W. T., Senda, A., Serlemitsos, P., Shibata, R., Soong, Y., Smith, R., Suzuki, M., Szymkowiak, A. E., Takahashi, H., Tamagawa, T., Tamura, K., Tamura, T., Tanaka, Y., Tashiro, M., Tawara, Y., Terada, Y., Terashima, Y., Tomida, H., Torii, K., Tsuboi, Y., Tsujimoto, M., Tsuru, T. G., Turner, M. J. L. ., Ueda, Y., Ueno, S., Ueno, M., Uno, S., Urata, Y., Watanabe, S., Yamamoto, N., Yamaoka, K., Yamasaki, N. Y., Yamashita, K., Yamauchi, M., Yamauchi, S., Yaqoob, T., Yonetoku, D., and Yoshida, A.: 2007, *PASJ* **59**, 1

Mittal, R., Hicks, A., Reiprich, T. H., and Jaritz, V.: 2011, *A&A* **532**, A133

Mittal, R., Hudson, D. S., Reiprich, T. H., and Clarke, T.: 2009, *A&A* **501**, 835

Morrison, R. and McCammon, D.: 1983, *ApJ* **270**, 119

Nagai, D., Kravtsov, A. V., and Vikhlinin, A.: 2007, *ApJ* **668**, 1

Navarro, J. F., Frenk, C. S., and White, S. D. M.: 1996, *ApJ* **462**, 563

Navarro, J. F., Frenk, C. S., and White, S. D. M.: 1997, *ApJ* **490**, 493

Nelson, K., Lau, E. T., and Nagai, D.: 2014, *ApJ* **792**, 25

Nevalainen, J., David, L., and Guainazzi, M.: 2010, *A&A* **523**, A22

Nulsen, P. E. J., Powell, S. L., and Vikhlinin, A.: 2010, *ApJ* **722**, 55

Omizzolo, A., Fasano, G., Reverte Paya, D., De Santis, C., Grado, A., Bettoni, D., Poggianti, B., D'Onofrio, M., Moretti, A., Varela, J., Fritz, J., Gullieuszik, M., Cava, A., Grazian, A., and Moles, M.: 2014, *A&A* **561**, A111

Oosterloo, T. and van Gorkom, J.: 2005, *A&A* **437**, L19

O'Sullivan, E., Forbes, D. A., and Ponman, T. J.: 2001, *MNRAS* **328**, 461

Ota, N., Nagai, D., and Lau, E. T.: 2015, *ArXiv e-prints 1507.02730v1*

Pacaud, F., Pierre, M., Refregier, A., Gueguen, A., Starck, J.-L., Valtchanov, I., Read, A. M., Altieri, B., Chiappetti, L., Gandhi, P., Garcet, O., Gosset, E., Ponman, T. J., and Surdej, J.: 2006, *MNRAS* **372**, 578

Padmanabhan, T.: 1993, *Structure Formation in the Universe*

Pawitan, Y.: 2001, *In all likelihood: statistical modelling and inference using likelihood*, Oxford science publications, Clarendon Press, Oxford

Peacock, J. A.: 1999, *Cosmological Physics*

Pearson, K.: 1896, *Philosophical Transactions of the Royal Society of London A: Mathematical, Physical and Engineering Sciences* **187**, 253

Peebles, P. J. and Ratra, B.: 2003, *Reviews of Modern Physics* **75**, 559

Peebles, P. J. E.: 1993, *Principles of Physical Cosmology*

Piffaretti, R., Arnaud, M., Pratt, G. W., Pointecouteau, E., and Melin, J.-B.: 2011, *A&A* **534**, A109

Pillepich, A., Porciani, C., and Hahn, O.: 2010, *MNRAS* **402**, 191

Pillepich, A., Porciani, C., and Reiprich, T. H.: 2012, *MNRAS* **422**, 44

Planck Collaboration, Ade, P. A. R., Aghanim, N., Armitage-Caplan, C., Arnaud, M., Ashdown, M., Atrio-Barandela, F., Aumont, J., Baccigalupi, C., Banday, A. J., and et al.: 2013a, *ArXiv e-prints 1303.5076v3*

Planck Collaboration, Ade, P. A. R., Aghanim, N., Armitage-Caplan, C., Arnaud, M., Ashdown, M., Atrio-Barandela, F., Aumont, J., Baccigalupi, C., Banday, A. J., and et al.: 2013b, *ArXiv e-prints 1303.5080v2*

Planck Collaboration, Ade, P. A. R., Aghanim, N., Arnaud, M., Ashdown, M., Aumont, J., Baccigalupi, C., Baker, M., Balbi, A., Banday, A. J., and et al.: 2011, *ArXiv e-prints 1101.2022v2*

Planck Collaboration, Ade, P. A. R., Aghanim, N., Arnaud, M., Ashdown, M., Aumont, J., Baccigalupi, C., Banday, A. J., Barreiro, R. B., Barrena, R., and et al.: 2015a, *ArXiv e-prints 1502.01598v1*

Planck Collaboration, Ade, P. A. R., Aghanim, N., Arnaud, M., Ashdown, M., Aumont, J., Baccigalupi, C., Banday, A. J., Barreiro, R. B., Bartlett, J. G., Bartolo, N., Battaner, E., Battye, R., Benabed, K., Benoît, A., Benoit-Lévy, A., Bernard, J.-P., Bersanelli, M., Bielewicz, P., Bonaldi, A., Bonavera, L., Bond, J. R., Borrill, J., Bouchet, F. R., Bucher, M., Burigana, C., Butler, R. C., Calabrese, E., Cardoso, J.-F., Catalano, A., Challinor, A., Chamballu, A., Chary, R.-R., Chiang, H. C., Christensen, P. R., Church, S., Clements, D. L., Colombi, S., Colombo, L. P. L., Combet, C., Comis, B., Couchot, F., Coulais, A., Crill, B. P., Curto, A., Cuttaia, F., Danese, L., Davies, R. D., Davis, R. J., de Bernardis, P., de Rosa, A., de Zotti, G., Delabrouille, J., Désert, F.-X., Diego, J. M., Dolag, K., Dole, H., Donzelli, S., Doré, O., Douspis, M., Ducout, A., Dupac, X., Efstathiou, G., Elsner, F., Enßlin, T. A., Eriksen, H. K., Falgarone, E., Fergusson, J., Finelli, F., Forni, O., Frailis, M., Fraisse, A. A., Franceschi, E., Frejsel, A., Galeotta, S., Galli, S., Ganga, K., Giard, M., Giraud-Héraud, Y., Gjerløw, E., González-Nuevo, J., Górski, K. M., Gratton, S., Gregorio, A., Gruppuso, A., Gudmundsson, J. E., Hansen, F. K., Hanson, D., Harrison, D. L., Henrot-Versillé, S., Hernández-Monteagudo, C., Herranz, D., Hildebrandt, S. R., Hivon, E., Hobson, M., Holmes, W. A., Hornstrup, A., Hovest, W., Huffenberger, K. M., Hurier, G., Jaffe, A. H., Jaffe, T. R., Jones, W. C., Juvela, M., Keihänen, E., Keskitalo, R., Kisner, T. S., Kneissl, R., Knoche, J., Kunz, M., Kurki-Suonio, H., Lagache, G., Lähteenmäki, A., Lamarre, J.-M., Lasenby, A., Lattanzi, M., Lawrence, C. R., Leonardi, R., Lesgourgues, J., Levrier, F., Liguori, M., Lilje, P. B., Linden-Vørnle, M., López-Caniego, M., Lubin, P. M., Macías-Pérez, J. F., Maggio, G., Maino, D., Mandolesi, N., Mangilli, A., Martin, P. G., Martínez-González, E., Masi, S., Matarrese, S., Mazzotta, P., McGehee, P., Meinhold, P. R., Melchiorri, A., Melin, J.-B., Mendes, L., Mennella, A., Migliaccio, M., Mitra, S., Miville-Deschênes, M.-A., Moneti, A., Montier, L., Morgante, G., Mortlock, D., Moss, A., Munshi, D., Murphy, J. A., Naselsky, P., Nati, F., Natoli, P., Netterfield, C. B., Nørgaard-Nielsen, H. U., Noviello, F., Novikov, D., Novikov, I., Oxborrow, C. A., Paci, F., Pagano, L., Pajot, F., Paoletti, D., Partridge, B., Pasian, F., Patanchon, G., Pearson, T. J., Perdereau, O., Perotto, L., Perrotta, F., Pettorino, V., Piacentini, F., Piat, M., Pierpaoli, E., Pietrobon, D., Plaszczynski, S., Pointecouteau, E., Polenta, G., Popa, L., Pratt, G. W., Prézeau, G., Prunet, S., Puget, J.-L., Rachen, J. P., Rebolo, R., Reinecke, M., Remazeilles, M., Renault, C., Renzi, A., Ristorcelli, I., Rocha, G., Roman, M., Rosset, C., Rossetti, M., Roudier, G., Rubiño-Martín, J. A., Rusholme, B., Sandri, M., Santos, D., Savelainen, M., Savini, G., Scott, D., Seiffert, M. D., Shellard, E. P. S., Spencer, L. D., Stolyarov, V., Stompor, R., Sudiwala, R., Sunyaev, R., Sutton, D., Suur-Uski, A.-S., Sygnet, J.-F., Tauber, J. A., Terenzi, L., Toffolatti, L., Tomasi, M., Tristram, M., Tucci, M., Tuovinen, J., Türler, M., Umana, G., Valenziano, L., Valiviita, J., Van Tent, B., Vielva, P., Villa, F., Wade, L. A., Wandelt, B. D., Wehus, I. K., Weller, J., White, S. D. M., Yvon, D., Zacchei, A., and Zonca, A.: 2015b, *ArXiv e-prints 1502.01597v1*

Planck Collaboration, Ade, P. A. R., Aghanim, N., Arnaud, M., Ashdown, M., Aumont, J., Baccigalupi, C., Banday, A. J., Barreiro, R. B., Bartlett, J. G., and et al.: 2015c, *ArXiv e-prints 1502.01589v2*

Planck Collaboration, Aghanim, N., Arnaud, M., Ashdown, M., Aumont, J., Baccigalupi, C., Banday, A. J., Barreiro, R. B., Bartlett, J. G., Bartolo, N., and et al.: 2015d, *ArXiv e-prints 1502.01596v1*

Planelles, S., Borgani, S., Dolag, K., Ettori, S., Fabjan, D., Murante, G., and Tornatore, L.: 2013, *MNRAS* **431**, 1487

Pratt, G. W., Böhringer, H., Croston, J. H., Arnaud, M., Borgani, S., Finoguenov, A., and Temple, R. F.: 2007, *A&A* **461**, 71

Pratt, G. W., Croston, J. H., Arnaud, M., and Böhringer, H.: 2009, *A&A* **498**, 361

Press, W. H. and Schechter, P.: 1974, *ApJ* **187**, 425

Press, W. H., Teukolsky, S. A., Vetterling, W. T., and Flannery, B. P.: 1992, *Numerical recipes in C. The art of scientific computing*

Pritychenko, B.: 2015, *ArXiv e-prints 1506.02978v2*

Randall, S., Nulsen, P., Forman, W. R., Jones, C., Machacek, M., Murray, S. S., and Maughan, B.: 2008, *ApJ* **688**, 208

Rasmussen, J. and Ponman, T. J.: 2007, *MNRAS* **380**, 1554

Read, A. M., Guainazzi, M., and Sembay, S.: 2014, *A&A* **564**, A75

Reichardt, C. L., Stalder, B., Bleem, L. E., Montroy, T. E., Aird, K. A., Andersson, K., Armstrong, R., Ashby, M. L. N., Bautz, M., Bayliss, M., Bazin, G., Benson, B. A., Brodwin, M., Carlstrom, J. E., Chang, C. L., Cho, H. M., Clocchiatti, A., Crawford, T. M., Crites, A. T., de Haan, T., Desai, S., Dobbs, M. A., Dudley, J. P., Foley, R. J., Forman, W. R., George, E. M., Gladders, M. D., Gonzalez, A. H., Halverson, N. W., Harrington, N. L., High, F. W., Holder, G. P., Holzapfel, W. L., Hoover, S., Hrubes, J. D., Jones, C., Joy, M., Keisler, R., Knox, L., Lee, A. T., Leitch, E. M., Liu, J., Lueker, M., Luong-Van, D., Mantz, A., Marrone, D. P., McDonald, M., McMahon, J. J., Mehl, J., Meyer, S. S., Mocanu, L., Mohr, J. J., Murray, S. S., Natoli, T., Padin, S., Plagge, T., Pryke, C., Rest, A., Ruel, J., Ruhl, J. E., Saliwanchik, B. R., Saro, A., Sayre, J. T., Schaffer, K. K., Shaw, L., Shirokoff, E., Song, J., Spieler, H. G., Staniszewski, Z., Stark, A. A., Story, K., Stubbs, C. W., Šuhada, R., van Engelen, A., Vanderlinde, K., Vieira, J. D., Vikhlinin, A., Williamson, R., Zahn, O., and Zenteno, A.: 2013, *ApJ* **763**, 127

Reichert, A., Böhringer, H., Fassbender, R., and Mühlegger, M.: 2011, *A&A* **535**, A4

Reiprich, T.: 2012, *Completing eHIFLUGCS: the Ultimate Precise and Accurate Local Baseline*, Chandra Proposal

Reiprich, T. H.: 2001, *Ph.D. thesis*, Max-Planck-Institut für extraterrestrische Physik, P.O. Box 1312, Garching bei München, Germany

Reiprich, T. H.: 2006, *A&A* **453**, L39

Reiprich, T. H., Basu, K., Ettori, S., Israel, H., Lovisari, L., Molendi, S., Pointecouteau, E., and Roncarelli, M.: 2013, *Space Sci. Rev.* **177**, 195

Reiprich, T. H. and Böhringer, H.: 2002, *ApJ* **567**, 716

Reiprich, T. H., Sarazin, C. L., Kempner, J. C., and Tittley, E.: 2004, *ApJ* **608**, 179

Retzlaff, J.: 2001, in D. M. Neumann and J. T. V. Tran (eds.), *Clusters of Galaxies and the High Redshift Universe Observed in X-rays*

Rich, J.: 2001, *Fundamentals of Cosmology*

Riemer-Sorensen, S.: 2014, *ArXiv e-prints 1405.7943v2*

Robertson, H. P.: 1935, *ApJ* **82**, 284

Roediger, E., Kraft, R. P., Nulsen, P. E. J., Forman, W. R., Machacek, M., Randall, S., Jones, C., Churazov, E., and Kokotanekova, R.: 2015, *ApJ* **806**, 103

Rosati, P., Borgani, S., and Norman, C.: 2002, *ARA&A* **40**, 539

Rozo, E., Bartlett, J. G., Evrard, A. E., and Rykoff, E. S.: 2014, *MNRAS* **438**, 78

Russell, H. R., Sanders, J. S., and Fabian, A. C.: 2008, *MNRAS* **390**, 1207

Rybicki, G. B. and Lightman, A. P.: 1979, *Radiative processes in astrophysics*

Sarazin, C. L.: 1988, *X-ray emission from clusters of galaxies*

Saro, A., Mohr, J. J., Bazin, G., and Dolag, K.: 2013, *ApJ* **772**, 47

Schellenberger, G. and Reiprich, T. H.: 2015, *A&A* **583**, L2

Schellenberger, G., Reiprich, T. H., Lovisari, L., Nevalainen, J., and David, L.: 2015, *A&A* **575**, A30

Schlegel, D. J., Finkbeiner, D. P., and Davis, M.: 1998, *ApJ* **500**, 525

Schneider, P. and Seitz, C.: 1995, *A&A* **294**, 411

Schuecker, P.: 2005, in S. Röser (ed.), *Reviews in Modern Astronomy*, Vol. 18 of *Reviews in Modern Astronomy*, pp 76–105

Seward, F. D. and Charles, P. A.: 2010, *Exploring the X-ray Universe*

Seyfert, C. K.: 1943, *ApJ* **97**, 28

Sheth, R. K. and Tormen, G.: 1999, *MNRAS* **308**, 119

Shi, X., Komatsu, E., Nagai, D., and Lau, E. T.: 2015, *ArXiv e-prints 1507.04338v1*

Skrutskie, M. F., Cutri, R. M., Stiening, R., Weinberg, M. D., Schneider, S., Carpenter, J. M., Beichman, C., Capps, R., Chester, T., Elias, J., Huchra, J., Liebert, J., Lonsdale, C., Monet, D. G., Price, S., Seitzer, P., Jarrett, T., Kirkpatrick, J. D., Gizis, J. E., Howard, E., Evans, T., Fowler, J., Fullmer, L., Hurt, R., Light, R., Kopan, E. L., Marsh, K. A., McCallon, H. L., Tam, R., Van Dyk, S., and Wheelock, S.: 2006, *AJ* **131**, 1163

Smith, G. P., Mazzotta, P., Okabe, N., Ziparo, F., Mulroy, S. L., Babul, A., Finoguenov, A., McCarthy, I. G., Lieu, M., Bahe, Y., Bourdin, H., Evrard, A. E., Futamase, T., Haines, C. P., Jauzac, M., Marrone, D. P., Martino, R., May, P. E., Taylor, J. E., and Umetsu, K.: 2015, *ArXiv e-prints 1511.01919v1*

Smith, R. J., Hudson, M. J., Nelan, J. E., Moore, S. A. W., Quinney, S. J., Wegner, G. A., Lucey, J. R., Davies, R. L., Malecki, J. J., Schade, D., and Suntzeff, N. B.: 2004, *AJ* **128**, 1558

Smith, R. K., Brickhouse, N. S., Liedahl, D. A., and Raymond, J. C.: 2001, *ApJ* **556**, L91

Snowden, S. L., Collier, M. R., and Kuntz, K. D.: 2004, *ApJ* **610**, 1182

Snowden, S. L., Egger, R., Freyberg, M. J., McCammon, D., Plucinsky, P. P., Sanders, W. T., Schmitt, J. H. M. M., Truemper, J., and Voges, W.: 1997, *ApJ* **485**, 125

Steinhauser, D., Haider, M., Kapferer, W., and Schindler, S.: 2012, *A&A* **544**, A54

Stevens, I. R., Acreman, D. M., and Ponman, T. J.: 1999, *MNRAS* **310**, 663

Strüder, L., Briel, U., Dennerl, K., Hartmann, R., Kendziorra, E., Meidinger, N., Pfeffermann, E., Reppin, C., Aschenbach, B., Bornemann, W., Bräuninger, H., Burkert, W., Elender, M., Freyberg, M., Haberl, F., Hartner, G., Heuschmann, F., Hippmann, H., Kastelic, E., Kemmer, S., Kettenring, G., Kink, W., Krause, N., Müller, S., Oppitz, A., Pietsch, W., Popp, M., Predehl, P., Read, A., Stephan, K. H., Stötter, D., Trümper, J., Holl, P., Kemmer, J., Soltau, H., Stötter, R., Weber, U., Weichert, U., von Zanthier, C., Carathanassis, D., Lutz, G., Richter, R. H., Solc, P., Böttcher, H., Kuster, M., Staubert, R., Abbey, A., Holland, A., Turner, M., Balasini, M., Bignami, G. F., La Palombara, N., Villa, G., Buttler, W., Gianini, F., Lainé, R., Lumb, D., and Dhez, P.: 2001, *A&A* **365**, L18

Sun, M., Donahue, M., and Voit, G. M.: 2007, *ApJ* **671**, 190

Sun, M., Jones, C., Forman, W., Nulsen, P. E. J., Donahue, M., and Voit, G. M.: 2006, *ApJ* **637**, L81

Sun, M. and Vikhlinin, A.: 2005, *ApJ* **621**, 718

Sun, M., Voit, G. M., Donahue, M., Jones, C., Forman, W., and Vikhlinin, A.: 2009, *ApJ* **693**, 1142

Sunyaev, R. A. and Zeldovich, I. B.: 1980, *ARA&A* **18**, 537

Sunyaev, R. A. and Zeldovich, Y. B.: 1972, *Comments on Astrophysics and Space Physics* **4**, 173

Takahashi, T., Mitsuda, K., Kelley, R., Aharonian, F., Akamatsu, H., Akimoto, F., Allen, S., Anabuki, N., Angelini, L., Arnaud, K., and et al.: 2014, in *Society of Photo-Optical Instrumentation Engineers (SPIE) Conference Series*, Vol. 9144 of *Society of Photo-Optical Instrumentation Engineers (SPIE) Conference Series*, p. 25

Tarrant, E. R. M., van de Bruck, C., Copeland, E. J., and Green, A. M.: 2012, *Phys. Rev. D* **85(2)**, 023503

Thomas, P. A., Colberg, J. M., Couchman, H. M. P., Efstathiou, G. P., Frenk, C. S., Jenkins, A. R., Nelson, A. H., Hutchings, R. M., Peacock, J. A., Pearce, F. R., White, S. D. M., and Virgo Consortium: 1998, *MNRAS* **296**, 1061

Tinker, J., Kravtsov, A. V., Klypin, A., Abazajian, K., Warren, M., Yepes, G., Gottlöber, S., and Holz, D. E.: 2008, *ApJ* **688**, 709

Tormen, G.: 1997, *MNRAS* **290**, 411

Truemper, J.: 1982, *Advances in Space Research* **2**, 241

Tucker, W. H. and Gould, R. J.: 1966, *ApJ* **144**, 244

Urry, C. M. and Padovani, P.: 1995, *PASP* **107**, 803

Valentinuzzi, T., Woods, D., Fasano, G., Riello, M., D'Onofrio, M., Varela, J., Bettoni, D., Cava, A., Couch, W. J., Dressler, A., Fritz, J., Moles, M., Omizzolo, A., Poggianti, B. M., and Kjærgaard, P.: 2009, *A&A* **501**, 851

Väliviita, J. and Palmgren, E.: 2015, *J. Cosmology Astropart. Phys.* **7**, 15

Varela, J., D'Onofrio, M., Marmo, C., Fasano, G., Bettoni, D., Cava, A., Couch, W. J., Dressler, A., Kjærgaard, P., Moles, M., Pignatelli, E., Poggianti, B. M., and Valentinuzzi, T.: 2009, *A&A* **497**, 667

Vikhlinin, A.: 2006, *ApJ* **640**, 710

Vikhlinin, A., Burenin, R. A., Ebeling, H., Forman, W. R., Hornstrup, A., Jones, C., Kravtsov, A. V., Murray, S. S., Nagai, D., Quintana, H., and Voevodkin, A.: 2009a, *ApJ* **692**, 1033

Vikhlinin, A., Kravtsov, A., Forman, W., Jones, C., Markevitch, M., Murray, S. S., and Van Speybroeck, L.: 2006, *ApJ* **640**, 691

Vikhlinin, A., Kravtsov, A. V., Burenin, R. A., Ebeling, H., Forman, W. R., Hornstrup, A., Jones, C., Murray, S. S., Nagai, D., Quintana, H., and Voevodkin, A.: 2009b, *ApJ* **692**, 1060

Vikhlinin, A., Markevitch, M., Murray, S. S., Jones, C., Forman, W., and Van Speybroeck, L.: 2005, *ApJ* **628**, 655

Voges, W.: 1992, *The ROSAT all-sky X ray survey*, Technical report

Voges, W., Aschenbach, B., Boller, T., Bräuninger, H., Briel, U., Burkert, W., Dennerl, K., Englhauser, J., Gruber, R., Haberl, F., Hartner, G., Hasinger, G., Kürster, M., Pfeffermann, E., Pietsch, W., Predehl, P., Rosso, C., Schmitt, J. H. M. M., Trümper, J., and Zimmermann, H. U.: 1999, *A&A* **349**, 389

von der Linden, A., Mantz, A., Allen, S. W., Applegate, D. E., Kelly, P. L., Morris, R. G., Wright, A., Allen, M. T., Burchat, P. R., Burke, D. L., Donovan, D., and Ebeling, H.: 2014, *ArXiv e-prints 1402.2670v1*

Walker, A. G.: 1935, *MNRAS* **95**, 263

Wang, Q. D., Owen, F., and Ledlow, M.: 2004, *ApJ* **611**, 821

Wargelin, B. J., Markevitch, M., Juda, M., Kharchenko, V., Edgar, R., and Dalgarno, A.: 2004, *ApJ* **607**, 596

Warren, M. S., Abazajian, K., Holz, D. E., and Teodoro, L.: 2006, *ApJ* **646**, 881

Warren, M. S., Quinn, P. J., Salmon, J. K., and Zurek, W. H.: 1992, *ApJ* **399**, 405

Watson, W. A., Iliev, I. T., D'Aloisio, A., Knebe, A., Shapiro, P. R., and Yepes, G.: 2013, *MNRAS* **433**, 1230

Weisskopf, M. C., Tananbaum, H. D., Van Speybroeck, L. P., and O'Dell, S. L.: 2000, in J. E. Truemper & B. Aschenbach (ed.), *Society of Photo-Optical Instrumentation Engineers (SPIE) Conference Series*, Vol. 4012 of *Society of Photo-Optical Instrumentation Engineers (SPIE) Conference Series*, pp 2–16

White, M., Scott, D., and Silk, J.: 1994, *ARA&A* **32**, 319

White, S. D. M., Efstathiou, G., and Frenk, C. S.: 1993a, *MNRAS* **262**, 1023

White, S. D. M., Navarro, J. F., Evrard, A. E., and Frenk, C. S.: 1993b, *Nature* **366**, 429

Willingale, R., Starling, R. L. C., Beardmore, A. P., Tanvir, N. R., and O'Brien, P. T.: 2013, *MNRAS* **431**, 394

Willson, M. A. G.: 1970, *MNRAS* **151**, 1

Wolf, M.: 1906, *Astronomische Nachrichten* **170**, 211

Wright, E. L., Eisenhardt, P. R. M., Mainzer, A. K., Ressler, M. E., Cutri, R. M., Jarrett, T., Kirkpatrick, J. D., Padgett, D., McMillan, R. S., Skrutskie, M., Stanford, S. A., Cohen, M., Walker, R. G., Mather, J. C., Leisawitz, D., Gautier, III, T. N., McLean, I., Benford, D., Lonsdale, C. J., Blain, A., Mendez, B., Irace, W. R., Duval, V., Liu, F., Royer, D., Heinrichsen, I., Howard, J., Shannon, M., Kendall, M., Walsh, A. L., Larsen, M., Cardon, J. G., Schick, S., Schwalm, M., Abid, M., Fabinsky, B., Naes, L., and Tsai, C.-W.: 2010, *AJ* **140**, 1868

Zhang, Y.-Y., Andernach, H., Caretta, C. A., Reiprich, T. H., Böhringer, H., Puchwein, E., Sijacki, D., and Girardi, M.: 2011a, *A&A* **526**, A105

Zhang, Y.-Y., Finoguenov, A., Böhringer, H., Kneib, J.-P., Smith, G. P., Kneissl, R., Okabe, N., and Dahle, H.: 2008, *A&A* **482**, 451

Zhang, Y.-Y., Laganá, T. F., Pierini, D., Puchwein, E., Schneider, P., and Reiprich, T. H.: 2011b, *A&A* **535**, A78

Zhang, Y.-Y., Okabe, N., Finoguenov, A., Smith, G. P., Piffaretti, R., Valdarnini, R., Babul, A., Evrard, A. E., Mazzotta, P., Sanderson, A. J. R., and Marrone, D. P.: 2010, *ApJ* **711**, 1033

Zhao, D. H., Jing, Y. P., Mo, H. J., and Börner, G.: 2009, *ApJ* **707**, 354

ZuHone, J., Markevitch, M., and Zhuravleva, I.: 2015, *ArXiv e-prints 1505.07848v1*

Zwicky, F.: 1933, *Helvetica Physica Acta* **6**, 110

Öpik, E.: 1922, *ApJ* **55**, 406

Acknowledgments

Many people supported me in the past years to finish this thesis, so I take the opportunity here to express my gratitude. Titles are omitted for brevity. Affiliation is AIfA, Universität Bonn, if not stated otherwise.
I want to thank my supervisor, Thomas Reiprich, for the opportunity to perform this interesting research in his group. Starting from an internship in 2011, which later turned out as the baseline for a research paper, during the Master Thesis and finally during this PhD, I always felt supported and well advised. The friendly attitude in the whole group, the patience and always helpful suggestions by Thomas Reiprich, made it very easy, beside the research, to enjoy the daily business.
I also want to thank Jürgen Kerp, who advised me during my studies with helpful comments. Not only he often showed me alternative perspectives, but also helped with personal advises.
I acknowledge support by the International Max Planck Research School (IMPRS) for Astronomy and Astrophysics at the Universities of Bonn and Cologne, and by the Bonn-Cologne Graduate School for Physics and Astronomy (BCGS).
Moreover, I want to highlight the support and advise by Lorenzo Lovisari, who always had time to carefully discuss any issue during my work, and to monitor, together with Thomas Reiprich, Jürgen Kerp and Benjamin Winkel (MPIfR, Bonn), the progress of my thesis in several thesis advisory committee meetings.
Many thanks to Yu-Ying Zhang, who gave me access to the data of velocity dispersion mass estimates of HIFLUGCS, and to Sebastian Bocquet for providing the latest results on the baryonic halo mass function.
For the X-ray cross calibration analysis I acknowledge support by the IACHEC community, especially I would like to give thanks to Jukka Nevalainen (Tartu Observatory, Toravere, Estonia) for the many discussions and helpful advises from which my work benefit a lot.
The CHEERS consortium, led by Jelle de Plaa and Jelle Kaastra (SRON, Utrecht, the Netherlands), gave me very good advises for the spectral analysis of emission lines and resonant scattering. I want to thank the members for the interesting discussions during several meetings.
As a member of the German eROSITA consortium, I acknowledge the advises during meetings for my cross calibration analysis.
I want to express my special gratitude to Craig Sarazin for his great hospitality during my visit at the University of Virginia (Charlottesville, VA, USA) and the nice discussions, and Laurence David (Harvard-Smithsonian Center for Astrophysics, Cambridge, MA, USA) for introducing me to many people at the CfA and the great cooperation on the cross calibration analysis.
Finally, I thank my colleagues and friends, for the many fruitful discussions and very helpful advises for my work (alphabetical order):
Douglas Applegate, Katharina Borm, Sandra Burkutean, Alberto Doria, Jens Erler, Holger Israel (Durham University, Durham, UK), Brenda Miranda, Aarti Nagarajan, Florian Pacaud, Miriam Ramos, Christoph Schneider (Ruhr-Universität, Bochum) Bharadwaj Vijaysarathy.

—Despite the distance—

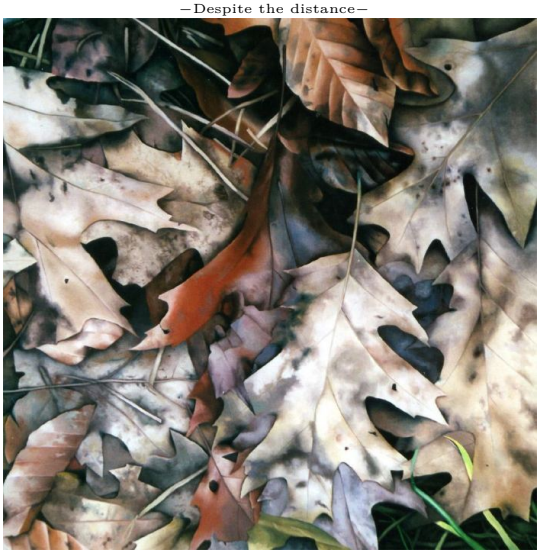

"Waldboden III" Hans G. Schellenberger (2001)